ERF and scale-free analyses of source-reconstructed MEG brain signals during a multisensory learning paradigm

Nicolas Zilber

UNIVERSITÉ PARIS SUD
Comprendre le monde, construire l'avenir®

STITS ECOLE DOCTORALE

Université Paris-Sud

Ecole Doctorale STITS
Sciences et Technologies de l'Information des Télécommunications et des Systèmes
Laboratoire: CEA Neurospin / INRIA Parietal

Discipline : Traitement du signal / Neurosciences

Thèse de doctorat

Soutenue le 10 mars 2014 par

Nicolas Zilber

ERF and scale-free analyses of source-reconstructed MEG brain signals during a multisensory learning paradigm

Analyses des champs évoqués et de l'invariance d'échelle des signaux cérébraux acquis en magnétoencéphalographie durant un paradigme d'apprentissage multisensoriel et reconstruits sur la surface corticale

Directeur de thèse :	M. Philippe Ciuciu	CEA, Neurospin, Saclay, France
Co-encadrant :	Mme. Virginie van Wassenhove	INSERM/CEA, Neurospin, Saclay, France

Composition du jury :

Rapporteurs :	Mme. Biyu Jade He	National Institutes of Health, Bethesda, USA
	M. Dimitri van de Ville	Univ. de Genève/EPFL, Genève, Suisse
Examinateurs :	M. Klaus Linkenkaer-Hansen	Univ. de Vrije, Amsterdam, Pays-Bas
	M. Fabrice Wendling	Univ. de Rennes 1, Rennes, France
	M. Ali Mohammad-Djafari	CNRS/Supélec/Paris-Sud, Gif-sur-Yvette, France
Invité :	M. Patrice Abry	CNRS/ENS Lyon, Lyon, France

Acknowledgments

Je souhaiterais remercier tout d'abord mes encadrants Philippe Ciuciu et Virginie van Wassenhove pour leur disponibilité, leur soutien et leur bienveillance. L'originalité de cette thèse leur revient avant tout car celle-ci est née du croisement de leurs domaines respectifs, à savoir ceux du traitement du signal et des neurosciences. Malgré parfois leurs différences de point de vue (inhérents à chacune de leur discipline), ils ont formé une super équipe et m'ont très bien encadré durant toute ma thèse.

I am also grateful to thank Biyu Jade He and Dimitri Van de Ville for reviewing my thesis and for sharing their comments to further improve the quality and the clarity of this manuscript. I would also like to thank Klaus Linkenkaer-Hansen, Fabrice Wendling and Ali Mohammad-Djafari for having accepted to serve as members of my thesis committee.

Un grand merci aussi à Patrice Abry pour ses conseils précieux sur l'analyse multifractale et à Alexandre Gramfort pour son aide à la résolution du problème inverse. Clairement, cette thèse n'aurait pas été ce qu'elle est sans leur collaboration.

Je souhaite aussi remercier Marco Buiatti et Leila Azizi ainsi que toutes les personnes de l'UNIACT pour leur aide à l'acquisition des données MEG et IRM : Véronique Joly-Testault, Gaëlle Médiouni-Cloarec, Laurence Laurier, Chantal Ginisty, Séverine Roger et Séverine Becuwe.

Je remercie aussi Anja Wühle et Michael Eickenberg pour avoir bien gentiment relu mon manuscrit de thèse pour l'une et mon article de Neuroimage pour l'autre.

Un très grand merci bien sûr à tous mes collègues et amis de Neurospin pour leur soutien et plus particulièrement à Anne, Anna, Baptiste, Lucille, Lucie et Toussaint pour avoir supporté mes chants dans l'open-space ainsi qu'aux «amis du café» : Antonio, Antoinette, Clémence, Laurence et compagnie... Vous me manquerez tous.

Je remercie bien entendu ma famille, mes frères et mes parents pour leur soutien inconditionnel.

Enfin, j'aimerais remercier Delphine pour tout son soutien, son amour et ses encouragements durant toutes ces années. Nos petits apéros du soir en guise de réconfort pendant la rédaction vont me manquer :p

Contents

List of Figures

List of Tables

List of Abbreviations

AC	Auditory Cortex
AV	AudioVisual (training with congruent acoustic textures)
AVn	AudioVisual (training with auditory random noise)
DFA	Detrended Fluctuation Analysis
dSPM	dynamic Statistical Parametric Mapping
EEG	Electroencephalography
ERF	Event-Related Field
fBm	fractional Brownian motion
FEF	Frontal Eye Field
fGn	fractional Gaussian noise
fMRI	functional Magnetic Resonance Imaging
hMT+	Human motion complex
IPS	Inferior Parietal Sulcus
ITC	Inferior Temporal Cortex
MEG	Magnetoencephalography
MNE	Minimum Norm Estimates
MRW	Multifractal Random Walk
mSTS	middle Superior Temporal Sulcus
pSTS	posterior Superior Temporal Sulcus
RDK	Random Dot Kinematogram
RHT	Reverse Hierarchy Theory
ROI	Region Of Interest
RSN	Resting-State Network
RT	Reaction Time
SSP	Signal-Space Projection

SSS Signal-Space Separation

TIL Task-Irrelevant Learning

V Visual (training)

vlPFC ventral lateral PreFrontal Cortex

WLBMF Wavelet-Leader Based Multifractal Formalism

Résumé en français

Contexte

La neuroimagerie fonctionnelle est une discipline relativement récente ayant pour but la compréhension des mécanismes cérébraux à l'origine de notre comportement, telles que nos capacités mentales (par exemple le langage, la perception, la conscience) ou certaines pathologies (la maladie d'Alzheimer ou de Parkinson), grâce à l'utilisation de techniques d'imagerie non-invasives (c-à-d ne nécessitant pas d'ouvrir le crâne). Considérant qu'un processus cognitif se réalise à travers l'activation spécifique de certaines aires cérébrales à des instants donnés, le choix du mode d'imagerie dépend essentiellement de la caractéristique d'intérêt (localisation ou décours temporel de l'activité) : ainsi par exemple, l'imagerie par résonance magnétique fonctionnelle (IRMf) mesurant le signal BOLD (de l'anglais *Blood-Oxygen-Level Dependent*) — soit les lentes variations du débit sanguin associées à l'activité neuronale — est la mieux qualifiée pour localiser les aires activées. Inversement, l'électroencéphalographie (EEG) et la magnétoencéphalographie (MEG) mesurent respectivement les champs électriques et magnétiques générés par les neurones et sont particulièrement adaptées pour connaître la dynamique temporelle de l'activité cérébrale (de l'ordre de la milliseconde).

Quelque soit le choix du mode d'imagerie, la plupart des études adoptent la même approche en se focalisant sur l'activation du cerveau associée à un évènement (tel que la présentation d'un stimulus ou la réponse du sujet) durant une tâche cognitive. C'est par exemple le cas en MEG avec l'analyse des champs évoqués (ou ERF, d'après l'anglais Event-Related Fields), dont le but est de caractériser la réponse temporelle des neurones en réponse à une stimulation externe. Le principe de cette méthode est relativement simple : en répétant le stimulus un grand nombre de fois et en moyennant le signal à travers tous ces essais, le rapport signal-sur-bruit augmente et seule la réponse «évoquée» reste intacte. Bien que cette approche soit efficace pour décrire les évènements neuronaux impliqués dans la tâche avec une bonne résolution temporelle, elle ne permet pas d'analyser l'activité spontanée — l'essentiel de l'activité cérébrale — et ce malgré son importance fonctionnelle [Gusnard 2001, de Pasquale 2010, Sadaghiani 2010]. Le cerveau reste en effet actif en l'absence de stimuli ou d'actions (tel qu'au repos ou durant le sommeil) et cette activité joue un rôle crucial par exemple dans le développement et la perception.

Les premières observations de l'activité spontanée ont été obtenues en EEG par Hans Berger en 1931 et se limitaient à décrire les ondes «alpha», un rythme cérébral oscillant autour de 10 Hz localisé principalement dans le lobe occipital. Depuis lors, les signaux mesurés en M/EEG sont traditionnellement décomposés en bandes oscillatoires (telles que par exemple, l'alpha, le beta ou le gamma dont les pics de puissance apparaissent à des fréquences différentes sur les spectres de Fourier) auxquelles on associe divers rôles fonctionnels. Cependant, cette approche

ne tient pas compte des propriétés que l'on sait arythmiques — ou non-oscillatoires — de l'activité neuronale [Bullock 2003].

Celle-ci présente en effet des fluctuations très lentes (inférieures approximativement à 1 Hz) caractérisées par un spectre de puissance diminuant en $1/f$ [Novikov 1997, He 2010], signe d'une dynamique temporelle invariante d'échelle — autrement dit fractale, ou bien encore autosimilaire [Bak 1988]. Le terme «fractale» fait généralement référence à des figures géométriques particulières (cf. Fig. A) qui restent identiques (soit de manière exacte, soit au sens *statistique*) quelque soit l'échelle à laquelle on les observe. De façon similaire, un signal temporel est dit «fractal» ou «invariant d'échelle» lorsque ses propriétés statistiques restent inchangées après une dilatation de l'axe temporel et une renormalisation appropriée. Deux implications possibles pour le fonctionnement neuronal sont alors envisageables : l'encodage de l'information peut être temporellement multiplexée et il peut se faire suivant différents niveaux de compression.

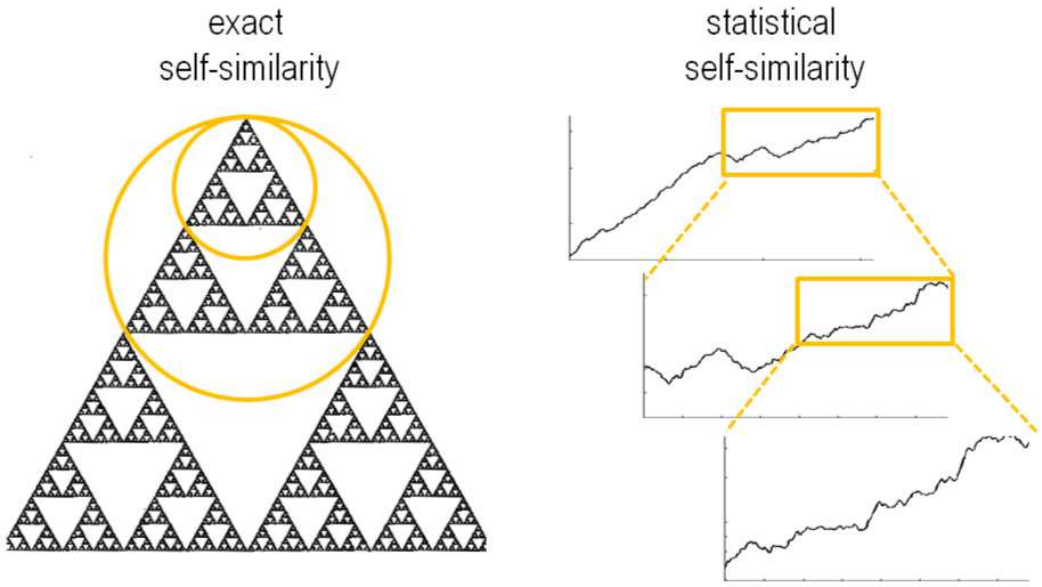

Figure A : Exemple de fractales. Le triangle de Sierpinski (*à gauche*) est une image fractale avec une autosimilarité exacte : le motif est rigoureusement identique à chaque échelle (indiquée par les cercles oranges). Dans le cas des signaux temporels fractals (*à droite*), l'autosimilarité est statistique : chaque version dilatée, puis renormalisée, possède les mêmes propriétés statistiques que la version d'origine (dans une certaine gamme d'échelle néanmoins, puisque limitée par la taille et l'échantillonnage du signal).

En pratique, les propriétés d'invariance d'échelle peuvent être décrites avec plus ou moins de détails : dans un premier temps, la connaissance d'un unique paramètre, appelé *autosimilarité*, nous permet de choisir correctement le coefficient de renormalisation en fonction du degré de dilatation de façon à ce que les propriété-

tés statistiques restent inchangées. Ce paramètre reflète aussi la régularité globale du signal et l'absence de temps caractéristique pouvant décrire sa dynamique (en terme de corrélation). Il peut être approximativement approché par l'exposant du spectre fréquentiel en $1/f$. Dans un second temps, une mesure plus fine appelée *multifractalité*, prend en compte les fluctuations locales — ou les singularités — à travers le temps qui ne peuvent être observées via un simple spectre de puissance. Autrement dit, la présence de multifractalité implique qu'une gamme continue de valeurs est nécessaire pour décrire la dynamique du signal et que la connaissance seule du paramètre d'autosimilarité n'est pas suffisante.

Dans la plupart des études de neuroimagerie, les analyses d'invariance d'échelle étaient non seulement limitées à l'estimation de l'autosimilarité, mais aussi réalisées avec des outils d'analyse (telle que l'analyse des fluctuations redressées ou en anglais DFA [Peng 1994, Linkenkaer-Hansen 2001]) manquant significativement de robustesse et de précision en présence de données non-stationnaires et non-gaussiennes [Veitch 1999]. Une meilleur approche, l'analyse par ondelettes, permet non seulement de surmonter ces difficultés mais en plus d'estimer conjointement la multifractalité. Dans cette thèse, nous proposons d'en tirer parti en utilisant la méthode récente du formalisme multifractal basé sur les coefficients d'ondelettes dominants (WLBMF en anglais) [Wendt 2007] dont la performance a été démontrée à la fois théoriquement et en pratique sur des données réelles [Ciuciu 2012].

Néanmoins, une question primordiale se pose : ces propriétés d'invariance d'échelle importent-elles vis à vis du comportement et du fonctionnement cérébral ? Plusieurs études expérimentales le suggèrent, en reportant notamment des modulations du spectre en $1/f$ (c-à-d de l'autosimilarité) en fonction de différents états cognitifs tels qu'entre du simple repos ou de l'activité liée à l'exécution d'une tâche [He 2011, Ciuciu 2012], différents stades de sommeil [Weiss 2009, He 2010], différents niveaux de performance associée à une tâche [Buiatti 2007, Wink 2008], des classes d'âge [Suckling 2008], les sexes [Jausovec 2010] et les pathologies [Maxim 2005, Suckling 2008]. Bien que peu d'études soient allés au delà de l'autosimilarité, toutes (exceptée une portant sur les micro-états en EEG [Van de Ville 2010]) s'accordent sur l'existence de multifractalité dans l'activité cérébrale [Shimizu 2004, Popivanov 2005, Ciuciu 2012, Suckling 2008, Wink 2008, Weiss 2009].

L'interprétation reste cependant difficile et de plus amples investigations sont nécessaires afin de comprendre dans quelle mesure la dynamique fractale est un marqueur fonctionnel de l'activité cérébrale. En accord avec une récente étude conduite en IRMf et montrant que l'apprentissage pouvait modifier l'activité du cerveau au repos [Lewis 2009], nous nous sommes demandés si, de façon similaire, les propriétés d'invariance d'échelle pouvaient aussi être modulées par l'apprentissage et si oui, comment celles-ci varieraient au cours de l'entraînement. Dans ce but, nous avons développé un paradigme d'apprentissage alternant des blocs de repos et d'exercice visuel et au cours desquels l'activité neuronale des participants serait enregistré en MEG (cf. Fig. B).

L'apprentissage est un processus cognitif fortement lié à la notion de *plasticité*, c-à-d la capacité du cerveau à se modifier à n'importe quel niveau structurel (par

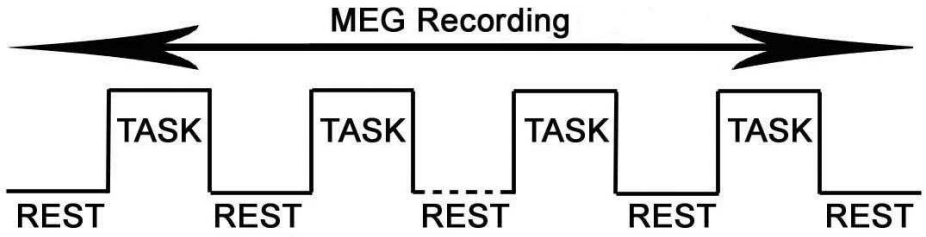

Figure B : Idée de base et conception du paradigme d'apprentissage. Afin de mieux comprendre le rôle fonctionnel de la dynamique fractale de l'activité cérébrale au repos et durant l'exécution d'une tâche, nous avons élaboré un paradigme dans lequel les participants s'entraîneraient à réaliser une tâche visuelle, interrompu périodiquement par des périodes de repos. Pendant tout ce temps, l'activité neuronale serait enregistré en MEG et soumis plus tard à une analyse multifractale.

exemple, synaptique, neuronal ou cortical). Historiquement, on pensait que la plasticité ne pouvait avoir lieu que durant une période critique dans l'enfance et qu'elle disparaissait chez les adultes. Depuis la fin des années 60 cependant, nous savons que le cerveau reste un système dynamique capable de s'adapter et de changer au cours d'une vie entière, permettant ainsi le développement, la mémorisation, l'acquisition ou l'amélioration de nouvelles compétences, et même la réparation de zones cérébrales endommagées. En particulier, la simple répétition d'une tâche visuelle (comme décrite dans notre paradigme) peut conduire à de l'apprentissage et à une plasticité spécifique ayant lieu dans les aires visuelles primaires. On appelle cela *l'apprentissage perceptuel* [Sasaki 2010]. Néanmoins, ce mécanisme peut être relativement lent et faible chez les adultes en l'absence d'entraînement efficace. Nous étions donc confrontés à un premier défi : proposer un entraînement suffisamment efficace pour induire de la plasticité en un court laps de temps chez tous nos participants.

Cela nous a amené à considérer le bénéfice potentiel apporté par l'apprentissage multisensoriel [Shams 2008] : les exemples de plasticité les plus impressionnants ont en effet été reportés chez les individus privés d'une modalité sensorielle [Bach-y Rita 2003]. Par exemple, la région corticale impliquée dans le traitement du mouvement visuel, hMT+, peut être «recyclée» pour le traitement du mouvement audio ou tactile chez les aveugles de naissance [Poirier 2005, Ricciardi 2007]. Plus généralement, des interactions multisensorielles ont été mises en évidence dans de nombreuses aires corticales et viennent contredire le point de vue classique que les aires sensorielles sont strictement indépendantes les unes des autres, jusqu'à remettre en question l'existence d'une spécificité sensorielle. Il a été ainsi suggéré, d'après la «théorie supramodale» [Pascual-Leone 2001], que certaines aires telle que hMT+ puissent présenter une sélectivité fonctionnelle indépendamment de la modalité sensorielle (audio, visuelle, tactile...) et par conséquent être recyclées. Plusieurs questions se posent alors [Bavelier 2010], notamment celle-ci : le recyclage fonctionnel est-il simplement la conséquence d'une perte sensorielle ayant

eu lieu très tôt, ou bien est-il soutenu par des aires supramodales pré-existantes [Bedny 2010, Morrone 2010, Dormal 2011] ?

Sans perdre de vue notre objectif principal (c-à-d comprendre l'impact de l'apprentissage sur l'invariance d'échelle de la dynamique cérébrale), nous nous sommes aussi intéressés à ce problème en cherchant à savoir si l'apprentissage, dans le cas d'un exercice de discrimination de cohérence visuelle, pouvait bénéficier d'un traitement supramodal. Dans ce but, de nouveaux stimuli ont été développés et consistent en des textures acoustiques partageant les statistiques temporelles de nuages de points visuels (RDK, de l'anglais Random Dot Kinematogram). Trois types d'entraînement ont été proposés durant l'enregistrement en MEG pour apprendre à discriminer la cohérence visuelle des points : un premier groupe de participants s'est entraîné sans son (V), un autre avec des textures acoustiques congruentes (AV) et un autre enfin avec un simple bruit audio (AVn). Notre hypothèse de base était qu'une stimulation audiovisuelle congruente (soit l'entraînement AV) permettrait d'obtenir un meilleur apprentissage visuel et une plus forte plasticité.

Objectifs

Afin d'accomplir les objectifs principaux de cette thèse, nous devons nous assurer au préalable que le paradigme d'apprentissage soit suffisamment efficace et bien contrôlé pour pouvoir combiner les mesures comportementales avec les enregistrements MEG de chaque participant. Cela fait l'objet de la première partie.

Ce travail contient alors deux objectifs :

- Comprendre les mécanismes neuronaux de l'apprentissage multisensoriel impliqué dans notre expérience au moyen d'analyses ERF classiques réalisées sur les signaux MEG reconstruits sur la surface corticale (c-à-d dans «l'espace source»). Plus précisément, nous voulons tester si la plasticité sensorielle peut être renforcée par un traitement multisensoriel/supramodal déjà présent chez des individus sains en comparant trois types d'entraînement (V, AV et AVn).

- Examiner plus en détails les propriétés d'invariance d'échelle de l'activité cérébrale et en comprendre le rôle fonctionnel et ses conséquences sur le comportement. Plus précisément, nous voulons savoir si la multifractalité et l'autosimilarité apportent de manière indépendante de l'information sur le fonctionnement cérébral et les processus impliqués dans l'apprentissage et la plasticité.

Ces deux points sont abordés respectivement dans la deuxième et la troisième partie de cette thèse.

Organisation et principaux résultats

Partie I — Acquisition des données et psychophysiques

Chapitre 1 — Paradigme et stimuli

Comment peut-on obtenir un apprentissage efficace en un court laps de temps ?

Pour répondre à cette question, nous proposons de faire un bilan des études psychophysiques et cognitives dédiées à l'apprentissage perceptuel et multisensoriel. Nous présentons ensuite le paradigme et les stimuli (cf. Fig. C et D) utilisés dans nos trois types d'apprentissage : visuel (V), audiovisuel impliquant l'utilisation de textures acoustiques (AV) ou d'un simple bruit audio (AVn). Dans la suite, nous ferons systématiquement référence à ce chapitre pour la description du protocole expérimental et des participants.

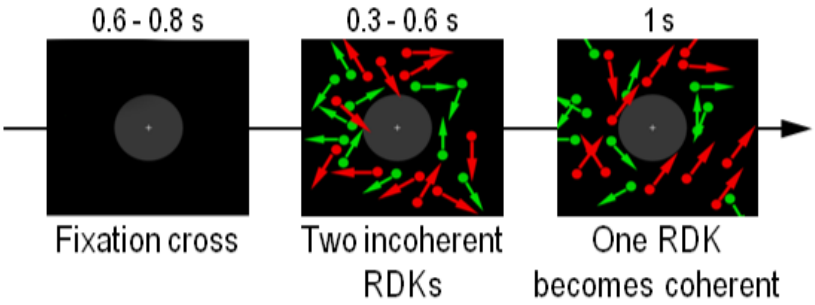

Figure C. Stimuli visuels. Le stimulus visuel pouvait être décomposé en trois phases : une croix de fixation seule (durant 0.6–0.8 s), suivi de l'apparition de deux nuages de points (RDKs) incohérents rouges et verts. Puis au bout de 0.3–0.6 s, l'un de ces RDKs devenait cohérent durant 1 s (ici 75% des points rouges partent dans la même direction). Les participants devaient indiquer la couleur du RDK cohérent indépendamment de la direction du mouvement.

Chapitre 2 — Psychophysiques

Les entraînements sont-ils bien efficaces d'un point de vue comportemental ?

Ici, nous analysons les mesures comportementales avant et après entraînement en fonction des trois catégories d'entraînement. Tous les participants se sont améliorés après seulement 20 min d'entraînement en discriminant plus facilement la cohérence visuelle et en répondant plus rapidement (Fig. E). Conformément à notre hypothèse, les individus entraînés en AV ont plus progressé que les autres (via une plus forte diminution du seuil perceptuel). De plus, l'absence significative de hausse du niveau de confiance semble indiquer que cet apprentissage se soit fait de manière implicite, excluant ainsi la possibilité d'une association consciente entre la cohérence des points visuels et celle des textures acoustiques. Ces premiers résultats semblent valider l'hypothèse d'un traitement supramodale bénéfique à l'apprentissage dans le cas AV. Ces données comportementales sont par la suite réutilisées dans les chapitres 5 et 7 afin d'en déduire leurs corrélats neuronaux.

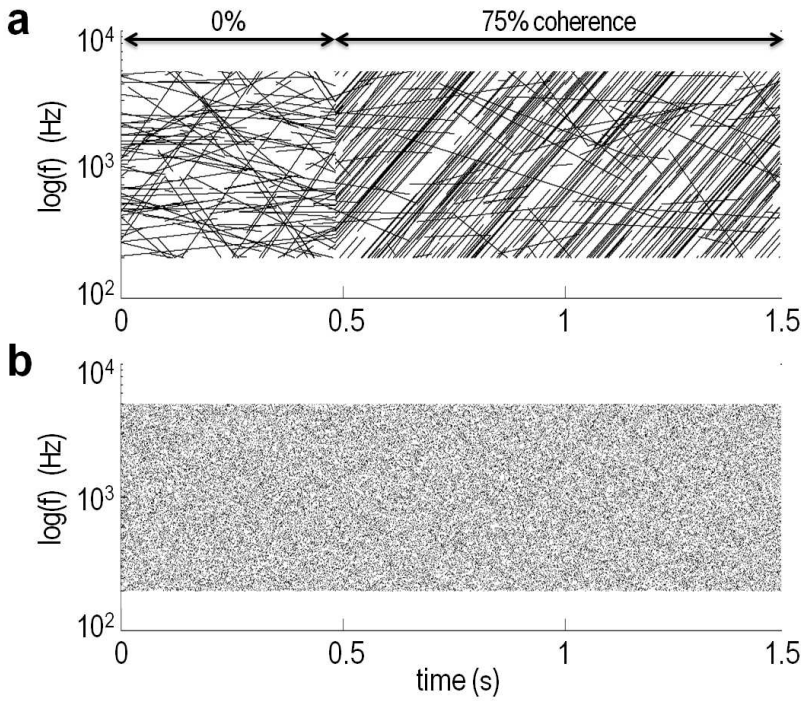

Figure D. Stimuli audio présentés durant les entraînements AV et AVn. Les spectrogrammes montrent la fréquence du signal (échelle logarithmique) en fonction du temps. **(a)** Exemple de texture acoustique utilisée pour les entraînements AV. Par analogie avec les RDKs, le niveau de cohérence correspond ici à la proportion de «rampes» ayant la même pente à un instant donné. Ici, la texture est incohérente durant 0.5 s puis cohérente à 75% pendant la seconde restante. **(b)** Bruit acoustique utilisé dans l'entraînement AVn. Ce son est totalement décorrélé avec les RDKs visuels mais possède la même amplitude, la même durée et le même domaine fréquentiel qu'une texture acoustique.

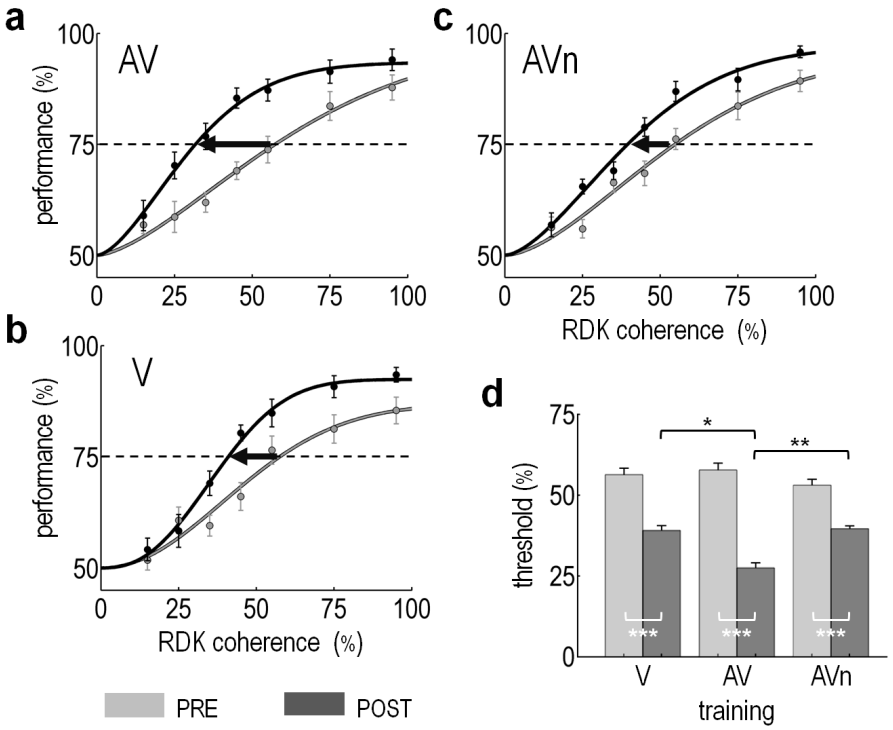

Figure E. Effets des entraînements sur le seuil perceptuel. La performance moyenne (±1 s.e.m.) est tracée en fonction des niveaux de cohérence visuelle dans les groupes AV **(a)**, V **(b)** et AVn **(c)** avant (PRE, gris clair) et après (POST, gris foncé) entraînement. Pour simple illustration, les courbes psychométriques sont approximées par des fonctions de Weibull dans chaque groupe. Le seuil perceptuel est défini par le niveau de cohérence visuelle d'un RDK correspondant à 75% de bonnes réponses. Une amélioration se traduit donc par une baisse du seuil (flèche noire). **(d)** Seuils de discrimination moyens (+2 s.e.m.) déduis des courbes de Weibull individuelles avant et après entraînement dans chaque groupe. Le seuil est significativement plus réduit dans le groupe AV que dans les groupes V et AVn. Le niveau de signification statistique est indiquée par *, ** et *** correspondant à des p-valeurs (corrigées avec Bonferroni) inférieures respectivement à 0.05, 0.01 et 0.001.

Chapitre 3 — La magnétoencéphalographie

Pourquoi et comment peut-on mesurer l'activité neuronale avec la magnétoencéphalographie ?

Pour pouvoir interpréter correctement les résultats des analyses ERF et des analyses fractales, il est crucial de bien comprendre la nature des signaux que nous utilisons. C'est pourquoi dans ce chapitre, nous présentons les principes neurophysiologiques de la MEG (exemple Fig. F) et les procédures classiques de pré-traitement des données. Nous décrivons ensuite les techniques permettant de résoudre le problème inverse, c-à-d de reconstruire l'activité corticale à l'origine des signaux observés dans les capteurs. Dans la dernière section, nous détaillons les paramètres de l'acquisition MEG, des méthodes de pré-traitement et de reconstruction des sources qui ont été utilisées aussi bien pour les analyses ERF que les analyses fractales.

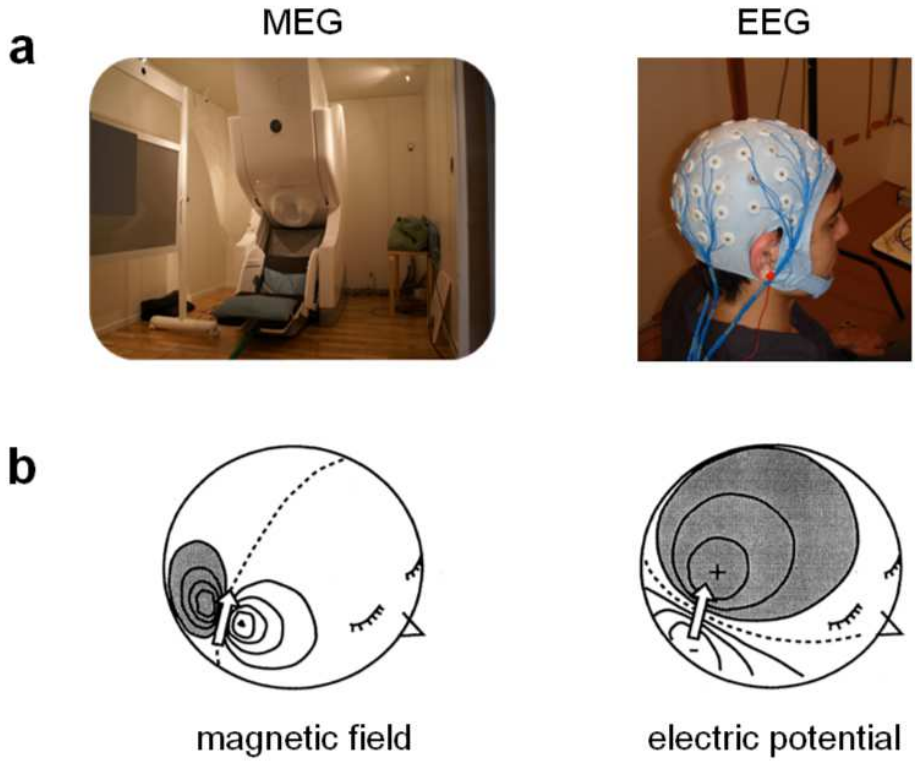

Figure F. La magnétoencéphalographie et l'électroencéphalographie. (a) Installation MEG utilisée actuellement à Neurospin (Neuromag Elekta LTD, Helsinki, Finlande) et bonnet EEG utilisé à l'université de Kyushu (Nexstim, Helsinki, Finlande). **(b)** Illustration schématique et idéalisée du champ magnétique et du potentiel électrique produits par une source neuronale tangentielle modélisée par un dipôle (flèche blanche). (Adapté de [Hämäläinen 1993]).

Partie II — L'analyse ERF standard

Chapitre 4 — Hypothèses neuronales

Que peut-on raisonnablement observer avec l'analyse ERF ?

Dans ce chapitre, nous décrivons tout d'abord les principes de l'analyse ERF (Fig. G). Puis, nous passons en revue les différents candidats neuronaux pouvant être potentiellement impliqués au cours de l'entraînement en se basant sur de précédentes études de neuroimagerie. Pour finir, nous élaborons quelques prédictions/hypothèses sur les corrélats neuronaux de l'apprentissage pouvant être observés avec l'analyse ERF.

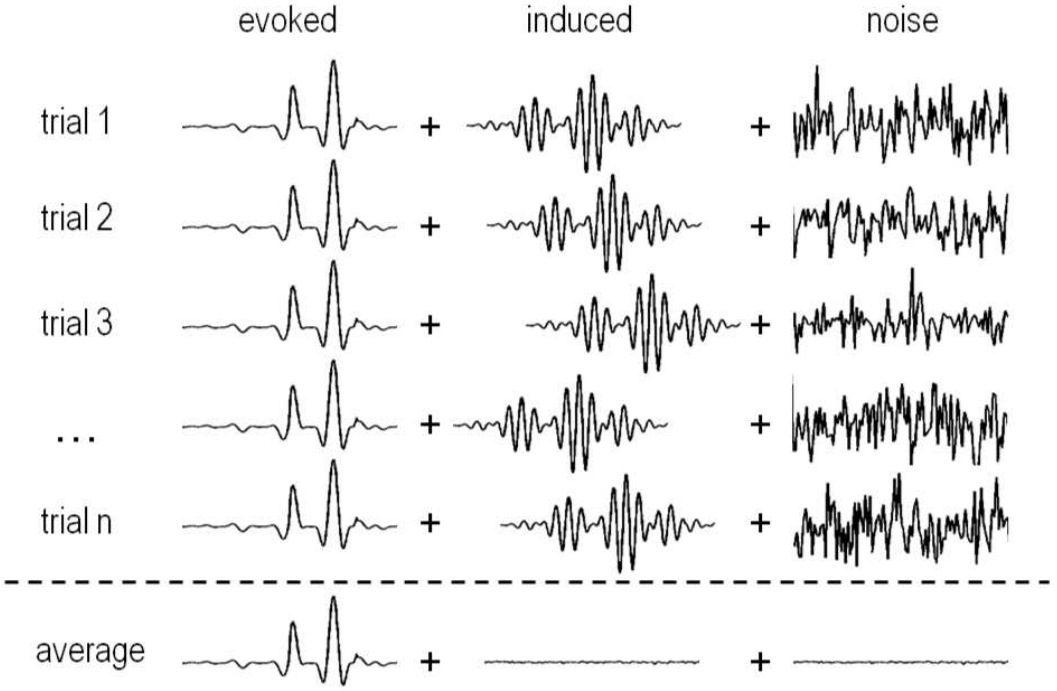

Figure G. Principes de l'analyse des champs évoqués. Le but de l'analyse ERF consiste à estimer l'activité évoquée en phase avec l'apparition d'un stimulus (ou plus généralement un évènement). Elle se base sur l'hypothèse que le signal est formé par trois composantes : évoquée, induite et aléatoire (c-à-d qui change à chaque essai). Contrairement à la composante évoquée, celle induite n'est pas calée en phase avec l'instant d'apparition du stimulus. Ainsi, les composantes induites et aléatoires sont fortement réduites lorsque le signal est moyenné à travers plusieurs essais, ne laissant intacte que la composante évoquée.

Chapitre 5 — Analyse ERF des données acquises en MEG

Peut-on expliquer d'un point de vue neuronal les différences comportementales observées entre les trois groupes d'entraînement avec l'analyse ERF ?

Ce chapitre présente les principaux résultats de l'analyse ERF conduite dans l'espace source en comparant l'activité avant et après apprentissage dans chaque groupe. Plusieurs mécanismes semblent être à l'origine de la progression des indi-

vidus : tout d'abord, l'augmentation de la réponse neuronale dans l'aire ventrale visuelle (ITC) commune aux trois groupes de participants suggère un renforcement de l'association couleur/mouvement pour des niveaux de cohérence visuelle facilement détectables. Communément aux trois groupes, l'apprentissage semble être reflété par une plus forte implication du cortex préfrontal ventrolatéral (vlPFC), ce qui s'expliquerait par une hausse de l'attention. Cependant, l'entraînement AV se distingue par un gain de sélectivité/plasticité dans l'aire corticale dédiée au traitement du mouvement visuel (hMT+), comme le montre les mesures neurométriques (Fig. H). De plus, le réseau impliqué dans l'analyse du mouvement visuel est plus large après un entraînement audiovisuel (AV et AVn) que visuel (V), ce qui suggère l'implication de régions corticales associatives ayant permis la plasticité dans hMT+, notamment celle d'aires multisensorielles telles que pSTS et mSTS (Fig. I). Nous interprétons ces résultats dans le contexte de la théorie de l'apprentissage hiérarchique inversé (introduite au chapitre 1) en montrant l'existence d'un traitement supramodal ayant permis d'améliorer le traitement associant couleur et mouvement et la discrimination de la cohérence visuelle.

Cette étude contribue, à notre connaissance, à montrer pour la première fois en MEG que l'information acoustique peut altérer de manière sélective les profils de réponse des aires visuelles chez les individus sains, et approfondir ainsi notre compréhension du traitement supramodal et d'une représentation invariante des objets dans le cortex. De plus, ces résultats peuvent avoir d'importantes implications pratiques dans l'élaboration de protocoles d'entraînement chez les personnes atteintes d'un handicap sensoriel ou utilisatrices d'appareils de substitution sensorielle.

Partie III — Analyse d'invariance d'échelle

Chapitre 6 — Propriétés d'invariance d'échelle : Définitions et applications

Pour quelle raison et de quelle manière devrions-nous réaliser des analyses fractales en MEG ?

Dans ce chapitre, nous expliquons tout d'abord le contexte ayant amené à étudier les propriétés d'invariance d'échelle de l'activité cérébrale (Fig. J). Nous donnons ensuite le cadre théorique/mathématique dans lequel sont définies l'autosimilarité et la multifractalité, ainsi que l'état de l'art des méthodes permettant d'estimer ces quantités. Nous nous attardons plus particulièrement sur la méthode utilisée au chapitre 7, c-à-d le formalisme multifractal basé sur les coefficients d'ondelettes dominants (WLBMF).

Chapitre 7 — Analyse de l'invariance d'échelle des données acquises en MEG

Y a t-il une quelconque information dans l'autosimilarité et la multifractalité des signaux MEG qui puisse nous permettre de mieux comprendre les processus neuronaux à l'origine de l'apprentissage et de la plasticité ?

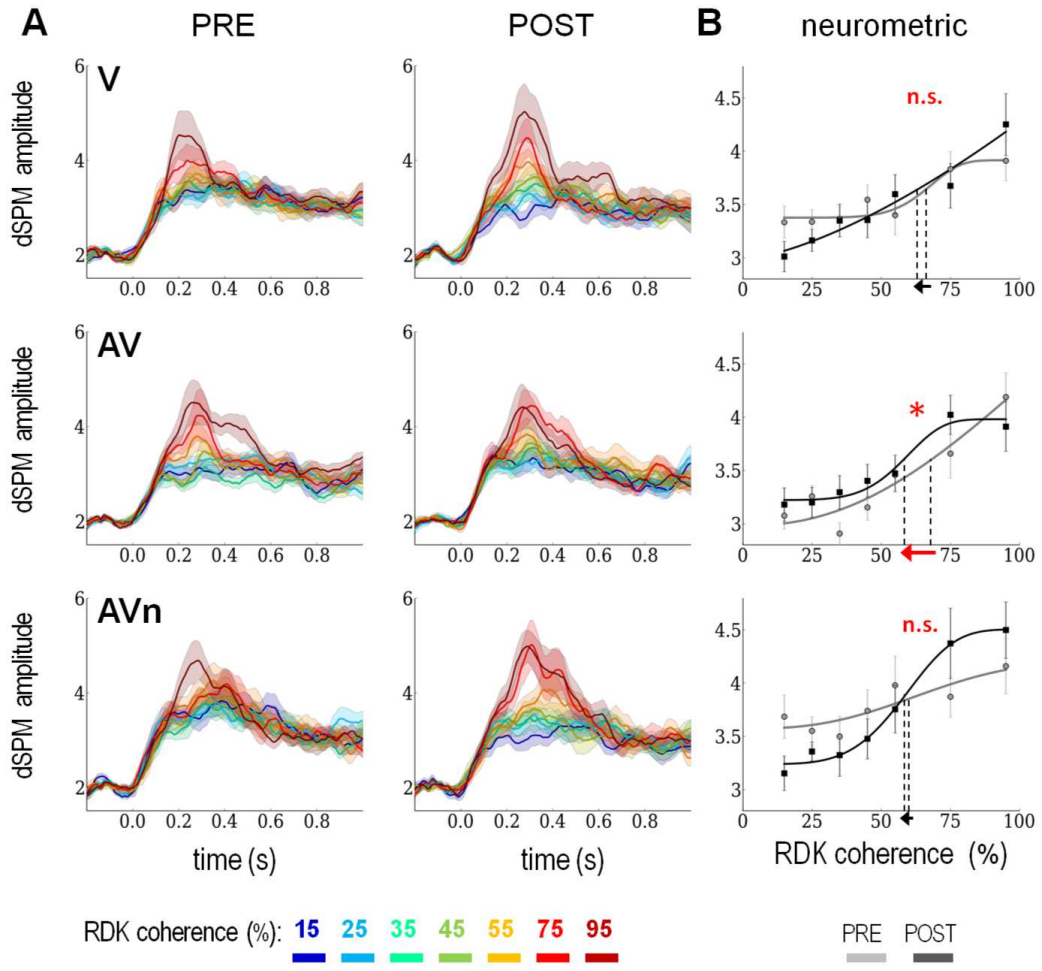

Figure H. Réponses évoquées dans hMT+ avant et après entraînement en fonction de la cohérence visuelle du RDK (A) et fonctions neurométriques (B). (A) La réponse évoquée apparait clairement dans chaque groupe environ 200 ms après l'apparition de la cohérence (à t=0). Plus la cohérence visuelle est élevée, plus l'amplitude de la réponse l'est aussi. Initialement, le profil de réponse est similaire dans les trois groupes. Celui-ci change après entraînement : V et AVn présentent un comportement similaire, à savoir un étalement de l'amplitude de la réponse évoquée en fonction de la cohérence. AV ne semble présenter aucun changement. Cependant, par similitude avec la psychométrie, l'amplitude (ici moyennée entre 0.2 et 0.5 s) peut être modélisée en fonction de la cohérence par une fonction de Weibull (courbes neurométriques). **(B)** En guise d'illustration, les courbes neurométriques estimées au niveau de chaque groupe sont présentées ici. Seul AV présente une diminution significative du seuil neurométrique. La sensibilité de hMT+ pour discriminer la cohérence s'est donc essentiellement améliorée dans le groupe AV.

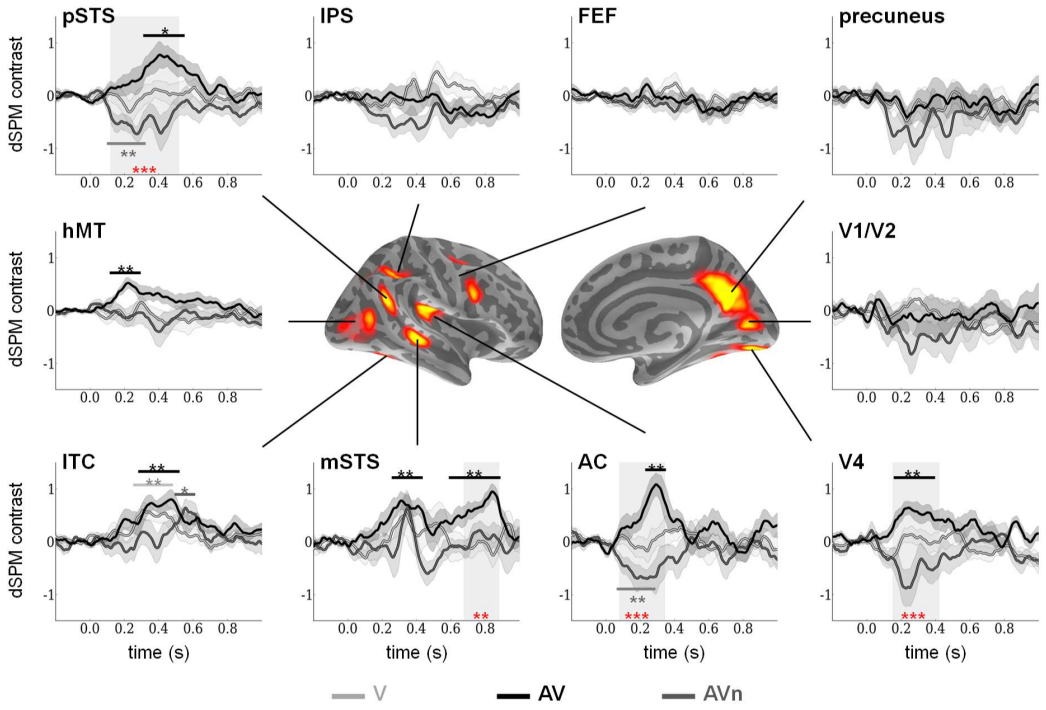

Figure I. Effets principaux de l'entraînement dans les trois groupes à travers tous les niveaux de cohérence. Après reconstruction des données MEG dans l'espace source (MNE-dSPM), les contrastes moyens (±1 s.e.m.) entre avant et après entraînement ont été calculés pour chaque groupe et dans chaque région d'intérêt en fusionnant tous les niveaux de cohérence. Les contrastes sont reportés en gris, noir et gris foncé pour les groupes V, AV et AVn respectivement. Les contrastes significativement non-nuls sont indiqués par des barres grises (V), noires (AV) ou gris foncées (AVn). Les effets principaux de l'entraînement V indépendamment du niveau de cohérence visuelle peuvent être observés dans ITC entre environ 200 et 400 ms après l'apparition de la cohérence. En AV, ces effets sont bien plus nombreux et peuvent être vus notamment dans hMT+, ITC, mSTS, V4, pSTS et le cortex auditif AC. En AVn, seuls ITC, pSTS et AC présentent des changements significatifs. Les effets du type d'entraînement sont testés avec un test de Fisher : les zones grisées indiquent la latence à laquelle une différence significative existe entre les trois groupes. Les étoiles rouges représentent leur niveau de signification statistique. Quatre régions capturent essentiellement ces différences : le STS median et postérieur, V4 et AC. Les p-valeurs corrigées inférieures à 0.05, 0.01 et 0.001 sont indiquées respectivement par les symboles *, ** et ***.

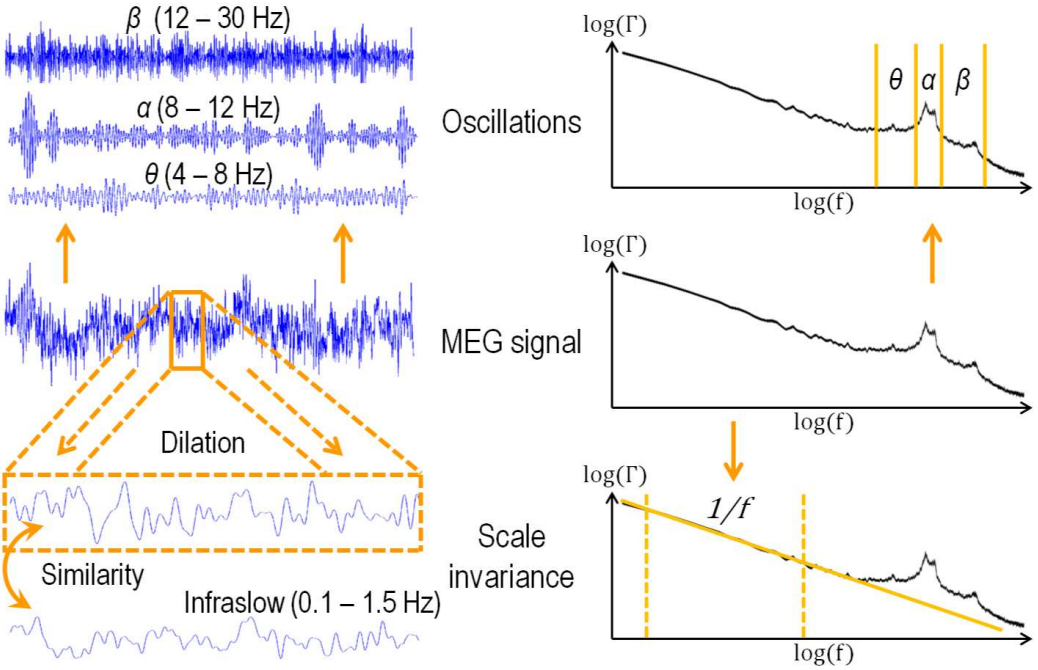

Figure J. Deux approches complémentaires : étude des oscillations ou de l'invariance d'échelle. Un signal MEG typique représenté dans le domaine temporel (*au milieu à gauche*) et fréquentiel (*au milieu à droite*) est habituellement décomposé sous forme d'oscillations (*en haut à gauche*) identifiées par leurs pics présents dans le spectre de puissance (*en haut à droite*) — ici theta (θ), alpha (α) et beta (β). De façon moins évidente, la puissance spectrale dans les basses fréquences présente une caractéristique en $1/f$, c-à-d une pente linéaire lorsque le spectre est tracé sur des axes logarithmiques (*en bas à droite*). Dans le domaine temporel (*en bas à gauche*), cela signifie que l'activité arrhytmique est invariante par échelle, autrement dit qu'elle possède les mêmes propriétés statistiques que sa version dilatée et renormalisée.

Ce chapitre est dédié à l'analyse d'invariance d'échelle des données MEG acquises dans notre expérience. Il contient deux études préliminaires et une étude principale. Dans un premier temps, nous avons vérifié l'existence de propriétés d'invariance d'échelle au niveau des capteurs (première étude préliminaire) et dans quelques aires restreintes sur la surface corticale (seconde étude préliminaire). Ces propriétés étaient modulées non seulement entre le repos et la tâche, mais aussi entre avant et après entraînement. Plus important, l'analyse principale montre que l'autosimilarité et la multifractalité estimées entièrement sur la surface corticale présentent un couplage dynamique dans quelques aires tout au long de l'entraînement : tandis que l'autosimilarité diminue généralement après apprentissage (corrélant parfois avec la progression comportementale telle que dans V4/ITC gauche et hMT+/pSTS droit), des aires plus spécifiques (telles que hMT+/pSTS et IPS) présentent aussi une augmentation de la multifractalité (cf. Fig. K). Ces effets opposés sont particulièrement intéressants car ils n'ont jamais été observés dans d'autres systèmes dynamiques (tel qu'en turbulence hydrodynamique ou dans le domaine de la finance) et ont lieu aussi lorsque les participants passent du repos à la tâche. Plus surprenant encore, la multifractalité de chaque individu converge au cours de l'entraînement vers un attracteur commun (cf. Fig. L) pouvant refléter la performance asymptotique de l'apprentissage.

Cette étude montre pour la première fois à notre connaissance que la capacité d'apprentissage d'un individu peut être prédite par l'indexage multifractal de son activité cérébrale. Ce résultat est à la fois nouveau et provocant car il offre une première interprétation neurophysiologique de la multifractalité observée dans le fonctionnement du cerveau humain. De plus, il remet en question le modèle de criticalité auto-organisée souvent employé pour interpréter la présence d'autosimilarité dans la dynamique cérébrale car celui-là ne permet pas d'expliquer l'origine de la multifractalité.

Discussion, conclusion et perspectives

Dans cette thèse, nous avons étudié les processus neuronaux de l'apprentissage perceptuel et de la plasticité en analysant de deux manières différentes des données MEG reconstruites dans l'espace source : d'une part via une analyse ERF classique, souvent utilisée en neurosciences pour identifier le décours temporel de l'activité neuronale suite à la présentation d'un stimulus d'intérêt, et d'autre part via une analyse de l'invariance d'échelle, une approche bien plus originale et inhabituelle permettant de caractériser l'organisation temporelle de l'activité cérébrale sur plusieurs échelles temporelles ou fréquentielles (limitée ici aux très basses fluctuations présentant un spectre de puissance de type $1/f$).

Comparaison entre l'analyse ERF et l'analyse multifractale

Aussi bien l'analyse ERF que l'analyse multifractale révèle des changements de l'activité cérébrale entre avant et après entraînement qui peuvent être interprétés

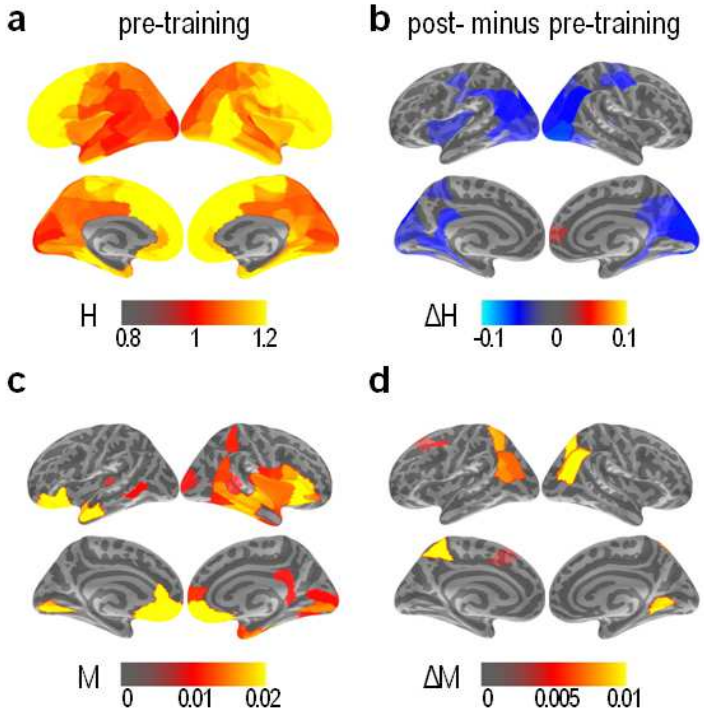

Figure K. Diminution de l'auto-similarité et augmentation de la multi-fractalité après entraînement. Cartes corticales de l'autosimilarité (H) et de la multifractalité (M) moyennes estimées sur les données MEG reconstruites dans l'espace source avant entraînement (colonne de gauche) et cartes des contrastes entre avant et après entraînement (colonne de droite). **(a)** L'autosimilarité moyennée sur tous les individus (groupe V et AV réunis) est comprise entre 0.8 et 1.2 et suit un gradient occipito-frontal. **(b)** Seules les aires montrant des changements significatifs d'autosimilarité après entraînement sont présentées. On observe essentiellement une diminution de l'autosimilarité dans la région occipito-pariétale. **(c)** Seules les aires présentant de la multifractalité de manière significative avant entraînement sont présentées. **(d)** Seules les aires montrant des changements significatifs de la multi-fractalité après entraînement sont présentées. De façon remarquable, seules quelques aires (notamment en pariétal) présentent une hausse de la multifractalité plus ou moins contenues dans celles présentant une diminution de l'auto-similarité.

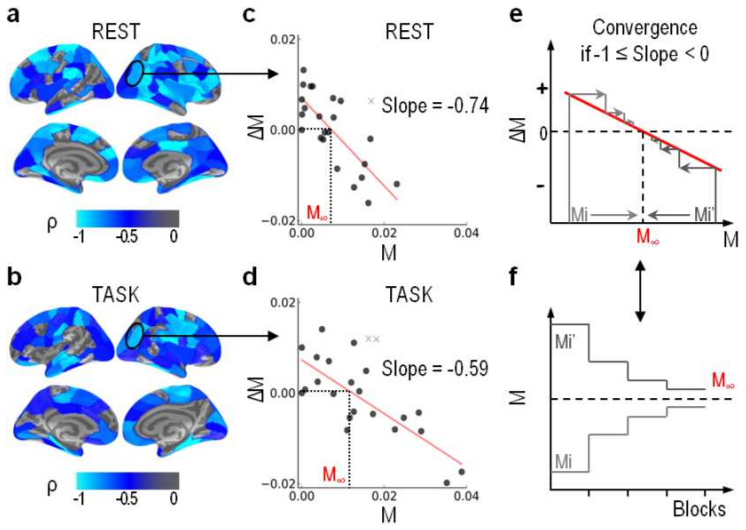

Figure L. La multifractalité converge vers un attracteur M_∞ aussi bien durant le repos que durant la tâche. (a, b) Dans chaque aire corticale, les coefficients de corrélation ont été estimés entre la variation moyenne de multifractalité ΔM de chaque individu estimée au cours des 4 blocs d'entraînement durant la tâche **(a)** ou le repos **(b)** et la quantité initiale M moyennée sur ces mêmes blocs. Le niveau de signification statistique de ces corrélations a été corrigée pour les comparasions multiples. Dans les deux conditions (repos ou tâche), nous n'obtenons que des anticorrélations. **(c, d)** Chaque régression ainsi obtenue dans une aire corticale — par exemple ici dans pSTS/hMT+ droit, indiquée par un cercle noir durant le repos et la tâche — peut être interprétée comme l'espace des phases de M durant l'entraînement. Plus précisément, la pente négative de la regression indique que M converge vers une valeur asymptotique M_∞ correspondant à $\Delta M = 0$. Plus cette pente se rapproche de -1, plus cette convergence est rapide. **(e, f)** Illustrations de la trajectoire idéalisée de M (espace des phases en haut, décours temporel correspondant en bas) avec deux valeurs initiales M_i et $M_{i'}$ convergeant chaque fois vers M_∞ dans le cas où la pente de régression est contenue entre -1 et 0.

comme de la plasticité fonctionnelle. L'identification avec ces deux approches d'aires communes telles que hMT+, pSTS, mSTS et ITC se révèle particulièrement intéressante ; l'interprétation neuronale est cependant assez différente. Il faut d'abord rappeler que ces deux analyses ont été menées sur deux domaines de fréquences quasi différents : entre 1 et 40 Hz dans le cas des ERFs et entre 0.1 et 1.5 Hz dans le cas de l'invariance d'échelle. Concernant l'approche classique (c-à-d les ERFs), la plasticité est essentiellement représentée par une augmentation (voire parfois une diminution) de l'activité neuronale à des latences particulières, reflétant ainsi une plus forte sensibilité des neurones (comme dans hMT+) ou un recrutement plus large d'une population synchronisée de neurones (comme apparemment dans pSTS) en réponse à un évènement précis. Inversement, un changement des propriétés d'invariance d'échelle indique une réorganisation temporelle de l'activité cérébrale sur une échelle de temps bien plus grande que celle de l'analyse ERF ($\sim$ 1 s), pouvant englober ainsi plusieurs évènements neuronaux.

Cela constitue en effet une différence importante : grâce à la très bonne résolution temporelle de la MEG, l'analyse ERF nous permet de «démêler» les mécanismes neuronaux en sélectionnant un instant particulier (par exemple dans notre étude, l'activité évoquée par l'apparition d'un mouvement visuel avec un certain niveau de cohérence). L'analyse d'invariance d'échelle, en revanche, ne nous permet pas de faire une telle distinction puisqu'elle est effectuée sur la totalité du signal ; cela pourrait ainsi expliquer pourquoi on observe de la plasticité dans un réseau plus large. Par exemple, l'activité dans le sulcus intrapariétal (IPS) varie en terme d'invariance d'échelle (baisse de l'autosimilarité et hausse de la multifractalité) tandis qu'elle ne présente aucun changement selon l'analyse ERF. Cependant, nous nous sommes focalisés ici sur les réponses évoquées liées au traitement neuronal du mouvement, excluant donc d'autres mécanismes tels que l'accumulation d'évidence sensorielle, la prise de décision, la réponse motrice ou bien le jugement de confiance. Nous suspectons fortement IPS de montrer de la plasticité dans l'un de ces cas. Nous pourrions le vérifier par exemple en estimant l'activité évoquée en phase avec la réponse du sujet. De plus, l'accumulation d'évidence apparaît généralement en ERF sous forme de variation très lente, qui peut donc avoir été retirée par le filtre passe-haut utilisé dans notre analyse.

Le gros avantage de l'analyse multifractale est qu'elle peut être appliquée sur n'importe quel jeu de données MEG, notamment durant le repos et le sommeil. En réduisant considérablement la dimension des données à deux valeurs (autosimilarité et multifractalité) par capteur (ou vertex) dans chaque enregistrement, nous avons été capables d'examiner la dynamique de l'apprentissage au cours des blocs expérimentaux successifs. La principale difficulté réside dans le choix de la gamme d'échelle sur laquelle l'analyse se porte et du paramètre γ qui détermine l'ordre d'intégration des données. Pour cela, on inspecte en pratique la densité spectrale de puissance de chaque capteur dans chacun des enregistrements... Ce qui peut devenir très fastidieux lorsque le nombre d'acquisitions augmente. Bien que l'analyse ERF soit théoriquement et conceptuellement plus simple, elle n'est pas pour autant plus facile à mettre en place : elle nécessite un contrôle temporel très précis des

évènements (ce qui s'avère extrêmement problématique si leur enregistrement est défectueux ou si les stimuli sont présentés avec une latence approximative). Bien que dans les deux cas, nous étions confrontés à la même difficulté, à savoir l'analyse au niveau des capteurs (due à la complexité de la tâche et l'absence de normalisation spatiale entre les individus), le choix de la méthode de reconstruction de source (MNE, dSPM ou sLORETA ?) avait bien plus d'impact sur les champs évoqués que sur les propriétés multifractales extraites des sources corticales. L'analyse d'invariance d'échelle est en effet insensible aux transformations linéaires (non-nulles), telles que la normalisation des estimées MNE par les méthodes dSPM et sLORETA.

Lien avec la hiérarchie oscillatoire

Une perspective intéressante serait d'examiner les propriétés oscillatoires des signaux MEG, ce que l'on peut considérer comme étant la contrepartie des propriétés d'invariance d'échelle (cf. chapitre 6). En effet, cela nous permettrait non seulement d'interpréter plus facilement la dynamique fractale du cerveau (en comparant simplement les résultats obtenus), mais aussi d'étudier le phénomène d'intégration à large échelle dans le contexte du traitement multisensoriel et de l'association couleur/mouvement (soit comment des entrées sensorielles éloignées spatialement peuvent interagir très tôt avant d'atteindre les aires d'association situées bien après dans le traitement hiérarchique).

Selon une théorie, les larges réseaux neuronaux interagiraient à travers la synchronisation de phase des rythmes oscillatoires, permettant ainsi l'intégration multisensorielle [Varela 2001]. Un tel mécanisme a été mis en évidence pour la première fois dans la bande gamma [Rodriguez 1999, Tallon-Baudry 1999] : une étude en EEG a montré par exemple que le le niveau de synchronisation gamma entre deux aires distantes était plus forte lors de la reconnaissance de visages que durant celle de figures abstraites [Rodriguez 1999]. D'autres études ont aussi montré que cette synchronisation était impliquée dans l'attention visuelle sélective [Talsma 2009]. Elle est par exemple plus élevée chez le singe lorsque celui-ci, au lieu d'être surpris, s'attend à voir un stimulus [Fries 2001].

A cela s'ajoute un autre phénomène encore plus intéressant, celui des «fréquences emboitées» : il existerait en effet un couplage entre l'amplitude des ondes gamma et la phase des basses fréquences [Buzsáki 2004, Fox 2007]. Cette hiérarchie oscillatoire est particulièrement pertinente en audiovisuel car elle possède une forte similitude avec le langage qui nécessite un traitement complexe pour pouvoir être décomposé [Giraud 2007]. De plus, un signal saillant dans une modalité donnée (par exemple auditive) pourrait recaler la phase des oscillations lentes dans une autre modalité (par exemple auditive) [Iurilli 2012], permettant ainsi de moduler l'état d'excitabilité des neurones [Schroeder 2008] et de permettre, ou non, l'intégration multisensorielle.

La hiérarchie oscillatoire est donc un concept qui a l'avantage d'expliquer les effets positifs et négatifs des interactions multisensorielles par la prise en compte des contraintes temporelles. Le principe des fréquences emboîtées est d'une importance cruciale car il a été montré qu'un phénomène similaire pouvait avoir lieu dans

l'activité cérébrale arythmique de type $1/f$, bien que celui-ci ne puisse pas être capturé par le paramètre d'autosimilarité. Il serait donc intéressant de tester si la multifractalité, par contre, peut refléter un tel mécanisme.

Autres perspectives

Les données acquises dans cette expérience n'ont pas encore été complètement exploitées et peuvent faire le sujet d'autres analyses. Par exemple, l'intégration multisensorielle peut être étudiée plus en profondeur à l'aide d'analyses standard (ERF, visualisation temps-fréquence) sur les quatre blocs d'entraînement. Nous pouvons aussi nous demander si les résultats concernant l'autosimilarité et la multifractalité au cours de l'entraînement sont spécifiques aux fluctuations lentes de l'activité cérébrale, ou si de semblables observations peuvent être faîtes en portant l'analyse WLBMF sur d'autres grandeurs telle que l'enveloppe des oscillations (qui présentent aussi des propriétés d'invariance d'échelle) ou les signaux acquis en IRMf (bien que la fréquence d'échantillonnage ne permette pas d'estimer la multifractalité aussi bien qu'en MEG).

Puisque la convergence vers la multifractalité asymptotique n'a été montrée qu'au niveau du groupe, il serait intéressant de tester cette curieuse propriété de manière isolée sur chaque individu en augmentant le nombre de blocs d'entraînement durant l'expérience. Si l'entraînement est suffisamment long et efficace, nous nous attendons à observer des changements significatifs des propriétés d'invariance d'échelle au repos. Une contribution méthodologique consisterait aussi à développer l'analyse WLBMF de manière à sélectionner les moments d'intérêt pour cibler un mécanisme neuronal particulier.

Enfin, la prochaine étape dans l'étude de la dynamique fractale du cerveau pourrait consister à proposer une extension multivariée de l'analyse WLBMF, afin d'estimer la connectivité non seulement fractale, mais aussi multifractale. Ces mesures pourraient être alors comparés avec celles de connectivité standard (telle que la cohérence, l'index de retard de phase ou la valeur calée sur la phase).

Introduction

Context

Functional neuroimaging is a relatively recent discipline that aims to understand the brain mechanisms at the origin of our behavior, whether mental capacities (e.g. language, perception, consciousness) or disorders (e.g. Alzheimer's and Parkinson's diseases) by making use of several non-invasive (i.e. that do not require opening the skull) imaging techniques. Traditionally, a cognitive process is supposed to be undertaken by one or several specific areas in the brain that activate at particular latencies. Depending on the characteristic of interest (location of areas or time course of activity), the imaging technique must be judiciously chosen: for instance functional magnetic resonance imaging (fMRI) measuring the so-called blood-oxygen-level dependent (BOLD) activity, i.e. slow changes of blood flow following neuronal activation, is best qualified to localize the activated areas. In contrast, electroencephalography (EEG) and magnetoencephalography (MEG) measure respectively the electric and magnetic fields generated by neuronal activity on the head surface and are best designed to track the temporal dynamics of neural events (on the order of milliseconds).

Independently of the chosen imaging modality, most studies adopt the same approach by focusing on brain activation associated with an event of interest, e.g. the onset of a stimulus or the participant's response to a cognitive task. This is for instance the case of the event-related field (ERF) analysis conducted in MEG, whose purpose is to characterize the time-course of the magnetic brain response modulated by an event. This method assumes that averaging data from several trials would reduce the noise while leaving the "evoked" response intact thanks to its invariant latency and shape. Although this method has been proven successful to describe the neural events involved in the execution of a task with great time resolution, it overlooks the major part of brain activity — i.e. spontaneous brain activity — in spite of its known functional relevance [Gusnard 2001, de Pasquale 2010, Sadaghiani 2010]. The brain is indeed still active in the absence of stimuli or actions (such as during rest or sleep), and this activity plays a crucial role for instance in brain development and perception.

The first observations of spontaneous activity in electrophysiology were carried out by Hans Berger in 1931 using EEG and consisted of a description of the well-known "alpha" waves, i.e. rhythmic cycles oscillating predominantly around 8–12 Hz in the occipital lobe. Since then, spontaneous activity in M/EEG is traditionally described in terms of neural oscillations and quantified by spectral measures revealing different frequency peaks readily observable in the power spectrum and associated with different functional roles (not only alpha, but also beta and gamma oscillatory activities for instance). This approach, however, does not account for the known arrhythmic — or non-oscillatory — properties of neural activity [Bullock 2003].

Indeed, the dynamics of neural activity in the infraslow domain (i.e. very slow activity below $\sim$ 1 Hz) are characterized by a $1/f$-type power spectrum [Novikov 1997, He 2010], a hallmark of *self-similar* — i.e. *scale-free* or *fractal* — temporal dynamics [Bak 1988]. Fractals (Fig. 1) usually refer to particular geometric figures that remain exactly or *statistically* (i.e. nearly) the same at every scale — in other words, they present the same structure no matter how much you zoomed in or out. Similarly in the domain of temporal signals, "fractal" or "scale-free" means that the statistical properties of a signal remain unchanged (or covariant) after time dilation and proper rescaling. Hence, two computational implications for brain function are that the encoding of information may be temporally multiplexed and that functional parsimony depends on the level of temporal compression.

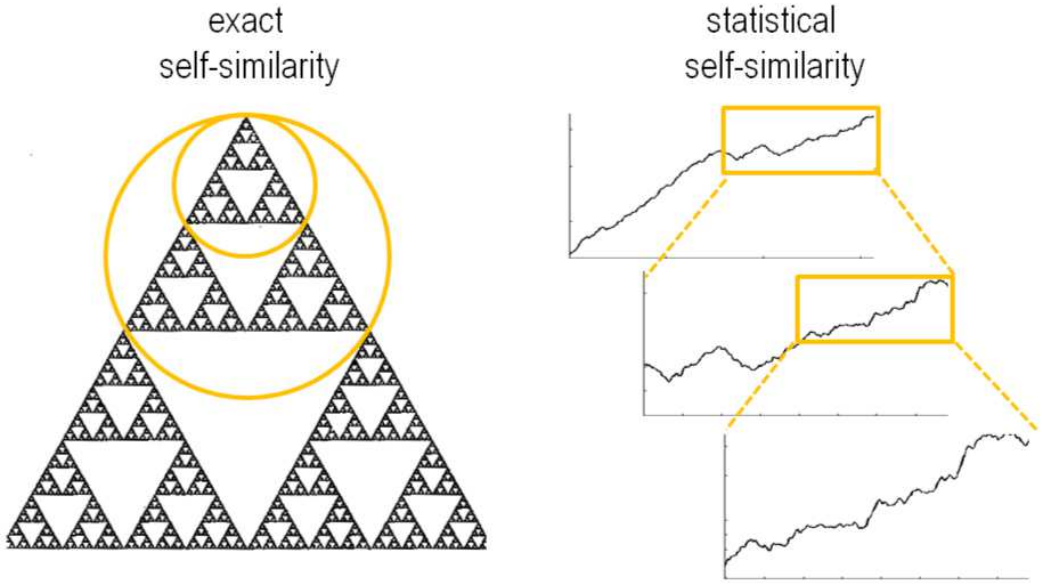

Figure 1: Example of fractal objects. The Sierpinski triangle (*left*) is a fractal image that illustrates exact self-similarity: the pattern is identical at all scales (indicated by orange circles). A fractal time series (*right*) is characterized by statistical self-similarity in a restricted range of scales (since limited by the length and the sampling of the time series): each dilated and properly rescaled version of the time series has the same statistical properties as the origin.

In practice, scale-free properties can be described at different levels of detail: the first one being referred as "*self-similarity*", a single parameter that indicates how the rescaling factor must be chosen as a function of the dilation to make the statistical properties invariant. It also reflects the global regularity of the signal and the absence of a characteristic correlation time in temporal dynamics and is coarsely approximated by the exponent of the $1/f$ spectrum. As a second level of details, multifractality reflects the local fluctuations — or singularities — along time that cannot be measured in the sole power spectrum. In other words, the presence of

multifractality implies that the self-similarity value is not enough to describe the temporal dynamics but instead, a continuous spectrum of values is required.

In most neuroimaging studies, scale-free analyses have been not only restricted to the assessment of self-similarity, but also carried out using analysis tools (e.g. detrended fluctuation analysis [Peng 1994, Linkenkaer-Hansen 2001]) that are known to significantly lack robustness and accuracy in the presence of non-stationary drifts and in non-Gaussian time series [Veitch 1999]. These issues can be overcome using a wavelet-based analysis, which in addition allows for the joint estimation of multifractality. In this thesis, we propose to capitalize on one of these methods, namely the recent wavelet-leader based multifractal formalism (WLBMF) [Wendt 2007] that has been shown to benefit from excellent theoretical and practical performance on real data [Ciuciu 2012].

Nonetheless, do these scale-free properties really matter for behavior and brain functioning? So it is suggested by several experimental studies reporting modulations of the $1/f$ spectra (i.e. self-similarity) in link with different cognitive states including task-driven and resting states [He 2011, Ciuciu 2012], stages of sleep [Weiss 2009, He 2010], task performance [Buiatti 2007, Wink 2008], ages [Suckling 2008], genders [Jausovec 2010] and pathologies [Maxim 2005, Suckling 2008]. Although investigations going beyond self-similarity were relatively scarce, all of them (excepted one investigating EEG micro-states [Van de Ville 2010]) reported multifractality in brain activity [Shimizu 2004, Popivanov 2005, Ciuciu 2012, Suckling 2008, Wink 2008, Weiss 2009]. The interpretation remains however difficult and further investigations are necessary to understand to what extend scale-free dynamics are functionally relevant. According to a recent fMRI study showing that learning could modify resting-state brain activity [Lewis 2009], we asked if, similarly, scale-free properties could be modulated by learning and how they would vary in the course of training. To that aim, we developed a learning paradigm alternating blocks of rest and visual task during which participants' brain activity would be recorded using MEG (cf. Fig. 2).

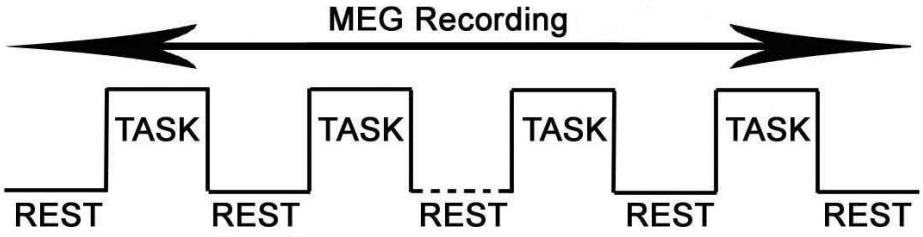

Figure 2: Basic idea and conception of the learning paradigm. In order to investigate the functional role of scale-free dynamics in rest- and task-related brain activity, we elaborated a paradigm in which participants would be trained to perform a visual task periodically interrupted by periods of rest, while being recorded with MEG. Further details on the paradigm and the nature of the stimuli are given in chapter 1.

Learning is a cognitive process that is closely related to the notion of *plasticity*, i.e. the capacity of the brain to modify its structural organization at any level (e.g. synaptic, neuronal or cortical). Historically, plasticity was thought to occur only during a critical period in childhood and to disappear in adults. Since the end of the 60's, we know however that the brain remains a dynamic system that can adapt and change throughout the entire life span, enabling development, memorization, new skill acquisition or improvement, and even recovery from brain damages. Interestingly, the repetition of a visual task (as described in our paradigm) can lead to learning and to specific plasticity occurring in the primary visual areas. This is referred to as *perceptual visual learning* [Sasaki 2010]. In adults however, the mechanism can be relatively slow and weak in the absence of efficient training. Our first challenge consisted thus of proposing a training sufficiently effective to entail plasticity in a short time and for all participants.

This led us to consider the potential benefits of multisensory learning [Shams 2008] and cross-modal plasticity. The most impressive examples of plasticity have been indeed reported in sensory-deprived individuals [Bach-y Rita 2003]; for instance the human motion area hMT+ (known to process visual motion) can be recycled for auditory or tactile processing in congenitally blind people [Poirier 2005, Ricciardi 2007]. More generally, evidence of multisensory interactions has been found throughout the cortex and has challenged the view that sensory systems are strictly independent, in turn questioning the innate specialization of sensory cortices. According to the "supramodal theory" [Pascual-Leone 2001], it has been suggested that some cortical areas such as hMT+ are naturally capable of functional selectivity irrespective of the sensory modality of inputs i.e. of functional recycling. However, several challenges have been raised [Bavelier 2010]: for instance, is functional recycling a consequence of early sensory deprivation or is it supported by pre-existing supramodal areas [Bedny 2010, Morrone 2010, Dormal 2011]?

Without losing sight of our main goal (i.e. to investigate the impact of learning on scale-free brain dynamics), we also addressed this issue by asking whether learning to discriminate visual coherence would benefit from supramodal processing. Novel stimuli were developed consisting of acoustic textures sharing the temporal statistics of visual random dot kinematograms (RDKs). Three groups of participants were trained in a difficult visual coherence discrimination task without sounds (V), with congruent acoustic textures (AV) or with auditory noise (AVn) while being recorded with magnetoencephalography (MEG). We hypothesized that visual learning and plasticity would benefit from matched audiovisual stimulation (i.e. AV training).

Objectives

In order to accomplish the main objectives of this thesis, we must ensure beforehand that the learning paradigm is sufficiently effective and well-controlled to further enable us to combine behavioral measures of learning with participants' brain activity recorded with MEG. This will be the subject of the first part.

The main purpose of this work is then twofold:

- To uncover the neural mechanisms of multisensory learning involved in our paradigm by carrying out standard ERF analyses on source-reconstructed MEG signals. More precisely, we aim to test if pre-existing multisensory/supramodal computations would enable down-stream sensory plasticity in healthy individuals by comparing three types of training (V, AV and AVn).
- To provide further knowledge on the functional role of scale-free properties and its implication for behavior. More precisely, we ask whether multifractality and self-similarity can bring functionally independent information regarding the neural processes involved in learning and plasticity.

These two points are tackled respectively in the second and third parts of this thesis.

Organization and contributions

Part I — Data acquisition and psychophysics

Chapter 1 — Paradigm and stimuli

How can we observe effective learning in a short period of training?

To address that question, we make an overview of psychophysical and cognitive studies dedicated to multisensory and perceptual learning. Next, we present the paradigm and stimuli involved in three types of training: visual (V), audiovisual using acoustic textures (AV) or auditory noise (AVn). In the following, we will systematically refer to this chapter for the description of the experimental design and the samples of participants.

Chapter 2 — Psychophysics

Are the trainings indeed effective at the behavioral level?

Here, we analyze the behavioral measures in pre- and post-training according to the three categories of training. All participants improved and as expected, the AV training was significantly more effective, suggesting that supramodal processing in AV boosted learning. These behavioral results will be reused in chapters 5 and 7 in order to derive their neural correlates.

Chapter 3 — Magnetoencephalography

How magnetoencephalography allows us to measure neural activity?

In order to interpret correctly the results of ERF and scale-free analyses, it is crucial to understand the nature of the analyzed signals. Therefore, we present in this chapter the neurophysiological basis of MEG and the standard preprocessing steps. We describe next the techniques used to solve the inverse problem, i.e. to estimate the underlying neuronal activity resulting in the signals observed at the sensor level. In the last section, we detail the procedure of the MEG acquisition,

preprocessing and source reconstruction that were used for both ERF and scale-free analyses.

Part II — Standard ERF analysis

Chapter 4 — Neural hypothesis
What can we reasonably uncover with the ERF analysis?

In this chapter, we first describe the principles of the ERF analysis. In addition, we review the neural candidates that can be involved during training on the basis of previous neuroimaging studies. Finally, we elaborate some predictions regarding the neural correlates of learning potentially revealed by the ERF analysis.

Chapter 5 — ERF analysis of acquired MEG data
Can we explain the behavioral differences between each training group at the neural level using standard ERF analysis?

This chapter presents the main results of the ERF analysis conducted in source space. First, the cortical area dedicated to the analysis of visual motion (hMT+) solely improved its selectivity/plasticity in the AV group as established by neurometric quantification. Second, the network implicated in the analysis of motion after AV and AVn training was much larger than in the V group, suggesting the selective implication of higher cortical regions in the plasticity of hMT+, notably of the prefrontal cortex (vlPFC) and multisensory regions (pSTS and mSTS). Altogether, we interpret our results in the context of the reverse hierarchical learning theory (introduced in chapter 1) by showing the implication of supramodal processing in optimizing color-motion binding and visual coherence discrimination.

Part III — Scale-free analysis

Chapter 6 — Scale-free properties: Definitions and applications
Why and how should we conduct scale-free analyses in MEG?

In this chapter, we first explain the context that led to investigate the scale-free properties of brain activity. We further give the theoretical framework in which self-similarity and multifractality are defined as well as a description of the state-of-the-art techniques used to assess these quantities. More particularly, we focus on the method used in chapter 7, namely the wavelet leader based multifractal formalism (WLBMF).

Chapter 7 — Scale-free analysis of acquired MEG data
Is there any information in self-similarity and multifractality of MEG signals that can improve our understanding of the neural processes underlying learning and plasticity?

This chapter is dedicated to the scale-free analysis of the MEG data acquired in our paradigm. It is composed of two preliminary analyses and of a main analysis.

We first reported scale-free properties at the sensor level (first preliminary study) and in restricted areas on the cortical surface (second preliminary analysis) that could be modulated between not only rest and task, but also pre- and post-learning. More importantly, the main analysis shows that self-similarity and multifractality assessed over the entire cortex are dynamically coupled in several cortical areas in the course of training: while self-similarity generally decreases after learning, more specific areas also present an increase of multifractality. These opposite effects are also observed when switching from rest to task. More surprising, the individual amount of multifractality converged during training towards a common attractor that could be associated with asymptotic performance.

Part I

Data acquisition and psychophysics

Chapter 1

Paradigm and stimuli

Contents

The establishment of the paradigm is a crucial step as it determines the questions that can be answered. To investigate the impact of learning on scale-free brain activity, we must put the odds on our side by optimizing the learning effect in a well-controlled paradigm. To that end, perceptual learning appeared as an appropriate choice because of its relative simplicity and the possibility to quantify it easily using psychophysical analysis methods. Likewise, targeting primary sensory areas via perceptual learning seems to be a judicious choice since their functional role remains so far the best understood in the human brain and hence should facilitate the analysis of neuroimaging and electrophysiological data.

The first section is therefore a non-exhaustive review of this concept. We were however confronted with an important challenge: how can we make perceptual learning faster and yet still effective while it usually requires several days? The next section is an introduction to the concept of multisensory integration and its benefits for perceptual learning. Based on what we know so far and on the questions that remain unsolved regarding multisensory learning, we developed a learning paradigm (presented in the next section) involving novel audiovisual stimuli (presented in the last section) that were expected to boost learning. To address the specificity of this particular audiovisual training, we compared it with two others training types: a visual one and another audiovisual one incorporating unspecific acoustic noise.

1.1 Perceptual learning

1.1.1 Definition

Perceptual learning consists of an implicit improvement in the perception of a stimulus and the discrimination of its features after a long and repeated exposure to that stimulus [Gibson 1963]. One of its greatest implications is that primary sensory areas remain plastic even in the adult brain. This property was thought indeed to disappear after the critical period, i.e. a short postnatal duration. For instance, the eye of a radiologist can better distinguish the pattern of a tumor on a X-ray image than an untrained eye [Sowden 2000]. In addition, research in this field has also been motivated by the possibility to extend our knowledge of the perceptual learning mechanism to more complex ones (e.g. memorization, categorization or abstract rules [Freedman 2008]). Therefore, a great body of literature in this area has emerged, though more dedicated to visual learning than other sensory modalities, and has been several times reviewed (for instance [Goldstone 1998, Gilbert 2001, Li 2004, Fahle 2005, Seitz 2005a, Sasaki 2010]).

Perceptual learning usually requires 3 to 10 days of practice in order to be effective but remarkably, its effects can last up to 1 or 3 years without any supplementary exercise. More precisely, a very short period of fast learning is first observed and is immediately followed by a much longer period of slow improvement. The newly acquired skills are then consolidated effortlessly and implicitly during complete cycles of sleep within 30 hours after training [Stickgold 2000].

One of the main characteristics of perceptual learning lies in its *specificity* to the trained feature, i.e. the impossibility to transfer the improvement to another type of stimulus. In psychophysics, such property is attributed to low-level plasticity (e.g. primary visual cortex) because each feature is processed early in distinct sensory fields. For instance, visual learning of features such as Vernier acuity, texture orientation, visual motion and spatial frequency have shown specificity to the stimulus location, orientation and direction. A very few studies have investigated the auditory perceptual learning, but so far only the spectral frequency and the temporal order and duration could be improved with perceptual learning and with more or less specificity [van Wassenhove 2007]. Interestingly, even complex features can also show some specificity, suggesting plasticity in higher-level areas or simultaneously in different low-level areas.

Nonetheless, specificity was not always reported in every study, even if the used stimuli were the same. Understanding the conditions under which a perceptual training could lead to specific or generalized learning became therefore crucial.

1.1.2 The Reverse Hierarchy Theory (RHT)

The Reverse Hierarchy Theory (RHT) [Ahissar 1997] attempts to reconcile contradictory studies using similar stimuli and reporting sometimes specificity and sometimes generalization of the learning. It is based on the observation that specificity is more often reported when using difficult tasks than easy tasks.

According to the RHT, the learning mechanism is organized in "cascade": a first modification in high-level areas modulated by attention and associated with easy conditions allows generalization of the learning. As the task becomes harder, areas located in lower levels of the hierarchical sensory pathway become recruited and lead to specialization. This top-down process must be however initialized by a trigger event called "Eureka effect" which consists of presenting a small set of stimuli in a very easy condition. This step is essential to enable perceptual learning as it would guide the prime access to appropriate learning sites. It corresponds typically to the familiarization block that precedes a learning paradigm. Consistent with the RHT, a study [Lu 2004] investigating the learning of a visual motion in the absence of hMT+ activation showed that learning was impossible if the task was too difficult. The training became however effective with an easier task and led to generalization of the learning.

The RHT was later linked to the mechanisms of perception [Ahissar 2009]: It is proposed that immediate perception is first supported by high-level representations (e.g. a house is first perceived and categorized as a "house" without needs of details). In this process, features available at lower levels (e.g. shapes, colors or brightness...) converge toward high-level areas but do not contribute equally to identification, as only crucial and relevant details are retained. However, if immediate perception is not sufficient for successful performance (e.g. if the signal-to-noise ratio is too weak or the stimulus duration too short), further scrutiny becomes necessary to recruit lower level populations and to access to details.

A important prediction of the RHT concerns the stimulus variability presented during training: the higher variability, the less likely plasticity will occur in low-level areas. Indeed, if the stimuli vary too much, the training will not target a specific low-level population. Conversely, the more similar two stimuli are, the more necessary the access to low-level populations becomes for their discrimination.

1.1.3 The role of attention

The role of attention in perceptual learning has long been questioned and remains debated. Although perceptual learning leads to an automatization of the task by releasing the dependence of performance from attentional control, the learning per se shows strong interaction with attention [Gilbert 2001]. Accounting for the plasticity/stability dilemma (i.e. uncontrolled plasticity results in instability), it has been proposed that attention plays a key role in selecting the relevant features on which the learning should be restricted.

However several studies have demonstrated that perceptual learning could occur even without attention or stimulus awareness. In the very first study [Watanabe 2001], a subliminal and task-irrelevant visual motion was presented in the background while subjects were engaged into another task. The repetitive exposure improved the perception of motion only in the direction of the subliminal stimulus. This type of learning was named task-irrelevant learning (TIL). In comparison to classical perceptual learning (i.e. task-driven learning), TIL seems to occur only at

a very low level and with a shorter duration [Watanabe 2002]. It can even lead to "misperception" [Seitz 2005b]!

This finding contradicts the RHT because TIL seems to occur without any top-down processes. A more recent study has even shown that it is possible to induce plasticity in primary visual cortex specific to a predetermined stimulus that was never presented [Shibata 2011]. In this experiment, subjects were trained to reproduce the same pattern of activity in V1/V2 corresponding to the presentation of an oriented Gabor patch with the only help of a visual feedback computed by online measures in fMRI and finally showed an improvement specific to the orientation. An explanation [Ahissar 2004] would be that TIL reflects another phenomenon named "adaptation" that is difficult to distinguish from perceptual learning. In this bottom-up process, the neural response to an invariant stimulus is automatically reduced after a long exposure in order to increase the system sensitivity to new stimuli.

Nonetheless, attention still plays a role because TIL happens only if the stimulus is weak enough to be undetected. Otherwise, the task-irrelevant stimulus is eliminated by regions that control attention such as the lateral prefrontal cortex [Tsushima 2006]. In other words, attention does not select relevant features, it suppresses irrelevant ones.

The distinction is then made between attention brought to specific features and reinforcement signals (such as reward or feedback, punishment, novelty...) that are more diffuse and reflect a general alerting state [Sasaki 2010, Seitz 2009]. Since all sensory inputs are boosted during this state, including coincident task-irrelevant inputs, this can elicit an implicit or statistical learning of subliminal features. Although reward is not essential, it can facilitate learning: for instance, the amount of cholinergic inputs to the brain (a source of implicit reward stemming from the nucleus basalis) can modulate the successfulness of learning [Li 2004]. However, the drawback of using feedback is that it can introduce a decision-making bias, which is usually unwanted.

1.2 Benefits of multisensory learning

1.2.1 Motivation

An important question is to know how perceptual learning can be made more efficient and lead to generalization. Because the most substantial cases of neural plasticity have been observed in sensory-deprived people and consisted of cross-modal refinements [Proulx 2012], the question raised whether healthy individuals could also benefit from such multisensory interactions. From the very numerous studies dedicated to this research field since the last 50 years (see for instance the following reviews [Bavelier 2002, Bach-y Rita 2003, Shams 2008, Murray 2009, King 2009, Talsma 2010, Shams 2010, Klemen 2012, Ricciardi 2011, Voss 2012, van Wassenhove 2012, Proulx 2012]), it came out that perceptual learning in one sensory modality can be improved by using multisensory stimuli during training. For instance, pairing a visual coherent motion with a congruent audi-

tory motion during training can lead afterwards to an improved detection of the visual motion alone and specifically to the trained direction [Seitz 2006]. According to Shams [Shams 2008], it is intuitively explained by the multisensory nature of our environment that is mirrored in our brain with a great number of multisensory interactions that can occur at different levels of the sensory processing. This interpretation challenges the strict independence view of sensory systems (e.g. [Driver 2000, Ghazanfar 2006]) and further questions the innate specialization of sensory cortices.

In addition, multisensory learning can sometimes allow the learning transfer from one modality to another (e.g., the presentation of a visual rhythm can generate the mental representation of an auditory rhythm [Grahn 2011]) and sometimes not (the improved discrimination of an auditory duration does not transfer to visual duration [Proulx 2012]).

It is therefore crucial to understand which type of multisensory interaction can fully contribute to improve learning and under which conditions it occurs. For instance, some multisensory illusions result mainly from an attentional modulation such as the stream-bounce illusion [Shams 2010], which consists of two identical visual objects moving towards each other. Adding a sound at the exact moment of the collision bias the perception toward a bouncing motion instead of seeing objects streaming through. Stochastic resonance [Klemen 2012] can also be at the origin of multisensory interactions: the addition of an acoustic white noise can contribute to exceed a detection threshold and consequently to facilitate the audiovisual speech comprehension [Ross 2007]. The most important interaction is the multisensory integration (i.e. when all sensory inputs converge at the perceptual level into a single, coherent and robust perceptual representation). For instance, the very strong McGurk effect [McGurk 1976] consists of perceiving a sound “da” while hearing “ba” and simultaneously lip-reading “ga”. Of less degree, the cross-modal dynamic capture illusion [Alink 2008] consists of two visual and auditory motions going in opposite directions. In this illusion, the sound is first perceived as going in the same direction as visual motion, indicating here a visual dominance. Further analysis in fMRI have shown an increased activity in hMT+ and a decreased activity in auditory cortex during the illusion, confirming the involvement of early sensory areas in the multisensory process.

1.2.2 Multisensory integration

Based on the observation that visual learning was facilitated only by using congruent audiovisual stimuli [Kim 2008], the multisensory integration seems to be the best candidate to optimize learning. The conditions to obtain multisensory integration consist of three basic rules that were defined from the observations made in the cat’s superior colliculus, a well-known multisensory area [Stein 1993]:

- *inverse effectiveness*: the more difficult the perception of the relevant stimulus, the more likely and stronger the multisensory integration;

- *temporal proximity*: stimuli must be close in time;
- *spatial proximity*: stimuli must be close in space.

Accounting for spatio-temporal brain dynamics has also some consequences on the last two rules [Murray 2009]: Contrary to the visual cortex which has a spatial retinotopic representation, the auditory cortex encodes spatial information by varying the response profiles of the same cell ensembles. Therefore, the spatial resolutions of auditory and visual stimuli do not project onto the cortex in the same way, modifying thus the spatial proximity between the stimuli in a physical sense. For the temporal proximity, the delay between the first response in the auditory cortex (∼20 ms post auditory stimulus) and the one in the visual cortex (∼50 ms post visual stimulus) must be accounted.

A principal hallmark of multisensory integration is the *superadditivity*: the behavioral/neural response to multisensory stimuli is greater than the sum of all responses observed separately in each modality [Meredith 1996]. Taken with the three previously mentioned rules, this set of properties enables the identification of multisensory areas that might be involved in the facilitation of perceptual learning. Whereas learning in one sensory modality is supposed to modify only the associated primary area, several mechanisms in multisensory learning are conceivable [Shams 2008]: multisensory learning can either reinforce the modification in the primary sensory area or also include multisensory association areas and connections. In the first case, the activation of another sensory area modulates the activity of the task-relevant sensory area (a mechanism also known as "subthreshold modulation" [Klemen 2012]). In the second case, the learning would have altered or created multisensory areas as well as connections between areas that would be still recruited after the training. This hypothesis is consistent with the observation that differences of performance between blind and sighted (resp. deaf and hearing) individuals are more pronounced when the task is complex such as in peripheral visual accuracy (resp. sound localization and recognition), which involves the recruitment of higher-level association areas [Bavelier 2002].

Multisensory learning is thus effective when using congruent stimuli that respect the spatio-temporal constraint. However, further considerations can be made about the choice of stimuli in order to improve the multisensory integration, and hence learning. Indeed, the evidence for automaticity in multisensory integration has been scarce [Talsma 2010, Kösem 2012] and raises the issue of what a multisensory feature would be like. For instance, the arbitrary association between an auditory white noise (whose intensity level is modulated between left and right loudspeakers) and a Random Dot kinematogram (RDK) does not significantly improve the perception of RDK coherence, even if directions are congruent [Alais 2004]. It was suggested that using other more ecological auditory stimuli would yield better effects. An fMRI study [von Kriegstein 2006] has shown that using audiovisual stimuli sharing redundant information (e.g. voice and visage) instead of arbitrarily coupled stimuli (e.g. voice and written names) led to better performance in a recognition task because the

cross-modal convergence of features could occur earlier in the processing hierarchy. This finding is consistent with the hypothesis of a supramodal brain organization.

1.2.3 The supramodal brain organization

The hypothesis of a supramodal, metamodal or amodal organization of the brain [Pascual-Leone 2001] was recently derived from the many observations made in sensory-deprived individuals using substitution-devices. An example of auditory-vision substitution device consists of a camera fixed on the head from which the image's pixels are converted into pitches (the frequency as a function of the height and the volume as a function of the brightness). After training, blind individuals are relatively able to recognize visual forms and localize objects [Bach-y Rita 2003]. The most famous example of tactile-vision substitution is Braille, i.e. reading using fingertips. Interestingly, sighted individuals who were temporary blindfolded and who learned Braille during 5 days showed the same pattern of activity in brain visual areas as congenitally blind subjects when reading Braille [Sadato 1996]. It has been even suggested that reading may be the first substitution device because it converts visual information into (mental) auditory information [Bach-y Rita 2003].

In the hypothesis of supramodality, each brain area is associated with the processing of a more abstract information regardless of the sensory modality (like the frequency, the structure of an object or the properties of a motion). If the information is mainly contained in one sensory modality, the associated area can appear specific to that modality. However, should this modality be no more accessible (like in blind or deaf individuals), the area can still take advantage of the information remaining in the other modalities. The supramodal representation proposes to reinterpret the classic view of visual and auditory areas as spatial and temporal areas [Pascual-Leone 2001, Proulx 2012].

For instance, the fusiform face area (FFA) and the parahippocampal place area (PPA) involved in face and place processing respectively, are also activated without visual stimuli. It could be argued that it is mental imagery, but these areas also activate in congenitally blind individuals when using tactile stimuli [Proulx 2012]. Another fMRI study [Striem-Amit 2012] showed that the classical distinction between the visual ventral and dorsal pathways (i.e. "what" and "where" pathways involved in shape/color and motion/location processing, respectively) also exists in congenitally blind individuals, suggesting that visual experience is not necessary to the development of these two paths. Moreover, similar ventral "what" and dorsal "where" pathways are also observed for the auditory system [Murray 2009] (i.e. associated with sound recognition and localization respectively), suggesting hence that these two pathways can be supramodal.

A particular brain area that appears to be supramodal is the visual motion area hMT+ [Voss 2012]. Indeed, hMT+ can be recruited by tactile and auditory [Poirier 2005] motion in blind individuals. The same observation can be made in sighted participants after blindfolding during five days [Poirier 2006], leading to the next question of knowing whether hMT+ could respond to auditory motion even

without previously blindfolding [Saenz 2008, Bedny 2010]. No activation was found except in sight-recovered subjects. However, by using more complex auditory stimuli designed with the "sonification" method to replicate the properties of an associated visual jump in the acoustic domain [Scheef 2009], hMT+ presented a BOLD auditory response. This suggests that hMT+ sensitivity to auditory motion may depend on the sound properties or on the audiovisual coupling that was presented. By investigating the role of hMT+ in tactile motion processing in fMRI [Ricciardi 2007], it was found that hMT+ also activated in sighted participants but in a more restricted area compared to congenitally blind subjects. More precisely, the dorsal part of hMT+ in sighted individuals was dedicated to the visual motion processing only, suggesting a specialization of this area due to visual experience.

Yet the hypothesis of supramodality raises the question of whether functional recycling is a consequence of sensory deprivation during a sensitive period [Bavelier 2010] or whether it relies on pre-existing supramodal computations [Bedny 2010, Morrone 2010, Dormal 2011]. In the latter case, an interesting theory [Ricciardi 2011, Proulx 2012] would be that multisensory learning takes advantage of the established supramodal representation by reinforcing and amplifying already present connections, and would appear in this manner as cross-modal plasticity. This assumption is based on the fact that cross-modal plasticity can often be observed in a short period of time, too short to make new connections.

It can seem now difficult to make the distinction between a supramodal and a multisensory area. According to [Voss 2012], a supramodal area performs the same operation independently of the unisensory modality whereas a multisensory area is dedicated to integrating inputs coming from different sensory areas to form a coherent percept.

By taking the RHT and the supramodal representation into account, a new hypothesis can be made to explain the interest of multisensory learning [Proulx 2012]: by using complex multisensory stimuli with redundant information, higher-order areas become recruited to sort all the different types of information coming from primary sensory areas and to redirect them towards appropriate supramodal areas. In addition, recruiting these higher-order areas would also enable learning generalization.

1.3 Paradigm

1.3.1 Procedure

The establishment of the paradigm was based on two motivations: i) To uncover the functional relevance of scale-free brain dynamics in both ongoing and evoked activity, ii) To address the issue of supramodal computations in motion processing and test whether visual perceptual learning can benefit from supramodal audiovisual training.

Accounting for these two points, the experiment consisted of several consecutive blocks (Fig. 1.1):

1. First of all, resting-state activity (eyes open, fixating a black screen) was recorded in MEG before any experience with the stimuli and the task. The duration of rest blocks had to be sufficient enough to enable a correct estimation of the scale-free properties but not too long to allow the subject to maintain its cognitive state and was thus set to 5 minutes.

2. The choice of using red and green mixed RDKs (see section 1.4) in the visual task necessitated to equalize the luminance of colors perceived by the participant. This was carried out by using the heterochromatic flicker photometry [Lee 1988]: it consists of displaying a static RDK whose color alternates at 15 Hz between red and green, while the participant adjusts the green intensity to minimize the sensation of flicker.

3. Participants were shortly familiarized with the task and the stimuli by receiving feedback on 16 very easy trials (i.e. RDK coherence set to 100%) to avoid confounding effects of perceptual improvement with the simple effect owing to a better comprehension of the task. This step can also be considered as the crucial "Eureka" effect of the RHT, necessary to trigger learning thereafter.

4. A **pre-training** test (∼12 min) evaluated participants' initial coherence discrimination threshold with levels of RDK coherence set at 15%, 25%, 35%, 45%, 55%, 75% and 95% (196 trials in total, 28 per coherence level). Importantly, no sounds were provided during this task. Participants were asked to report as accurately and fast as possible which of the two RDKs was most coherent by selecting the "green" or "red" button. Priority was given to accuracy. The same instructions were given in all subsequent task blocks. Additionally in this block, participants were asked to rate their confidence on a scale of 1 to 5 after each response. Because this block could be relatively long, a short break (no more than 30 s) was proposed in the middle of the test (i.e. after the 98th trial) to allow the participant to rest his eyes.

5. The **training** consisted of four blocks comprising a recording of resting-state activity followed by approximately 5 min of task performance. Three types of training were considered: the visual task could be effectuated with no sound (V group), with correlated acoustic textures (AV group) or with uncorrelated acoustic noise (AVn group). In AV and AVn conditions, participants were told to neglect the sound. The V condition was a control training to verify that visual learning indeed benefited from audiovisual training. The AVn condition was a supplementary control to dissociate between mechanisms mediated by supramodal representations (i.e. AV congruence) and simple attentional mechanisms. Participants were trained on four coherence levels (112 trials, 28 per each level) that were determined on the basis of their initial performance, i.e. corresponding to ±20% and ±10% of their pre-training coherence discrimination threshold.

6. Following a last recording of resting-state activity, a **post-training** test was again carried out in the same conditions as in pre-training (and crucially without sound) to estimate the participant's threshold and see whether the latter decreased (thus reflecting learning) or not.

7. After post-training, a passive MEG **localizer** was used to localize hMT+. It consisted of 120 presentations of one red RDK that was incoherent during 0.5 s and that either became coherent (95% of coherence, 60 trials) or else remained incoherent (0% of coherence, 60 trials) during 1 s.

Moreover, in all task blocks, inter-stimulus intervals (ISI) spanned 0.6–0.8 s and participants received no feedback. The color of the most coherent RDK was counterbalanced and the directions of coherent motion were pseudo-randomized. Experiments were run in a darkened soundproof magnetic-shielded room (MSR). Participants were seated in upright position under the MEG dewar facing a projection screen placed 90 cm away. The refresh rate of the projector was 60 Hz. Sound pressure level was set at a comfortable level (∼62 dB) for all participants. Participants were explained the task and stayed in contact at all times with the experimenter via a microphone and a video camera. Stimuli were designed using Matlab (R2010a, Mathworks Inc.) with Psychtoolbox-3 [Pelli 1997] on a PC (Windows XP).

It is worth noting that the task duration depended of course on the number of trials and the trial duration, but also on the participant's reaction time. Because the total duration of an MEG acquisition is not allowed to exceed 90 minutes (due to ethical regulations), the number of blocks composing the training as well as the number of trials used to assess participants' performance had to be judiciously chosen to fulfill this constraint while guarantying a successful training and subsequently a fruitful analysis.

The MEG session was systematically followed by a short MRI session in which the individual's brain anatomy as well as two datasets of BOLD-fMRI resting-state activity (2 x 9 min, eyes closed) were acquired.

1.3.2 Participants

All participants were right-handed, had normal or corrected-to-normal vision and normal hearing and were aged between 18 and 28 years (mean age in years: 22.1±2.2 s.d.). Participants were randomly split into three groups assigned to a different training: visual (V, $n = 12$, 4 females), audiovisual using acoustic textures (AV, $n = 12$, 6 females) or audiovisual using acoustic noise (AVn, $n = 12$, 6 females). Before the experiment, all participants provided a written informed consent in accordance with the Declaration of Helsinki (2008) and the local Ethics Committee on Human Research at NeuroSpin (Gif-sur-Yvette, France).

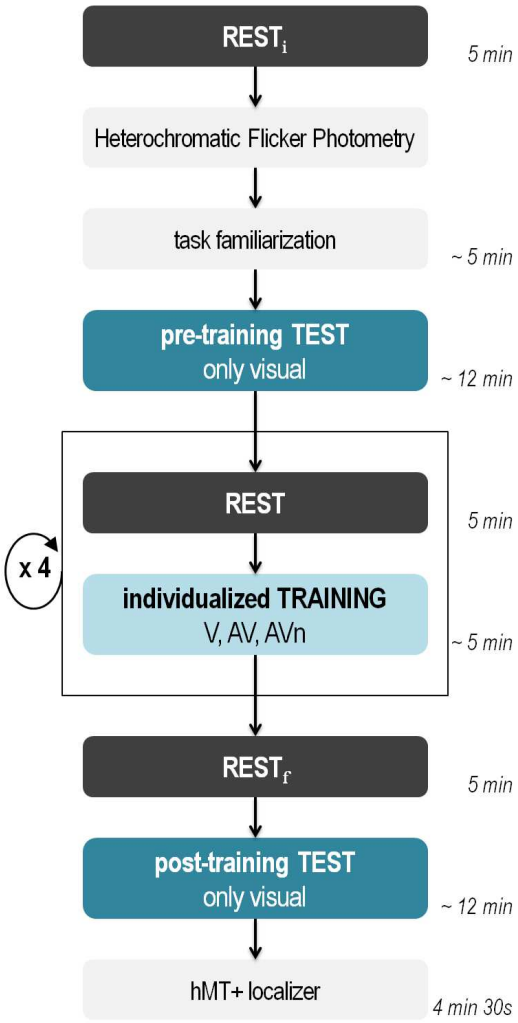

Figure 1.1: Experimental paradigm. Each individual underwent an MEG session alternating rest (in black) and task (in blue) blocks. Prior to any task, a first MEG recording of resting state (REST$_i$) was carried out. Next, the equiluminance of the red and green RDKs was calibrated using Heterochromatic Flicker Photometry. In addition, we made sure that subjects understood the task and were familiarized enough with the stimuli by presenting a few easy trials (RDK coherence set to 100%) that included feedback. In the pre-training block, all participants were presented with stimuli that were solely visual and ranged from very hard (15%) to very easy (95%) RDK coherence levels. The pre-training data established the set of coherence levels for the training session based on the individual's coherence discrimination threshold. In the following four training blocks preceded each time by a rest block, participants were trained with four levels of RDK coherence without feedback. The training could be visual only (V), audiovisual using acoustic textures (AV) or audiovisual using acoustic noise (AVn). After a last rest block (REST$_f$), the individual's coherence discrimination threshold was again tested under visual alone stimulation. In the last block, an MEG localizer provided an independent means to localize the Human motion area hMT+. An estimation of the duration is indicated beside each block.

1.4 Stimuli

1.4.1 Visual stimuli

In order to investigate the hypothesized supramodal property of the visual motion area hMT+ (cf. section 1.2.3), we decided to use Random Dot Kinematograms (RDKs), which are roughly speaking clouds of moving dots. The RDK coherence is defined as the proportion of dots moving in the same direction: the more coherent the RDK, the easier is the perception of a global motion (by contrast with the local motion of each dot). This visual feature is known indeed to be processed by hMT+.

Previous studies in multisensory learning [Seitz 2006, Kim 2008] have also used RDKs paired with auditory motion but contained from our point of view an important flaw: the sound was not orthogonal to the task — i.e. the task could be performed only based on the auditory information, by simply closing eyes. In these studies, a single RDK was presented consecutively in two sequences (one with and one without motion) and the participants were asked to indicate in which sequence the RDK was coherent. Even with eyes closed, participants could find the correct answer by listening closely the sound emitted in each sequence (stationary vs. spatially moving white noise). In another experiment [Kim 2012], the experimenter managed to make the sound orthogonal to the task by presenting the same sound in the two sequences, to the risk of allowing the elaboration of a new strategy: participants could make their decision based on how congruent visual and auditory stimuli were within each sequence. As an alternative, we designed a novel task implicating motion-color binding and coherence discrimination between two intermixed red and green isoluminant RDKS (Fig. 1.2). In this manner, the sound did not provide any information on the color and was thus orthogonal to the task.

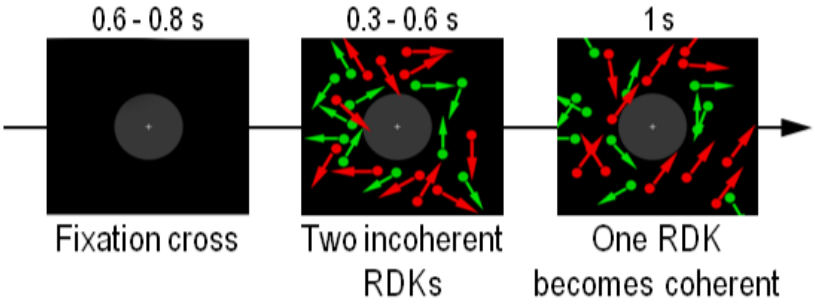

Figure 1.2: Visual stimuli. A trial consisted of the presentation of a fixation cross followed by the apparition of two intermixed and incoherent RDKs (red and green populations). After a delay of 0.3 to 0.6 s, one of the two RDKs became coherent (here the red one). Participants were asked to report the color of the coherent RDK irrespective of the motion direction. Inter-stimulus intervals were randomly drawn from 0.6 to 0.8 s.

To prevent local tracking of dots, a white fixation cross was located at the center

of a 4°gray disk acting as a mask. RDKs were presented within an annulus of 4°– 15°of visual angle. Dots had a radius of 0.2°. The flow of RDKs was 16.7 dots per deg^2.sec with a speed of 10°/s. During the first 0.3 to 06 s of a trial, both RDKs were incoherent. The duration of the incoherent phase was pseudo-randomized on each trial to prevent participants' expectation of the transition to coherent motion within a trial, thereby increasing task difficulty. After the incoherent phase, one of the RDKs became coherent for 1 s. The direction of coherent dots was comprised in an angle of 45°– 90°around the azimuth. 50% of the trials were upward; the other 50% were downward coherent motion. At each frame, 5% of all dots were randomly reassigned to new positions and incoherent dots to a new direction of motion. Dots going into collision in the next frame were also reassigned a new direction of motion. It is worth noting that dot motion was rectilinear and not Brownian, which had for effect to increase the difficulty of the task. A coherent dot is indeed more conspicuous among incoherent dots following Brownian motion than moving rectilinearly [Barlow 1997]. Moreover, this type of motion would fit better the properties of acoustic textures.

1.4.2 Auditory stimuli

The choice of the sound paired with RDKs was motivated according to several criteria: it must be orthogonal to the task, not too obvious to drive participant's attention and more important, it must contain redundant information with the RDK's coherence in an ecological manner. Different "natural" mappings exist between acoustic and visual properties: for instance, a high pitch was spontaneously associated in a fast classification task with a small size, an angular shape and an object placed at top of the visual field [Evans 2010]. The amplitude modulation of a sound can also be linked to the spatial frequency of a Gabor patch in a consistent and absolute way [Guzman-Martinez 2012]. Of more interest for us, a variation of pitch can bias the perception of vertical motion of two superimposed gratings [Maeda 2004]. In this illusion, an ascending pitch is associated with an upward motion and a descending pitch with a downward motion.

Based on this last observation, our choice has been made on using *acoustic textures* introduced by Overath et al [Overath 2010] that we further developed to be analogous and congruent to RDKs (Fig. 1.3a).

Each visual dot was designed as if to emit a sound $s(t)$ corresponding to a linear frequency-modulated ramp whose slope depended on the direction taken by the visual dot: $s(t) = \cos(2\pi e^{slope.t+\log(f_0)}.t)$ where $slope = 2\tan(\varphi)$. The angle between the direction of the dot and the azimuth is denoted by φ and the initial sound frequency is denoted by f_0. For instance, a visual motion direction of 45°corresponded to a slope of 2 octaves per second in the acoustic space. The maximal slope authorized in acoustic space was set to 16 octaves/s corresponding to visual motion directions of 82.9°– 90°. Each ramp f_0 was attributed according to the initial vertical position of the corresponding visual dot: the lower the position of the dot on the screen, the lower the f_0 in acoustic space. Hence, a visual dot moving upwards

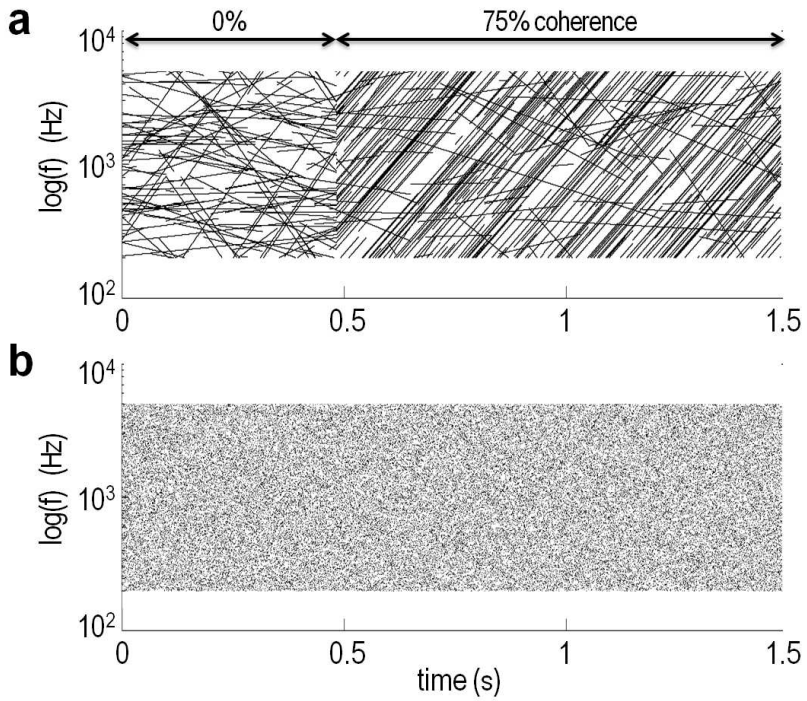

Figure 1.3: Auditory stimuli presented during AV and AVn training. Spectrograms are plotted in log(frequency) as a function of time. **(a)** Sample spectrogram depicting an acoustic texture used in AV training. By analogy to a visual RDK, the level of coherence in an acoustic texture was defined as the number of frequency ramps sharing the same slope in a given frequency range. Here, the spectrogram illustrates an incoherent acoustic texture lasting 0.5 s followed by a 75% coherent acoustic texture lasting 1 s. **(b)** Sample spectrogram of an acoustic noise used in AVn training. This sound is unrelated to the visual RDKs and has the same amplitude, duration and frequency range as the acoustic texture.

emitted a sound with an ascending ramp whereas a visual dot moving downwards had an acoustic ramp with a negative slope. The auditory frequencies were bounded between 200 and 5000 Hz. Should a ramp cross one of these limits, it "continued" at the other extreme of this frequency band (toroidal boundary conditions). The duration of a ramp was identical to the life-time of a visual dot. Importantly, when visual dots moved coherently, they did not necessarily emit the same sound because the initial auditory frequencies likely differed. However, the variations of the sounds (i.e. the slopes of the ramps) were identical. Hence, unbeknownst to participants, the quantification of visual coherence in RDK matched the proportion of ramps having the same slope in acoustic space.

To test the specificity of this sound, acoustic textures were replaced by uninformative acoustic noise of same duration and same amplitude in the AVn training (Fig. 1.3b). The emitted sound $y(t)$ was also designed to be confined in the same frequency range (200–5000 Hz): $y(t) = \cos(2\pi \mathrm{e}^{rand \cdot (\log(f_{max}) - \log(f_{min})) + \log(f_{min})} . t)$, where *rand* denotes the uniformly distributed pseudorandom function whose values are contained in the interval $[0, 1]$, $f_{min} = 200$ Hz and $f_{max} = 5000$ Hz.

All auditory stimuli were created with a sampling frequency of 44.1 kHz.

Chapter 2

Psychophysics

Contents

Psychophysics refer to a discipline in experimental psychology that aims to link the properties of a physical stimulus and the way we perceive it. Here, the analysis of behavioral data (i.e. performance, reaction time and confidence rating) is an important step in order to evaluate the efficiency of the three trainings (V, AV and AVn) and ultimately to validate our paradigm before going into further analysis of MEG data.

Results are presented in the first section and consist of comparing pre- and post-training data within each training group, followed by a complementary analysis of performance and reaction time in the course of training. As expected, participants trained in AV conditions significantly outperformed participants trained in V and AVn although they were unaware of their progress. These results, discussed in the last section, suggest that AV training could have benefited from the supramodal processing of coherence — redundantly present in both acoustic textures and coherent RDKs.

2.1 Results

2.1.1 Comparison of pre- and post-training

In this section, all results reported here focus on the comparison of the pre- and post-training tests in which no acoustic information was delivered to participants.

Hence, we do not address here the issue of multisensory integration *per se* and rather report the effect of participants' training history on the behavioral changes implicated in a novel visual motion coherence discrimination task.

A mixed-design ANOVA containing the within-subjects factor test (pre- and post-training) and the between-subjects factor training (V, AV and AVn) was carried out separately on the perceptual thresholds, the confidence ratings and the Reaction times (RTs) using the R software (R Core Team 2013). If a main effect of the factor test was found, a post-hoc analysis using Bonferroni-corrected paired t-tests on each group was further conducted. Likewise, a main interaction between factors test and training was further analyzed with a Bonferroni-corrected two-sampled t-test between each pair of groups.

2.1.1.1 Perceptual threshold

The coherence discrimination threshold was set to 75% of performance (i.e. correct answers) and quantified by fitting a Weibull function [Wichmann 2001] to each individual's psychometric curve using:

$$\Psi(coh, \lambda, \alpha, \beta) = \lambda - (\lambda - 0.5\mathrm{e}^{-(\frac{coh}{\alpha})^{\beta}}),$$

with *coh* as motion coherence level, Ψ as the fitted psychometric function, and λ, α and β the parameters determined by the damped Gauss-Newton method (see Fig. 2.1a–c). The initialization parameters required for that method were specified as follows: $\lambda_0 = 1$, $\alpha_0 = 1 - \frac{1}{\mathrm{e}}$ and $\beta_0 = \alpha_0 + \mathrm{e}$.

The analysis of the threshold changes before and after training (Fig. 2.1d) by using a mixed-design ANOVA indicated that: i) in the pre-training test, all participants performed similarly well on the coherence discrimination task and the observed perceptual thresholds did not differ between the three groups ($F_{2,33} = 1.12$, $p = 0.34$), ii) in all groups, training successfully improved participants' performance ($F_{1,33} = 132$, $p = 4.5e-13$) and iii) a significant interaction between types of training and tests was found ($F_{2,33} = 8.3$, $p = 1.2e-3$). More precisely, the post-hoc analysis confirmed our prediction by showing that the AV group significantly outperformed the two other groups after training.

2.1.1.2 Reaction time (RT)

RTs were measured following the apparition of the coherent RDK. In this analysis, only RTs associated with correct responses were kept and sorted as a function of the level of coherence by taking the corresponding median value (to exclude extreme outliers). As expected, a first observation of pre-training data shows that RT decreases as the RDK coherence level increases (Fig. 2.2a–c). In addition, RT is homogeneously reduced after training across all RDK coherence levels.

The analysis of the mean RT changes before and after training averaged over all coherence levels (Fig. 2.2d) by using a mixed-design ANOVA showed a significant reduction of mean RTs after training in all groups ($F_{1,33} = 95$, $p = 3e-11$) without

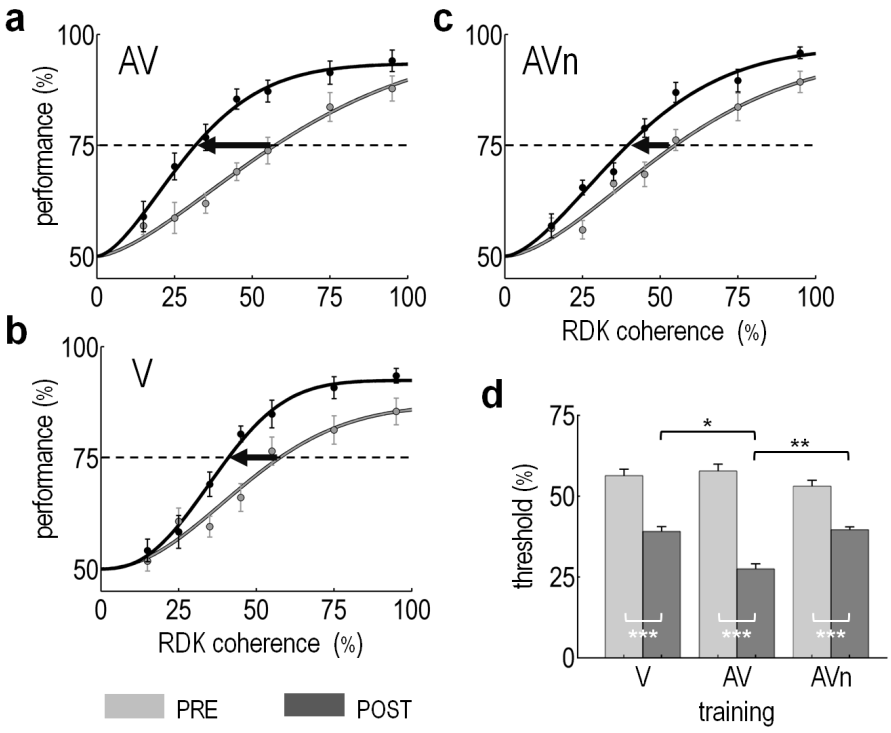

Figure 2.1: Threshold changes as a function of training type. Mean performance (±1 s.e.m.) as a function of visual coherence levels in AV **(a)**,V **(b)** and AVn **(c)** groups before (PRE, light grey) and after (POST, dark grey) training. For illustration, Weibull functions were fitted to the mean psychometric curves in each group. The mean perceptual threshold corresponds to the mean coherence value of one RDK population with a correct response rate of 75% (black dashed line). Perceptual threshold improvements are indicated with black arrows. **(d)** Mean discrimination thresholds (+2 s.e.m.) obtained from each individual Weibull function in PRE- and POST-training for each group. Perceptual threshold improvements were significant in all groups. As can be readily seen after training, the threshold in the AV group was significantly lower than the one obtained in the V and AVn groups. Bonferroni-corrected p value inferior to 0.05, 0.01 and 0.001 are indicated by *, ** and ***, respectively.

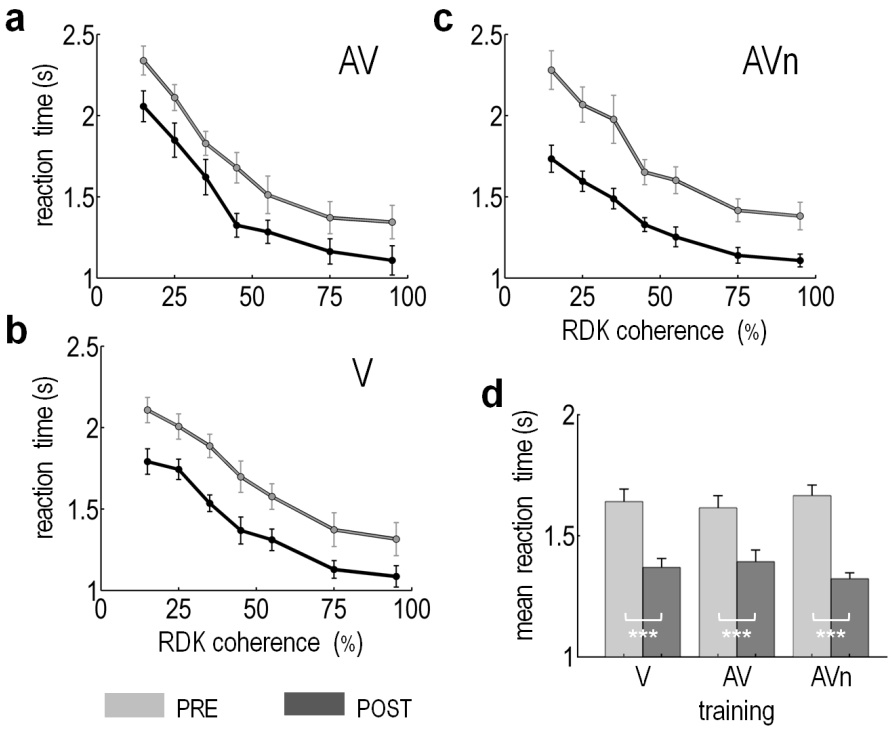

Figure 2.2: RT decreases irrespective of training type. Mean RT (±1 s.e.m.) as a function of RDK coherence in AV **(a)**,V **(b)** and AVn **(c)** groups before (PRE, light grey) and after (POST, dark grey) training. After training, reaction times decreased for all coherence levels in all groups. **(d)** Mean RT (+2 s.e.m.) averaged over all coherence levels and subjects in each group in PRE and POST training. All three groups showed a significant decrease in their RT without distinction between training types. ***: Bonferroni-corrected p value inferior to 0.001.

any interaction between types of training ($F_{2,33} = 1.5$, $p = 0.23$). No statistical distinction between groups could be made before and after training ($F_{2,33} = 0.007$, $p = 0.99$).

We also asked if individual RT reductions were correlated with the corresponding threshold decreases within each group separately. In each case, the computed Pearson correlation coefficient was not significantly different from 0 (V: $\rho = 0.52$, $p = 0.08$; AV: $\rho = -0.27$, $p = 0.4$; AVn: $\rho = 0.04$, $p = 0.9$).

2.1.1.3 Confidence rating

Participants were asked to rate their confidence after each trial following their coherence discrimination response on a discrete numeric scale ranging from 1 ("not sure at all") to 5 ("sure and certain"). The values were first sorted and averaged over trials as a function of RDK coherence. Among the different measures of performance awareness used in implicit learning (e.g. post-decision wagering, feeling of warmth, rule awareness on a discrete or continuous scale), confidence rating is a well-established means to assess conscious knowledge in decision making (e.g. [Dienes 2008]) and has been recently shown to be sensitive and exhaustive enough to capture the largest range of consciousness [Wierzchoń 2012]. Here, we can see in pre-training (Fig. 2.3a–c) that essentially the middle values (2, 3 and 4) were used by participants. Except for V, the confidence rating does not seem to change much after training.

By analyzing the mean confidence rating changes before and after training averaged over all coherence levels (Fig. 2.3d) with a mixed-design ANOVA, a significant increase of confidence rating ($F_{1,33} = 7.2$, $p = 0.011$) was found, without interaction with training types ($F_{2,33} = 1.35$, $p = 0.27$). However, this effect was attributed solely to the group V after post-hoc analysis. Moreover, the three groups could not be statistically distinguished ($F_{2,33} = 0.61$, $p = 0.55$).

We also verified separately within each group if participants' threshold decreases were correlated with the individual variations of confidence. In each case, the computed Pearson correlation coefficient was not significantly different from 0 (V: $\rho = -0.03$, $p = 0.93$; AV: $\rho = 0.42$, $p = 0.17$; AVn: $\rho = -0.14$, $p = 0.66$).

2.1.2 Complementary analysis during training

We can wonder if the differences observed in post-training between the three groups already appeared during training. It is worth reminding that here, contrary to the previous section, the conditions under which the task was performed clearly differed in each group V, AV and AVn (i.e., without sound, with correlated acoustic textures or uncorrelated noise, respectively). The direct effects of multisensory integration are thus questioned. During training, we only measured the performance (i.e. accuracy) and the RTs corresponding to four levels of coherence set around the individual's initial threshold. The number of coherence levels was thus insufficient to allow the assessment of the perceptual threshold in these blocks. As an alternative,

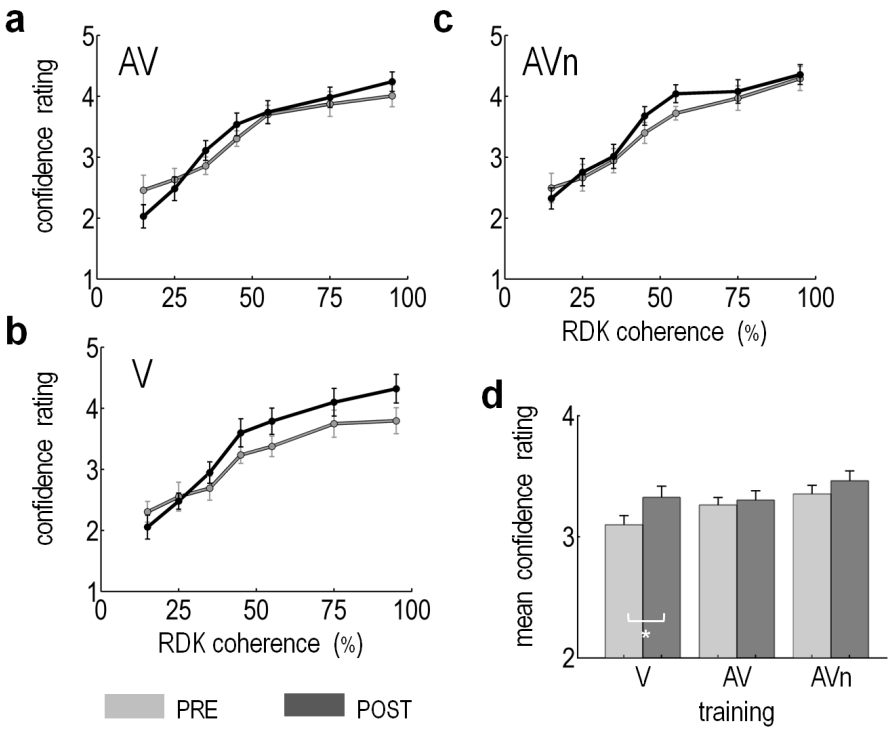

Figure 2.3: Weak changes of confidence ratings. Mean confidence rating (± 1 s.e.m.) as a function of RDK coherence in AV **(a)**,V **(b)** and AVn **(c)** groups before (PRE, light grey) and after (POST, dark grey) training. **(d)** Mean confidence rating (+2 s.e.m.) averaged over all coherence levels and subjects in each group in PRE and POST training. Only participants in the V group presented a significant increase of confidence. *: Bonferroni-corrected p value inferior to 0.05.

we averaged the performance and RTs over the four levels of coherence and examined their course over the four training blocks (Fig. 2.4a–b).

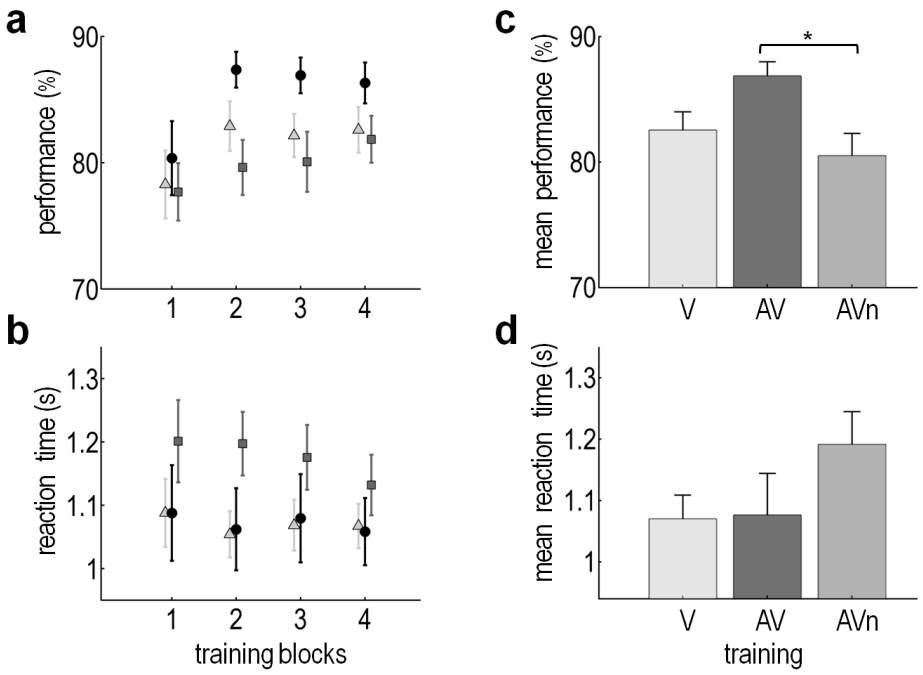

Figure 2.4: Performance and RT during V, AV and AVn training. Mean performance **(a)** and RTs **(b)** (± 1 s.e.m.) over the four blocks of training in condition V (light grey triangles), AV (black circles)and AVn (dark grey squares). Contrary to RTs, performance changes significantly over blocks. AV training is in average faster than V, which is in turn slightly faster than AVn. Participants in the AVn condition seem to be slower than the others, although they appear to reduce the gap in the end. **(c)** Mean performance (+2 s.e.m.) averaged over the last three training blocks in V, AV and AVn. Participants in AV significantly outperform those in AVn. **(d)** Mean RT (+2 s.e.m.) averaged over the first three training blocks in V, AV and AVn. Although RT in the AVn condition appears to be higher, it is not significant. *: Bonferroni-corrected p value inferior to 0.05.

By carrying out a mixed-design ANOVA with the within-subjects factor training block (1, 2, 3 and 4) and the between-subjects factor training (V, AV and AVn) separately on the performance and the RTs, we found a significant change of performance over the blocks ($F_{3,99} = 6.74$, $p = 3.4e-4$) but surprisingly no significant change of RT ($F_{3,99} = 1.37$, $p = 0.26$). With regards to performance, the three groups seem to dissociate starting from the second block (see Fig. 2.4a). A F-test was hence carried out on the mean performance averaged over the three last blocks to test for any statistical differences between V, AV and AVn (Fig. 2.4c) and was indeed rejected ($F_{2,33} = 4.85$, $p = 0.014$). A post-hoc analysis (using R software's Tukey Honestly Significant Differences) showed indeed a significant difference between the AV and

AVn conditions ($p = 0.012$). On the other hand, an F-test carried out on the mean RTs averaged over the first three sessions (i.e. where AVn appears higher than V and AV) did not reveal any statistical differences ($F_{2,33} = 1.56$, $p = 0.23$) (Fig. 2.4d).

2.2 Discussion

The main analysis comparing pre- and post-training data clearly demonstrates that AV training improves visual learning and that these effects cannot be accounted for simple attentional mechanisms. Otherwise, AVn training should be as effective as AV training. Participants trained with acoustic textures outperformed the others only in term of sensitivity (i.e. greater discrimination threshold reduction) but were not faster or more confident in their responses (actually, only V participants became significantly more confident).

2.2.1 Supramodal objects and cross-sensory feature matching

As previously reviewed in chapter 1, multisensory information has been shown to benefit perceptual learning [Shams 2008]. However, the observed perceptual improvements are generally small and can require a long training time: with ten days of training, presenting auditory motion cues has been shown to improve visual direction discrimination [Seitz 2006] and acoustic cues can alter the direction of visual motion [Freeman 2008, Hidaka 2011].

Here, consistent with the hypothesis that using redundant multisensory information should yield greater benefits [Alais 2004], we capitalized on cross-sensory feature matching namely, the temporal coherence between auditory spectral changes and visual spatial patterning over time. The temporal coherence of audiovisual information is inherent to natural stimuli: in particular, the envelope of auditory speech is known to correlate with the speaker's facial gestures ([Grant 2000, Schwartz 2004] and more generally, auditory pitch and visual spatial frequency undergo automatic cross-sensory matching [Maeda 2004, Evans 2010]. The comodulation of audiovisual signals is thus a fundamental attribute of natural scenes that enables the brain to appropriately bind sensory features belonging to the same physical object, albeit processed through different sensory processing streams. Hence, by using matched audiovisual correspondences, we expected rapid cross-sensory mapping allowing for more efficient learning in the AV group as compared to the control AVn and V groups. In agreement with this hypothesis, the AV group significantly outperformed the V and control AVn groups, suggesting that the mere presence of sound is not sufficient to improve visual coherence discrimination and rather, that the correlated temporal structure imposed on the audiovisual stimuli during training largely benefited visual discrimination.

2.2.2 Speed-accuracy trade-off

As expected, all individuals responded more quickly after training. More surprising however, this improvement occurred without any distinction between the three groups, although AV training was more efficient in reducing the discrimination threshold. This can be first explained by the instructions given to participants to prioritize accurate responses. By doing so, participants were expected to develop the same strategy and the same speed-accuracy trade-off [Liu 2012].

In addition, the uncorrelated variation of these two variables might reflect two different mechanisms that have been learned. For instance, the decrease of RT could reflect the learning in color-motion binding whereas the decrease in perceptual thresholds would indicate a better coherence discrimination. A closer inspection of RTs and performance during training indicates a strong dissociation between these two variables: participants were indeed already faster in the first block and did not show any further improvement in the next blocks. Conversely, they became more accurate only in the next blocks. Even in presence of acoustic textures, AV participants were not significantly faster than the others while they performed better. Conversely, the presence of acoustic noise seemed initially to hinder AVn participants in responding as fast as the others, although the effect is not significant at the group-level. This weak effect might be explained by the relatively low value of the sound pressure level that was set to minimize cross-modal shifts of attention.

2.2.3 Implicit learning

An additional intriguing feature was that unlike V learners, the confidence rating of the AV and AVn groups did not change after learning. The lack of increased confidence rating in participants undergoing multisensory training rules out the possibility of a conscious cross-sensory mapping or a cognitive strategy developed by participants to accomplish the task and strongly suggests that audiovisual mapping occurred at an implicit level during training, which is consistent with the notion of automatic binding in multisensory integration [Talsma 2010] and with the fact that implicit learning of statistical contingencies can occur across sensory modalities [Seitz 2007, Mitchel 2011].

A possibility to explain the gain of confidence in V is that the conditions were the same across test and training blocks (i.e. without sound), contrary to AV and AVn groups. Hence, the gain of confidence could reflect a greater familiarity with the task. This hypothesis is consistent with the fact that perceptual improvement did not correlate with the gain of confidence — even among V participants. To further test this hypothesis, it would have been necessary to include confidence ratings during training (which was impossible for timing reasons) and compare them between groups. Additionally, the pre- and post-training perceptual thresholds specifically focused on data collected in visual alone conditions in all three groups, thereby alleviating the possibility of divided attentional effects during task performance. Another explanation would be to account for inter-individual differences in confidence rating

irrespective of learning [Song 2011].

2.2.4 Unresolved questions

Last but not least, it is quite remarkable that all participants improved in this visual motion discrimination task within only 20 minutes of training. As previously mentioned, this novel task was complex enough to involve different mechanisms that could be potentially learned (i.e. color-motion binding and RDK coherence discrimination). Because the visual task's novelty mainly consists of labeling the color of the coherent RDK, we suspected this mechanism to require little time to be learned. The specificity of such learning could have been verified for instance by testing participants with a new pair of colored RDKs (e.g. orange and magenta) or with RDKs of different shapes (e.g. squares and triangles) but same color.

Instead, we predicted that the improvements in coherence discrimination thresholds observed in all groups would be reflected by functional plasticity in early sensory areas involved in global motion processing such as the human motion area hMT+. This hypothesis can be verified only by overcoming the limitations of psychophysics, that is by analyzing the MEG data.

Chapter 3

Magnetoencephalography

Contents

As we were interested in tracking non-invasively the dynamics of cortical activity during perceptual learning, magnetoencephalography appeared as the best qualified technique thanks to its high time resolution. In addition, by collecting a great amount of data, it would enable us to accurately assess scale-free properties of time series such as multifractality.

In the first section, we review the physiological origins of the signal measured by MEG. We further present the instrumentation and the different preprocessing methods that are generally required to remove unwanted interference from the signal of interest. In the next section, we review the different methods of source reconstruction that can be used to localize the neural sources of the MEG signals. This step can be particularly crucial in group studies as it accounts for the individual's brain anatomy. For further details, the reader can refer to [Gramfort 2009a, Hansen 2010]. In the last section, we detail the procedure of the MEG acquisition, preprocessing and source reconstruction that was used for both ERF and scale-free analysis.

3.1 Basics of magnetoencephalography

The first human EEG recordings were carried out by the German physiologist and psychiatrist Hans Berger in 1929. About 40 years later, the first successful MEG acquisition was done at the Massachusetts Institute of Technology by David Cohen on healthy and epileptic subjects. MEG and EEG are closely related, as they measure respectively the magnetic and electrical activity of a same neuronal population in the brain, with a 1 ms time resolution. They are also completely non-invasive: not only they do not require opening the skull, but they also do not expose individuals to x-rays, radioactive tracers or to strong magnetic fields. These two technologies differ however in size and cost (Fig. 3.1a): EEG is relatively cheap (about ten thousand dollars) and easy to manipulate whereas MEG is more expensive (several millions of dollars) and bulky. For this reason, EEG is still more widely used than MEG, particularly for clinical applications (e.g. epilepsy, language disorder) [Hughes 1994, Hämäläinen 1993]. As it can be seen on Fig. 3.1b, the information brought by MEG and EEG from a same source activity in the brain is orthogonal and complementary [Hämäläinen 1993]. However, MEG offers better spatial resolution (up to some millimeters in the best conditions). In addition, the electric currents measured by EEG on the scalp is strongly attenuated as it must penetrate resistant layers of different electric conductivities such as meninges, cerebrospinal fluid, dura mater, bones of the skull, galea, and skin.

The electromagnetic activity measured by MEG and EEG comes essentially from the cortical surface which contains approximately 10^{10} neurons. Neurons consist of a cell body (named soma), several dendrites and an axon along which action potentials propagate. When action potentials reach a synapse, they trigger the release of neurotransmitters, which in turn activate the opening of selective ion channels in the dendritic membrane of the post-synaptic cell. This generates a post-synaptic potential and thereby an ionic current in the dendrite due to the chemical concentration gradients. The sole activation of one neuron is not enough to be measured by EEG or MEG: only the synchronized activation of tens of thousands of neurons can be detected. Because the duration of an action potential is too short (~ 1 ms) to allow synchronization, post-synaptic potentials (which last several tens of millisecond) are likely the main contributors to the measured electromagnetic field. In addition, the currents associated with action potentials in the axons flow in opposite directions, nullifying the corresponding magnetic field.

Another condition for post-synaptic potentials to sum up is that they must have the same direction. Contrary to stellate neurons whose dendrites are oriented in all directions, pyramidal neurons have a thick and relatively long dendrite (called apical dendrite) orthogonal to the cortical surface and are thus well designed to generate post-synaptic potentials in the same direction. Moreover, the primary current in dendrites also alters the distribution of free charges in the surrounding tissue, generating passive ohmic currents named volume currents. In certain configurations (e.g. for a radial source in a spherical conductor), the external field resulting from the primary and volume currents cancels out [Hämäläinen 1993]. Hence, MEG

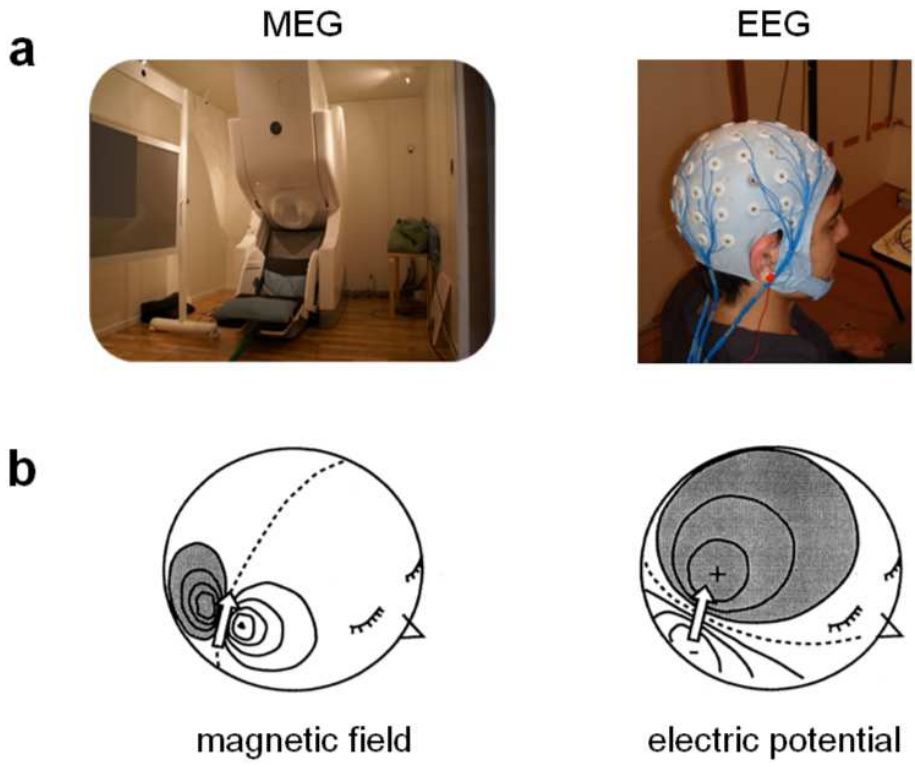

Figure 3.1: Magnetoencephalography versus electroencephalography. (a) Current MEG equipment used at Neurospin (Neuromag Elekta LTD, Helsinki, Finland) and EEG equipment used at Kyushu university (Nexstim, Helsinki, Finland). **(b)** Schematic illustration of idealized magnetic-field and electric-potential patterns produced by a tangential dipole source (white arrow). (Adapted from [Hämäläinen 1993]).

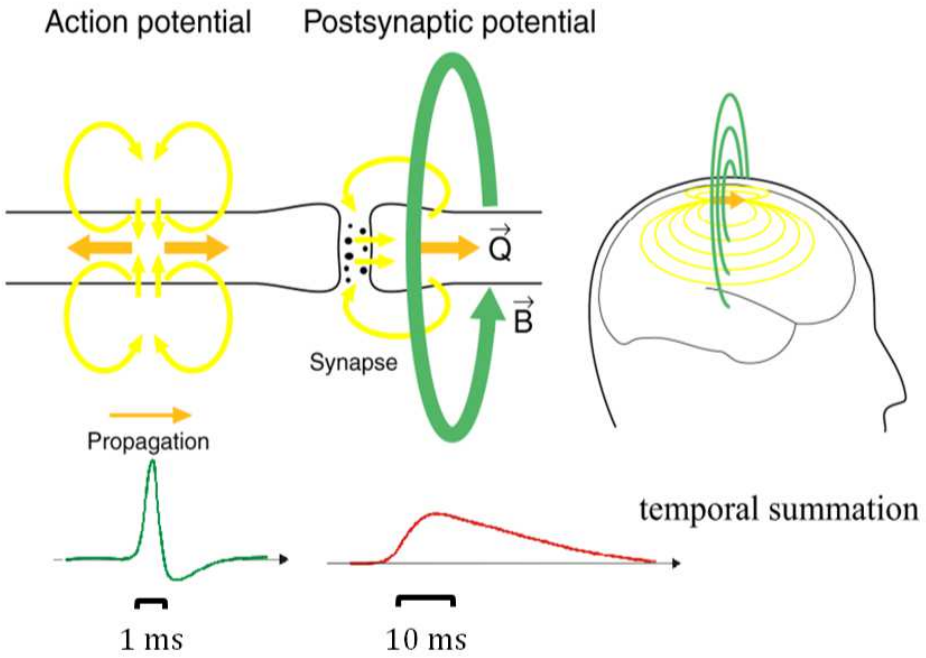

Figure 3.2: The brain magnetic field arises in the dendrites. The magnetic and electrical fields $\vec{B}$ and $\vec{E}$ and the current dipole $\vec{Q}$ are plotted in green, yellow and orange respectively. The magnetic field measured outside the head results from the synchronized summation of tens of thousands of post-synaptic potentials for two reasons: 1) the temporal summation is more likely to be effectuated in the dendrites thanks to the long duration of post-synaptic potentials (several tens of milliseconds) 2) The magnetic field generated by action potentials is strongly attenuated as electric charges flow in both directions. (Adapted from Elekta's MEG overview).

reflects essentially the activity coming from the fissures of the cortex, i.e. sulci (see Fig. 3.3).

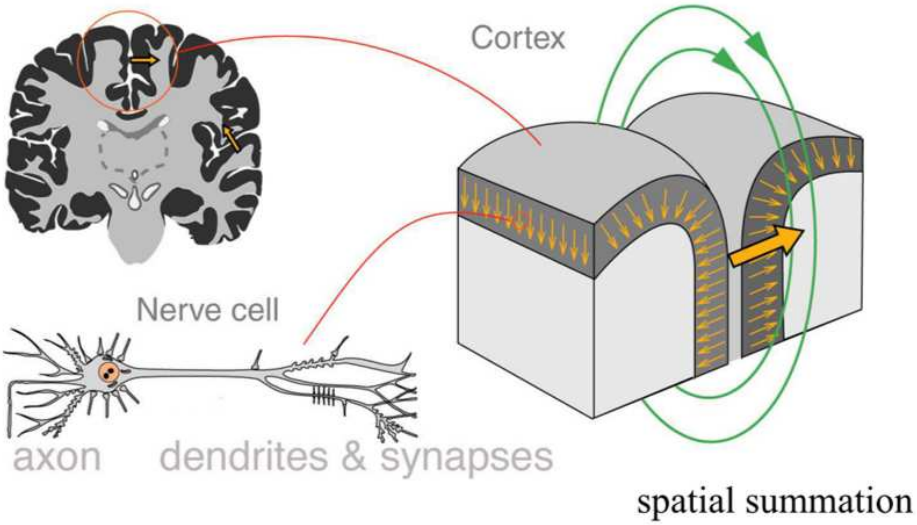

Figure 3.3: Effect of the pyramidal cell orientation. The resulting external magnetic field (in green) is the sum of all magnetic fields generated by the tangential current dipoles (in orange) that are situated in the pyramidal cells of a cortical sulcus. Sources at the top of a gyrus produce radial fields that are not detectable by MEG. (from Elekta's MEG overview).

With a cortical sheet of approximately 4 mm of thickness and 2500 cm^2 of surface [Hämäläinen 1993], the density of pyramidal neurons should theoretically allow 1 mm^2 of activation to be detectable [Hansen 2010]. It appears however that the minimal detectable activity spreads over an area of about 100 mm^2 [Gramfort 2009a].

3.2 Instrumentation and preprocessing

3.2.1 The MEG equipment

The late development of MEG with regards to EEG originates from the challenging difficulty in measuring extremely weak magnetic fields (i.e. below 1 pT) such as the one emitted by the brain. This became only possible with the introduction of a sufficiently sensitive sensor named SQUID (for Superconducting Quantum Interference Device) in the late 1960s by James Zimmerman. The SQUID can be roughly described by a ring immersed in liquid helium at a very low temperature ($T < -269$ C°) in order to be maintained in a superconducting state. In that condition, any current circulating in the loop continues infinitely without Joule effect losses. Conversely in presence of a static magnetic field, a shielding current appears on the surface and gives rise to an opposite magnetic field of same amplitude that prevents the generation of an internal current. In addition, two thin layers of electric insulators (also

named Josephson junctions) are inserted in the ring and perturb the electron flow (that still cross the insulators by tunnel effect). This interference yields an indirect measure of the superficial current, and hence of the external magnetic field.

In MEG devices, SQUIDs are rather small (less than 1 mm of diameter) and necessitate sensor coils to collect the magnetic flux from a much larger area [Hansen 2010]. The simplest sensors are *magnetometers* (Fig. 3.4a) and consist of a single pick-up coil made of superconducting material that measure the magnetic field component along the direction perpendicular to the surface of the coil. Another type of sensors less sensitive to external disturbances are the *gradiometers* that measure the spatial gradient of the magnetic field by deducting the current flowing through a second compensation coil. In this manner, they are insensitive to homogeneous magnetic field coming from distant sources and more effective in measuring the inhomogeneous field produced by nearby sources, such as neural currents in the brain. The two coils of a gradiometer can either be placed along the same radial axis (axial gradiometers, Fig. 3.4c) or side-by-side in the same plane (planar gradiometers, Fig. 3.4b). The planar gradiometers are advantageously more compact (allowing a greater number of sensors) and are more sensitive to sources located right beneath them (whereas axial gradiometers better capture sources located at their periphery).

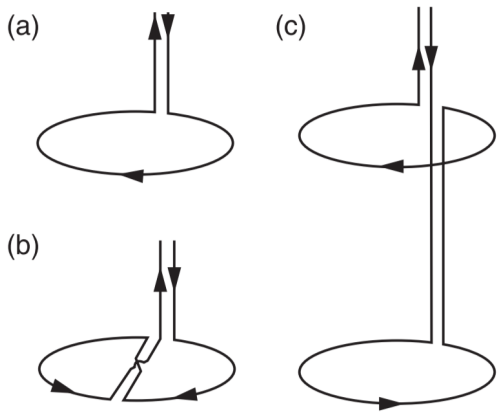

Figure 3.4: Types of sensor coils. (a) Magnetometer . **(b)** Planar gradiometer. **(c)** Axial gradiometer. A magnetometer consists of a single pick-up coil which makes it sensitive to homogeneous magnetic field produced by distant sources. Planar and axial gradiometers possess two coils wound in opposite directions, making them sensitive only to the local inhomogeneous field. As readily observed, a planar gradiometer is much more compact than an axial one. (from [Hämäläinen 1993]).

Magnetometers and gradiometers are then assembled into a sensor array to permit simultaneous measures of brain magnetic field at diverse locations of the head. They are contained in a helmet named Dewar (after the inventor James Dewar) that prevents heat transfer between the helium and the outside (i.e. about 300 C°of difference!). This is indeed critical, given that the distance between the subject's scalp

and the coil sensors must be minimized to yield the better signal-to-noise ratio.

Not only MEG signals are very weak and difficult to detect, but they are also drowned out by the environmental noise: fluctuations in the earth's magnetic field, movements of vehicles or elevators, waves emitted by radio and television... One of the most important means to protect MEG signals is the use of a magnetically shielded room (MSR). Its walls are made of ferromagnetic layers that considerably reduce the field strength within the room, yielding an attenuation of approximately 60 dB above 100 Hz and 20 dB below 0.1 Hz [Hansen 2010]. It can be combined with another shielding technique based on eddy currents flowing through aluminium, that allows to increase the shielding factor at high frequencies (40 dB above 100 Hz) [Hansen 2010]. This passive system can be enhanced by active compensation: the external field is measured by magnetometers and is counterbalanced by an opposite field generated by coils installed around the room. In addition, the residual noise inside the MSR can be measured by reference sensors situated some centimeters away from the subject's head and subsequently subtracted.

3.2.2 Preprocessing methods

After MEG acquisition and prior to preprocessing, the very first step is to meticulously inspect raw data in order to detect and exclude bad channels that can be "flat", full of "jumps" or that present "crazy" behaviors. Although this can be very tiring and time-consuming, it should not be neglected: automatic correction provided by the following preprocessing methods often fails in such cases.

Signal-space separation (SSS). Instead of using reference channels, external interference can be removed offline with the SSS method [Taulu 2004], which also has the advantage to reduce sensor and movement artifacts. By exploiting the physics of magnetic fields and the geometry of the sensor array, SSS attributes the origin of the signal to two subspaces — either inside or outside a sphere centered on the head. Only the contribution from the sphere is conserved as it contains the signal of interest emitted by neural sources. More precisely, it exploits the Maxell's equations (see equation (3.1) in the next section) and the fact that sensors are contained in a source-free volume, implicating that the magnetic field $\vec{B}$ derives from a potential Φ:

$$\vec{rot}\vec{B} = \vec{0} \quad \Rightarrow \quad \vec{B} = -\vec{grad}\Phi$$

The signal space containing neural sources is then delimited by a sphere of which parameters (center and radius) are set as a function of the device configuration and the position of the head. Φ is thus expressed in spherical coordinates. In addition, the non-divergence of $\vec{B}$ yields :

$$\Delta\Phi = div(\vec{grad}\Phi) = 0$$

This is the Laplace's equation and its general solution $\Phi(r, \theta, \varphi)$ in spherical coordinates is a linear combination of elementary *spherical harmonic functions*

$\Upsilon_{l,m}(\theta,\varphi)$[1]:

$$\Phi(r,\theta,\varphi) = \sum_{l=0}^{\infty}\sum_{m=-l}^{l}(A_{l,m}r^{-1-l} + B_{l,m}r^{l})\Upsilon_{l,m}(\theta,\varphi)$$

These functions form an orthogonal infinite basis on which Φ can be decomposed. However, the limited number of sensors imposes to truncate the series of harmonic functions describing Φ. In the SSS framework, the first term containing the scale factor r^{-l-1} represents the signal subspace as its divergence at the origin reflects the presence of sources close to the center of the sphere. Conversely, the interference subspace is represented by the second term scaled by a factor r^{l} diverging at infinity for distant sources. Data are thus expressed in the spherical harmonic space as a sum of these two subspaces, and subsequently reconstructed using only the term associated with the signal space.

This method is mainly effective in removing interference from distant sources but less when it comes from nearby sources. This can be partly remedied by extending SSS to the temporal dimension [Taulu 2009]. Close sources are essentially physiological noise such as the electrical activity of the heart and muscular contractions (Fig. 3.5) which generate artifacts 10 to 100 times higher than the signal of interest. More important, the ionic currents of the eyes dramatically perturb the signal at any saccades or blinks. Also in presence of moving magnetic particles, the signal becomes completely unreadable. This is why individuals undergoing an fMRI acquisition have to wait at least 24 hours before participating to an MEG acquisition.

Signal-space projection (SSP). In practice, SSP [Uusitalo 1997] is used in combination with principal component analysis (PCA) to remove cardiac and ocular artifacts. Similarly to SSS, the approach consists of projecting data into two subspaces (signal vs. noise) but using this time statistical properties. It exploits the fact that external interference and neural sources generate a different spatial pattern across sensors. The first step is to select data segments locked on the apparition of an artifact: for instance by using an electrocardiogram (ECG) or an electrooculogram (EOG) to detect cardiac and ocular artifacts respectively. PCA is then applied on the averaged (better SNR) or concatenated (better statistical power) data segments and transforms them into a set of linearly uncorrelated components via a spatial filter. After selecting the artifact components (usually the ones of greatest variance), data are projected on the orthogonal sub-space that assumed to correspond to the signal. By doing so, the rank of data is reduced by the number of artifact components and the signal topography is slightly altered. Consequently in case of source reconstruction, the projection matrix must be preserved and applied again during the computation of the forward operator to ensure unbiased estimation [Gramfort 2013].

[1] The spherical harmonics have the following form in the real domain:
$\Upsilon_{l,m}(\theta,\varphi) = P_l^m \cos\theta \cos m\varphi$, where P_l^m is an associated Legendre function.

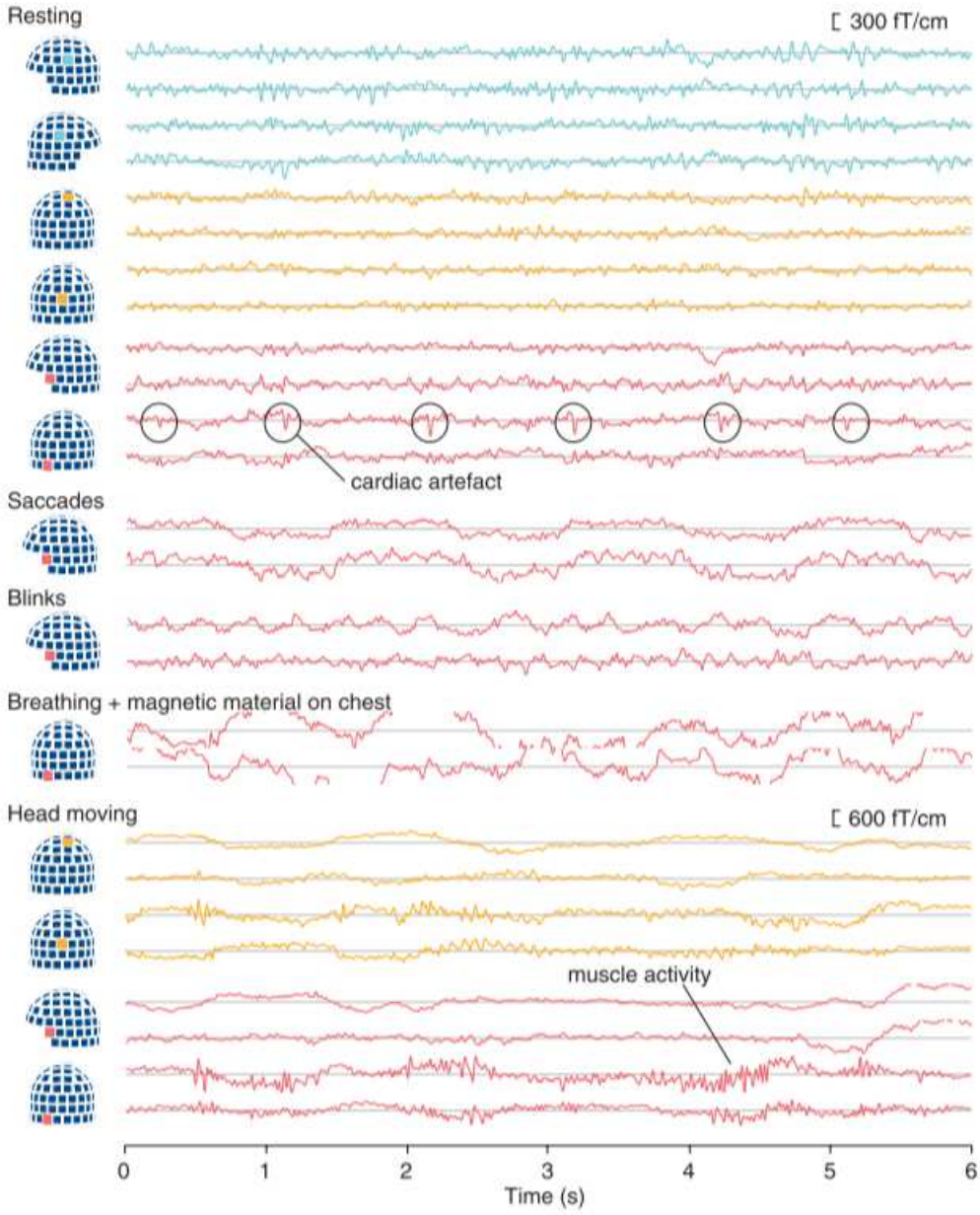

Figure 3.5: Normal vs. artifactual signals on representative MEG channels (planar gradiometer pairs). Top rows show typical raw MEG traces from a resting subject (note the regular cardiac artifact on the lowest sensors), whereas the lower traces display typical biological artifacts and a breathing-induced signal from a magnetic particle on the chest of the subject. (from [Hansen 2010]).

SSP can also be employed alternatively with the independent component analysis (ICA)[Herault 1986]. Similarly to PCA, this blind source separation method is a spatial filter that extracts statistically independent components from the data. This approach is particularly well adapted if the artifacts occur independently from neural activity and if they are non-Gaussian. It requires however a certain expertise to recognize the artifact components given that all components are normalized (unitary variance and zero mean). Different algorithms exist such as the JADE [Comon 1994], Infomax [Bell 1995] or the most commonly used fastICA [Hyvärinen 2000] algorithms but are beyond the scope of this chapter.

3.3 Source reconstruction

Because MEG measures the magnetic field generated by neurons outside of the head, it does not directly inform on the localization of brain activations. For that purpose, it requires modeling the head and the mechanism that gives rise to an external magnetic field from a given configuration of sources: this is called the *forward problem* and has been reviewed for instance by [Hämäläinen 1993, Mosher 1999]. Once the model has been established, the procedure can be inverted and the sources at the origin of the MEG measurements can be estimated: this is called the *inverse problem* (see for instance reviews of [Baillet 2001, Darvas 2004].

3.3.1 The forward problem

The physical mechanism relating the magnetic field $\vec{B}$ and the electric field $\vec{E}$ to the sources' charge density ρ and current density $\vec{J}$ are given by the Maxwell's equations:

$$\begin{cases} div\vec{E} &= \frac{\rho}{\varepsilon} \\ r\vec{o}t\vec{E} &= -\frac{\partial \vec{B}}{\partial t} \\ div\vec{B} &= 0 \\ r\vec{o}t\vec{B} &= \mu(\vec{J} + \varepsilon\frac{\partial \vec{E}}{\partial t}) \end{cases} \tag{3.1}$$

where ε is the electrical permittivity of the medium and μ is the magnetic permeability.

These equations can be simplified under certain assumptions. Firstly, the permeability of head tissues is the same as in free space ($\mu = \mu_0$). Secondly, the time derivatives can be neglected because the frequencies of the brain magnetic field rarely exceeds 100 Hz [Hämäläinen 1993]: this is the quasi-static approximation. As a consequence of the Maxwell's equations, electric and magnetic components are decoupled and propagation times are insignificant. This also implies that the electric field derives from a potential V:

$$r\vec{o}t\vec{E} = \vec{0} \quad \Rightarrow \quad \vec{E} = -gr\vec{a}dV \tag{3.2}$$

As described in section 3.1, the current density $\vec{J}$ measured by MEG is the sum of a primary current flow $\vec{J}^p$ passing through the dendrites of activated neurons and

a passive volume current flow $\vec{J_v}$ propagating in the medium by conductivity. The latter can be expressed by Ohm's law: $\vec{J_v} = \sigma\vec{E}$, where σ denotes the electrical conductivity of the medium. Combining this relation with the previous one (3.2) and injecting them in the equation (3.1) under quasi-static approximation yields:

$$\begin{array}{rcl} \vec{rot}\vec{B} & = & \mu(\vec{J^p} - \sigma\vec{grad}V) \\ \Rightarrow \quad \vec{div}\vec{J^p} & = & \vec{div}(\sigma\vec{grad}V) \end{array} \tag{3.3}$$

In the forward problem, the current density $\vec{J^p}$ is known and V is the unknown variable. Once V is known by solving this equation, $\vec{B}$ can be computed from the Bio-Savart law:

$$\vec{B}(\vec{r}) = \frac{\mu_0}{4\pi}\int_{\mathbb{R}^3}(\vec{J^p} - \sigma\vec{grad}V) \wedge \frac{\vec{r} - \vec{r'}}{\|\vec{r} - \vec{r'}\|^3}\, d\vec{r'} \tag{3.4}$$

In order to solve the forward problem, we need [Gramfort 2013]:

- a model of elementary source.
- an approximation of electromagnetic properties of the head.
- the position and the orientation of the sensors as well as the geometry of the pick-up coils.

With regards to the first point, the linearity of the Maxwell's equations implies indeed that once the solution for an elementary source is known, the fields generated by much more complex sources can be easily obtained by superposition. Because the distance between neural sources and the sensors is relatively high enough (several cm) compared to the thickness of the cortical sheet (∼4 mm), the primary current $\vec{J^p}$ is usually approximated by a current dipole $\vec{Q}$ at position $\vec{r}_Q$ with the following relation: $\vec{J^p}(\vec{r}) = \vec{Q}\,\delta(\vec{r} - \vec{r}_Q)$, where δ denotes the Dirac delta function. As a consequence, the magnetic field depends linearly on the amplitude of the dipole $\|\vec{Q}\|$,while it depends non-linearly on its orientation $\vec{\Theta}_Q = \frac{\vec{Q}}{\|\vec{Q}\|}$ and its location $\vec{r}_Q$ [Baillet 2001]. Hence the forward problem can be reformulated as the determination of the leadfields, i.e. the forward operator that allows to compute the output of a sensor induced by a unit current dipole.

The main difficulty to solve the equation (3.3) resides in modeling the distribution of the conductivity σ of the head. The simplest solution is to model the head with several homogeneous concentric spheres of different conductivities representing for instance the brain, the meninges and the skull. In that case, the equation can be solved analytically by using the spherical harmonic functions (cf. the SSS method). Moreover, the spherical geometry makes the total magnetic field independent of the conductivity. This model is however not very realistic and can be improved by using other anatomical imaging modalities such as computed tomography (CT) or anatomical magnetic resonance imaging (aMRI). This is necessary when using EEG because the conductivity greatly influences the distribution of the electric field.

Because of the geometrical complexity of the head structures revealed by imaging modalities, the equation (3.3) must be solved numerically with techniques such as the finite difference methods (FDM), the finite element methods (FEM) and the boundary element methods (BEM) [Gramfort 2009a]. With FDM, the spatial derivatives are approximated by finite differences with a constant step on a cubic grid. This can however lead to a "staircase" effect if the surface is too complex. FEM is a more elaborated technique that can work with any surface by using unstructured grids (such as triangles in 2D or tetrahedrons in 3D). It consists of approximating the solution of the equation 3.3 by its weak form at a properly chosen discretization level. BEM is employed when an homogeneous conductivity is attributed to each part of the head (e.g. $\sigma = 0.3$ S/m for the brain and the scalp and $\sigma = 0.006$ S/m for the skull with the MNE software [Gramfort 2013]). The equations 3.3 and 3.4 are then transformed into integral equations on each domain of constant conductivity while $\sigma = 0$ outside. By tessellating each domain with n sub-triangles of constant electric potential, we obtain a linear system of n equations to solve. It is worth noting that the electrical conductivity is in reality anisotropic: it is indeed 10 times greater in the direction of the fibers of the white matter than in the transverse directions. Therefore, the model could be improved by including tissue anisotropy information brought by diffusion MRI [Haueisen 2002].

Finally, the estimation of the output b_k of the k^{th} MEG sensor caused by a an elementary current dipole $\vec{Q}$ is approximated by the weighted current sum:

$$b_k = \sum_{p=1}^{N_k} w_{k,p} \vec{B}(\vec{r}_{k,p}, \vec{Q}).\vec{n}_{k,p} \tag{3.5}$$

where $\vec{r}_{k,p}$ describes the N_k locations within the pick-up coil loop with an attributed scalar weight $w_{k,p}$ and the corresponding unit vector $\vec{n}_{k,p}$ normal to the plane of the loop. The weights $w_{k,p}$ take into account the geometry of the coils and are usually given by the MEG manufacturer. The position and orientation of the MEG sensors relatively to the head is given by small head-position indicator (HPI) coils attached to the head surface. Prior to the MEG acquisition, they are digitized in a coordinate frame defined by fiducial landmarks (i.e. the left and right preauricular points and the nasion). This is indeed necessary because contrary to the EEG cap, the MEG helmet is not fixed on the subject's head, allowing for movements (especially for small heads).

When using anatomical MRI recordings, a co-registration procedure is necessary to translate the MEG device coordinate system into the MRI device coordinate system. This is done by identifying manually the landmarks used during the MEG digitization on the MRI image. In this manner, a common head coordinate system is defined for both modalities. The identification of the landmarks can be more accurate by using artificial fiducial markers made of hydrogel component that appear as a bright ring on the MRI scan.

3.3.2 The inverse problem

The inverse problem consists of determining the neural sources at the origin of the measurements. This is possible once the forward operator has been obtained for all elementary source locations and orientations composing the so-called source space. In practice, the source space is defined by a grid of M nodes (using FDM, FEM or BEM methods) on which each node $i = 1..M$ is represented by one dipole oriented normally to the cortical surface or three dipoles with orthogonal orientations in the more general framework. By denoting $\vec{m}$ the $N \times 1$ signal vector measured in sensor space, $\vec{s}$ the (unknown) $3M \times 1$ dipole amplitude vector defined in source space (here without orientation constraint), $\mathbf{G}$ the $N \times 3M$ forward (or gain) matrix and $\vec{\varepsilon}$ the $N \times 1$ vector of measurement errors, we obtain the following equation to be solved :

$$\vec{m} = \mathbf{G}\vec{s} + \vec{\varepsilon} \tag{3.6}$$

In practice, $M \gg N$. However, even if the number of sources did not exceed the number of sensors, the inverse problem would be still ill-posed. The only knowledge of the electromagnetic field outside of a conductor is indeed insufficient to determine the distribution of the primary current flowing through the conductor. In other words, the solution to such problem is not unique. For instance the absence of an external magnetic field can be misinterpreted as an absence of current sources even though there is a radial dipole in a spherically symmetric conductor that turns out to be magnetically silent.

An additional information on the source distribution is thus required to make the solution unique. Therefore, all source reconstruction methods are based on *a priori* assumptions of which the diversity explains the abundant literature on that subject (2000 articles referenced in PubMed in 2008!) [Hansen 2010]. Depending on the underlying assumptions (e.g. the number of sources), these methods can be classified into two categories — namely either as discrete or distributed source approaches.

3.3.2.1 Discrete source approaches

Dipole and multidipole fitting methods are the most representative methods of discrete source approaches which assume that the measured data have been produced by a fixed number K of discrete sources, i.e. equivalent current dipoles (ECD). While the number of the dipoles is supposed to be constant, their amplitude $s_i = \|\vec{q}_i\|_2$ (and optionally their position $\vec{r}_i$ and orientation $\vec{\Theta}_i$) can vary over time. Parametric dipole fitting algorithms consist of setting either all dipoles at once or one dipole after another. In the first case, a data fit cost function such as the Frobenius ℓ_2-norm[2] of the residual is minimized:

$$\min_{i=1..K} \|\vec{m} - \sum_{i=1}^{K} \vec{g}_i(\vec{r}_i, \vec{\Theta}_i) s_i\|_F^2$$

[2]Frobenius ℓ_2-norm: $\|\mathbf{A}\|_F^2 = \mathrm{Tr}\mathbf{A}\mathbf{A}^T = \sum_{i=1}^{m}\sum_{j=1}^{n}|a_{ij}|^2$, where $\mathbf{A}$ is a $m \times n$ matrix, Tr denotes the matrix trace and $\mathbf{A}^T$ is the conjugate transpose of $\mathbf{A}$

where $\vec{g}_i$ denotes the forward field produced by the i^{th} dipole that depends on the position and the orientation of the dipole.

The optimization is conducted first on the non-linear parameters $\vec{r}_i$ and $\vec{\Theta}_i$ and then on the linear parameters s_i and can be carried out with a large set of minimization methods ranging from Levenberg-Marquardt and Nelder-Meade downhill simplex searches to global optimization schemes [Baillet 2001].

This method is mainly limited by the number of dipoles the user has to fix a priori: as soon as the number of dipoles increases, the chance to be trapped in local minima increases because of the nonconvexity of the cost function [Baillet 2001]. Furthermore, a large number of dipoles can result in overfitting the data, regardless of the quality. According to [Hämäläinen 1993], the dipoles must be sufficiently distant in space ($> 4cm$) and time. Therefore, this approach is mainly adapted for simple stimuli activating isolated primary areas (such as an auditory beep or a visual flash) but is completely powerless to estimate sources in resting-state activity. In practice, the proposed solution should be also obvious in sensor space.

3.3.2.2 Distributed source approaches

In these approaches, the current magnitude $\vec{s}$ of all dipoles covering the source space is estimated, without *a priori* on the number of sources. Hence, sources are not strictly said a set of focal sources but are rather distributed over the entire source space. Two main approaches exist, namely beamforming and minimum-norm estimates (MNE) approaches. They differ in the way of estimating the elements of $\vec{s}$: in the former, they are estimated separately at each grid location whereas in the latter, they are estimated all at once.

Beamforming. These methods, also referred as "scanning methods", were first introduced in the radar and sonar community in the 70's to increase the sensitivity of radar arrays to signals originating from a source of interest. Beamforming has been later applied to MEG and EEG in the late 90's [Van Veen 1997] (see for instance the review on beamforming by [Hillebrand 2005]). A beamformer is basically a set of spatial filters $\mathbf{W} = \{\mathbf{w}_1, \mathbf{w}_2, ..., \mathbf{w}_M\}$, defined on a grid of M nodes over the entire brain volume (or surface). Considering the triplet of dipoles with orthogonal orientations on the i^{th} node of the grid, the output of the beamformer is the 3×1 vector $\vec{y}$ formed as the product of the $3 \times N$ spatial filtering matrix $\mathbf{w}_i^T$ with the $N \times 1$ measurement vector $\vec{m}$, i.e. $\vec{y} = \mathbf{w}_i^T \vec{m}$. The weighting coefficients of the filter are supposed to be chosen in such a manner that the activity coming from the dipoles on that node is selectively enhanced while interferences from sources at all other locations are suppressed.

The estimation of this filter is based on the hypothesis that sources are all uncorrelated. For instance, the linearly constrained minimum variance (LCMV) [Van Veen 1997] method makes use of the data covariance matrix $\mathbf{C}$ to constrain the gain at the targeted location while minimizing the energy coming from elsewhere. Under the hypothesis of uncorrelated sources, this constrained optimization problem

is solved with the method of Lagrange multipliers and the solution is given by:

$$\mathbf{w}_i^T = (\mathbf{g}_i^T \mathbf{C}^{-1} \mathbf{g}_i)^{-1} \mathbf{g}_i^T \mathbf{C}^{-1}$$

where $\mathbf{g}_i$ denotes the forward field produced by the triplet of dipoles located on the i^{th} node. As it can be seen, a major requirement in this method is that the covariance matrix is accurately estimated and invertible. This becomes an important issue for source analysis of event-related fields (ERFs), since the covariance matrix can become rank-deficient: notably if the number of time samples in the selected epoch is not sufficient (compared to the number of sensors) or if the number of averaged trials is remarkably high enough to cancel out the (background) signal in sensors that do not contain any evoked activity.

In practice, the covariance matrices can be regularized by using truncated eigenvalues or Tikhonov regularization. Beamformers are hence usually more used for the analysis of raw continuous data, such as in resting-state studies.

Minimum norm estimates (MNE). The basic idea of MNE [Hämäläinen 1994] is to choose among the infinity of solutions to equation (3.6) the simplest one, i.e. of minimal norm (traditionally the ℓ_2-norm). In that case, all other solutions derive from it by adding any source current "invisible" to the sensors (i.e. orthogonal to the leadfields). In other words, MNE consists of solving a constrained optimization problem, which is usually formulated with the Lagrangian formalism:

$$\min_{\vec{s}} \|\vec{m} - \mathbf{G}\vec{s}\|_F^2 + \lambda \|\vec{s}\|_F^2, \ \lambda > 0 \tag{3.7}$$

The parameter λ controls the "trade-off" between the fidelity to measurements and noise sensitivity. It balances the reconstruction error and the regularity of the solution. The advantage of using the ℓ_2-norm is that the solution to equation (3.7) can be easily obtained via a simple matrix multiplication:

$$\begin{aligned} \vec{s} &= (\mathbf{G}^T\mathbf{G} + \lambda\mathbf{I})^{-1}\mathbf{G}^T\vec{m} \\ &= \mathbf{G}^T(\mathbf{G}\mathbf{G}^T + \lambda\mathbf{I})^{-1}\vec{m} \end{aligned} \tag{3.8}$$

where $\mathbf{I}$ is the identity matrix. In practice, computing the estimate based on the first equality turns out to be difficult because of the size of the matrix $(\mathbf{G}^T\mathbf{G} + \lambda\mathbf{I})$ to be inverted (approximately 10000×10000!)due to the great number of dipoles covering the space source. On the other hand, the second equality (derived using the Woodbury matrix identity) allows to compute and to inverse a relatively small matrix (about 300×300) depending on the number of sensors.

In this first approach, the noise originating from the sources is not taken in consideration and the sensor noise is represented by a unique parameter λ that is set arbitrarily. In the Bayesian framework, these two types of noise are modeled by Gaussian variables of which the spatial covariance matrices are denoted by $\mathbf{R}$ and $\mathbf{C}$ for respectively the sources and the sensors. The optimal solution $\vec{s}$ is then obtained by estimating the maximum a posteriori (MAP) and is finally given by [Hämäläinen 1994]:

$$\vec{s} = \mathbf{R}\mathbf{G}^T(\mathbf{G}\mathbf{R}\mathbf{G}^T + \mathbf{C})^{-1}\vec{m} \tag{3.9}$$

We observe that the standard MNE corresponds to the case where $\mathbf{R} = \mathbf{I}$ and $\mathbf{C} = \lambda\mathbf{I}$.

Alternatively, it has been proposed to replace the ℓ_2-norm by the ℓ_1-norm in order to make the spatial distribution of currents more parsimonious. This was done however to the detriment of good temporal properties brought by the ℓ_2-norm which smoothed current time courses (avoiding "jumps" or discontinuities), making the estimates physiologically plausible. A solution is to use conjointly the two norms (refered as the *mixed* ℓ_{12}-norm [Gramfort 2009b, Gramfort 2011]) by first applying the ℓ_2-norm along the time axis and then the ℓ_1-norm along the spatial axis. Recently, the computation time of these methods has considerably improved [Gramfort 2012].

The main default of minimum norm solutions is that they are biased towards the superficial sources (i.e. close to the sensors). The *weighted minimum norm* (WMN) method was proposed to cope with this problem by normalizing the source covariance matrix: instead of minimizing $\|\vec{s}\|$, WMN tries to minimize $\mathbf{W}\vec{s}\|$, where $\mathbf{W}$ is an invertible and diagonal weighting matrix. Each weigthing coefficient w_{ii} on the diagonal is set according to the amplitude of the corresponding forward operator $\vec{g}_i$ by the following relation: $w_{ii} = \|\vec{g}_i\|_F^{\gamma}$, where $\gamma > 0$ is a parameter to set manually.

Another way to attenuate the bias towards the superficial sources is to employ noise-normalized methods such as the *dynamic Statistical Parametric Mapping* (dSPM) and *sLORETA*. In addition, they quantify the statistical significance of the reconstructed current estimates while reducing the spread of the sources [Hauk 2011]. It is noteworthy that these methods do not modify the shape of the current estimate time courses given by MNE. dSPM [Dale 2000] tries to account for the reconstruction incertitude due to measurement errors by normalizing the estimates on each vertex with the noise sensitivity (i.e. the standard deviation of the estimate obtained when reconstructing from sensor noise). If the dipole orientation is fixed, the dSPM estimates follow a Student's law that tend to a normal distribution when the number of samples used to estimate the noise covariance is large (e.g. when using empty-room acquired data). In the sLORETA method [Pascual-Marqui 2002], the variability coming from the sources is also taken into account, in such a way that the location error is null in the absence of noise. In practice, the source covariance is not observed and, without any learning procedure, is fixed a priori (usually set to the identity matrix). Under real experimental conditions, the results observed with these two methods do not differ greatly though [Hauk 2011].

3.4 Data acquisition during the learning paradigm

Since the ERF and scale-free analyses have been carried out on the same data set, the description of the data acquisition, preprocessing and source reconstruction is quasi-identical. They are thus presented in this section.

3.4.1 MEG data acquisition

Brain magnetic fields were recorded in a magnetically shielded room using a 306 MEG system (Neuromag Elekta LTD, Helsinki). MEG recordings were sampled at 2000 Hz and band-pass filtered between 0.03–600 Hz. Four head position coils (HPI) measured participants' head position before each block; three fiducial markers (nasion and pre-auricular points) were used for digitization and anatomical MRI (aMRI) immediately following MEG acquisition. Electrooculograms (EOG, horizontal and vertical eye movements) and electrocardiogram (ECG) were simultaneously recorded. Prior to the session, 5 minutes of empty room recordings were acquired for the computation of the noise covariance matrix.

3.4.2 Anatomical MRI acquisition and segmentation

The T1 weighted aMRI was recorded using a 3-T Siemens Trio MRI scanner. Parameters of the sequence were: voxel size: 1.0 x 1.0 x 1.1 mm; acquisition time: 466s; repetition time TR = 2300ms; and echo time TE= 2.98 ms. Cortical reconstruction and volumetric segmentation of participants' T1 weighted aMRI was performed with FreeSurfer (http://surfer.nmr.mgh.harvard.edu/). This includes: motion correction, average of multiple volumetric T1 weighted images, removal of non-brain tissue, automated Talairach transformation, intensity normalization, tessellation of the gray matter white matter boundary, automated topology correction, and surface deformation following intensity gradients [Dale 1999, Fischl 2000]. Once cortical models were complete, deformable procedures could be performed including surface inflation [Fischl 1999a] and registration to a spherical atlas [Fischl 1999b]. These procedures were used with MNE [Gramfort 2013] to morph individuals' current source estimates onto the FreeSurfer average brain for group analysis.

3.4.3 MEG data preprocessing

Raw bad channels were first detected after visual inspection of all data sets. Signal Space Separation (SSS) was then carried out using MaxFilter to remove external interferences and noisy sensors [Taulu 2006]. Ocular and cardiac artifacts were removed by creating signal space projections (SSP) based on average-locked responses to the QRS heart complex recorded with ECG and to the blinks recorded with EOG. About 2 to 3 components were projected out of the raw data.

In the case of ERF analyses only, raw data were next band-pass filtered between 1–40 Hz and down-sampled to 250 Hz.

3.4.4 Co-registration and source reconstruction

The co-registration of MEG data with the individual's aMRI was carried out by realigning the digitized fiducial points with the multimodal markers visible in MRI slices. We used a two-step procedure to insure reliable co-registration: using MRI-LAB (Neuromag-Elekta LTD, Helsinki), fiducials were aligned manually with the

multimodal markers on the MRI slice. An iterative procedure realigned all digitized points (about 30 more supplementary points distributed on the scalp of the subject were digitized) with the scalp of the participant with the MEG coordinates using the mne_analyze tools within MNE [Gramfort 2013].
Individual forward solutions for all source locations located on the cortical sheet were next computed using a 3layers boundary element model [Hämäläinen 1989, Mosher 1999] constrained by the individual's anatomical MRI. Cortical surfaces were extracted with FreeSurfer and decimated to about 5120 vertices per hemisphere with 4.9 mm spacing. The gain, noise and source covariance matrices were used to calculate the depth-weighted (parameter $\gamma = 0.8$) minimum-norm inverse operator. The inverse operator was applied using a loose orientation constraint on individuals' brain data [Lin 2006] by setting the transverse component of the source covariance matrix to 0.4.

The reconstructed estimates differed here between ERF and scale-free analyses:

- For the ERF analysis, the estimates were noise-normalized using dSPM [Dale 2000] and their orientation were pooled by taking the norm, resulting hence in manipulating only positive values.

- For the scale-free analysis, only the radial components of the minimum-norm estimators were kept, since taking the norm is a non-linear transformation that would modify the scale-free properties (see Chapter 7).

For both analyses, the reconstructed MNE/dSPM estimates time series were interpolated onto the FreeSurfer average brain for group analysis [Fischl 1999b] and common referencing.

Part II

Standard ERF analysis

Chapter 4

Neural hypothesis

Contents

The previous chapter was dedicated to the basic principles of MEG and the methods usually employed (preprocessing, source reconstruction) to yield ready-to-analyse data. Our next concern is now to comprehend the cortical mechanisms underlying the perceptual improvements reported in chapter 2 that can be revealed using standard approaches such as the event-related field (ERF) analysis.

In this chapter, we introduce first the basics of this analysis and its implicit assumptions. Since the task in our paradigm is of relatively high complexity (involving color-motion binding and multisensory processing), a necessary review of all neural sites potentially involved during training is proposed in the next section according to the existing literature. Finally, we elaborate some predictions regarding the neural correlates of learning based on the reverse hierarchy theory (RHT) and under the hypothesis of a supramodal processing.

4.1 Basics of the event-related field (ERF) analysis

4.1.1 Principle

One of the most standard approaches in M/EEG studies is the analysis of *evoked responses*, i.e. neural activation phase-locked to a particular event such as the onset (or offset) of a stimulus. They are essentially characterized by their latencies (since they occur at the same time from trial to trial) and by their amplitudes (since

they are supposed to have the same shape). In practice, they are detected within the second following (or sometimes preceding) the stimulus onset or the subject's response. The underlying hypothesis of ERF analyses is that evoked activity is embedded in random activity (e.g. ongoing brain activity and sensor noise) that makes its detection on a single-trial basis very difficult. In terms of signal processing, the signal $s_k(t)$ recorded at the k^{th} trial is supposed to be the sum of a trial-invariant signal of interest $e(t)$ and a zero-mean Gaussian noise $n_k(t)$ uncorrelated across trials and not time-locked to the event. Consequently, the signal-to-noise ratio (SNR) can be improved by averaging several tens or hundreds of epochs locked on the same event:

$$\begin{array}{ccccccc} s_k(t) & = & e(t) & + & n_k(t) & \text{trial } k \\ \downarrow & & \downarrow & & \downarrow & \\ \hat{s}(t) & \approx & e(t) & + & 0 & \text{average over } N \text{ trials.} \end{array}$$

By doing so, the noise amplitude is reduced by a factor equal to $\sqrt{N}$. As previously said, this method implicitly assumes the noise to be zero-mean, which is in practice assured by high-pass filtering the continuous raw signal (since evoked activity is relatively sparse with respect to the entire recording). In other words, it necessitates to remove the $1/f$ behavior observed in the infraslow activity (cf. chapter 6). In addition, averaging over epochs also results in smoothing the signal and these effects are thus similar to those of a low-pass filter. If we assume indeed that evoked responses are slightly shifted by a small time jitter across trials, the corresponding phase jitter increases dramatically for high frequencies (and thus reduces the constructive summation of averaging). This is why MEG signals are usually band-pass filtered (between for instance 1–40 Hz) and subsequently down-sampled.

Importantly, we should emphasize that evoked activity is not the only form of activity produced by (or at least related to) a task or a stimulus: the so-called *induced* activity also refers to systematical effects occurring across trials but not strictly phase-locked to the event and hence vanishes through averaging (cf. Fig. 4.1). Whereas evoked activity is said to reflect mainly bottom-up driving processes, induced activity is often associated with top-down modulation. The latter component is usually observed by plotting the mean spectrogram (time-frequency representation assessed with the short Fourier transform) or scalogram (time-scale representation using continuous wavelets) averaged over all trials (since square values do not cancel out) and after subtraction of the power of the average (i.e. the evoked component).

4.1.2 Response profile and comparison with BOLD fMRI signals

The early salient evoked responses are usually transient (i.e. of short duration) and more stable in time than longer-latency responses, which often jitter across trials and increase in duration. As a result, they appear in the average as sustained responses that progressively fade in. Contrary to fMRI BOLD responses that often persist throughout the entire presentation of a stimulus, ERFs reflect more the sudden changes (i.e. onset or offset) of a stimulus (Fig 4.2). This is why slowly increasing

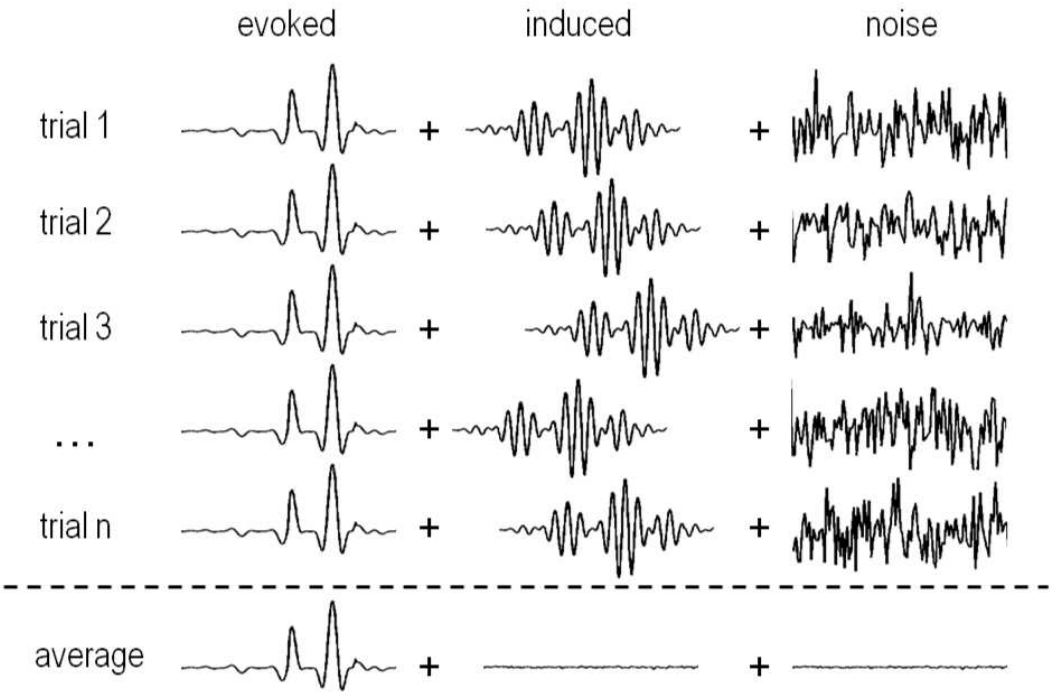

Figure 4.1: Basics of the event-related field analysis. The ERF analysis consists of focusing on the evoked activity phase-locked to the apparition of an event. It assumes that the signal is the sum of three components: an evoked, an induced and a random component (that changes at every trial). Contrary to the evoked component, the induced response is not phase-locked to the timing of the event. As a result, both the induced and the noise components are considerably reduced when averaging the signal across trials, leading to the emergence of the evoked component.

sustained evoked activity is sometimes interpreted as a neural marker of evidence accumulation.

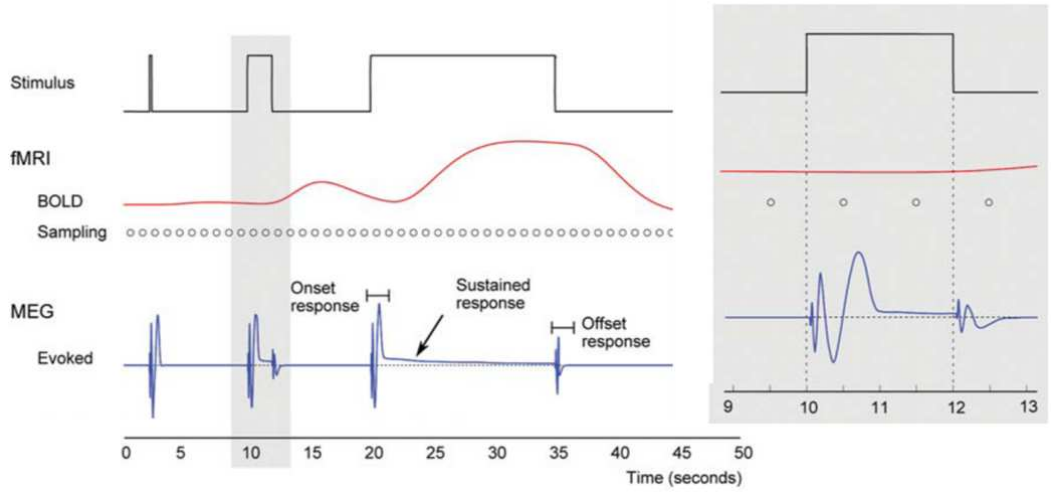

Figure 4.2: Comparison between BOLD and MEG evoked responses. Schematic responses to stimuli of 0.2 s, 2 s and 15 s in duration. A lagged prominent BOLD response is obtained only with stimulation persisting for several seconds. In contrast, MEG evoked responses are elicited by stimulus onsets and offsets independently of stimulus duration. A relatively weak sustained response can be possibly observed. Due to the sluggishness of the BOLD signal, it is sufficient to sample it to 1 Hz (illustrated here by the dots, for a repetition time $TR = 1$ s). The MEG onset responses typically last for less than a second and change orders of magnitude more rapidly than BOLD, thus necessitating sampling rates above 300 Hz approximately. Adapted from [Hansen 2010].

Thanks to the great temporal resolution of MEG (cf. chapter 3), the evoked response can be tracked with good temporal accuracy. Because of this high sensitivity, ERF analysis can easily suffer from negligence in the preparation of stimuli and task controls. For instance, a slight jitter in the timing of a sound delivered to the subject might considerably modify the early auditory response unless it is accounted in the definition of the epoch. Conversely, it is often necessary to inject a random (but known) jitter in the timing of events to avoid the apparition of a temporal trend in the signal reflecting the expectation of the subject as well as a peak in the power spectrum corresponding to the frequency of the stimulus presentation.

In contrast, fRMI experiments are less sensitive to the timing issue. fMRI signal reflects changes in the oxygen consumption following 5–10 s after neural activation via the slow haemodynamic function, yielding a relatively low time resolution. In addition, the sampling rate is limited by the acquisition process (at best one whole-head fMRI image every second). The measured neural activity is thus very slow and undersampled (Fig. 4.2). Consequently, the experimental design in fMRI differs greatly from the one used for ERF analysis in MEG (and EEG). In an event-related

design with jittered stimulus timing, the shape of the response can be approximately recovered by combining several trials sampled at different times. However, in the most commonly used block design, the fMRI signal is cumulated over rapidly successive identical trials to increase the SNR and consequently loses the temporal information. The cognitive process of interest is then usually identified by contrasting two conditions, assuming that irrelevant events such as e.g. manual responses cancel out. MEG studies do not easily accommodate with this kind of approach if the undesirable events have different dynamics.

In conclusion, ERF analyses require perfectly well controlled designs in order to extract exactly the wanted information that do not correspond to the optimal designs conducted in fMRI. As a general rule, the designs used in psychophysical studies are usually well adapted to EEG and MEG studies.

4.2 Neural mechanisms possibly involved in training

In this section, we present the potential neural candidates activated during the three types of training that can possibly undergo plasticity in post-training. Recent electrophysiological and neuroimaging studies using similar stimuli are thus reviewed to help us to establish our hypothesis.

4.2.1 Discrimination of visual motion coherence

4.2.1.1 The human motion area hMT+

Converging evidence of an area located in the human extrastriate cortex and activated by visual motion has now been well established across electrophysiological and neuroimaging studies. By analogy with the primate middle temporal (MT) and medial superior temporal (MST) areas that showed sensitivity to motion directions and greater responses to global coherent motion, their human homologs form the so-called hMT+/V5 complex (hereafter simply denoted by hMT+). hMT+ can be functionally localized using PET [Watson 1993] and fMRI [Tootell 1995] in response to global and even illusory motion [Zeki 1993] and is usually found in both hemispheres with however a great spatial variability across individuals (e.g. a variation of 27 mm in the left hemisphere reported by [Watson 1993]).

The hMT+ response profile was characterized in several EEG and MEG studies as a function of several parameters such as speed, direction, dot density, stimulus eccentricity and coherence [Lam 2000, Maruyama 2002, Nakamura 2003, Aspell 2005, Händel 2007, Becker 2008]. They all reported peak latencies ranging around 150–300 ms (depending on the above-mentioned parameters) and usually followed by sustained activity (often interpreted as accumulation of evidence). For instance, the latency and the amplitude of the response were shown to be sensitive to motion speed (the faster the motion, the earlier and the greater the response) and to dot density independently on the nature of the motion (incoherent vs. coherent) [Maruyama 2002]. In another study, the latency of the response to a coherent RDK

could be modulated by the speed of an incoherent RDK presented just before the transition [Lam 2000]. Importantly, the response amplitude has the particularity to increase as a function of coherence [Nakamura 2003, Aspell 2005] provided that the dot density is large enough [Händel 2007]. Spectral analysis revealed two components correlating positively and negatively with motion coherence in hMT+: the first (positive) one was found in the very low frequencies (around 3 Hz) and reflected evoked activity whereas the other one oscillated in the alpha domain and corresponded to induced activity [Händel 2007].

These observations are consistent with the neuronal properties of MT and MST reported in monkey studies that have shown that neurons in these areas had a large receptive field and were selectively sensitive to motion speed and direction. The perception of global motion was initially thought to be the result of the integration of all activated neurons; yet it would not explain why on the one hand, activity in hMT+ increased as a function of motion coherence and on the other hand, hMT+ also responded to incoherent random motion. This could be explained by the existence of two types of neurons responsive either to "local" (e.g. a single moving dot) or to "global" (e.g. a group of coherent dots) motion [Aspell 2005]. Neurons of the former category are more numerous but with the emergence of a global coherent motion, their activity decreases while that of neurons of the latter category increases. Therefore, if the employed stimulus recruits enough "global" neurons to compensate and exceed the loss of activity from "local" neurons (notably depending on the stimulus size, i.e. a large eccentricity), the activation of hMT+ should increase as a function of coherence. This is why the effect of coherence on the amplitude of the response in hMT+ crucially depended on the stimulus size and the dot density used in studies [Aspell 2005, Becker 2008].

4.2.1.2 Other areas involved in motion perception

Although hMT+ is the main area known to process visual motion in the human brain, several studies report the existence of other brain regions involved in motion perception, depending on the nature of the motion.

For instance, "second-order" motions refer to stimuli that are not based on contrasts of luminance between background and foreground (by opposition to first-order motion) but on other features such as isoluminant colors (known as opposed motion). In a monkey study, contrarily to expectations, no activation was observed in MT and MST during the presentation of these stimuli although monkeys reported correctly the direction of the motion [Ilg 2004]. An fMRI study revealed that the posterior superior temporal sulcus (pSTS) was in fact the area recruited to the processing of these stimuli [Noguchi 2005]. In the same line, patients with lesions in pSTS and in the frontal eye field (FEF) were almost incapable of perceiving complex movements of humans and animals (known as "biological motion") but had less difficulty to detect a simple motion as that of RDKs [Saygin 2007].

A great body of evidence converges towards the notion of a hierarchical processing of motion whose complexity increases along the dorsal pathway (i.e. starting

from the occipital visual cortex, traveling through the parietal lobe and terminating in the prefrontal area). For instance, the evoked response to a change of motion direction observed by fMRI and MEG [Ahlfors 1999] appeared first in hMT+ and was consecutively observed in V3A, V1/V2 and finally in pSTS and FEF where responses were more sustained. This propagation was simultaneously observed along the lateral (via hMT+) and medial (via V6) dorsal path [Pitzalis 2013]. The initial activation detected in the primary visual cortex V1 was attributed to the first step of local motion processing [Movshon 1996]. Depending on the nature of the task and the motion complexity, higher-order areas along the dorsal pathway can be recruited: for instance, in a visual motion categorization task, the lateral intraparietal (LIP) cortex and the ventrolateral prefrontal cortex (vlPFC) showed successively in a bottom-up fashion category selectivity modulated by attention [Swaminathan 2012]. These areas (as well as FEF) were also shown to be involved in perceptual decisions and decision making following the accumulation of sensory evidence represented in hMT+ [Heekeren 2008].

In our experimental paradigm, the task did not only consist of discriminating motion coherence, but also labeling the correct color to the coherent RDK. We can thus sensibly expect several areas to be recruited in the mechanism of motion-color binding, including of course hMT+ for the perception of colored motion [Thiele 2001].

4.2.2 Color-motion binding

A widely accepted hypothesis in neural processing of vision is the existence of two distinct streams [Ungerleider 1982] originating both from the occipital cortex and separating into two directions: one towards the parietal lobe (dorsal stream) and one towards the temporal lobe (ventral stream). The visual dorsal stream is not only involved in motion processing (as previously mentioned) but more generally in extracting visual objects' spatial features ("where?") and in the guidance of actions ("how?"). Conversely, the visual ventral stream is associated with object recognition ("what?") such as color and shapes and processes more complex objects (e.g. faces and houses) as one proceeds from posterior to anterior temporal lobe. These two streams slightly differ also by the nature of the thalamic inputs they receive [Ungerleider 1994]: the dorsal stream predominantly receives its inputs from magnocellular layers (large cells sensitive to low spatial and high temporal frequencies) whereas the ventral stream receives comparably as many inputs from magnocellular layers as ones from parvocellular layers (small cells sensitive to high spatial and low temporal frequencies). Interestingly, a similar description for the auditory system exists and consists of two auditory ventral and dorsal streams originating from the anterior and posterior auditory cortex [Rauschecker 2000].

The binding problem arises from the following statement: since different (although partly overlapping) networks are responsible for extracting color, shape and motion information, how do they converge towards a unified and coherent percept? A first idea was that spatially segregated features could be processed simultaneously and bound through synchronization; this hypothesis was however rejected by several

psychophysical studies showing that color and shape changes were processed before motion changes [Zeki 1997, Moutoussis 1997, Viviani 2001] and later confirmed by an MEG study that found about 100 ms of difference between the early responses evoked by color and the later responses evoked by motion changes [Amano 2006].

Alternatively, a network larger than those involved in the processing of single features may be engaged to undertake the binding mechanism. For instance, a colored motion grouping task showed BOLD activation in two contiguous yet segregated areas of the intraparietal cortex, depending on the criterion (color or motion) upon which participants recognized the stimuli [Zeki 2013]. The crucial role of the lateral prefrontal cortex observed in numerous categorization tasks can also be linked to the mechanism of binding. Since vlPFC is a major site of convergence between ventral and dorsal streams, it was suggested to be a sort of "supervisor" [Freedman 2008] that would extract the representation of a (potentially abstract) object from the collected information processed by other areas such as the inferior temporal cortex (ITC) and LIP. In contrast to vlPFC which is able to learn new categorization rules, ITC had the particularity to present only automatic (i.e. non-arbitrary) categorization based on the physical properties of stimuli. vlPFC is also associated with selective attention of color embedded in motion [Sakagami 2001, Hamker 2005] and has been also suggested to be in competition with FEF for the control and modulation of V4 and ITC [Hamker 2005].

4.2.3 Perception of acoustic textures

During training, acoustic textures or simply acoustic noise were delivered to AV and AVn participants respectively (cf. section 1.4). Auditory information is known to be processed by the auditory cortex, located bilaterally in the superior part of the temporal cortex (more precisely the primary area in the Heschl's gyrus and surrounding associated areas in the belt, e.g. planum temporale). Sound is processed in primary area according to a tonotopic organization that spatially separates high and low frequencies, similarly to the properties of the cochlea.

Acoustic textures are complex auditory objects defined both by their "boundaries" (sudden changes of coherence, i.e. time-frequency statistical properties) and their intrinsic characteristic (coherence itself). Perception of these two properties are referred to as "*segregating*" and "*representation*" respectively. Overath and colleagues showed in a recent fMRI study [Overath 2010] that segregating was first processed in primary auditory and association cortices while representation of acoustic textures was perceived afterward in higher-order association areas. Interestingly, the haemodynamic response in pSTS increased as a function of the difference of coherence between two consecutive textures.

In another fMRI study using similar auditory stimuli also necessitating integration over time and frequency to be discriminated from background incoherent noise [Teki 2011], bilateral intraparietal sulci (IPS) and pSTS showed an increased activation as a function of duration and coherence, possibly reflecting accumulation of evidence.

In our experiment however, the acoustic textures were always accompanying the presentation of the colored RDKs, potentially (and hopefully) leading to audiovisual (AV) integration and/or participating to supramodal processing. The analysis on these data (i.e. to address the question of multisensory integration per se) has not been conducted yet but will be followed up in the future.

4.2.4 Multisensory processing

Multisensory integration can be seen as a more general concept of feature binding (cf. section 4.2.2) this time across sensory modalities. Although the putative existence of multisensory areas is commonly accepted, their definition and the method to identify them is still debated [Klemen 2012]. Before going further, we should insist once again on the difference between multisensory and supramodal areas (cf. chapter 1): supramodal areas are dedicated to the processing of an abstract property that can be contained in any type of stimuli and thus always effectuate the same operation independently of the sensory modality; multisensory areas receive signals of different sensory modalities to integrate them and to form a coherent percept [Voss 2012]. Therefore, the identification of supramodal or multisensory areas by means of functional neuroimaging requires different approaches [Klemen 2012, Beauchamp 2004b].

Multisensory areas are usually identified in healthy individuals on the base of several criteria. A first approach would be to consider only areas showing exclusively activation to multimodal stimuli (hence not responsive to stimuli within a single modality); this method is however too restrictive and usually fails to exhibit areas with such properties. The standard way to identify multisensory areas is to select first those presenting an interaction between sensory modalities known as "*superadditivity*", i.e. when the response to a multimodal stimulus is superior to the sum of the responses observed for each isolated sensory modality. The contrary effect (i.e. when the inequality is in the other direction) known as "*subadditivity*" is less specific to multisensory integration since it fails for instance to disentangle multisensory sites from supramodal areas or from areas that are equally active in all conditions (e.g. such as the motor cortex during the subject's motor response) [Beauchamp 2004b]. A second criterion is to observe inverse effectiveness, i.e. a positive correlation between the superadditivity effect and the difficulty to perceive the stimulus. Finally, multisensory areas are supposed to be located in such a manner that signals arriving from different modalities approximately coincide (spatio-temporal proximity). In the case of AV integration, such area would be located for instance between the auditory and visual cortices.

According to these criteria, mSTS and more particularly pSTS appear to be a major site of AV integration as reported in numerous studies [Benevento 1977, Bruce 1981, Beauchamp 2004a, Beauchamp 2004b, Lewis 2010, Klemen 2012]. For instance, pSTS is involved in the learning of arbitrary AV paired-associations [Tanabe 2005], the integration of AV features required for object categorization [Werner 2010], AV synchrony judgment [Lewis 2010, Powers 2012] and discrimination of AV motion direction [von Saldern 2013]. These findings are also supported

by the anatomic description of pSTS showing that this area receives both inputs from the auditory and visual cortices [Howard 1996]. There are thus at least two reasons to see pSTS implicated in our task: not only it is a multisensory area, but it is also implicated in motion processing (cf. section 4.2.1.2).

In addition, the role of the lateral prefrontal cortex in multisensory processing has been recently questioned since anatomical tracing has revealed that auditory and visual "where" and "what" pathways converged to the dorsal and ventral parts of this area [Romanski 2007, Ungerleider 1982, Klemen 2012]. In particular vlPFC was shown to be implicated in the representation of complex audiovisual objects [Romanski 2004, Romanski 2012] combining for instance faces and voices [Romanski 2007]. vlPFC is thus an area of particular interest since it is located at the junction of all streams, both relevant for color-motion binding and multisensory integration (see Fig. 4.3).

Since several studies have shown that hMT+ responded more to congruent than incongruent AV motion [Lewis 2010, Scheef 2009], it has been suggested that hMT+ was also multisensory [Klemen 2012]. Such observation can also be interpreted with supramodality: the more auditory and visual motion share redundant information, the more AV motion is congruent and the more hMT+ is activated. This interpretation is also supported by the fact that, contrary to mSTS and pSTS that seem to be involved in any audiovisual processing, hMT+ shows a specific sensitivity to motion coherence. The identification of supramodal areas remains however a challenge: for instance, we could select any area responding to more than one isolated sensory modality, yet to the risk of selecting other co-activating areas not directly involved in sensory processing. Another practical issue consists of distinguishing two "mixed" neuronal populations that respond each to a different sensory modality [Klemen 2012]: if the spatial resolution is too weak, the same area seems to be activated for both modalities and can be erroneously interpreted as a supramodal area. This could be for instance the case of the middle superior temporal sulcus (mSTS) whose "patchy organization" made of multisensory, visual and auditory selective neurons could only be revealed by using high-resolution parallel fMRI [Beauchamp 2004a]. So far, the most convincing way to identify (potential) supramodal areas has been done by comparing brain activities of sensory-impaired individuals with healthy ones (cf. section 1.2.3). Consistent with the hypothesis of supramodality, responses to auditory and tactile motion in congenitally and temporary blind people was observed in hMT+ [Poirier 2005, Poirier 2006].

4.3 Plausible neural correlates of learning

According to [Gilbert 2001], the effects or perceptual learning at the neural level can take several forms depending on the mechanism encoding the information, among which:

- A larger population of neurons can be recruited in response to the trained stimulus. The underlying hypothesis is that neurons can respond to several

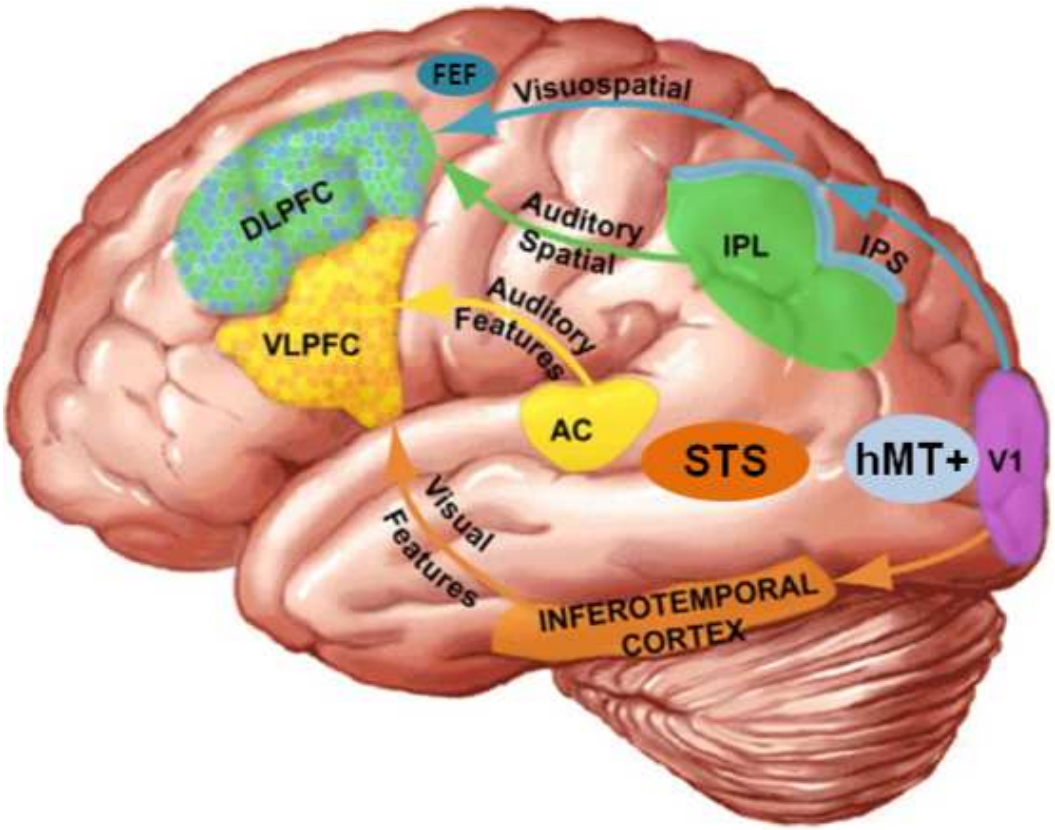

Figure 4.3: Areas potentially recruited during training. In our task, both dorsal (blue arrows) and ventral (orange arrows) visual processing pathways are likely involved: the former to discriminate visual motion coherence and the latter to process color. These two streams converge in the lateral prefrontal cortex respectively in the dorsal (dlPFC) and ventral (vlPFC) parts, where the last stage of motion-color binding can possibly occur. Interestingly, this area is also the site of convergence of auditory dorsal (green arrows) and ventral (yellow arrows) streams, suggesting a possible multisensory interaction occurring during AV and AVn trainings. Our main hypothesis is that the coherence of acoustic textures can facilitate visual motion coherence processing thanks to the supramodal properties of hMT+. IPS: spatial attention site, hMT+: supramodal motion sensitive area, ITC: object sensitive area, STS: multisensory and second-order motion sensitive area and FEF: spatial attention and eye-movement control. Adapted from [Klemen 2012].

stimuli and that the probability of detection is encoded by the number of neurons responding coherently to the stimulus.

- The size of the neuronal population activated by the trained stimulus is reduced in order to decorrelate neuron spiking activities. This implies that optimal conditions of stimulus detection are reflected by a better tuning of neurons, i.e. by increasing their specificity to a given type of stimuli and making them as different as possible.

- The size of the recruited neuronal population does not change; they act however more in synchrony with each other, yielding hence a greater response. In that case, the information would be essentially encoded in time.

Contrary to the second scenario, the first one is consistent with the Hebbian rule, i.e. a reinforcement of synaptic connections following the joint activation of pre- and post-synaptic cells. Other scenarios are indubitably possible — for instance a recent study [Gu 2011] reported a global decrease of the inter-neuron noise (hence a increase of the SNR) in the dorsal MST of a trained monkey without however refined tuning of neurons.

Independently of this, learning can also be reflected by a change of the cortical locus responding to the trained stimulus, the apparition of a larger network and top-down influences. As previously reviewed in section 4.2, a great list of areas implicated during training can potentially present plasticity. According to previous M/EEG studies investigating auditory [van Wassenhove 2007] and visual [Hamamé 2011] perceptual learning, we can expect to observe an increase of the ERF amplitudes at earlier latencies with respect to the trained stimuli. Here, we mainly expect hMT+ to present selective plasticity after having benefited from supramodal processing of coherence in AV training. We do not exclude yet the possibility that perceptual decision might also be at the origin of the behavioral improvement of our participants (cf. chapter 2), which would be conceivably observed in the intraparietal sulcus [Sasaki 2010].

Assuming that plasticity occurred in hMT+ through the mechanism described by the RHT (cf. section 1.1.2), it would have been mediated by higher-order areas such as vlPFC. Moreover in the case of AV training, we can sensibly expect that greater plasticity in hMT+ would have been possibly relayed by the recruitment of multisensory areas (e.g. mSTS, pSTS) — as suggested by the cross-modal plasticity observed in deaf people [Sadato 2005]. We can also wonder if these areas would be still activated after training, i.e. in the absence of acoustic textures during the execution of the visual task only.

Chapter 5

ERF analysis of acquired MEG data

Contents

In the previous chapter, we presented the basis of event-related field (ERF) analysis in MEG and the plausible neural correlates of learning that we expect to see in our paradigm. As previously reviewed in chapter 1, multisensory interactions are ubiquitous in cortex and recent work suggests that sensory cortices may be supramodal (i.e. unspecific to the sensory modality of inputs). Here, we tested this hypothesis by asking whether learning to discriminate visual coherence would benefit from supramodal processing. Consistent with this hypothesis, the psychophysical results presented in chapter 2 show that participants trained with congruent acoustic textures (AV) significantly outperformed participants trained without sound (V)

or with auditory noise (AVn, control group) although they were unaware of their progress. We now investigated the associated neurophysiological correlates by contrasting the MEG source-reconstructed evoked responses to motion coherence before and after training.

In the first section, we detail materials and methods among which the selection of epochs and regions of interest (ROIs) and the statistics. Results are presented in the next section: common to all, vlPFC showed surprising selectivity to the learned coherence levels whereas selectivity in visual motion area hMT+ was only seen for the AV group. Additionally, activity in multisensory cortices (mSTS, pSTS) correlated with post-training performances solely for the AV group. Altogether, the latencies of these effects suggest feedback from vlPFC to hMT+ possibly mediated by temporal cortices in AV and AVn groups. In the next section, results are discussed and interpreted in the context of the Reverse Hierarchy Theory (RHT) of learning in which supramodal processing optimizes visual perceptual learning by capitalizing on sensory-invariant representations — here, global coherence levels across sensory modalities. Conclusions are drawn in the last section.

5.1 Materials and methods

The paradigm, the stimuli and the sample of participants ($N = 3 \times 12$) are described in section 1.3. The parameters of the MEG data acquisition and preprocessing as well as the source reconstruction method (i.e. noise-normalized dSPM-MNE) are detailed in section 3.4. Here, we explain the computation of ERFs, the selection of regions of interest (ROIs) and the statistical analyses used for this study.

5.1.1 Definition of events and regions of interest (ROIs)

5.1.1.1 Selection of events

For the main ERF analysis, data were epoched from −200 ms (baseline) to +1000 ms around the onset of coherent RDK and baseline-corrected. Epochs were averaged for each individual according to the conditions of interest, namely: across all coherence levels (196 trials) or for each coherence level (28 trials). Trials corrupted by muscle or movement artifacts (less than 10% of all trials) were rejected by visual inspection using Fieldtrip (http://www.ru.nl/fcdonders/fieldtrip).

Additionally, epochs were averaged according to each individual's pre- and post-training thresholds into three categories: "*hard*" (coherence levels below the POST-training threshold), "*learned*" (coherence levels between the PRE- and the POST-training thresholds) and "*easy*" (coherence levels above the PRE-training threshold).

Evoked responses were smoothed with a Savitzky-Golay filter [Savitzky 1964] consisting of fitting a 2^{nd} order polynomial to each sliding window of 35 samples. This procedure is approximately equivalent to the application of a low-pass filter of 3 dB cutoff frequency set to 37.5 Hz [Schafer 2011] without reduction of peak amplitudes.

5.1.1.2 Functional localizer for hMT+ and selection criteria for the ROIs

One major prediction in this study was that the perceptual improvements in coherence discrimination thresholds would be commensurate with post-training activity in hMT+ which is known to be responsive to global and translational motion processing (cf. chapter 4). Hence, after source reconstruction, hMT+ was localized on a per individual basis by contrasting the current source estimate obtained to the presentation of 95% coherent motion against the incoherent (0%) portion of the hMT+ localizer. Specifically, the evoked response fields (ERFs) elicited by the transition to full coherence in the visual display (i.e. going from 0% to 95% coherence) were contrasted with the ERFs elicited at the same latency but in the absence of transition (i.e. 0% of coherence). A first inspection of the ERF contrast averaged over all individuals in sensor space (Fig. 5.1a, upper and middle panel) showed a main evoked response spanning $\sim$ 100 to $\sim$ 300 ms post-transition onset. The evoked response was source reconstructed using MNE-dSPM (cf. section 3.4); the extent of the area hMT+ in source space was determined by thresholding the average source estimate amplitudes over 100–300 ms above the 90^{th} percentile of all dSPM values covering the entire cortex (Fig. 5.1a, lower panel).

Figure 5.1b reports additional regions of interest (ROI) or labels which were identified at the group-level by source reconstruction of the grand average evoked field response to the presentation of incoherent visual RDKs which combined data from all three training groups (V, AV and AVn) in the pre- and in the post-training sessions. The most responsive areas (selected by thresholding to the 90^{th} percentile of all dSPM values) were manually labeled using the Freesurfer neuroanatomical parcellation. The obtained ROIs comprised: bilateral primary and secondary visual cortices (V1 and V2, respectively), precuneus, visual area V4, hMT+, Inferior Temporal Cortex (ITC), Auditory Cortex (AC), posterior Superior Temporal Sulcus (pSTS), Inferior Parietal Sulcus (IPS), frontal eye-field (FEF) and the right middle Superior Temporal Sulcus (mSTS). The time courses reported in a label were computed by averaging dSPM estimate time courses over all vertices within the label. It is worth noting that dSPM values are here only positive and hence do not cancel out after averaging. Sample grand average times courses over all coherence levels in these ROIs are provided for pre- and post-training in Fig. A.1 and Fig. A.2 (see appendix A).

5.1.2 Statistics

The effect of training was tested using the POST minus PRE contrasts across all coherence levels separately for each ROI using F-tests combined with non-parametric permutation tests [Maris 2007] that provide corrected p-values for multiple comparisons. For each signed permutation ($N = 20000$), time clusters were defined on the basis of temporal adjacency by regrouping samples whose F-statistic was larger than 3.3 (i.e. p-value inferior to 0.05 for an F-test with 2×33 degrees of freedom). Cluster-level statistics were then calculated by taking the sum of the

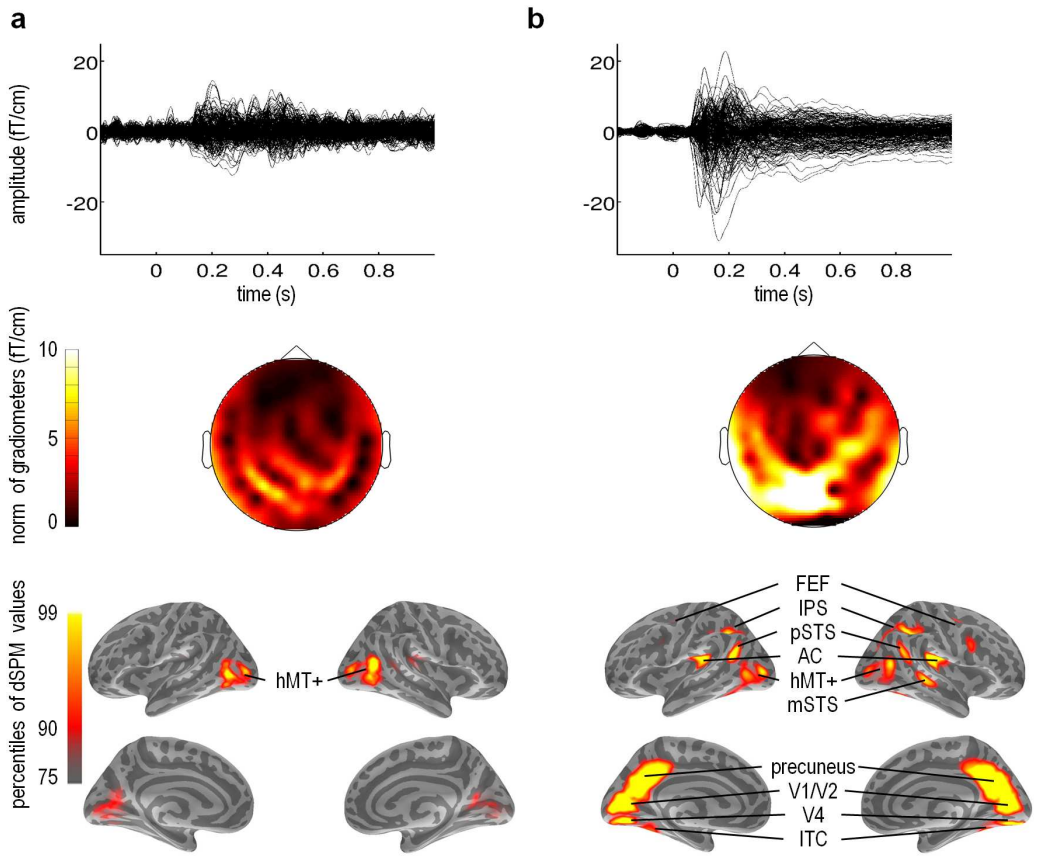

Figure 5.1: MNE (dSPM) source reconstruction and regions of interest (ROIS). (a) Evoked Response Fields (ERF) in sensor space (planar gradiometers) obtained in response to the presentation of the hMT+ localizer. Here, we report the evoked component obtained by subtracting the ERF obtained for fully incoherent motion (0%) from the ERF obtained for a 95% coherent motion. These data were collected during the localizer block and pulled across all individuals (i.e. all three training groups: V, AV, and Avn for a total of n=36 participants).The time course of all gradiometers (Global Field Power) is provided in the top graph; the topography of the differential evoked component averaged over 100 to 300 ms post-coherence onset is provided for the norm of the gradiometers in the middle graph; the corresponding current source estimates using MNE-dSPM illustrate the mean localization of hMT+ obtained with this MEG localizer. **(b)** ERF in sensor space (planar gradiometers) obtained in response to the presentation of incoherent visual RDKs. PRE and POST training data were pulled together across all three training groups (n=36) in order to define the regions of interest. The time course of the ERFs obtained at the onset of all visual stimuli is depicted in the top graph for all gradiometers (Global Field Power). A distinct evoked component can be seen spanning 100 to 250 ms. The topography of the ERF is provided in the middle graph for the norm of gradiometers averaged over 100 to 300 ms post-incoherence onset. The corresponding current source estimates using MNE-dSPM are provided in the bottom graph. The extent of a given label or region of interest (ROI) in source space was defined by thresholding the estimates at the 90^{th} percentile of all dSPM values. FEF: frontal-eye-field. IPS: Inferior Parietal Sulcus. pSTS: posterior Superior Temporal Sulcus. AC: auditory cortex. mSTS: middle Superior Temporal Sulcus. ITC: Inferior Temporal Cortex.

F-values within the cluster. Only temporal clusters with corrected p-values ≤ 0.05 are reported. The significance of the contrasts were also tested in each group using non-parametric pairwise two-tailed permutation tests with the cluster threshold set to 2.2 (i.e. p-value inferior to 0.05 for a two-sided t-test with 11 degrees of freedom).

All correlation tests were assessed with Pearson correlation coefficients ρ under the null hypothesis H_0: $\rho = 0$ and with the alternative H_1: $\rho \neq 0$ using a Student t-test on the statistic $t = \frac{\rho\sqrt{n-2}}{\sqrt{1-\rho^2}}$, where n is the number of samples. Outliers were automatically detected and rejected by using a leave-one-out approach [Weisberg 2005] consisting of estimating the distribution $N(m, \sigma)$ of residuals based on $(n-1)$ observations (each observation is left out one after another). Extreme residuals (i.e. above and below $m \pm k\sigma$, where $k = 2.5$ is considered to be a reasonable choice [Rousseeuw 1987]) are identified and the corresponding observations set as outliers.

5.2 Results

5.2.1 hMT+ selective plasticity in AV group

According to previous reports [Ahlfors 1999, Lam 2000, Maruyama 2002, Nakamura 2003, Aspell 2005, Amano 2006, Händel 2007, Mercier 2009], the amplitude of the evoked response originating from hMT+ increases with the coherence level of RDK stimuli irrespective of participants' performance. As a first approach, we thus classified trials as a function of the physical coherence of the visual stimuli (i.e. 7 coherence levels ranging from 15% to 95%) separately in pre- and post-training and for each training group. After source reconstruction, a similar pattern of response in hMT+ could be seen in all three groups starting from $\sim$ 200 ms and extending to 500ms post-stimulus onset (Fig. 5.2a).

One hypothesis on the origin of perceptual improvements observed in the three training groups was that the selectivity of the hMT+ response to the presentation of coherent RDK would increase after training. When contrasting the average hMT+ response profiles in pre- and post-training (Fig. 5.2a), the spread of the hMT+ response amplitudes indeed seemed much larger in the V and AVn groups in post-training; however, and surprisingly, the AV group did not appear to show such changes. In fact, a linear regression of the amplitude of the hMT+ estimate as a function of the coherence level of the stimuli clearly showed that the AV group — contrarily to the V and AVn groups — showed no significant differences in pre- vs. post-training (Fig. 5.2b, beta values). At first glance, this result would suggest that the superior perceptual improvements observed in the AV group could not be accounted for on the basis of hMT+ plasticity.

However, using a similar approach to psychometric characterization, hMT+ sensitivity to motion coherence can be characterized for each individual by a neurometric function [Britten 1992, Gold 2010] from which a threshold can be derived. One advantage of neurometric thresholds is that they are comparable to psychometric functions pending on the experimental conditions [Britten 1992]. Hence, to better

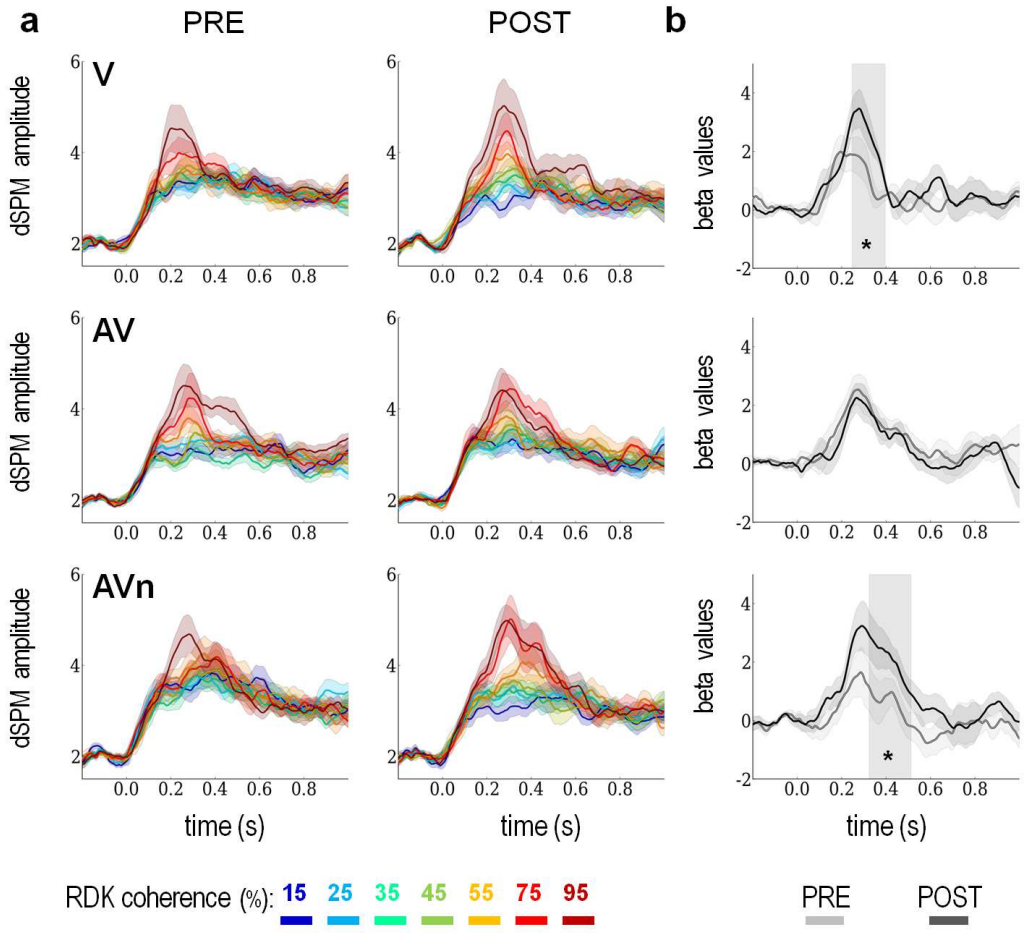

Figure 5.2: Cortical response in hMT+ as a function of visual RDK coherence levels. (a) Time course of current source estimates (dSPM amplitudes) in bilateral hMT+ for the different training groups (V: top graph, AV: middle graph and AVn: bottom graph) as a function of RDK coherence levels (cf. legend for color scheme). Data obtained in the PRE and POST training blocks are reported in the left and right panels, respectively. A prominent evoked response peaking at $\sim$ 200 ms post-coherence onset can readily be seen in all groups and for all coherence levels. Additionally, the higher the visual coherence, the higher the amplitude of the cortical response. While the profile of responses was similar across the three groups before training, a distinct response pattern was found after training. Specifically, the V and AVn showed an increased spread of the response amplitudes as a function of visual coherence levels whereas the AV group did not show such spread. **(b)** Mean beta values ($\pm$1 s.e.m.) obtained from a linear regression between the dSPM values in hMT+ and the 7 coherence levels at each sample point for each individual in groups V, AV and AVn (top, middle and bottom row, respectively), before (PRE, grey) and after (POST, black) training. Shaded areas highlight the latencies of significant changes of beta provided by a pairwise cluster permutation algorithm. Consistent with the increased spread of amplitudes, the beta values significantly increased in V (around 250–400 ms) and in AVn (around 320–500 ms) after training; no changes were observed in AV suggesting that changes in neural activity in hMT+ for the group AV cannot account for the group's perceptual improvements.

understand the selectivity of the response profile in hMT+, we selected the 200–500 ms time period post-coherence onset and fitted a Weibull function Y to the averaged source estimate amplitudes as a function of stimulus coherence levels on a per individual basis, in pre- and post-training separately:

$$Y(coh, M, m, \alpha, \beta) = M - (M - m)e^{-\left(\frac{coh}{\alpha}\right)^{\beta}},$$

with *coh* as motion coherence level and M, m, α and β the parameters determined by the damped Gauss-Newton method. Each fit allowed deriving a neurometric threshold defined as the stimulus coherence level corresponding to half the amplitude of the sigmoid curve (see Fig. 5.3 panel a for examples of individual fits and panel b for the group data).

Using this procedure, the only significant decrease in neurometric threshold was observed in the AV group ($t_{11} = -2.34$, $p = 0.039$; Fig. 5.3b). This approach suggested a particular neural strategy in hMT+ response selectivity pending on participants' training history, namely: in the V and AVn group, larger selectivity can be seen at the extreme coherent levels, whereas in the AV group, better selectivity is seen in those levels of coherence close to perceptual threshold. Interestingly, although no correlation could be found between neurometric and psychometric thresholds when separately considering the pre- and post-training data, the correlation between the changes in perceptual and neurometric thresholds was significant in each separate group and across all individual irrespective of their training history (Fig. 5.4).

Altogether, these results strongly suggest that the hMT+ response to a given RDK coherence level significantly changed as a function of an individual's training history; nevertheless, and surprisingly, the hMT+ sensitivity to RDK coherence discrimination appeared to have only improved in the AV trained group but not in others.

5.2.2 Classification of coherence levels as a function of the individual improvement

In order to narrow down the specific effects of training in hMT+ response, we further classified data according to each individual's perceptual improvement. Specifically, participants underwent individualized training; they were not trained hence on the same set of coherence levels during the training blocks but rather on a selected set based on an individual's initial discrimination threshold measured in the pre-training block. Hence, participants were not trained on the same set of coherence levels albeit all were tested on the same 7 coherence levels in pre- and post-training blocks.

On the basis of this, we classified the 7 RDK coherence levels into three sets solely based on their learned discriminability — i.e. irrespective of the physical RDK coherence levels — in order to sort data in the pre- and post-training blocks. The three categories were "*hard*", "*easy*" and "*learned*". The "*hard*" category consisted of all stimuli that remained below an individual's perceptual threshold after training

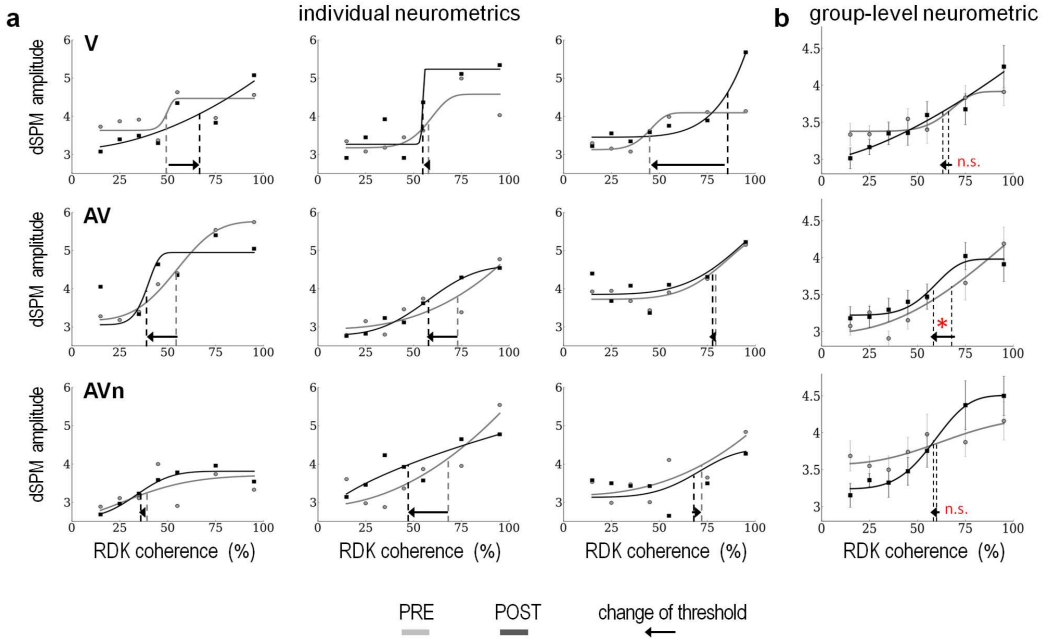

Figure 5.3: Neurometric function in hMT+. The amplitude of the current source estimates (dSPM) in hMT+ were averaged between 200 and 500 ms post-coherence onset as a function of the seven coherence levels in V (top), AV (middle) and AVn (bottom). This quantification was performed for the PRE (grey) and the POST (black) training data. Each individual's brain response in hMT+ was quantified for each coherence levels. To obtain an individual's neurometric function, the amplitudes of the current source estimates in hMT+ were plotted as a function of visual RDK coherence level. Each individual's neurometric function thus allowed deriving a neurometric threshold via Weibull fits (i.e. the level of coherence corresponding to half the amplitude of the sigmoid curve). **(a)** Examples of individual neurometric curves for three participants belonging to the V, the AV and the AVn groups (top, middle and bottom rows, respectively). **(b)** Averaged fits along with the mean individuals' data. The neurometric thresholds obtained in PRE and POST were compared by carrying out a two-tailed paired t-test. Using this method, we show that neither V or AVn showed a significant change in threshold (V: $t_{11} = -0.2$, $p = 0.84$; AVn: $t_{11} = -0.36$, $p = 0.72$) whereas AV showed a significant decrease of threshold ($t_{11} = -2.34$, $p = 0.039$). This suggests that the neural response to a given coherence level, hence the neural selectivity in hMT+, has significantly changed according to the type of training provided to the participants. Specifically, the sensitivity to coherence discrimination in hMT+ only improved in the AV group.

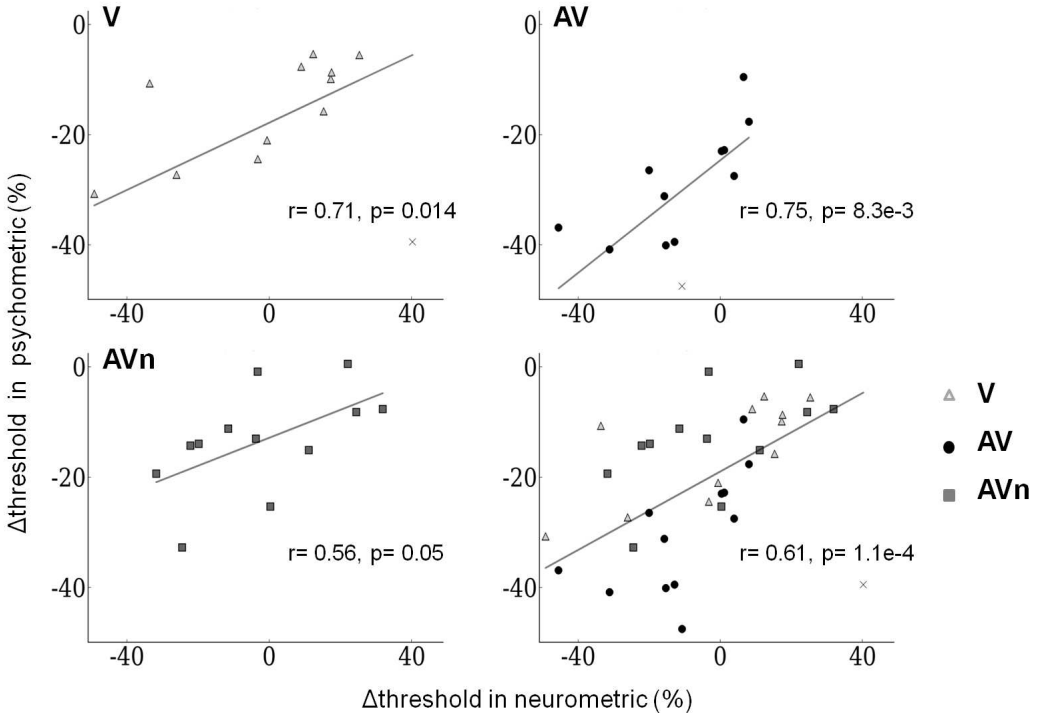

Figure 5.4: Changes in visual coherence discrimination thresholds as a function of changes in neurometric thresholds before and after training. Differences in individuals' perceptual thresholds before and after training (POST-PRE) are reported as a function of the individuals' variation in neurometric thresholds on per training group basis (V: top left; AV: top right; AVn: bottom left; all groups: bottom right). In all three training groups, individuals' improvements in coherence discrimination thresholds were significantly correlated with the observed changes in neurometric thresholds derived from source estimate activity in bilateral hMT+. Specifically, correlations were the highest in the V and AV groups (V: $r = 0.71$, $p = 0.014$; AV: $r = 0.75$, $p = 8.3e-3$, respectively) but also in the AVn group (r= 0.56, p= 0.05). When grouping all individuals, a significant correlation was preserved (bottom right, $r = 0.61$, $p = 1.1e-4$) . 'x' denote statistical outliers.

(i.e. RDK coherence levels that never benefited from training and did not become perceptually discriminable for a given participant). Conversely, the "*easy*" category corresponded to those stimuli that were already above the individual's discrimination threshold before training. Most importantly, the "*learned*" category consisted of all RDK coherence levels that became discriminable (i.e. from below to above an individual's discrimination threshold after training). We then hypothesized that plasticity should be precisely reflected by a change of neural activity elicited by the "*learned*" category and not others.

5.2.2.1 Selective training in hMT+ only seen in AV group

Hence, on the basis of these three perceptual categories, we first examined the mean variations (POST - PRE) of the responses in hMT+ averaged over 200 to 500 ms (Fig. 5.5) in order to compare them with the previous results. Significant differences were found between the three groups in the "*learned*" ($F_{2,33} = 5.4$, $p = 0.0091$) and "*hard*" ($F_{2,33} = 4.8$, $p = 0.015$) categories. Specifically, the V and AVn groups shared a similar pattern of responses across the three categories: opposite variations in "*hard*" and "*easy*" categories were observed only in V and AVn groups, consistent with the observed spread of hMT+ responses as a function of the RDK coherence levels (Fig. 5.2). To the contrary and consistent with the shifts in neurometric thresholds (Fig. 5.3b), the AV group presented a significant response profile to the "*learned*" category ($t_{11} = 3.23$, $pcor = 2.4e - 2$, bilateral paired t-test with Bonferroni correction).

This result was confirmed by a finer analysis of the entire time course differences in hMT+ (Fig. 5.6, first column) when carrying out a pairwise cluster permutation algorithm (cf. Table 5.1): AV was indeed the only group to show a significant response increase for the "*learned*" coherence levels spanning 160–390 ms post-coherence onset. Hence, with this analysis, we consistently observe that only those individuals with a history of AV training showed a significant change in hMT+ activity that directly relates to the observed perceptual improvements and those stimuli that underwent a significant change in perceptual discriminability.

5.2.2.2 Extended selectivity to other ROIs

Considering that hMT+ did not always present selective changes to the "*learned*" coherence levels notably in the V and the AVn groups, we then asked whether other cortical areas could significantly contribute to the obtained perceptual improvements. To that aim, neural responses in the observed regions of interest (ROIs, Fig. 5.1) were quantified and contrasted in pre- and post-training as a function of the same perceptual categories (Fig. 5.6).

As previously done for hMT+, contrasts of post- minus pre-training were separately tested for each group and each category by using a pairwise cluster permutation algorithm. For clarity, only those ROIs and time courses presenting significant differences are reported in Fig. 5.6 and a summary of significant cluster values and

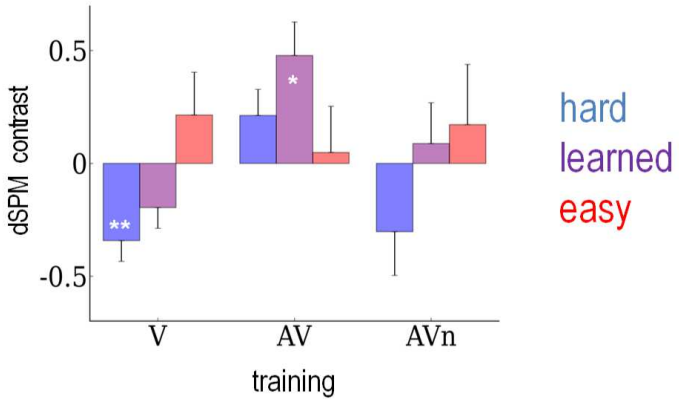

Figure 5.5: Functional selectivity in hMT+ for AV training. Coherence levels were formally classified into three groups according to participants' perceptual improvements (see main text): "*hard*" (blue), "*learned*"(purple) and "*easy*" (red). Post- minus pre-training mean dSPM contrasts (± 1 s.e.m.) in hMT+ averaged over a period of 200 to 500 ms post-coherence onset for each training group V, AV and AVn are shown as a function of these relative coherence levels. Two different patterns clearly emerge: while V and AVn present opposite variations in the extreme categories ("*hard*" and "*easy*"), AV is characterized by a greater response in the "*learned*" category. Accordingly, significant differences between groups were found for the learned ($F_{2,33} = 5,4$, $p = 0.0091$) and hard ($F_{2,33} = 4.8$, $p = 0.015$) coherence levels. A post-hoc analysis (Bonferroni) showed that differences for "*learned*" coherence levels were significant in the AV group ($t_{11} = 3.23$, $pcor = 2.4e{-}2$) and differences for the "*hard*" coherence levels were significant in the V group ($t_{11} = -3.73$, $pcor = 9.9e - 3$). '*': corrected p values inferior to 0.05, '**': corrected p values inferior to 0.01.

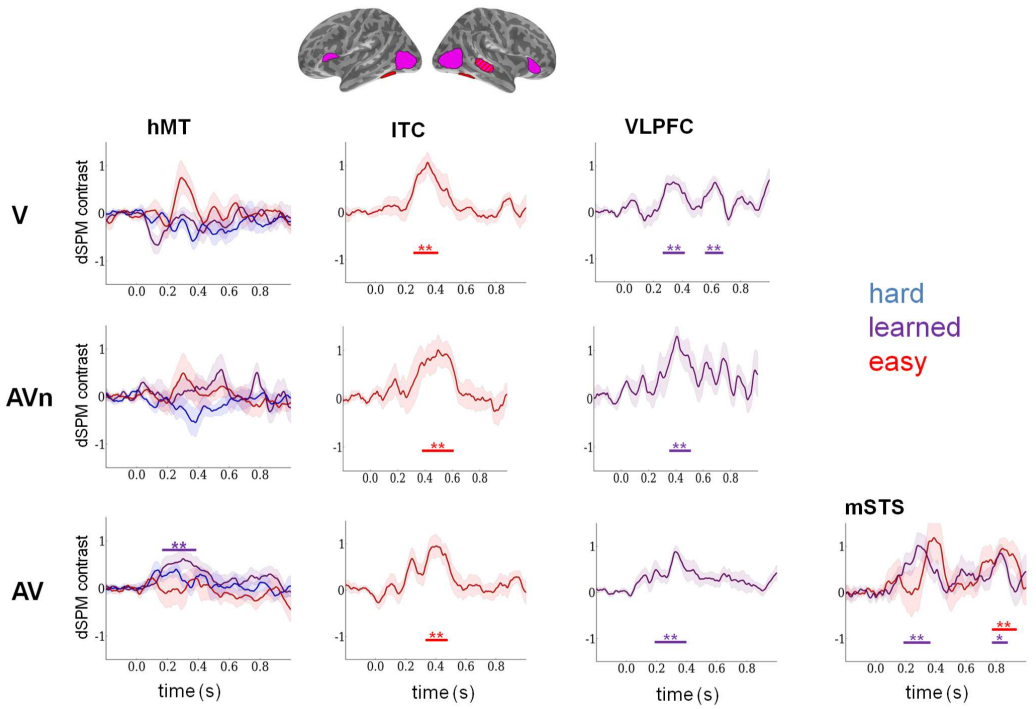

Figure 5.6: Functional selectivity in regions of interest (ROIs) after V, AV and AVn training. Coherence levels were formally classified into three groups according to participants' perceptual improvements (see main text): "*hard*" (blue), "*learned*"(purple) and "*easy*" (red). Post- minus pre-training mean dSPM contrasts (±1 s.e.m.) are reported for all three groups (V: top; AVn: middle; AV: bottom). In hMT+, all categories are reported while in other ROIs only categories with significant differences are shown for better clarity. Strikingly, only AV presented a significant difference in hMT+ observed as an increase of amplitude for the "*learned*" coherence levels. When considering all other ROIs defined in Fig. 5.1, only AV presented significant time clusters for the "*learned*" coherence levels in right mSTS while all groups presented significant increases in response to the "*easy*" category in ITC. The analysis was extended to bilateral ventro-lateral PreFrontal Cortex (vlPFC) which remarkably revealed significant time clusters for all three groups but solely for the "*learned*" coherence levels. Significant clusters were determined using a pairwise cluster permutation algorithm and are indicated below curves with bars. '*': corrected p values inferior to 0.05, '**': corrected p values inferior to 0.01.

latencies is also provided in Table 5.1. First, and common to all three groups, a significant response increase in post-training was observed in ITC but solely for the "*easy*" category; different latencies were however noticeable in each group (Fig. 5.6, second column): the response in the V group spanned $\sim$ 250 to 410 ms, $\sim$ 330 to 480 ms in the AV and $\sim$ 380 to 610 ms in the AVn group. This pattern suggests that color-motion binding in this task may have equally improved in all participants irrespective of training when the coherence discrimination was easiest.

No significant differences were otherwise seen for any other perceptual categories in these ROIs. As no other significant changes for the "*learned*" category were seen in all ROIs to account for V and AVn perceptual improvements, we added a selection criterion for our analysis. Specifically, several lines of research have shown that the lateral prefrontal cortex is a major site of convergence for the dorsal and ventral visual [Ungerleider 1982] and auditory [Rauschecker 2000] streams but also an important site of multisensory convergence [Romanski 2004, Romanski 2007, Romanski 2012]. We thus extended our analysis to bilateral vlPFC and the ROI was delimited based on the Freesurfer neuroanatomical parcellation. Strikingly, significant time clusters were found in this region specifically for the "*learned*" category and for all three groups (Fig. 5.6, third column). Two significant clusters were seen in V spanning $\sim$ 260 to 390 ms and 550 to 680 ms; one surprisingly early significant cluster was seen in AV spanning $\sim$ 190 to 390 ms and one significant cluster in AVn spanning $\sim$ 350 to 510 ms. In addition, the AV group (Fig. 5.6, fourth column) was the only group which presented a significant response increase in both the learned and the easy category in right mSTS at late latencies ($\sim$ 770 to 930 ms) but also, and crucially, significant changes for the "*learned*" category at the same latencies as in hMT+ (i.e. $\sim$ 200 to $\sim$ 400 ms).

Altogether, these results strongly suggest that the boost in sensitivity observed in hMT+ may not result from local plasticity but from the engagement of a larger network in the computations of color-motion binding and coherence discrimination including prefrontal regions.

5.2.3 A larger network distinctively dissociate the three training groups

We now ask whether a non-selective training effect can be observed irrespective of the RDK coherence levels across all three groups, thereby reflecting an overall effect of improvements in the task. Similar to previous analyses, the evoked responses elicited by the presentation of all RDK coherence levels were grand-averaged, source reconstructed and averaged within each ROI as defined in Fig. 5.1.

The time courses in pre- and post-training data are illustrated in Figures A.1 and A.2 (see appendix A), respectively. With the exception of visual area V4, no significant differences were observed between the three groups before training (Fig. A.1). In post-training, the time courses across the three groups significantly differed only in right mSTS (Fig. A.2). The source amplitudes in the different ROIs were

ROI	V	AV	AVn
	LEARNED category		
hMT+	n.s.	160 : 390 ms, $p = 0.0059$	n.s.
mSTS	n.s.	180 : 360 ms, $p = 0.0088$ 770 : 880 ms, $p = 0.019$	n.s.
vlPFC	260 : 390 ms, $p = 0.0019$ 550 : 680 ms, $p = 0.0054$	190 : 390 ms, $p = 0.0044$	350 : 510 ms, $p = 0.0098$
	EASY category		
ITC	250 : 410 ms, $p = 0.0064$	330 : 480 ms, $p = 0.0054$	380 : 610 ms, $p = 0.0029$
mSTS	n.s.	770 : 930 ms, $p = 0.0068$	n.s.

Table 5.1: Summary of significant clusters observed in Figure 5.6. Latencies and corrected p values are provided for each ROIs (rows) and for each training group (columns).

then contrasted between the pre- and post-training blocks and tested with a cluster permutation algorithm in each group (Fig. 5.7).

First, all three groups presented a main effect of training in ITC corresponding to positive clusters at increasing latencies, namely in V: 260 to 500 ms; in AV: 300 to 540 ms and in AVn: 500 to 630 ms. Second, no additional effects were found for the V group. Third in the AV group, a large network was observed revealing significant post-training responses increase in hMT+ (130 to 290 ms post-coherence onset), in right mSTS with two temporal clusters (250 to 440 ms and 600 to 900 ms) post-coherence onset, in V4 (160 to 400 ms), in pSTS (320 to 560 ms) and in AC (210 to 340 ms). Fourth and interestingly, pSTS and AC presented opposite effects for AVn, with decrease activity in post-training for latencies of 120 to 320 ms in pSTS and of 60 to 280 ms in AC.

In order to directly contrast the three training groups, a F-test was combined with a cluster permutation algorithm: the earliest effect was observed in AC starting at 80 ms post-coherence onset (and lasting 260 ms), rapidly followed by a long sustained differentiation in pSTS spanning 120 to 520 ms and in V4 between 160 and 400 ms. A late main effect was observed in the right mSTS at the latencies spanning 680 to 880 ms. All latencies and p values of significant clusters in Fig. 5.7 are provided in Table 5.2.

To better comprehend the role of mSTS and pSTS, the post- minus pre- contrasts of source estimate amplitudes were plotted as a function of post- minus pre-

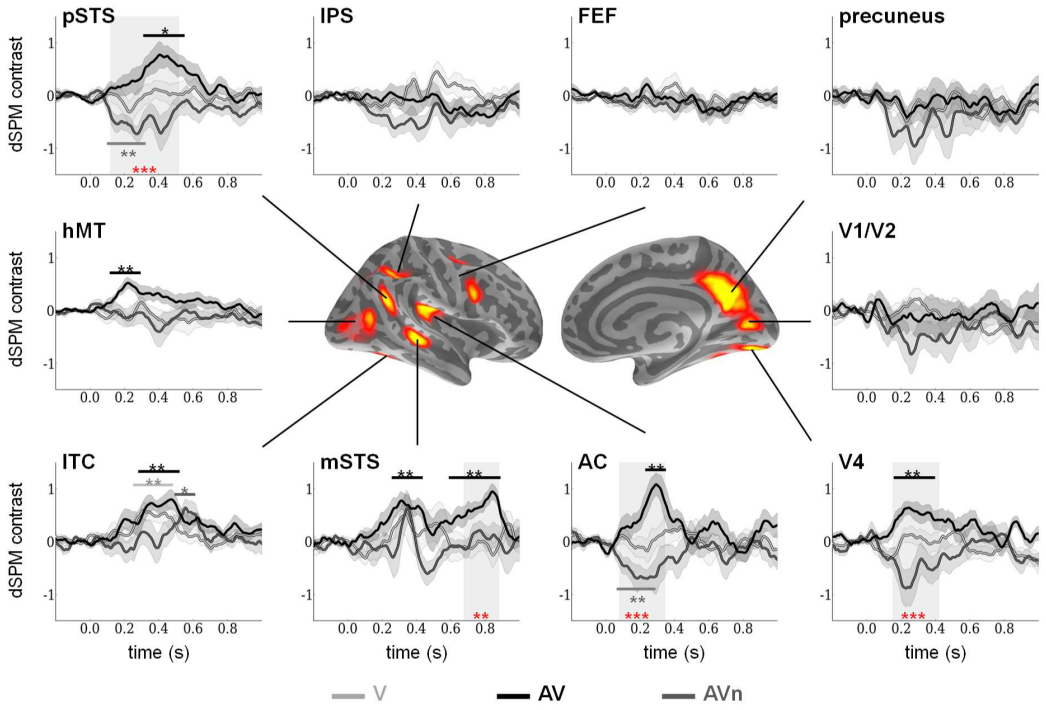

Figure 5.7: Main effects of training in all three groups across all coherence levels. Post- minus pre-training contrasts of mean current source estimates (dSPM, ±1 s.e.m.) across all RDK coherence levels and for each region of interests (see Fig. 5.1). Differential time series are reported in light grey for V, in black for AV and in dark grey for AVn. The effect of training in a given group was tested with a two-tailed paired t-test combined with a cluster permutation algorithm: significant differences are indicated with light grey bars (V), black bars (AV) and dark grey bars (AVn). In V, main effects of training irrespective of coherence levels can be seen in ITC from $\sim$ 200 to 400 ms post-coherence onset. In AV, main effects are seen in several regions including hMT+, ITC, mSTS, V4, pSTS and AC. In AVn, main effects are seen in ITC, pSTS, and AC. In order to test the main effects of training type (V, AV or AVn) irrespective of coherence levels, a F-test was performed in combination with a cluster permutation algorithm for all ROIs. The shaded areas highlight the latencies of significant differences between the training groups; red stars indicate the corresponding degree of significance. As can be seen, four main regions capture the main differences across the three training groups, namely: middle and posterior STS, V4 and AC. * corrected p values inferior to 0.05; ** corrected p values inferior to 0.01 ; *** corrected p value inferior to 0.001.

pre- vs. post-training — all coherence levels				
	t-tests			F-tests
ROI	**V**	**AV**	**AVn**	**V, AV, AVn**
hMT+	n.s.	130 : 290 ms, $p = 0.0044$	n.s.	n.s.
mSTS	n.s.	250 : 440 ms, $p = 0.0083$ 600 : 900 ms, $p = 0.0015$	n.s.	680 : 880 ms, $p = 0.0055$
pSTS	n.s.	320 : 560 ms, $p = 0.016$	120 : 320 ms, $p = 0.0078$	120 : 520 ms, $p = 0.0007$
V4	n.s.	160 : 400 ms, $p = 0.0068$	n.s.	150 : 420 ms, $p = 0.00095$
ITC	260 : 500 ms, $p = 0.007$	300 : 540 ms, $p = 0.0049$	500 : 630 ms, $p = 0.029$	n.s.
AC	n.s.	210 : 340 ms, $p = 0.0088$	60 : 280 ms, $p = 0.0049$	80 : 340 ms, $p = 0.00075$

Table 5.2: Summary of significant clusters observed in Figure 5.7. Latencies and corrected p values are provided for each ROIs (rows) and for each training group (columns).

performance separately for each group (Fig. 5.8). A significant correlation was observed in both ROIs but again, solely for the AV group. This result suggests that while mSTS and pSTS are not selective to the RDK coherence levels, these regions play a significant role in the task improvements observed in the AV group but not in the other groups.

5.2.4 Summary and working hypothesis

Altogether, our results highlight the distinct contribution of different cortical areas either selective to the RDK coherence levels or to the type of training history of participants in the different groups. A summary and working hypothesis is provided in Figure 9 on the functional role of the ROIs contribution to perceptual improvements observed in the three groups of participants.

5.3 Discussion

In this study, we asked whether learning to discriminate visual coherent motion would rapidly benefit from hearing matched acoustic features. To this end, three groups of participants underwent training with visual (V), correlated (AV) or arbitrary (AVn) audiovisual pairings while being recorded with MEG. As previously shown in chapter 2, all three groups showed a significant decrease of their visual coherence discrimination thresholds after a short training; however, participants in the

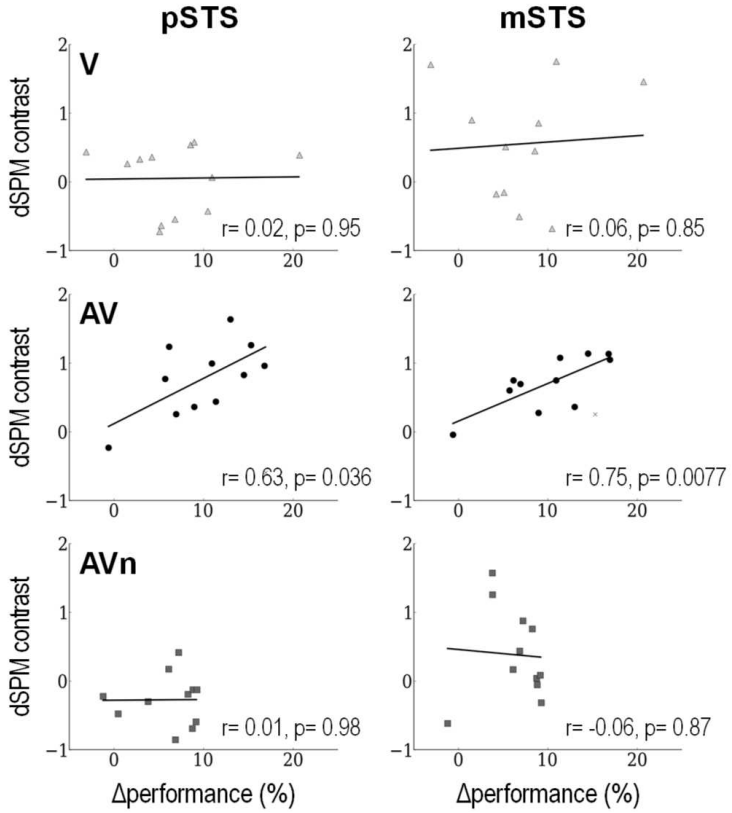

Figure 5.8: Main effects of training in bilateral pSTS and right mSTS are uniquely observed in the AV group. Mean dSPM contrasts in bilateral pSTS (left column) and right mSTS (right column) as a function of individuals' mean performance increases over all coherence levels in V (top), AV (middle) and AVn (bottom). dSPM contrasts were computed by collapsing all RDK coherence levels and averaged over the time windows corresponding to significant differences in AV (i.e. over 320–560 ms in pSTS and 250–440 ms in mSTS) as reported in Table 5.2. Significant positive correlations between overall performance and source estimate amplitude were observed solely in the AV group specifically in pSTS and in mSTS. 'x': automatically detected outliers.

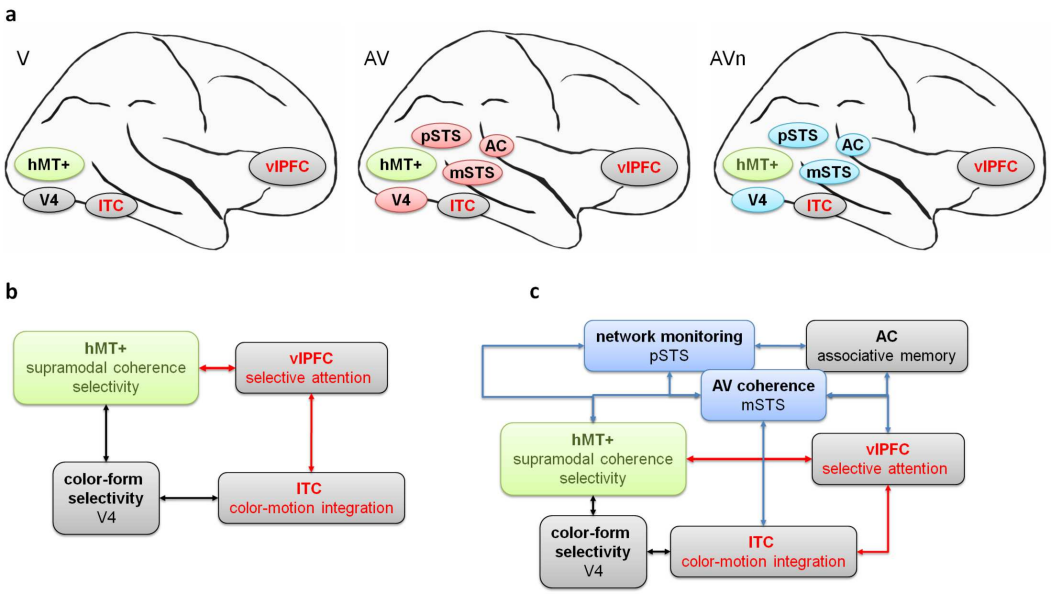

Figure 5.9: A working hypothesis for supramodal processing and reverse hierarchy plasticity. **(a)** Synthetic illustration of ROIs showing significant post-training changes in neural responses after training in the V, AV and AVn groups. Significant changes in hMT+, V4, ITC and vlPFC were common to all three groups whereas pSTS, mSTS, and AC were specific to the multisensory AV and AVn groups. The network observed in post-multisensory training thus implicated more regions than in visual training. Strikingly, the pattern of activation in the control AVn group and in the AV group was notably reversed in several regions including pSTS, AC, mSTS and V4: this suggests selective modulations of these cortical regions based on the stimuli presented during training. **(b)** A basic hypothesis for the functional network implicated in visual learning in the V group. **(c)** Working hypothesis for the functional network implicated in the AV and the AVn groups. The distinctive pattern of cortical activity that significantly dissociated the three training groups was a significant increase and decrease of activity in AV and AVn, respectively for the pSTS, mSTS, AC and V4, suggesting direct functional connectivity in these regions. No significant change of activity was observed in V in these regions. Common to all three training groups, hMT+ and vlPFC showed discriminable cortical responses as a function of the learned coherence levels. Additionally, all three groups showed an increased activity in ITC only for the easy coherence levels. In hMT+, the increase spread of neural response was shared by V and the control AVn, whereas selective activity was seen solely for the AV group. Altogether , our results suggest a regulation of hMT+ activity by upstream computations notably in the AV and AVn groups.

AV group significantly outperformed participants in the V and AVn groups. Intriguingly, V participants were the only ones showing a significant increase in confidence rating.

Here we found that all three groups showed common dynamic activation patterns in two distinct cortical regions (ITC and vlPFC): a comparable post-training increase of neural activity in the ventral visual stream (ITC) suggested that color-motion binding consistently improved when coherence discrimination was easily achieved. Additionally, all three groups showed increased neural response in vlPFC specifically for the learned coherence levels, suggesting a strong and selective implication of prefrontal cortex in learning. Conversely, distinct patterns of activity distinguished the three groups of participants: the multisensory trained groups (AV and AVn) showed an opposite pattern of post-training activity in a network comprising pSTS, mSTS, and AC (cf. Fig. 5.9). This suggests that multisensory training fundamentally altered the network implicated in the analysis of visual coherent motion stimuli and that a uni- vs. a multi-sensory training can selectively shape the activity of the implicated network. Third, and crucially, AV participants were the only group showing a post-training gain of selectivity in hMT+ as captured by a significant shift in the neurometric threshold.

Altogether, we interpret our results as evidence for supramodal processing elicited by the presentation of coherent audiovisual features. Our results suggest that supramodal processing during training allowed the fine-tuning of downstream selectivity in visual cortices, consistent with the reverse hierarchy hypothesis [Ahissar 2004, Proulx 2012]. If this hypothesis is correct, multisensory training can open new empirical venues for the understanding of top-down plasticity in perceptual learning and greatly speed up the use of sensory-substitution devices in sensory-impaired population.

5.3.1 Supramodal object representation in vlPFC?

As previously mentioned in chapter 1, the audiovisual stimuli used during training were specifically designed to mimic the correspondences of auditory and visual attributes predicted from natural communication stimuli such as speech and monkey vocalizations although we arguably avoided possible overt semantic categorizations (face, speech). These audiovisual features rely on the correlated temporal structuring of acoustic and visual information and focused on the spectrotemporal attributes of the signals requiring color-motion binding for overt response ("red (green) RDK is most coherent"). Hence, during training, the matching between visual and acoustic features would likely be comparable to the one taking place in the context of natural stimuli.

In her recent review, Chan [Chan 2013] contrasts the evidence in favor of a domain general vs. a domain specific contribution of vlPFC and suggests that vlPFC primarily represents object-feature information. In our study, a possible interpretation for the selective activation to the learned coherence levels observed in vlPFC (Fig. 5.6), irrespective of training groups, may be the increased representational

salience of supramodal coherence, namely the combined (auditory and/or visual) features enabling the neural representation of a "coherent object" irrespective of its color or direction of motion — hence, supramodal coherence. In the context of learning, the enhanced activation may be relevant by virtue of binding across visual and/or auditory streams specifically for those levels of coherence newly recognized. vlPFC is a known site of convergence for the dorsal and visual streams of both auditory and visual systems and a major site of convergence for the representation of multisensory information [Romanski 2007, Romanski 2012]. Interestingly, vlPFC has also been implicated in the representation of communication signals in monkey recordings [Sugihara 2006] suggesting that this region is particularly well-suited for the computations of natural and matched cross-sensory stimuli such as the ones utilized here. These results are further consistent with several neuroimaging studies showing the implication of vlPFC for semantic retrieval and response selection in the context of multisensory processing [Werner 2010].

5.3.2 Functional selectivity of hMT+ : psycho- and neurometric thresholds

Although previous studies have reported activation in hMT+ to the presentation of auditory stimuli [Poirier 2005, Poirier 2006] and matched audiovisual motion [Alink 2008, Scheef 2009, von Saldern 2013], the evidence for auditory motion processing in this region is scarce. From a neurophysiological standpoint, it has been shown that the presentation of visual and audiovisual motion elicits the same neural response in motion area MT [Ilg 2004] but so far no significant response to the presentation of auditory motion alone was observed in this region. Hence, and by far, the most convincing evidence for the capabilities of hMT+ to compute motion processing supramodally — i.e. irrespective of the sensory modality of inputs — comes from studies of sensory-impaired and blind populations [Morrone 2010, Voss 2012, Ricciardi 2013] in which functional recycling can readily be observed for the benefit of other sensory modalities (cf. chapter 1).

One study [Bedny 2010] has notably suggested the existence of a sensitive period around 2 years of age for the acquisition of visual functional selectivity in this region. Additionally, the lack of exposure to visual information was shown to prevent visual selectivity in this region although hMT+ in late blind populations can be functionally recycled to the benefit of auditory motion processing. In this context, we asked whether a short-training capitalizing on cross-sensory matching could benefit plasticity in this region. In particular, comprehensive reviews have recently suggested that hMT+ could benefit from top-down processing as a major means to achieve supramodal selectivity [Morrone 2010, Proulx 2012].

One crucial result of our study is that in healthy individuals, selectivity in hMT+ can significantly benefit from correlated audiovisual sensory inputs during training. By means of neurometric characterization of MEG signals in hMT+, we showed that during a short training, neural plasticity in this cortical region was only achieved in the AV group and not in the V and AVn groups. Hence, the direct compari-

son of perceptual discrimination and neurometric thresholds suggest that although all three groups performed better after training, only the AV group showed a significant change in neurometric threshold and thus conservatively displayed perceptual learning and plasticity [Goldstone 1998, Gilbert 2001, Fahle 2005, Seitz 2005a]. This observation is particularly relevant in complementing a recent discussion on the interpretation of psychometric thresholds in perceptual learning studies [Gold 2013].

Additional analyses conducted on the datasets obtained during training will shed light on the specific contribution of auditory information during audiovisual processing and the integrative mechanisms leading to the differentiation of the network in the multisensory trained groups. The changes in neurometric thresholds observed in hMT+ are particularly puzzling in light of recent lack of evidence for neurometric threshold or slope changes after training in this region [Gold 2010]. Below, we extend our discussion on the selective network dynamics that was shown to dissociate the three training groups and elaborate a working hypothesis on the implication of supramodal processing for the top-down fine tuning of motion coherence processing in hMT+.

5.3.3 Reverse hierarchy and supramodal processing

A more extended network of regions was seen in multisensory trained participants notably implicating pSTS, mSTS, and AC. Crucially, while activation increased in these regions in the AV group, activation decreased in these regions in the control AVn group. These areas showed no changes in the V group. This pattern of results shows that after training, identical visual stimuli are processed differently pending participants' training history even if the implication of vlPFC, ITC and V4 is preserved in all cases.

First, mSTS is characterized by a patchy organization of multisensory, auditory and visual selective neurons [Beauchamp 2004a] and has systematically been implicated in the analysis of multisensory timing with possible feedback to sensory cortices [Noesselt 2007]. In post-training data, pSTS and mSTS correlated with participants' improved coherence discrimination threshold in the AV group: one possible interpretation is that during training, mSTS processed coherent AV motion and transferred selectivity to hMT+ post-training. The modulation of hMT+ by mSTS could either enhance the salience of visual coherent motion during training [Lewis 2010] or facilitate the extraction of task-relevant features for visual processing [Sasaki 2010]. Consistent with this interpretation, no mSTS activity was seen in the V group and decreased activity was seen in the AVn group.

Crucially then, the functional role of mSTS in post-training tests was preserved even in the absence of multisensory inputs: this suggests that plasticity implicating both uni- and multi-sensory neural populations found in mSTS occurred during AV and AVn training. However, the limited spatial resolution of MEG cannot disentangle the possible contribution of different neural populations in this region during or after training.

Second, pSTS has also been classically implicated in multisensory integration (cf. chapter 4) and has recently been shown to mediate the temporal narrowing of audiovisual integration [Powers 2012]. Specifically, changes of effective connectivity between pSTS and downstream sensory regions have been reported after repeated presentations of temporally coincident audiovisual stimuli [Powers 2012]. pSTS is thus largely implicated in the temporal association of multisensory information but is also associated with the analysis of second-order visual motion [Noguchi 2005] and biological motion [Saygin 2007]. Considering that post-training response patterns in pSTS were opposite in AV and AVn, this region may play a switch role that selectively enables the communication of mSTS with the ventral visual stream (V and AV, AVn groups, respectively). It is here crucial to note that the differences solely illustrate participants' training history and not the mere presence or absence of AV stimulation.

In sum, we suggest that AV training favored supramodal computations of coherence in multisensory regions during training (mSTS) which remained engaged even in the absence of multisensory stimulation for the benefit of visual processing (hMT+) via pSTS (Fig. 5.9). Previous studies have reported activation of hMT+ to the presentation of auditory [Poirier 2005] and matched audiovisual motion [Alink 2008, Scheef 2009]; we thus extend these findings by showing a selective tuning of hMT+ response to the presentation of coherent visual motion after AV training. In light of recent connectivity measures implicating pSTS [Powers 2012], our results provide the first evidence for supramodal processing enabling reverse hierarchy of learning onto visual-specific areas [Ahissar 2004, Morrone 2010, Proulx 2012]. This scheme is consistent with the view that higher cortices may generalize learning and fine-tune downstream selectivity notably when considering the selectivity of vlPFC in all three groups [Ahissar 1997, Ahissar 2004].

5.4 Conclusions

These results suggest that the temporal structure of multisensory features can profoundly affect the analysis of sensory information and de facto implicate multisensory regions.

Importantly, our results suggest that the spatiotemporal coincidence principle [Stein 1993] is not only fundamental for supramodal processing but also critical in shaping up downstream neural selectivity of sensory areas. As such, the use of sensory features that naturally map across sensory modalities provide a first step towards understanding the representation of multisensory invariance or supramodal objects in the brain.

Practical implications of this research are foreseeable for the optimization of sensory substitution devices making use of natural cross-sensory mapping in audition, somatosensation and vision [Bach-y Rita 2003, Amedi 2007].

Part III

Scale-free analysis

Chapter 6

Scale-free properties: Definitions and applications

Contents

In the previous chapter, we analyzed the change of event-related fields further to perceptual learning. As previously said, the ERF analysis attempts to answer the question of *when* (and optionally where) the neural response evoked by a stimulus (or more generally any observable event) occurs, assuming implicitly the existence of a characteristic time scale.

When carrying out scale-free analyses, the aim is however quite different: the question is not about when, but rather *how* neural activity is *temporally organized* across all time scales. In this chapter, we first review the context and motivations of conducting scale-free analyses in neuroimaging. We present next the theoretical definition as well as an intuitive interpretation of the two main parameters estimated in scale-free analyses, namely self-similarity and multifractality. Finally, we describe the Wavelet Leader Based Multifractal formalism (WLBMF) used to estimate these parameters.

6.1 Context

The main drawback of ERF analysis is that it completely fails in characterizing brain activity in the absence of events, such as during rest or sleep. A growing body

of evidence shows indeed that spontaneous (or ongoing) brain activity plays a major role in cognitive functions, as reviewed in [Sadaghiani 2010, Papo 2013].

6.1.1 The role of brain spontaneous activity

Spontaneous activity refers to the modulation of measured brain signals that cannot be attributed to any explicit events, such as resting-state activity. Most studies using neuroimaging or electrophysiological recordings focused on task-related brain activity, considering rest as a sort of passive baseline function. However, since the discovery of a default mode network (DMN) whose activity systematically increased at rest and decreased during task [Raichle 2001], spontaneous activity gained importance for the understanding of brain function [Gusnard 2001] and became an intensive research topic in neuroscience and brain neuroimaging. In addition, it was argued that 95% of the energy spent by the brain is dedicated to maintaining spontaneous brain activity [Fox 2007]. This led to the analysis of resting-state networks (RSNs) revealed by BOLD functional connectivity in the low frequency range of approximately 0.01–0.1 Hz by using mainly methods such as (model-driven) seed-based correlation analysis (SCA) and (data-driven) spatial independent component analysis (ICA) [Cole 2010]. For instance, it was shown that the dorsal (DAN) and ventral attention networks (involved respectively in endogenous and exogenous control of attention) were constantly present in brain activity, even in the absence of stimuli [Fox 2006]. Another study showed variations of the functional connectivity between visual and frontal areas in resting-state following a visual task according to the stimuli used (faces or complex scenes) [Stevens 2010].

However, the relative stability of RSNs across cognitive states (task, sleep, anesthesia...) and their similarity with anatomical networks can be taken as an argument to claim that RSNs are nothing else than physiological markers of anatomical connections or neurovascular dynamics. This is contradicted by several studies showing evidence of a correlation between inter-individual differences of performance and the corresponding degree of functional connectivity [Martin 2012]. For instance, the covariance structure of spontaneous activity at rest was modified after visual perceptual learning in networks implicated in the task (i.e. the DAN, DMN and visual area) accordingly to the individual behavioral improvements [Lewis 2009]. Similar results were reported using other paradigms: e.g. the detection of auditory stimuli predicted by the level of activity in the DAN, DMN and the auditory cortex [Sadaghiani 2009], memory consolidation reflected by an increase of the connectivity between the hippocampus and the lateral occipital complex [Tambini 2010], the performance of a memory task predicted by the degree of negative correlation between the DMN and the working memory network [Sala-Llonch 2012], the performance of a visual discrimination task predicted by the functional connectivity between visual and prefrontal cortices [Baldassarre 2012] and four weeks of motor skill learning accompanied by a stronger connectivity within the motor network [Ma 2011]. At the individual level, spontaneous prestimulus activity could also predict the visual motion discrimination on a trial-to-trial basis [Sapir 2005, Hesselmann 2008].

A solution to disentangle the vascular and neural mechanisms underlying the BOLD RSNs can consist of using EEG and MEG to investigate their electrophysiological correlates.

6.1.2 Oscillatory vs. non-oscillatory approaches

M/EEG data are classically decomposed into distinct oscillatory bands according to conspicuous peaks observable in their power spectrum (see Fig. 6.1). They were given names such as δ (1–3 Hz), θ (4–8 Hz), α (8–12 Hz), β (12–30 Hz) and γ ($>$ 40 Hz) and appeared to be involved in different cognitive mechanisms (e.g. slow-wave sleep for δ, memorization for θ, weariness for α, concentration for β and conscious perception for γ). Contrary to ERF/ERP analysis, this approach has the advantage to allow the characterization of electrophysiological data acquired at rest or sleep.

Although the frequencies of these oscillatory bands are much higher than the maximal frequency observable with BOLD fMRI (due to a relatively low sampling frequency), their power (or amplitude) fluctuates approximately at the same rhythm as the slow large-scale BOLD RSNs, allowing direct comparisons between these two modalities. For instance, simultaneous measures of fMRI and EEG in resting-state showed positive and negative correlations between the BOLD signal of areas associated with attentional processing and EEG β and α power respectively [Laufs 2003]. More generally, evidence of a correlation between several BOLD RSNs and EEG power variations were found in all oscillatory bands with specific couplings (e.g. the ventro-medial prefrontal cortex with γ power and the visual cortex with δ and θ powers) [Mantini 2007]. Later, DMN and DAN were estimated by carrying out SCA on the time-dependent MEG power and were similar to the networks revealed by fMRI in the range of θ, α and β bands (with the difference that MEG RSNs were less stable and varied more across different cognitive states) [de Pasquale 2010].

In line with the "segregationist" view on ongoing activity (i.e. the association of a frequency band and a spatial organization to a given functional role) [Sadaghiani 2010], several studies analyzed the connectivity of spontaneous M/EEG signals in each oscillatory band [Siegel 2012]. They reported a great variety of networks [Liu 2010] modulated by several factors such as body weight [Babiloni 2011], genders [Jausovec 2010] or Alzheimer's disease [Stam 2006]. Recent findings show however that these oscillatory bands are not functionally independent but are rather well organized via phase-amplitude cross-frequency couplings, leading to the notion of an oscillatory hierarchy or nested frequencies [Buzsáki 2004, Lakatos 2005, Gireesh 2008, He 2010, Miller 2010]. More precisely, the phase of very slow fluctuations seems to drive the amplitude of higher frequency oscillations [Monto 2008].

It can be asked then whether the oscillatory approach is not too simplistic as it completely overlooks the major part of neural activity that fluctuates very slowly ($<\sim$ 1 Hz) in an arrhythmic manner [Bullock 2003, Freeman 2009]. Interestingly, the temporal dynamics of this *infraslow* activity (also named *slow cortical potential*)

measured with electrocorticography (ECoG) correlate with those of spontaneous BOLD fluctuations [He 2008, He 2009]. Both of them are characterized by a power-law (or $1/f$-type) power spectrum $\Gamma(f) \sim C|f|^{-\beta}$ [Novikov 1997, Bullmore 2004, He 2010] that indicates *self-similar* (i.e. *scale-free* or *fractal*) temporal dynamics [Keshner 1982] according to the following property:

$$\frac{\Gamma(f_2)}{\Gamma(f_1)} \sim \Gamma(\frac{f_2}{f_1}), \qquad \forall f_1, f_2.$$

As it can be seen on Fig. 6.1, the $1/f$ characteristic of the infraslow activity appears as a linear slope in the log-scale power spectrum. In the time domain, it means that M/EEG signals filtered in the very low frequencies cannot be statistically differentiated from their rescaled dilated version (in limited scale ranges depending on the extent of the $1/f$ — here less than 1 Hz). This can be intuitively explained by the fact that a dilation in the time domain corresponds to a contraction in the frequency domain.

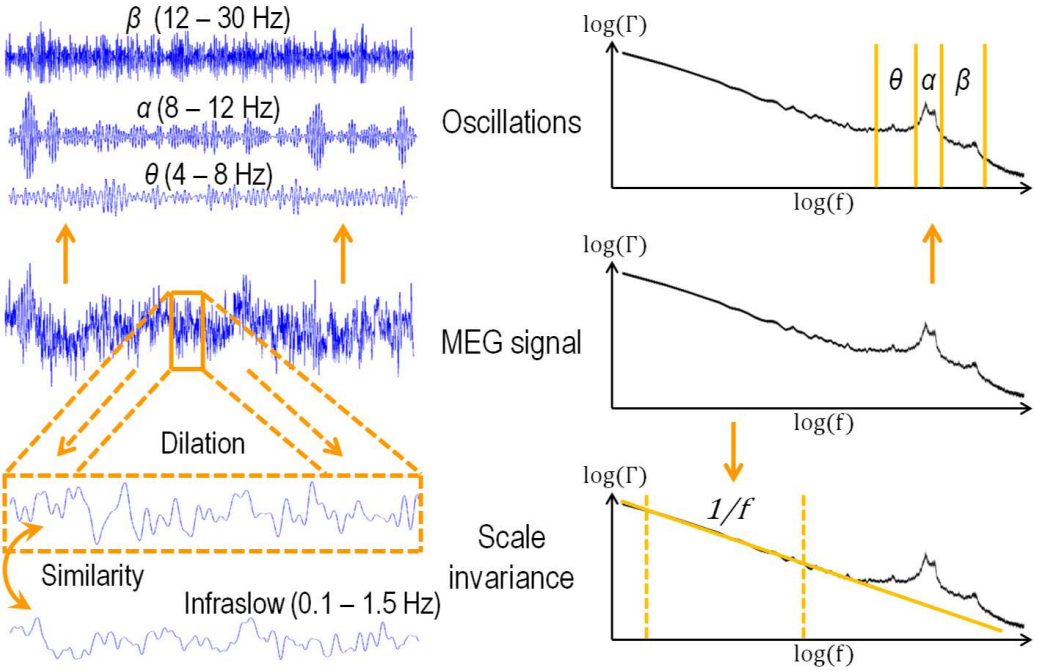

Figure 6.1: Oscillations vs. scale invariance. A typical MEG signal in time and frequency domains (*middle left* and *right*) is usually decomposed into oscillations (*top left*) whose peaks are prominent on the power spectrum (*top right*) — here theta (θ), alpha (α) and beta (β). Less conspicuous however, the power in the infraslow domain presents a $1/f$ characteristic that corresponds to a linear slope on the log-scale power spectrum (*bottom right*). As it can be seen in time domain (*bottom left*), it means that this arrhythmic activity is scale invariant, i.e. it shares the same statistical properties with its rescaled dilated version.

This property is actually very ubiquitous in dynamic systems (fully developed turbulence, internet traffic, earthquakes, stock market exchange, ...) [He 2010]. In the context of brain imaging, fractal dynamics were initially attributed to the intrinsic $1/f$ electronic device noise and was systematically removed by high-pass filtering or normalization of M/EEG data. This assumption became however less certain as a growing body of evidence showed variations of this property as a function of different cognitive states including rest- versus task-related activity [He 2011, Ciuciu 2012], stages of sleep [Leistedt 2007, Weiss 2009, He 2010], task performance [Buiatti 2007, Wink 2008, Monto 2008], awareness [Tagliazucchi 2013], ages [Suckling 2008, Smit 2011] or genders [Jausovec 2010, Ahmadi 2013] and pathologies (Alzheimer's diseases [Maxim 2005, Montez 2009, Gomez 2009], epilepsy [Kannathal 2005, Serletis 2012], alcoholism [Kannathal 2005] and anxiety [Tolkunov 2010]), suggesting plausible neurophysiological origins.

It is worth noting that the amplitude fluctuations within each oscillatory band also present self-similar properties [Linkenkaer-Hansen 2001, Stam 2004, Hardstone 2012] and have been recently correlated to the power law observed in behavior [Palva 2013]. Another scaling behavior was found in the EEG microstates (fluctuating at ~ 10 Hz) and correlated with the dynamics of fMRI RSNs [Van de Ville 2010]. There are hence different scaling behaviors that all appear functionally relevant but the link between them is still unclear. Nevertheless, global scale-free activity appears to provide a functionally relevant description of brain organization across different temporal and anatomical scales [Werner 2008].

6.1.3 The origin of the neural $1/f$

The arrhythmic infraslow activity comes from long-lasting excitatory post-synaptic potentials in superficial layers that spread over a large spatial extent, explaining the observation of long-range brain networks [He 2009].

The origin of its $1/f$-type spectrum remains however controversial [Buzsaki 2012]. For instance, scale-free properties are often associated with the concept of self-organized criticality [Bak 1987, Linkenkaer-Hansen 2001, Werner 2008, Chialvo 2010], a general model introduced in physics that generates spatial self-similarity coupled with temporal $1/f$ "noise" [Bak 1988]. A system with such dynamic is trapped into a state of highest susceptibility, where any single perturbation (at the level of a neuron for the brain) has a very small (yet non-null) chance to propagate through non-linear interactions towards larger scales (i.e. populations of neurons) and finally modify the entire system state. This phenomenon has been observed through neuronal avalanches [Beggs 2003, Plenz 2007, Petermann 2009, Klaus 2011] of which size and lifetime followed both an inverse power law. On a larger scale, both the topological properties and the temporal dynamics of RSNs extracted from resting-state fMRI time series present scale-free properties. Moreover, self-organized criticality has been replicated in neuronal models assuming dynamical synapses [Levina 2007] or taking into account brain plasticity and adaptation [de Arcangelis 2006, Drew 2006, de Arcangelis 2010]. Another neural net-

work model proposed by [Poil 2012] was also able to generate scale-free dynamics of avalanches and oscillations similar to the human alpha waves. In the graph theory, self-organized criticality was associated with the small-world topology of brain networks [Bassett 2006, Bullmore 2009] and its low metabolic cost [Bullmore 2012].

In strong opposition to this view, other studies have shown that scaling in local field potentials do not originate from spike avalanches [Dehghani 2012, Baranauskas 2012] and rather suggested that the $1/f$ noise results from the frequency filtering of extra-cellular currents (i.e. ionic diffusion) [Bédard 2009]. By far, there is no compelling evidence of a dependency between the scale-invariance observed in time dynamics and the power-law cluster size distribution observed in the topology of brain networks.

These two explanations do not take however in consideration the multifractality observed in some neuroimaging studies, another scale-free property of brain temporal dynamics (see section 6.3). A more general model of self-organized criticality would be hence necessary [Aschwanden 2013].

6.2 Self-similarity

6.2.1 Definition

Scale-free essentially implies that the statistical properties of a signal $X(t)_{,t>0}$ remain unchanged after time dilation and proper rescaling. With the specific self-similar modeling of scale-free dynamics, the proper rescaling is assumed to depend on a single parameter $H > 0$ (often referred to *self-similarity parameter*, and sometimes as the *Hurst exponent*):

$$X(t) \overset{d}{=} a^{-H} X(at), \qquad \forall a > 0,\ \forall t > 0 \tag{6.1}$$

where $\overset{d}{=}$ stands for equality in distribution. The equation (6.1) can be reformulated in terms of statistical moments of $X(t)$ and by setting $a = \frac{1}{t}$:

$$\mathbb{E}|X(t)|^q = |t|^{qH} \mathbb{E}|X(1)|^q, \qquad \forall t > 0,\ \forall q : \mathbb{E}|X(t)|^q < +\infty. \tag{6.2}$$

Equation (6.2) means that each (finite) statistical moment varies with the number of samples according to a power law whose exponent is linearly related to the q^{th} order. Another consequence is that self-similar processes are necessarily non-stationary, which complicates their analysis. However, their increments $Y(n) = X(n+1) - X(n)_{,n\geq 0}$ remain stationary: the most simple and representative one is the fractional Brownian motion (fBm), whose increment process corresponds to a stationary fractional Gaussian noise (fGn). In that case, the Hurst exponent H characterizes both processes and is strictly comprised between 0 and 1. H is associated with the notion of self-similarity for an fBm and with the notion of long or short range dependence for an fGN. The latter notion comes from the auto-covariance function of the fGn (correctly defined since it is stationary) which

decreases as a power law for large lag τ:

$$\rho_Y(\tau) = \mathbb{E}Y(n+\tau)Y(n) \sim \tau^{-\gamma}, \qquad \tau \to +\infty,\ \gamma \in [0,2]. \tag{6.3}$$

The equation (6.3) means that it is not possible to define a characteristic time-scale τ_0 beyond which correlations cancel out (contrary to the usual and traditional modeling of exponential decreases). The parameters H and γ are linearly related by the relation $H = 1 - \gamma/2$ and quantify the correlation decrease: while $H = 1/2$ indicates the absence of correlation (i.e. similar to a white Gaussian noise), $H < 1/2$ betrays negative correlation and $H > 1/2$ marks long range positive correlation also called *long memory* (i.e. what happens now will still have some influence long time after). Since the concepts of self-similarity and long-range dependence are closely related, both terms are equivalently used in practice and are often referred as "scaling".

Furthermore, the equation (6.3) can be reformulated in the frequency domain via Fourier transformation, yielding the following property of the power spectral density $\Gamma_Y(f)$ of an fGn process:

$$\Gamma_Y(f) \sim f^{-\beta}, \qquad f \to 0, \text{ where } \beta = 1 - \gamma = 2H - 1. \tag{6.4}$$

The fGn and fBm are thus characterized by a $1/f$-type power spectrum whose exponent β ranges between -1 and 1 for an fGn and between 1 and 3 for a fBm (since it is the cumulated sum of an fGn). For more details on these two processes, the reader can refer to [Samorodnitsky 1994].

The self-similarity paradigm often amounts to modeling time series in a dichotomous manner either as fGn or as fBm. This point of view is however not necessary. The fGn and fBm processes can be considered as the outputs of a fractional integration (of parameter $H - \frac{1}{2}$ and $H + \frac{1}{2}$ respectively) of a white (i.e. delta-correlated) Gaussian process. The sole parameter H governs the entire covariance structure and thus, with Gaussianity, completely defines fGn and fBm. With no more need of distinction between fGn and fBm, their classical definition implying two distinctive Hurst exponents with $0 < H < 1$ can be theoretically extended to a single $H \geq 1$ (with the recourse of the notions of generalized processes and tempered distributions [Samorodnitsky 1994]), while preserving the original intuition: the larger H, the more long term the covariance is and thus the more structured the process is. This is in line with the intuitive approach that self-similarity reflects the global regularity of a signal: as H increases (from 0.2 to 1.8), the signal becomes smoother (see Fig. 6.2).

6.2.2 Estimation methods

In practice, the electrophysiological signal is essentially modeled as either an fGn or an fBm (cf. the review [Eke 2002]). Several methods have been developed to assess the Hurst exponent H directly or via other fractal measures such as the $1/f$ slope β or the fractal dimension D, in either time or frequency domains.

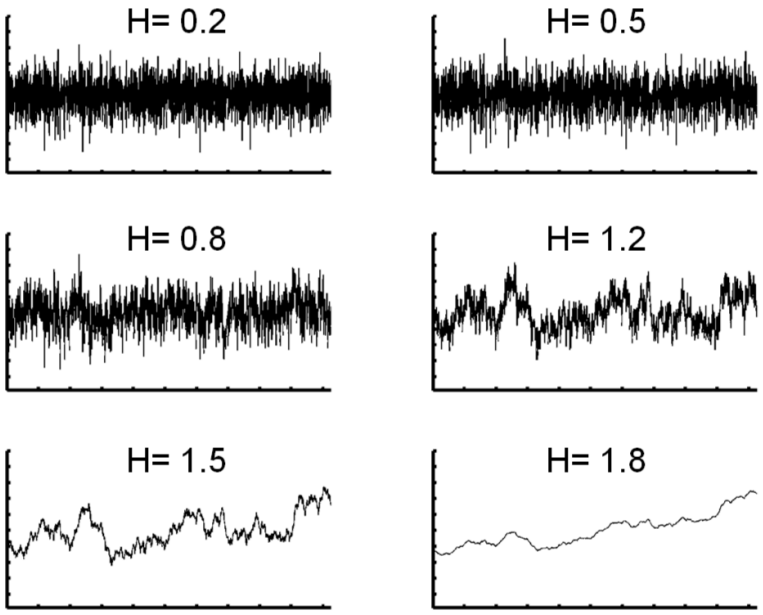

Figure 6.2: Example of a signal with increasing self-similarity. Time courses of a same signal for different values of H (extended definition allowing $H \geq 1$). They were synthesized by using the circulant embedded method [Dietrich 1997] with the same seed generator and normalized to unit variance. H starts at 0.2 (i.e. short memory fGn) and ends at 1.8 (i.e. long memory fBm). Note that $H = 0.5$ corresponds to a white Gaussian noise and $H = 1.5$ corresponds to Brownian motion. Importantly, as H increases, the signal becomes smoother.

Estimation of the β slope in power spectrum. One of the most simple methods is to use standard spectrum estimation such as the windowed-averaged Welch's periodogram $\Gamma_{\text{Welch}}(f)$ of a signal X:

$$\begin{aligned} &\Gamma_{\text{Welch}}(f) = \tfrac{1}{n}\textstyle\sum_{k=1}^{n} \hat{\Gamma}_X(f,k), \\ &\text{with } \hat{\Gamma}_X(f,k) = |\textstyle\sum_{p=1}^{t_k - t_{k-1}} w(p) X(t_{k-1}+p) \mathrm{e}^{-2\pi f p}|^2, \end{aligned} \tag{6.5}$$

where $w(p)$ is a window function (such as Hamming's window) and the set $\{t_k\}_{k=0..n}$ defines the boundaries of n (possibly overlapped) segments into which the original signal is split up. The exponent β is then estimated by fitting a regression line on the log-scale periodogram in the appropriate scaling range (i.e. in the frequency range of the power law). The performance of this method is however very weak since it assumes the signal to be stationary and it does not assess directly H. In addition, it has been shown that the high-frequency part of the spectrum often deviates from a pure $1/f^{\beta}$ [Eke 2002].

This method is still very useful to identify the presence of scaling in data and the frequency (or scale) range where this property holds and has been applied in some neuroimaging [Novikov 1997, Tolkunov 2010] and cognitive [Gilden 1995, Clayton 1997] studies.

Autocorrelation Analysis. The autocorrelation function $c(\tau)$ of an fGn as a function of lag τ is given by:

$$c(\tau) = \frac{1}{2}(|\tau+1|^{2H} - 2|\tau|^{2H} + |\tau-1|^{2H}).$$

Note that for an fBm, the definition must be extended to a time-dependent function $c(t,\tau)$ since that process is non-stationary. H can be then estimated by fitting this theoretical function to the estimated autocorrelation of the signal $X(k)$:

$$\hat{c}(k) = \frac{\frac{1}{N-k-1}\sum_{i=k+1}^{N}(X(i)-\hat{\mu})(X(i-k)-\hat{\mu})}{\frac{1}{N-1}\sum_{i=1}^{N}(X(i)-\hat{\mu})^2}, \qquad \text{with } \hat{\mu} = \frac{1}{N}\sum_{i=1}^{N} X(i),$$

where N is the number of data samples. In practice, the autocorrelation analysis does not use all the lags for estimating H but only the first ones since the values are very close to zero for longer lags, making the estimation less statistically reliable. This is a major inconvenience for the estimation of H, which is usually done in a very low frequency range.

Detrended Fluctuation Analysis (DFA). Introduced by Peng and colleagues in 1994 [Peng 1994] to study the long-range correlation in DNA sequences, DFA has become one of the most popular methods to assess self-similarity in physiological data and more particularly in brain signals (see for instance [Linkenkaer-Hansen 2001, Goldberger 2002, Buiatti 2007, Monto 2008,

Montez 2009, He 2011, Palva 2013, Tagliazucchi 2013] and the review dedicated to it [Hardstone 2012]).

This analysis exploits the relation (6.2) at the 2^{nd} order of the statistical moment indicating that the fluctuations of the signal (i.e. the standard deviation) should follow a power law as a function of the number of samples. Before calculating the standard deviation at a given scale, the linear trend is removed in order to make the analysis less sensitive to false correlation induced by trends persisting over longer time-scales.

In practice, the signal $X(k)$ is first summed ($Y(k) = \sum_{i=1}^{k} X(k)$) and next split into K consecutive segments (generally with 50% overlap) of equal size L. On the i^{th} segment, the linear trend $Y_i^{\text{trend}}(k)$ is removed using a least-square fit and the variance $\sigma_{L,i}^2$ of the detrended data segment is estimated. The fluctuation function $\langle F(L) \rangle$ is then defined as the root mean square of the mean variance over all identically L-sized detrended data segments and follows a power law:

$$\langle F(L) \rangle^2 = \frac{1}{K} \sum_{i=1}^{K} \sigma_{L,i}^2 \sim L^{\alpha}.$$

After estimating this quantity for different sizes L (generally spaced on a logarithmic scale), the DFA exponent α is derived from the linear regression when plotting $\log\langle F(L) \rangle$ versus $\log L$. In its extended definition, the Hurst exponent H can be simply assimilated to the DFA exponent α. Otherwise, the signal is modeled by a fGn for $0 < \alpha < 1$ (and $H = \alpha$) and by a fBm for $1 < \alpha < 2$ (and $H = \alpha - 1$).

This method is essentially used in M/EEG to characterize the amplitude fluctuations of neuronal oscillations: after band-pass filtering the data in a frequency band of interest, DFA is usually applied to the amplitude envelope extracted with the Hilbert transform.

Coarse Graining Spectra Analysis (CGSA). This method aims to estimate the spectral exponent β in the power spectrum by separating first the fractal and oscillatory components. The basic idea is to exploit the equation (6.1) in the spectral domain: since a fractal signal X is equal in distribution with its version $a^{-h}X_a$ (i.e. dilated by a factor a and rescaled by a^{-H}), their cross-power spectrum $a^{-H}S_{XX_a}$ should be identical to the power spectrum S_{XX} of the original signal. In contrast, if the signal only contains harmonics, the cross-power spectrum would be considerably reduced and close to 0.

A convenient way to compute the power spectrum of the fractal part of the signal without prior estimation of the Hurst exponent H consists of computing the quantity:

$$P(f) = \sqrt{S_{XX_a} S_{XX_{1/a}}}.$$

The β slope (and consequently H) is then derived from this power spectrum.

6.3 Multifractality

All the series analysis tools presented in the previous section are known to significantly lack robustness in disentangling true scaling phenomena from non-stationary drifts or in accurately estimating H when drifts are superimposed to actual scale-free properties. In addition, their statistical estimation performance significantly decreases when analyzed data are non Gaussian [Veitch 1999]. The non-Gaussianity has another important consequence: the scale-free temporal dynamics in data may exhibit a more complex behavior than self-similarity, namely multifractality.

6.3.1 Definition

Multifractality can be read as a model for scale-free temporal dynamics that encompasses and enriches strict self-similarity, in so far as it enables to account for local fluctuations — or singularities — along time that cannot be measured in the sole power spectrum. The relation (6.2) is reformulated in a more general manner:

$$\mathbb{E}|X(t)|^q = |t|^{\zeta(q)}\mathbb{E}|X(1)|^q, \qquad \forall t > 0,\ \forall q : \mathbb{E}|X(t)|^q < +\infty, \tag{6.6}$$

where $\zeta(q)$ is called the scaling function (see Fig. 6.3). In the absence of multifractality, this function is linear ($\zeta(q) = qH$, see equation (6.2)) and hence fully characterized by a unique parameter H. This is why there is neither interest nor benefit to analyze data at statistical order other than 2. This also implies that Gaussian processes cannot be multifractal.

In presence of multifractality however, the function $\zeta(q)$ is no more linear but concave and its complete description requires the use of all (finite) statistical orders (including negative and fractional orders). The characterization of the process is hence represented by a whole collection of parameters.

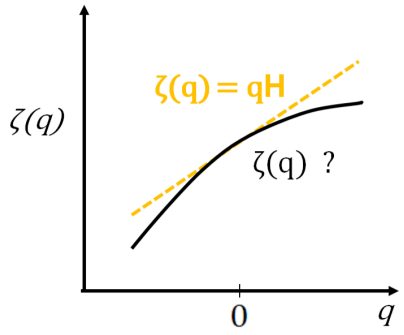

Figure 6.3: Scaling function with or without multifractality. In the absence of multifractality (i.e. for monofractal processes), the scaling function $\zeta(q)$ (*in orange*) varies linearly with the statistical moment q and proportionally to the Hurst exponent H. The knowledge of H is thus sufficient to know $\zeta(q)$. However, in presence of multifractality (*black curve*), the function $\zeta(q)$ is no more linear and must be estimated for each statistical moment.

These parameters are related to the fluctuations along time of the local regularity of a signal $X(t)$ measured by the so-called *Hölder exponents* $h(t)$. They are defined as the largest positive exponents α such that the local variations of $X(t)$ around t_0 can be compared to a local power law behavior:

$$|X(t) - X(t_0)| \leq |t - t_0|^{\alpha}.$$

the Hölder exponents are particularly interesting to study and quantify singularities, i.e. local points that do not allow taking a derivative. Intuitively, they give a much finer account of the local regularity of a function than the usual notions of continuity and differentiability.

Since describing the collection of Hölder exponents h as a function $h(t)$ over time would result in tracing a completely meaningless and discontinuous curve, is is often given in the form of a *multifractal spectrum* (Fig. 6.4) that can be interpreted as a sort of histogram. More precisely, the multifractal spectrum maps to each value h the Hausdorff dimension $D(h)$ reflecting the space-filling degree of the set of points on the real line where the Hölder exponent equals h. In other words, singularities associated with the exponent h are almost everywhere in the signal if $D(h) = 1$ and are rarer if $D(h) < 1$. It comes that the Hölder exponent with the largest Hausdorff dimension (i.e. corresponding to the maximum of the multifractal spectrum) is the most common singularity strength and can be approximated to the Hurst exponent H of the entire series. The width of this spectrum can be associated with a measure of the amount of multifractality (hereafter referred to as M).

In practice, the multifractal spectrum $D(h)$ and the the scaling function $\zeta(q)$ are related by:

$$D(h) = \min_{q \neq 0}(1 + qh - \zeta(q)). \tag{6.7}$$

This operation is called the Legendre transform and is bijective thanks to the concavity of $\zeta(q)$. This relation allows to interpret the typical concave shape of multifractal spectra in terms of statistical moments q [Aschwanden 2013]: the left leg describes the fewer, larger amplitude events, which correspond to large positive q, whereas the right leg reflects the more common, smaller, singularities described by large negative q.

An intuitive interpretation linking the notions of self-similarity and multifractality is illustrated in Fig. 6.4. It consists of considering multifractality as local fluctuations over time around the global $1/f$ slope associated with the Hurst exponent. Imagine you can estimate the power spectrum at each time point perfectly. Self-similarity would correspond to the global $1/f$ slope averaged over all time points while multifractality would coarsely reflect its variance. These fluctuations are however not random but present a structured pattern over time that appears on the multifractal spectrum (their Hausdorff dimension would be null otherwise).

The most commonly used models generating multifractal dynamics belong to the family of multiplicative cascade processes, among which the multifractal random walk (MRW). This non-Gaussian process with stationary increments is defined as

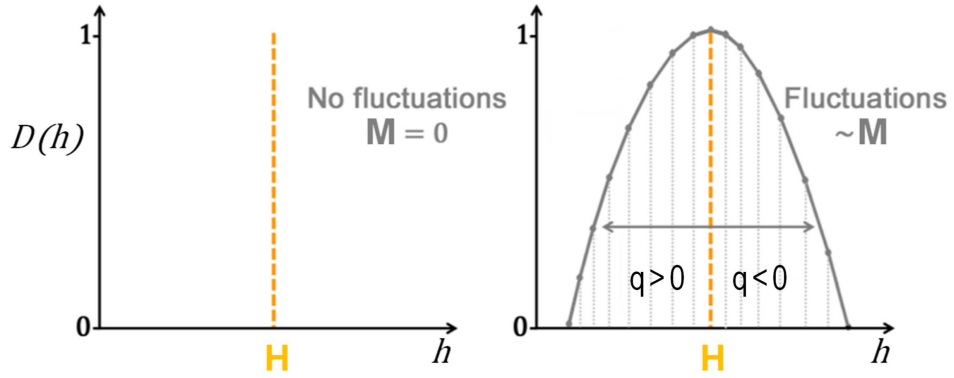

Figure 6.4: Multifractal spectra with or without local fluctuations. Multifractal spectra reveal the distribution of Hölder exponents h (abscissa) in the signal by indicating their associated Hausdorff dimension $D(h)$ (ordinate). In the absence of multifractality (left), the multifractal spectrum shows a single Hölder exponent H named Hurst exponent. Local fluctuations over time around this exponent changes the spectrum into a concave curve (right) whose broadness corresponds to the amount of multifractality M.

the fractional integration (of parameter $H - \frac{1}{2}$) of the product of a white (i.e., delta-correlated) Gaussian noise with the exponential of another independent process whose covariance is controlled in amplitude by M and decreases logarithmically slowly [Bacry 2001]. The multifractal framework can thus be read as an extension of fGn to an MRW. Parameter H keeps the intuitive interpretation of global and overall dependence and structure for the process, while the added parameter M permits to induce departure from Gaussianity and local fluctuations in time of the regularity of the signal (cf. Fig. 6.5).

6.3.2 Estimation methods

The following methods presented here were all applied in the field of medical signal analysis (see for instance the review of [Lopes 2009]) and can all be used to assess not only self-similarity, but also multifractality. The parameter M is usually defined as the full width at half maximum of the estimated multifractal spectrum.

Box-counting. The box-counting method is generally used to compute the fractal dimension D of a spatial object but it can be applied to a time series by considering it as a two-dimensional picture. It consists of covering a binary image by a series of grids of decreasing size r (the boxes) and to attribute a normal measure $M_i(r)$ to each box indexed by i.

If only self-similarity is to be assessed, the measure is simply a binary value (1 if the signal is contained in the box, 0 otherwise). In that case, the so-called *capacity*

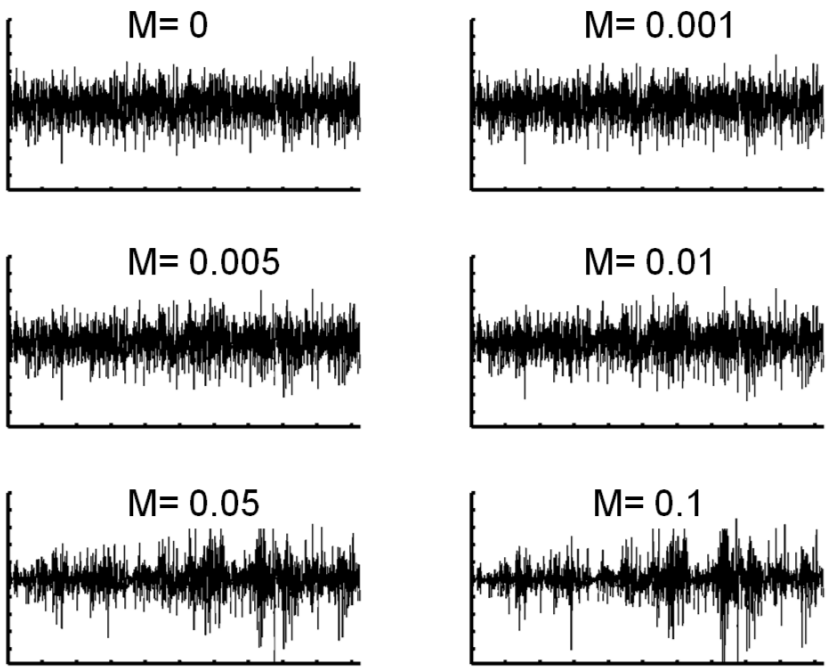

Figure 6.5: Example of a signal with increasing multifractality. Time courses of a same multifractal random walk (MRW) [Bacry 2001] with constant self-similarity parameter $H = 0.5$ and different values of M. They were synthesized with the same seed generator and normalized to unit variance. Initially, the signal corresponds to a white Gaussian noise ($M = 0$). Multifractality appears as local fluctuations over time that induce departure from Gaussianity and that cannot be observed in the power spectrum. Note that M values usually range around 0.01–0.02 in real-world data. Extreme values such as $M \gg 0.1$ would likely be the results of non-stationary artifacts in electrophysiological data.

dimension D_c is given by:

$$D_c = -\lim_{r\to 0} \frac{\log(\sum_i M_i(r))}{\log(r)}.$$

The Hurst exponent is then given by $H = 2 - D_c$. This method was used for instance on consecutive EEG data segments to localize epileptic seizures in time as a function of a time-varying piecewise H [Accardo 1997].

The extended analysis to multifractality requires a more detailed measure such as the proportion of pixels contained in each box in order to assess the generalized fractal dimension $D(q)$ from which the multifractal spectrum can be further derived [Chhabra 1989]:

$$D(q) = -\frac{1}{1-q}\lim_{r\to 0} \frac{\log(\sum_i |M_i(r)|^q)}{\log(r)}, \quad \text{and } D(1) = -\lim_{r\to 0} \frac{\sum_i M_i(r)\log(M_i(r))}{\log(r)}.$$

It is worth noting that the capacity dimension corresponds to the generalized fractal dimension for $q = 0$. This method is however very sensitive to the grid position, especially for negative values of q. A first solution can be to relocate randomly the grid at each iteration of box size r.

Multifractal Detrended Fluctuation Analysis (MDFA). This method [Kantelhardt 2002] is an extended version of DFA and is identical in the first steps to the procedure described in section 6.2.2. This time, the fluctuation function $F_q(L)$ is calculated for different orders q:

$$F_q(L)^q = \frac{1}{M}\sum_{i=1}^{M} \sigma_{L,i}^q.$$

It can be seen that standard DFA is obtained for $q = 2$. MDFA consists of analyzing the scaling behavior at each order q by linearly regressing $\log F_q(L)$ versus $\log L$ under the assumption that $F_q(L) \sim L^{\zeta(q)}$. While the MDFA yields similar performance than WLBMF (see next section) and WTMM [Kantelhardt 2002] on numerical simulations, they can give very different results on real-world data; MDFA seems indeed more adapted to detect the fractality of an fBm [Figliola 2010].

Wavelet Transform Modulus Maxima (WTMM). This method is one of the most used to assess multifractality in physiological signals [Ivanov 1999, Goldberger 2002, Shimizu 2004, Wink 2008, Suckling 2008, Popivanov 2006, Serletis 2012]. It relies on the continuous wavelet transform by using the second derivative of the Gaussian function as mother wavelet (see appendix B for more details on wavelets). After computing the continuous wavelet coefficients $C_X(a,t)$ of the time series $X(t)$ at times t and scales a, a "skeleton" of L maxima lines along scales is extracted. This is done by connecting each local maximum of $|C_X(a,t)|$ at scale a to the temporally closest maxima at scales $a-1$. The greatest value $|C_{sup}(k)|$ encountered along the k^{th} maxima line is subsequently

collected and the following partition function $Z(a,q)$ of order q at scale a is then calculated:

$$Z(a,q) = \sum_{k=1}^{L} |C_{sup}(k)|^q \sim a^{\zeta(q)-1}.$$

The multifractal spectrum can then be obtained from the Legendre transform of $\zeta(q)$. The relatively high computation cost of this method (due to the computation of continuous wavelets and maxima lines) usually constraints its use to the analysis of 1D signals only, which is not the case for the WLBMF (that uses discrete wavelets).

6.4 The Wavelet-Leader Based Multifractal Formalism (WLBMF)

The wavelet-leader based multifractal formalism (WLBMF) [Wendt 2007] has been recently shown to provide practitioners with a fast, theoretically efficient and practically robust framework for multifractality assessment in real-world data and has been recently used in neuroimaging studies to assess multifractality [Ciuciu 2008, Van de Ville 2010, Ciuciu 2012].

Let $X(t)$ be a time series and N_Ψ the number of vanishing moments of the Daubechies mother wavelet $\Psi_0(t)$ (cf. Appendix B). By analogy with the 2^{nd} order power spectrum defined in the frequency domain, the so-called structure functions of the q^{th} statistical order (including negative and fractional orders) at the scale j are defined as:

$$S_X(j,q) = \frac{1}{n_j} \sum_{k=1}^{n_j} |d_X(j,k)|^q, \tag{6.8}$$

where n_j is the number of discrete wavelet coefficients $d_X(j,k)$ available at scale j. It has been shown [Jaffard 2006] that such estimators reproduce accurately the scale-free properties of X:

$$S_X(j,q) \approx F_q 2^{j\zeta(q)}, \tag{6.9}$$

where F_q is a strictly positive constant dependent of q. The estimation of the structure functions leads hence to the knowledge of $\zeta(q)$ and further to the multifractal spectrum $D(h)$ through a Legendre transform. The concave shape of $\zeta(q)$ enables us to write its polynomial expansion around its maximum:

$$\zeta(q) = \sum_{p=1}^{\infty} c_p (\frac{q^p}{p!}). \tag{6.10}$$

The coefficients c_p are called *log-cumulants*. A meaningful interpretation of these log-cumulants can be found from the expansion of the multifractal spectrum $D(h)$ derived from equations (6.10) and (6.7):

$$D(h) = 1 + \frac{c_2}{2!}\left(\frac{h-c_1}{c_2}\right)^2 + \frac{-c_3}{3!}\left(\frac{h-c_1}{c_2}\right)^3 + \frac{-c_4 + \frac{3c_3^2}{c_2}}{4!}\left(\frac{h-c_1}{c_2}\right)^4 + ... \tag{6.11}$$

The four first log-cumulants give then a relevant approximation on the concave shape of $D(h)$. Firstly, the coefficient c_1 characterizes the location of its maximum and can be thus assimilated to the Hurst exponent H that measures self-similarity in monofractal processes (cf. Fig. 6.4). Though not rigorously exact, this correspondence sufficiently holds for the analysis of most real-world data [Wendt 2007, Ciuciu 2008]. Secondly, the coefficient c_2 corresponds to the width of the spectrum (i.e. the curvature of $\zeta(q)$) and captures hence multifractality (for monofractals $c_2 = 0$). Because c_2 is by definition negative, we can set $M = -c_2$ to manipulate only positive values. Thirdly, the degree of symmetry of the curve (i.e. skewness) is indicated by c_3 and reflects the degree of inhomogeneity between rarer large amplitude ($q > 0$) and more common, small amplitude, singularities ($q < 0$). Finally, the expression $c_4 - \frac{3c_3^2}{c_2}$ gives information on the flatness of the curve (i.e. similarly to kurtosis). In practice, the expansion is often truncated to the second order yielding only c_1 and c_2 (hence H and M).

The coefficients c_p are related to the cumulants $C_X(j,p)$ of order p of the variable $\ln|d_X(j,.)|$ by the following relation:

$$C_X(j,p) = c_{0,p} + c_p \ln 2^j.$$

Therefore, c_p can be estimated by means of linear regressions in $\ln 2^j$ versus $C_X(j,p)$, where the estimates $\hat{C}_X(j,p)$ are obtained from standard cumulant estimators [Kendall 1977]:

$$\hat{C}_X(j,p) = \hat{m}_{j,p} - \sum_{n=1}^{p-1} \binom{p-1}{n-1} \hat{C}_X(j,n)\hat{m}_{j,n-k}, \qquad \text{with } \hat{m}_{j,p} = \frac{1}{n_j}\sum_{k=1}^{nj} \ln|d_X(j,k)|^p.$$

Last but not least, this method can be considerably improved by replacing the discrete wavelet coefficients $d_X(j,k)$ by the so-called *wavelet leaders* $L_X(j,k)$, defined as the local suprema of discrete wavelet coefficients within a local neighborhood and over all finer scales (Fig. 6.6):

$$L_X(j,k) = \sup_{\substack{j' \le j \\ k' \in \lambda_{j'}}} |d_X(j',k')|, \qquad \text{where } \lambda_{j'} = \lfloor (k-2)2^{j-j'}+1,\ (k+1)2^{j-j'} \rfloor. \quad (6.12)$$

It has been indeed demonstrated that multifractal attributes are correctly estimated using wavelet leaders rather than wavelet coefficients [Wendt 2007]. In addition, WLBMF is complemented by a non-parametric time-scale bootstrap procedure that enables the construction of confidence intervals and hypothesis tests (such as $c_2 < 0$ or $M > 0$ for testing the presence of multifractality).

An important prerequisite for multifractal analysis is to identify the range of scales (or frequencies) over which the linear fits will be carried out. This can be done by a first inspection on the log-scaled power spectrum or equivalently a wavelet-based spectrum (called log-scale diagram) to verify the presence of a power law. The quality of the linear regression can be further supported by the bootstrap confidence intervals.

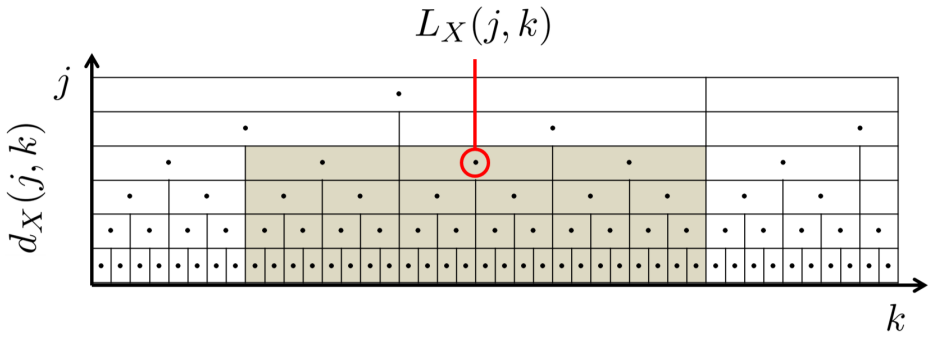

Figure 6.6: Definition of wavelet leaders. The wavelet leader $L_X(j,k)$ at scale j and position k on a dyadic grid is defined as the largest wavelet coefficient $L_X(j,k)$ within a local time neighborhood and at all finer scales (gray shaded area).

The number of vanishing moments N_Ψ is also an issue: on the one hand, it should be theoretically large enough to stabilize the estimates of the function structures $\zeta(q)$ of negative order ($q < 0$) while on the other hand, a too large value of N_Ψ can degrade the accuracy of the estimation due to larger border effects [Wendt 2009a]. A reasonable solution is to choose the smallest $N_\Psi > h_{\max}$ (where $h_{\max}$ is the maximal Hölder exponent present in the multifractal spectrum) such that the multifractal estimates do not vary much if N_Ψ increases.

Another important point is that this analysis is only adapted for bounded functions, i.e. with positive minimal regularity. In other words, the minimal Hölder exponent $h_{\min}$ with a non-null Hausdorff dimension in the multifractal spectrum must be strictly positive. A solution is to integrate the data at an order γ sufficiently high (i.e. $\gamma > h_{\min}$) to make $h_{\min}$ positive. In practice for MEG data, $h_{\min}$ was sometimes comprised between -1 and 0. The signals were hence systematically integrated once.

Chapter 7

Scale-free analysis of acquired MEG data

Contents

In the previous chapter, we presented the context and motivations of conducting scale-free analyses in neuroimaging as well as the methods to estimate the parameters of self-similarity (denoted by H) and multifractality (denoted by M) in time

series. As previously said, the multifractal properties of MEG infraslow activity during rest and task have been scarcely addressed. By analyzing the data acquired during the learning paradigm (cf. chapter 1) with the wavelet-leader based multifractal formalism (WLBMF), we asked whether multifractality and self-similarity can bring functionally independent information regarding the neural processes implicated in learning and plasticity.

For all these analyses, WLBMF was always carried out on the integrated time series using a Daubechies mother wavelet with 3 vanishing moments and within a restricted scale range (j = 9–14 in the first study and j =10–14 in the next ones, corresponding respectively to $f \approx 0.1$–3 Hz and $f \approx 0.1$–1.5 Hz). Moreover, only data from the V and AV groups were used here for the main reasons that i) AVn data were acquired much later as a control group for the ERF analysis 2) although increasing the statistical power, they would also reduce the effect of learning since it was the less effective training. Nonetheless, we briefly propose a comparison of the three trainings in the section discussion of the main analysis.

The first section presents two preliminary studies. In the first one, we verified that MEG signals in sensor space possess indeed scale-free properties and asked if differences could be already observed between rest- and task-related activities. At the sensor level, they were statistically significant only by taking the norm of gradiometers, a property slightly deviating from behavior of standard fGn and fBm processes. In the second preliminary study, we investigated the scale-free properties of source-reconstructed MEG signals restricted to some regions of interest (ROIs) revealed by the ERF analysis (cf. chapter 5). We observed a modulation of these properties before and after learning that differed between AV and V training.

The second section is dedicated to the main study, in which we assessed the scale-free properties of MEG signals in the course of training after reconstruction over the entire cortex. Contrasting brain activity before and after learning showed intertwined modulations of self-similarity and multifractality in distinct cortical regions that were implicated in the task. Crucially, each individual's multifractality parameter converged towards an attractor value that was common to all individuals suggesting the existence of an asymptotic behavioral performance for all. In other words, this study shows that the distance of an individual's multifractality to the common attractor value predicts an individual's learning ability.

7.1 Preliminary analyses

7.1.1 Analysis in sensor space

The aim of this preliminary analysis was to investigate the presence of scaling in MEG data at the sensor level by using standard spectral estimators and the WLBMF (see section 6.4 for more details). In addition, we asked if the scale-free attributes would also vary between two cognitive states, namely rest (R) and passive viewing of visual motion (VM).

To that aim, we analyzed the data recorded during the hMT+ localizer (i.e. VM) and during the first block of rest (i.e. Rest_i, here denoted by R) without distinction between the 24 participants in V and AV groups (cf. section 1.3). For more information on the acquisition of the MEG data, the reader is referred to chapter 3, section 3.4.

Although no significant difference could be found when analyzing direction-specific gradio- or magneto-meters, statistical differences are exhibited when analyzing the norm of gradiometers. The surprising changes induced by the norm were better explained by modeling the MEG signals with multifractal random walks (MRW) than fractional Gaussian noise (fGn) and fractional Brownian motion (fBm).

7.1.1.1 Power law spectrum on MEG recordings

For each subject, each session and each sensor, we computed Welch's power spectrum estimate derived in Eq. (6.5). A representative spectrum computed by averaging all latitudinal gradiometers (grad_1) is shown in Fig. 7.1 in black and dark blue lines for the R and VM sessions, respectively. The presence of scaling or $1/f$ behaviour clearly appears as a linear slope in this *log–log* plot over the (0.1–3 Hz) frequency range. In addition, this $1/f$ power spectral density is clearly different from that measured during the empty recording (light blue line in Fig. 7.1), thus ruling out the hypothesis that the $1/f$ is simply driven by the electronic device noise. Interestingly, the power of acquisition noise is upper bounded by that measured during brain activity recordings. Finally, α- and β-band oscillations emerge during the presentation of visual motion stimuli and even more during the rest, while they do not appear in the empty recording.

As a comparison with the previous method, we also estimated the structure functions $S^d(j,q)$ for $q = 2$ only (cf. section 6.4). Structure functions at this 2^{nd} statistical order are indeed equivalent to the power spectrum while estimated using discrete wavelets. On a dyadic grid, frequencies f and scales j are related one another by $f = \frac{3}{4}\frac{f_s}{2^j}$, where f_s is the sampling frequency. The resulting wavelet-based spectrum also named log-scale diagram ($\log_2 S^d(j,2)$ vs. $\log_2 2^j = j$) averaged over all latitudinal gradiometers is shown in Fig. 7.1 where green, red and yellow lines represent respectively the R, VM and empty recordings. In contrast to Welch's periodogram $\Gamma_{\text{Welch}}(f)$, the $S^d(j,2)$ estimates are less sensitive to oscillation peaks. Discrete wavelets are thus more appropriate to analyse the $1/f$ behaviour in low frequencies. In addition, since the estimation was carried out by using the whole data length, we also verified its stability by conducing separately the same analysis on each half of the signal: the results were very similar.

This preliminary result confirmed the presence of scaling in the data, which cannot be attributed to the sensor noise. It also shows the advantage of using discrete wavelets for analyzing the $1/f$ spectrum. Although spectral analysis provides restricted information on the scale invariance properties, it allows us to determine the scale range on which the WLBMF analysis should be applied. In the following, we

analyse the multifractal properties in the scale range $[j_m, j_M] = [9, 14]$ (i.e. in the frequency range 0.1–3 Hz), since the log-scale diagram is linear in this part.

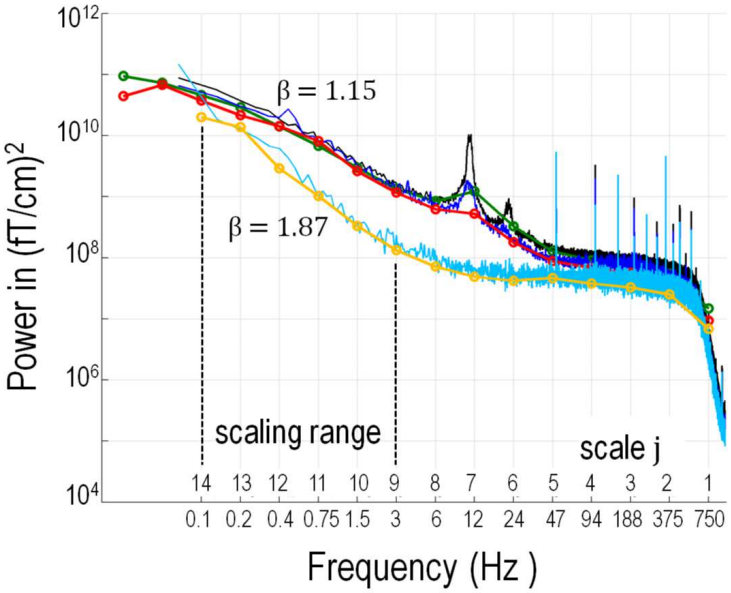

Figure 7.1: Log–log plot of spectrum estimates averaged across all latitudinal planar gradiometers. Welch's periodograms are plotted in black (R), dark blue (VM) and light blue (Empty). Wavelet-based estimates are plotted in green (R), red (VM) and yellow (Empty). Scaling can be observed in the scale range of $j \in [9, 14]$, i.e. between 0.1 and 3 Hz.

7.1.1.2 WLBMF analysis on all sensors

Self-similarity H and multifractality M were estimated by using the WLBMF method (see section 6.4) for each subject on the integrated time series (i.e. the cumulative sum) measured in each sensor and for each channel type: magnetometers (mag) and gradiometers along the latitudinal (grad_1) and longitudinal (grad_2) directions (hence in total 3×102 sensors). The same procedure was used to estimate H and M at rest (R) and during passive viewing of visual motion (VM). The mean values averaged over all subjects are plotted for all sensor types in Fig. 7.2.

In both sessions, all sensors exhibit large self-similarity ($H > 0.75$), with systematically higher values in the frontal regions (meaning more self-similar) than in the occipito-parietal ones. This observation is consistent with previous studies conducted in EEG and MEG sensors [Weiss 2009, Dehghani 2010]. A one-sided t-test was carried out in each sensor and each session to localize regions and sensor types exhibiting long memory (null hypothesis H_0: $H \leq 0.75$ versus H_1: $H > 0.75$) and was rejected everywhere even after Bonferroni correction ($p_{corr} \leq 10^{-6}$). It is also worth noting that $H > 1$ in certain sensors, which violates the validity of fBm model.

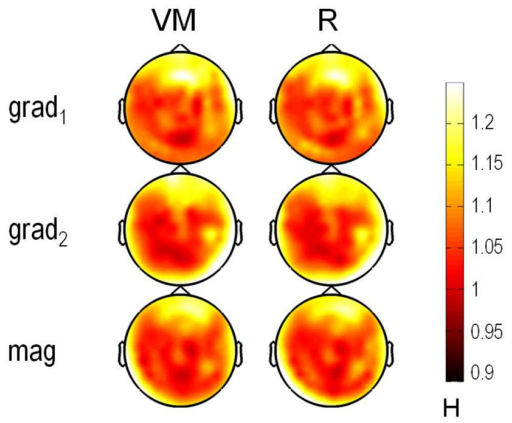

Figure 7.2: Mean self-similarity distribution over sensors at the group-level. All sensors show significant long memory ($H > 0.75$), with greater values in the frontal area. No significant differences appear however between the two blocks R and VM. Grad_1, Grad_2: orthogonal planar gradiometers; Mag: magnetometers.

In the same manner, Fig. 7.3 shows the topographies of the mean estimates of multifractality M averaged over all subjects. Multifractality ($M > 0$) is observed on the gradiometers located in the occipito-parietal regions. It is however not significant at the group-level when performing a one-sided t-test in each sensor (null hypothesis H_0: $M \leq 0$ versus H_1: $M > 0$): due to a large between-subject variability, H_0 was not rejected after Bonferroni correction ($p_{\text{uncorr}} \approx 10^{-2}$) for a False Positive Rate (FPR) of 5%.

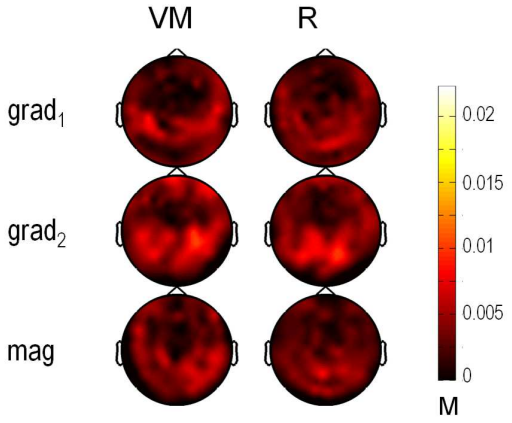

Figure 7.3: Mean multifractality distribution over sensors at the group-level. Contrary to self-similarity, multifractality is restricted to some sensors that vary with individuals. As a result, no specific sensors could be identified to present significant multifractality at the group-level. In addition, no significant differences appear between the two blocks R and VM. Grad_1, Grad_2: orthogonal planar gradiometers; Mag: magnetometers.

Paired t-tests were also computed to compare the R and VM blocks, where the null assumption consists of assuming the same mean values of H and M in each sensor between the two blocks. The null hypotheses H_0: $H_R = H_{VM}$ and H_0: $M_R = M_{VM}$ were rejected in none of the sensors, indicating that no significant difference can be exhibited between ongoing and task-related activity. However, in several MEG studies, the signal of interest is usually considered as a non-linear combination of both types of gradiometers, namely the ℓ_2-norm of gradiometers. Therefore, we decided to analyse the norm of gradiometers too.

7.1.1.3 WLBMF analysis on the norm of gradiometers

As each pair of gradiometers is orthogonal, their norm is simply defined by $\|\vec{\text{grad}}\| = \sqrt{\text{grad}_1^2 + \text{grad}_2^2}$. As already done, we estimated the self-similarity and multifractality parameters for the 102 pairs of gradiometers $\|\vec{\text{grad}}\|$ and then computed their mean values averaged over individuals in R and VM blocks separately.

A very noticeable result (Fig. 7.4, left) is the global reduction of self-similarity shown by the decrease of H in both sessions (compared to Fig. 7.2). Nonetheless, the self-similarity remains large enough to be statistically significant everywhere ($H > 0.5$). We then compared the two sessions by computing the contrast $\Delta H = H_R - H_{VM}$ in each sensor and for all individuals (see the mean contrast in Fig. 7.4, middle) and testing the statistical significance of this difference using a paired t-test (null hypothesis H_0 in each sensor: $H_R = H_{VM}$). As shown in Fig. 7.4 (right), significant differences ($p_{corr} < 10^{-2}$) emerge in the occipital area where $\Delta H > 0$. This finding is consistent with the literature dealing with the task-induced modulation of scale-free properties [He 2011, Ciuciu 2012] observed in fMRI.

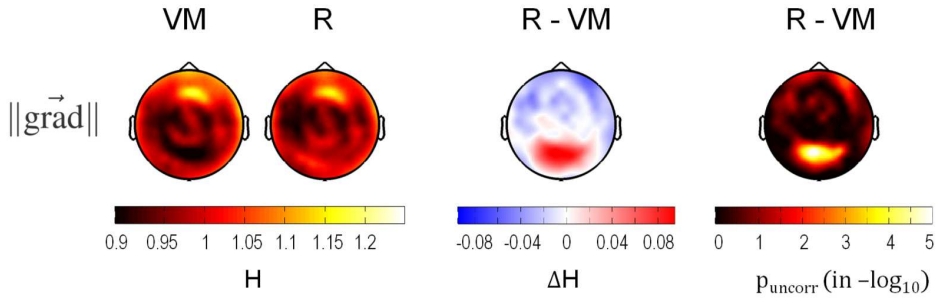

Figure 7.4: Self-similarity distribution computed with the norm of gradiometers. *Left*: Mean self-similarity averaged over all participants during rest (R) and passive viewing of a visual motion (VM). *Middle*: Mean difference between the R and VM blocks. *Right*: Uncorrected p-values resulting from the between-session paired t-test.

The multifractal behaviour of the norm $\|\vec{\text{grad}}\|$ measured through the values of M is emphasized in Fig. 7.5. As it can be seen, the amount of multifractality increases by taking the norm (when comparing with Fig. 7.3). In addition, multifractality is

more pronounced in the block R than in the block VM in the occipito-parietal area ($\Delta M = M_R - M_{VM} > 0$ in Fig. 7.5, middle). More precisely, this area seems to correspond to the region targeted by the hMT+ localizer (cf. Fig. 5.1a). The statistical paired t-test performed in each sensor with H_0: $M_R = M_{VM}$ was significant in this area but not enough to survive to Bonferroni correction for FPR=5%.

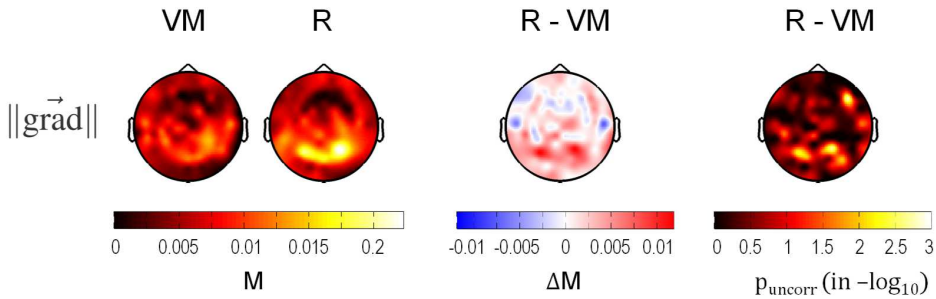

Figure 7.5: Multifractality distribution computed with the norm of gradiometers. *Left*: Mean multifractality averaged over all participants during rest (R) and passive viewing of a visual motion (VM). *Middle*: Mean difference between the R and VM blocks. *Right*: Uncorrected p-values resulting from the between-session paired t-test.

7.1.1.4 Simulation with multifractal random walks (MRW)

To understand the impact of the ℓ_2-norm on the multifractal properties, we considered a simplified problem where $\text{grad}_1 = \text{grad}_2$, meaning that $\|\vec{\text{grad}}\| \propto \sqrt{\text{grad}_1^2} = |\text{grad}_1|$. Hence, our simulation amounts to estimating the multifractal properties of a MRW process X after taking the absolute value $|X|$ and to see whether it would reflect the behavior observed in our data. We synthesized 200 MRW processes [Bacry 2001] with different values of multifractality ($M_X \in \{0, 0.005, 0.01, 0.05\}$) and self-similarity ($H_X$ equally spaced from 0 to 1.25). In the case $M_X = 0$, the MRW process is equivalent to a fGn if $0 < H_X < 1$ and a fBm for $H_X > 1$.

Given that the proportion of sign changes p_{sign} in X is the only parameter that induces regularity changes in $|X|$ (i.e. no addition of irregularity if X is always positive or negative), p_{sign} was expected to be the main cause of these observations. Importantly, Fig. 7.6a shows that p_{sign} is related to the Hurst exponent H_X in the case of a fGn and a MRW (if $H_X < 1$) and that it is independent of M_X. This can be intuitively explained by the fact that these processes are zero-mean and that H_X reflects the degree of fluctuations around their average. It is also noteworthy that MEG signals are approximately zero-mean too due to the online high-pass filtering (> 0.03 Hz).

We can hence manipulate the proportion of sign changes by modifying the value of H_X. According to [Helgason 2011], the theoretical behavior of $H_{|X|}$ as a function of H_X is known for a fGn: it depends on the Hermite rank of the function $x \longrightarrow$

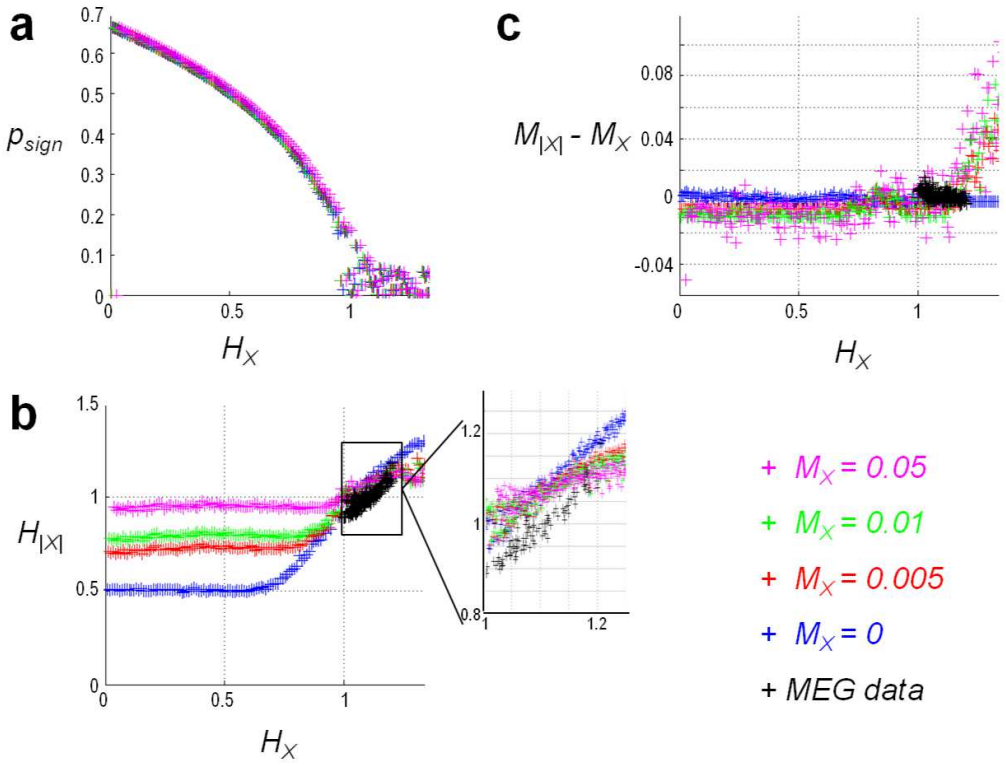

Figure 7.6: How does the norm impact the scale-free properties of a signal X. 200 MRW processes were several times synthesized with different values of multifractality M_X. The case $M_X = 0$ corresponds to a fGn for $H_X < 1$ and a fBm for $H > 1$. Scale-free properties of MEG data (grad_1 and $|\text{grad}_1|$) are also plotted in black. **(a)** The proportion of sign changes p_{sign} decreases with the self-similarity parameter H_X of a MRW independently of multifractality M_X. As soon as $H_X > 1$, p_{sign} remains at a very low level. **(b)** Variation of the Hurst exponent $H_{|X|}$ as a function of H_X for different amounts of multifractality. The fGn (in blue, $H_X < 1$) shows a decrease of self-similarity accordingly to the theoretical prediction (see main text), while injecting multifractality raises the floor value of $H_{|X|}$. In the case $H_X > 1$, applying the norm on X does not modify its Hurst exponent if $M_X = 0$ (i.e. $H_{|X|} = H_X$ for an fBm). MRW processes (with $M_X > 0$) also present a linear variation which slightly differs however as $H_{|X|} < H_X$ and which is closer to experimental MEG data (as it can be seen on the zoomed graph). **(c)** Difference of multifractality $M_{|X|} - M_X$ as a function of H_X. Contrary to MRW processes with $M_X > 0$, the norm does not induce multifractality or estimation bias on a fGn and a fBm.

$|x|$, defined as the index of the first non-zero coefficient of its Hermite polynomial expansion [1]. Here, the Hermite rank is equal to 2, and $H_{|X|}$ is given by:

$$H_{|X|} = \begin{cases} 2H_X - 1, & H_X \geq 0.75 \\ 0.5, & \text{otherwise} \end{cases} . \tag{7.1}$$

In the case of a fBm, the Hurst exponent remains theoretically unchanged ($H_{|X|} = H_X$) since $|X| \approx X$. In agreement with the theory, we observed indeed the expected behavior of $H_{|X|}$ in the absence of multifractality (Fig. 7.6b, blue curve). In the case of a MRW with $M_X > 0$, the theoretical results are unknown. The simulations show that the behavior is close to a fGn and also depends of M_X (Fig. 7.6b). In addition, we overlapped on the same graph (black curve) the values estimated in the latitudinal gradiometers (grad_1 and $|\text{grad}_1|$) and averaged over all subjects. A closer inspection shows that long memory in MEG data decreases even more than what is predicted by our models.

Fig. 7.6c illustrates the change of multifractality $M_{|X|} - M_X$ as a function of H_X for our different models as well as for MEG data. As it can be seen, taking the norm does not modify the estimation of multifractality for fBm and fGn processes (i.e. the processes remain monofractal). In the case of MRW processes, we observe a slight reduction of multifractality if $H_X < 1$ and conversely a more important increase of multifractality if $H_X > 1$. This pattern seems to reflect more the behavior of MEG data.

Therefore, the apparent contrast in the occipital area when analyzing the norm of gradiometers can be explained by the number of sign changes in the gradiometers (or by their phase) and the initial presence of multifractality. Because gradiometers measure the spatial derivative of the magnetic fields in two orthogonal directions, a change of sign suggests a change of source orientation or even perhaps of the source itself. Moreover, these simulations confirm that MEG signals are better modeled by MRW than by fGn or fBm.

7.1.1.5 Discussion and conclusion

We have demonstrated the presence of long memory in MEG data over all sensors. A small amount of multifractality was observed on the gradiometers in the occipital and parietal scalp regions. Interestingly, only the norm of gradiometers exhibits a modulation of the multifractal properties between ongoing and task-related activity. Additionally, this modulation was very localized to an area probably sensitive to the nature of the stimuli (as assessed by the ERF analysis, cf. chapter 5). It would be very interesting to change the sensory context (e.g. auditory stimuli only) in order

[1] Hermite polynomials $H_m(x)$ of order m are defined by $H_m(x) = (-1)^m \mathrm{e}^{x^2/2} \frac{d^m}{dx^m} \mathrm{e}^{-x^2/2}, m \geq 0$. For instance, $H_0(x) = 1$, $H_1(x) = x$, $H_2(x) = x^2 - 1$... They form an orthogonal basis of the Hilbert space $L^2(\mathbb{R}, \mathrm{e}^{-x^2/2} dx)$, which means that any real square-integrable function $f(x)$ can be expanded in Hermite polynomials as $f(x) = \sum_{m=0}^{\infty} c_m H_m(x)$. Let $\langle f, g \rangle = \int_{-\infty}^{+\infty} f(x) g(x) \mathrm{e}^{-x^2/2} dx$ be the inner-product, the coefficients c_m are then obtained as follows: $c_m = \frac{\langle f, H_m \rangle}{\langle H_m, H_m \rangle}$. In the case of $f(x) = |x|$, the first two coefficients c_0 and c_1 are null since $f(x)$ is an even function.

to check whether the modulation moves to the expected auditory regions, further confirming the specificity of our results.

The norm of gradiometers seems to capture more information. This is largely due to the nonlinear nature of the norm and the number of sign changes in the zero-mean gradiometer signals. The contrast between R and VM in the occipital area can be interpreted as a higher rate of source orientation changes in hMT+ during the presentation of RDK. Importantly, we propose that this result should extend to a more general concept: in any imaging modalities (e.g. fMRI), the knowledge of any nonlinear transformation in the generative model of the data can be crucial to correctly interpret its multifractal properties.

The statistical analysis in sensor space at the group-level is limited by the absence of spatial normalization across the individuals: not only their brain anatomy is different, but also their head position inside the Dewar. This is particularly relevant regarding the individual sparse distribution of multifractality over sensors. This led us hence to carry out further analysis in the source space. Another factor that might explain the weak difference between rest- and task-related activities at the sensor level is that the subject was not truly engaged in the task but only performs as passive viewing of visual motion.

7.1.2 Analysis in source space

After having investigated the modulation of scale-free properties between ongoing and evoked activities in sensor space, we now asked whether refined modulations of scale-free properties could be observed after visual learning in rest- and task-related activities for two types of training: V and AV. Based on recent findings reporting that spontaneous activity at rest is modified by learning [Lewis 2009], we hypothesized that V and AV groups should present different changes in self-similarity H and multifractality M. The psychophysical results show indeed that AV training is more efficient than V (cf. chapter 2). Crucially, specific functional plasticity in hMT+ was only induced by the AV learning, confirming the effectiveness of the AV training (cf. chapter 5).

7.1.2.1 Source reconstruction procedure

According to the ERF analysis, the neural network involved in training is too complex to analyze data in sensor space (besides the issue of group-level analysis). The continuous signals acquired during the learning paradigm were hence source-reconstructed by estimating their minimum-norm estimates (see section 3.4). As a consequence of the previous analysis conducted in sensor space, we paid particular attention to avoid any non-linear transformation that would modify the scale-free properties, such as taking the norm of source dipoles. Therefore, we only kept their radial components (note that this is also the recommended procedure to carry out time-frequency analysis in the source space).

Since the number of samples is extremely large (approximately 600.000 samples per recording block), as well as the number of vertices covering the cortical mesh for source-reconstruction (10242 vertices per hemisphere), we limited this preliminary analysis to five regions of interest (ROIs) identified for each individual in the ERF study (cf. chapter 5): 1) the hMT+ complex involved in visual motion processing, 2) the visual area V4 involved in color processing, 3) the inferotemporal cortex (ITC) involved in object recognition, 4) the middle superior temporal sulcus (mSTS) and 5) the posterior superior temporal sulcus (pSTS), that are both involved in multisensory processing.

In the main analysis, the scale-free properties are estimated over the whole cortex decomposed into 138 labels provided by the cortical parcellation of Freesurfer. In both cases, time series reconstructed at vertices belonging to the same label were regrouped and averaged into a unique time series. In this procedure, time series' signs were flipped according to vertices' anatomical orientation in such a way that signed activations would not cancel out after averaging (which is the standard label averaging procedure used by the MNE software). We verified that the WLBMF estimates did not dramatically differ between 1) first averaging (sign-flipped) signals over vertices of a same label and computing WLBMF estimates and 2) computing first WLBMF estimates in all vertices and averaging over each label (see Fig. 7.7). We rejected the second option as it was computationally intensive and not realistic (more than 10000 vertices for only 306 sensors).

7.1.2.2 Difference between V and AV in self-similarity

For each ROI and for each subject, we estimated the self-similarity H of the reconstructed MEG signal during the rest and the execution of the task before and after training (i.e. blocks REST_i, REST_f, pre- and post-training TESTs, cf. Fig.1.1). We verified that the spectral properties of the signals did not dramatically change before and after source reconstruction by visually inspecting the Welch's periodograms. The scaling range common to all spectra was defined over the scale range $j = [10, 14]$ (i.e. over the frequency range $f = [0.1, 1.5]$Hz).

The mean differences $\Delta H = H_{\text{POST}} - H_{\text{PRE}}$ after AV (left) and V (right) training in each ROI are shown in Fig. 7.8a. A one-tailed one-sample t-test was carried out in each ROI to assess the statistical significance of the difference. Non-significant differences ($p_{corr} \geqslant 0.05$, Bonferroni corrected) are indicated with grey colors and group-level standard deviations are indicated with bars. Significant decreases of self-similarity are reported after both trainings in hMT+, and are specifically observed in ITC and mSTS for AV and in V4 and pSTS for V. Importantly, the scale-free properties of the task-related activity evolved globally in the same direction irrespective of the training type.

However, if we look at the mean differences of self-similarity in brain signals recorded at rest before and after training, we observe significant decreases only for the AV group in hMT+ as shown in Fig. 7.8.b. In contrast to evoked activity, the training type is better distinguished in the resting state activity (i.e. ongoing fluc-

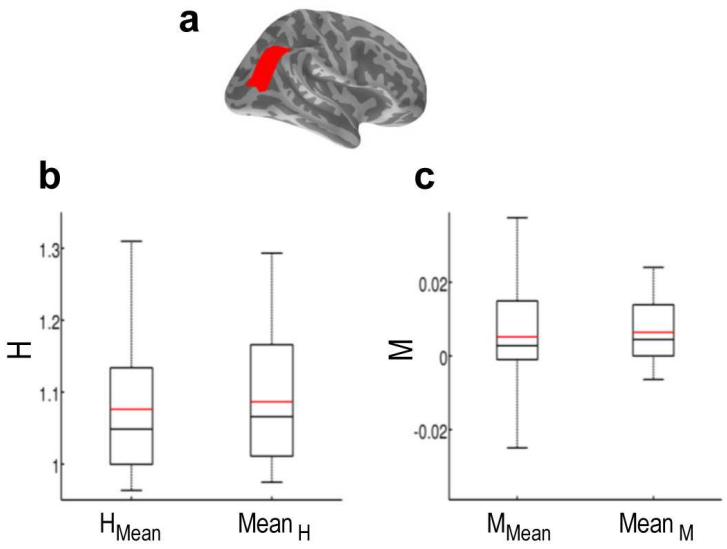

Figure 7.7: Impact of averaging sign-flipped signals over all vertices in one label on scale-free properties. **(a)** For all participants, raw signals measured in TASKi (cf. paradigm in section 1.3) were reconstructed in all vertices of the same label colored in red (right pSTS / hMT+). Amounts of self-similarity H and multifractality M were estimated in all vertices and averaged to be compared with the values of H and M when estimated directly from averaging sign-flipped signals over the label. **(b)** H boxplot showing the distribution of individual H values estimated on the mean signal (left) and averaged over all H values in each vertex (right). No statistical differences were observed (two-tailed paired t-test, $t_{23} = -1.2$, $p = 0.26$). **(c)** M boxplot showing the distribution of individual M values estimated on the mean signal (left) and averaged over all M values in each vertex (right). No statistical differences were observed (two-tailed paired t-test, $t_{23} = -0.47$, $p = 0.64$). The median is reported in black; the average in red. Boxes contain values between the first and the third quartiles. Whiskers extend to the 5^{th} and 95^{th} percentiles.

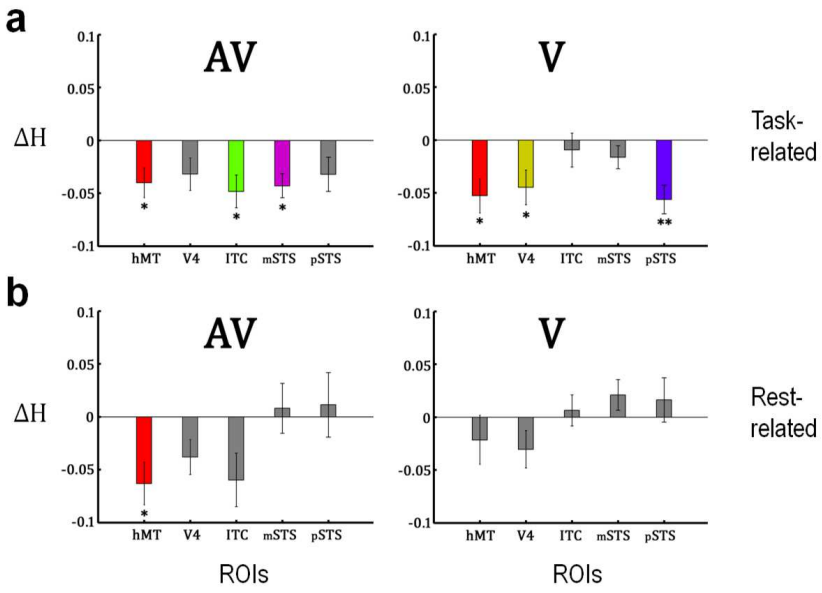

Figure 7.8: Changes of self-similarity following V and AV training. In each group, the contrast ΔH has been measured from the source reconstructed MEG signals measured during pre- and post-training tests **(a)** and during the first and last blocks of rest **(b)**. ROIs presenting no significant differences after Bonferroni correction are colored in grey. * and ** indicate a corrected p-value inferior to 0.05 and 0.01 respectively.

tuations) in which only AV trained participants present a decrease of self-similarity in cortical areas involved in plasticity.

7.1.2.3 Difference between V and AV in multifractality

Fig. 7.9 shows the mean differences of multifractality ΔM between pre- and post-training in evoked (panel a) and ongoing (panel b) activity. Again, a one-tailed one-sample t-test was carried out in each ROI and Bonferroni corrected to assess the statistical significance of the difference. We only found significant increases of multifractality in the V group in V4, suggesting a modulation of the multifractal properties during evoked activity with the training type. Moreover, no significant mean differences of multifractality at rest could be found, as reported in panel b.

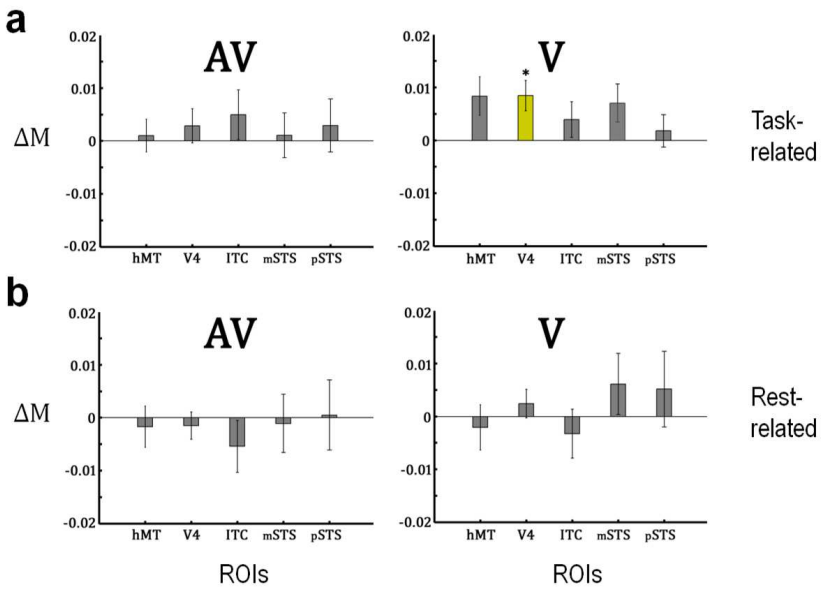

Figure 7.9: Changes of multifractality following V and AV training. In each group, the contrast ΔM has been measured from the source reconstructed MEG signals measured during pre- and post-training tests **(a)** and during the first and last blocks of rest **(b)**. ROIs presenting no significant differences after Bonferroni correction are colored in grey. *: corrected p-value inferior to 0.05.

7.1.2.4 Discussion and conclusion

In this preliminary study, we analyzed for the first time the scale-free properties of brain infraslow activity measured by MEG and reconstructed on the cortical surface. In this manner, we could identify the neural sources for each individual and overcome the classic issue of spatial normalization across the participants that arises in sensor space.

This analysis exhibits modulations of self-similarity and multifractality entailed by perceptual learning. More precisely, our results show a reduction of self-similarity

in task-related activity that occurs after both trainings, without clear distinction between the natures of the learning process. It might be interpreted as an increase of the neural excitability [He 2011, Maxim 2005] that would allow the participants to respond more quickly after the stimulus onset. Indeed, all participants' reaction time after training considerably decreased irrespective of the training type (cf. chapter 2). Alternatively, these changes can also be attributed to a highest level of attentional focus.

Moreover, we observed an additional reduction of self-similarity in spontaneous activity of hMT+ after AV training only. Given that AV training was not only the most effective training but also the only one to induce specific plasticity in hMT+, these changes in self-similarity in resting-state activity might reflect functional plasticity. This is consistent with other studies in fMRI showing that learning sculpts resting-state activity [Lewis 2009].

No explanation has been given yet concerning the sporadic presence of multifractality in brain signals. Here, we observed an increase of multifractality during the task only after V training. These fluctuations of scale-free properties might reflect transient changes induced by an unachieved training that would disappear as soon as the asymptot is reached (i.e. like in AV learning). They might also reflect an attentional modulation that could indicate the absence of a true perceptual learning.

The interpretation and the significance of these results is however limited by the small number of areas considered here: 1) we cannot affirm their specificity and 2) contradictory results can be found in other areas. To overcome this issue, we must thus analyze the whole cortex. In addition, we have not exploited yet all the MEG recordings acquired during the learning paradigm. They might bring supplementary information for the comprehension of the mechanism relating the modulations of self-similarity and multifractality to perceptual learning.

7.2 Main analysis

Based on the preliminary analyses, we know that MEG signals are characterized by long memory and multifractality in the infraslow domain that can be modulated not only between rest and task but also by perceptual learning. Several questions remain however, among which: whether these modulations are specific to areas involved in the task, whether multifractality and self-similarity interact during learning and plasticity and how these properties are related to the individual behaviors.

To address these questions, we computed the WLBMF estimates of self-similarity H and multifractality M of MEG source-reconstructed signals in all blocks of rest, test and training (cf. learning paradigm in section 1.3) over the whole cortex by using the Freesurfer parcellation (138 labels, see section 7.1.2.1 for more details).

We found specific interplays between self-similarity and multifractality in distinct cortical regions that correlated with individual learning. Most astonishing, all individuals' multifractality parameters in these regions converged towards a single

attractor value: the distance between an individual's and the attractor's multifractality parameter predicts the individual's learning.

7.2.1 Results

In this study, we used the data of 24 participants (V and AV groups) without any distinction between the training categories. This was first motivated by the need to increase the statistical power of the analysis conducted over the whole cortex as well as to reduce the complexity of the paradigm by addressing the question of the impact of visual learning on scale-free properties only (i.e. without regards to the role of multisensory integration).

For illustration purposes and common referencing, results are shown on the FreeSurfer average brain [Fischl 1999b].

7.2.1.1 Self-similarity and multifractality over the cortical surface

Similarly to preliminary analyses, MEG power spectra were first randomly inspected for different MEG sensors and for all individuals and sessions. All inspected spectra showed a $1/f$ behavior over frequencies ranging in $f = 0.1$–1.5 Hz, which corresponds to scales ranging in $j = 10$–14. The same procedure was carried out on source reconstructed data and replicated for different individuals and cortical regions. Representative power spectra averaged over all individuals and cortical labels during the first experimental blocks (Rest_i and pre-training TEST) are shown in Fig. 7.10. Coherent with Fig. 7.1 drawn in sensor space, a modulation between rest and task can also be observed in both the $1/f$ domain and the prominent peak of alpha (8–12 Hz).

Subsequently, the WLBMF analysis was carried out on source-reconstructed MEG data over the entire cortical surface, for all individuals and all experimental blocks. We first assessed how self-similarity (H) and multifractality (M) were organized during rest and task before any training had taken place. To insure that the effects would not be attributable to reconstruction-induced artifacts, we compared the same quantifications estimated in sensor space on a representative participant (see Fig. 7.11). WLBMF estimates in sensor and source spaces shared the same range of values and had similar distributions.

At the group-level, a self-similarity topography was consistently observed across all participants in the shape of an occipito-frontal gradient (Fig. 7.12a). During pre-training, the measured parameter H was significantly greater than 0.5 (which would correspond to white noise) and ranged from 0.8 to 1.2. The presence of multifractality (i.e. $M > 0$) was then tested over the whole cortical surface: only occipital, temporal and inferior frontal regions showed a significant amount of multifractality during pre-training (Fig. 7.12c).

At rest, self-similarity and multifractality showed a very similar topography (figure not shown) and were correlated across individuals during rest and task. Specifi-

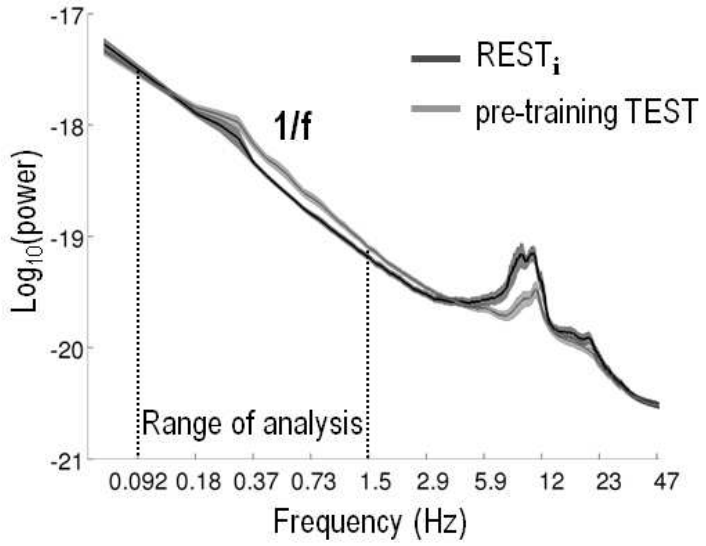

Figure 7.10: Power spectra of reconstructed MEG cortical currents. Mean Welch'speriodograms during the first block of rest (REST_i, in black) and the pre-training TEST (gray) averaged over all participants and labels (± 1 s.e.m) are plotted in logarithmic coordinates. The $1/f$ spectrum indicates the presence of scaling in the range $j = 10$–14 corresponding to the frequency range $f = 0.092$–1.5 Hz. Multifractal analysis was thus conservatively performed in this restricted scale range.

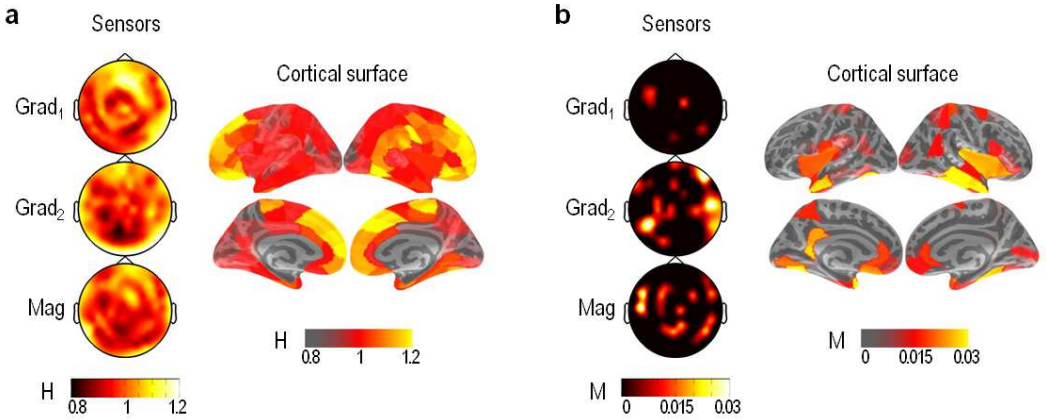

Figure 7.11: Self-similarity and multifractality topographies of a representative individual in sensor space and source space during pre-training. **(a)** H topography in the three sensor types (left) and on the cortical surface with MNE reconstruction (right). **(b)** M topography in the three sensor types (left) and on the cortical surface with MNE reconstruction (right). Only positive M-values are shown. The ranges of H and M values in sensor and source space are very similar, as well as their distribution (H occipito-frontal gradient, multifractality in parietal and temporal regions). Grad_1, Grad_2: orthogonal planar gradiometers; Mag: magnetometers.

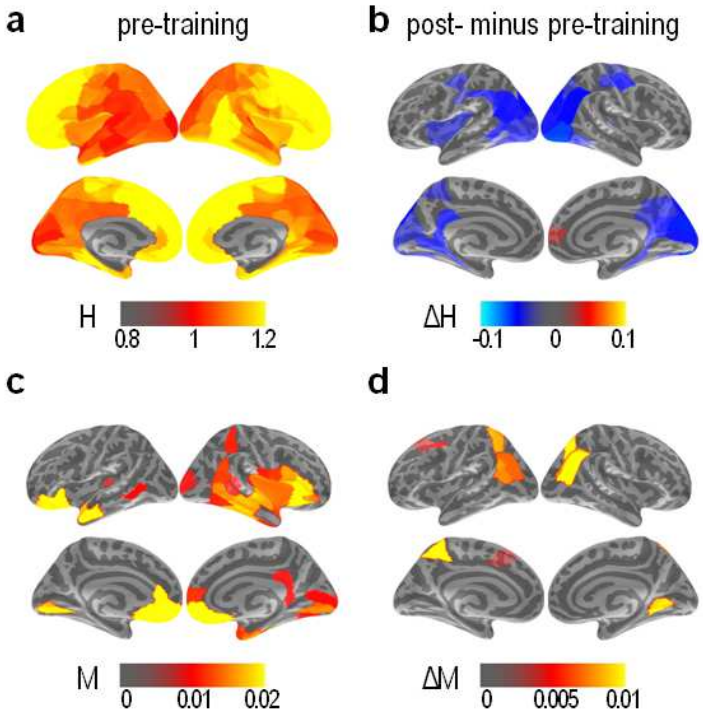

Figure 7.12: Decrease of self-similarity and increase of multifractality after training. Cortical maps of self-similarity (H) and multifractality (M) of source-reconstructed MEG data averaged over all subjects during pre-training test (left column) and maps of post- minus pre-training contrasts of these scale-free properties (right column). **(a)** Average self-similarity ranges from 0.8 to 1.2 and followed an occipito-frontal gradient increase. **(b)** Only labels showing significant differences of self-similarity (i.e. $\Delta H \neq 0$, $p < 0.05$ after FDR correction) between pre- and post-training are displayed. Training mainly induced a decrease of self-similarity in the occipito-parietal regions thereby intensifying the initial H gradient. **(c)** Only labels showing significant multifractality (i.e. $M > 0$, $p < 0.05$ after FDR correction) before training are displayed. **(d)** Only labels showing significant differences of multifractality (i.e. $\Delta M \neq 0$, $p < 0.05$ after FDR correction) between pre- and post-training are shown. Remarkably, training increased multifractality in some of the same areas presenting a decrease in self-similarity. However, the latter observation was confined to parietal regions.

cally, self-similarity was systematically larger at rest than during task whereas multifractality was systematically smaller at rest than during task (Fig. 7.13).

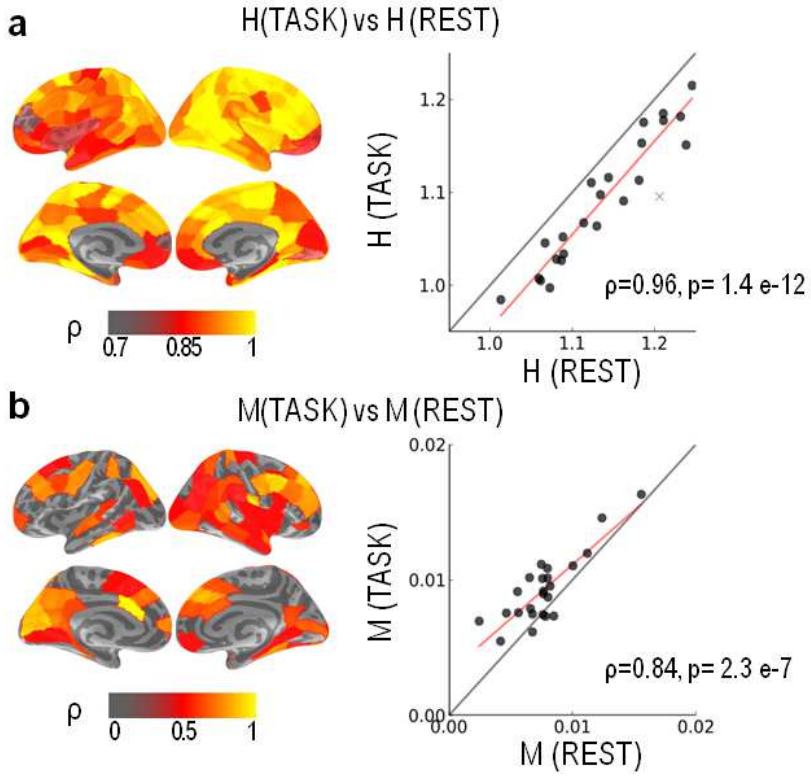

Figure 7.13: Modulation of scale-free properties between rest and task. **(a)** In all labels, the mean self-similarity H averaged over all rest blocks was correlated with mean self-similarity averaged over all task blocks for all individuals ($\rho \neq 0$, $p < 0.05$ all labels survived after FDR correction). The scatterplot is averaged over all significant labels and shows that i) if an individual has higher self-similarity at rest than another individual, he also has higher self-similarity during the task and ii) self-similarity at rest is greater than during the task. **(b)** Only labels presenting a significant correlation between the mean amount of multifractality M averaged over all rest blocks and the mean M over all task blocks for all individuals ($\rho \neq 0$, $p < 0.05$ after FDR correction) are shown. The scatterplot is averaged over all significant labels and shows that i) if an individual presents more multifractality at rest than another individual, he also presents more multifractality during the task and ii) multifractality during the task is greater than at rest. Automatically detected outliers are indicated by 'x'.

Second, we investigated whether training induced changes in self-similarity and multifractality during rest and task. A first crucial observation showed that the range of frequencies (or scales) over which scale-free properties is present was not significantly modified during task. Additionally, significant decreases of H between pre- and post-training TESTs were mainly found in the occipito-parietal region;

this decrease of self-similarity thus accentuated the occipito-frontal gradient initially observed (Fig. 7.12b). Even more remarkably, a significant increase of multifractality in post-training was found approximately in the same cortical regions, yet in a much more specific fashion (Fig. 7.12d). No significant changes were obtained between the first and last rest blocks (REST_i and REST_f, respectively).

7.2.1.2 Decreased self-similarity correlates with learning

To investigate whether these variations were functionally relevant, the decreases of self-similarity between pre- and post-training TESTs were correlated with hit rates and confidence ratings on a per individual basis. Three specific cortical regions showed significant correlations (Fig. 7.14a): in the left V4/inferior temporal cortex, H decreases positively correlated with increased hit rates (Fig. 7.14c); in the right posterior superior temporal cortex (pSTC) and human motion area (hMT+), decreases in H positively correlated with increased confidence ratings (Fig. 7.14d).

A similar analysis this time carried out on resting-state data ($\mathrm{REST}_f - \mathrm{REST}_i$) showed that in the middle superior temporal cortex (mSTC, Fig. 7.14a) H variations were negatively correlated with increased hit rates (Fig. 7.14b). The observed increases in multifractality did not correlate significantly with any behavioral index.

The decrease in H observed in the occipito-parietal regions after training was accompanied by an intensification of the occipito-frontal H gradient. We thus tested whether perceptual improvements could be attributed to this intensification: computing the correlation coefficients between gradient changes and task improvements (hit rate and confidence rating) lead to no significant effects. Similarly, we investigated whether H per se was correlated with performance but no significant correlations were found between H and individual performances measured in pre- and post-training TESTs.

7.2.1.3 Changes of self-similarity and multifractality are anticorrelated

Although the reported increase of multifractality did not correlate with behavioral improvements, its specific location partially coincided with cortical regions showing a decrease in self-similarity: this suggested a plausible coupling between these two properties. We thus proceeded with testing separately ongoing and task-related activity: specifically, we asked whether the average consecutive changes of self-similarity and multifractality during the four training blocks (task or rest) were correlated across all individuals.

To that aim, the individual mean variations of self-similarity and multifractality over four consecutive blocks (of only task or rest) during training were computed using a linear parametric contrast in each label and for each individual:

$$\langle \Delta M_{.,l,s} \rangle = \frac{-3M_{1,l,s} - M_{2,l,s} + M_{3,l,s} + 3M_{4,l,s}}{6},$$

where $M_{b,l,s}$ is the amount of multifractality estimated in the block b, label l of subject s. This method is equivalent to computing the average of all combina-

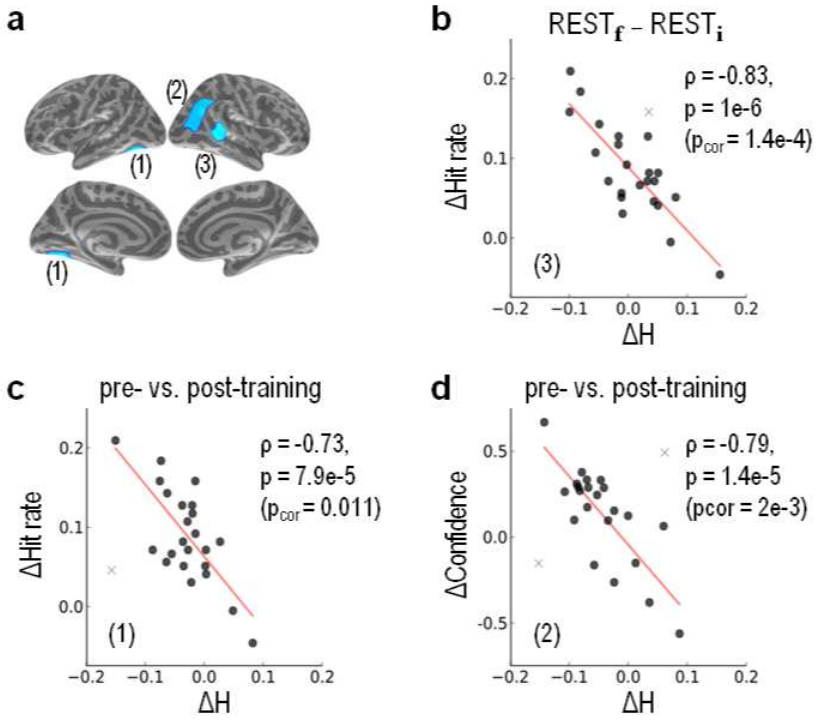

Figure 7.14: Behavioral correlates of self-similarity changes induced by training measured at rest and during task. **(a)** Cortical labels presenting a significant correlation ($\rho \neq 0$, $p < 0.05$ after FDR correction) between H and behavioral measures (hit rate and confidence ratings) in the pre- vs. post-training task or rest. Distinct cortical regions were negatively correlated with changes in H: (1) left V4/inferior temporal cortex (ITC), (2) right posterior superior temporal cortex (pSTC) and Human motion area (hMT+) and (3) right middle superior temporal cortex (mSTC). **(b)** Hit rate differences for all individuals as a function of variations of H in REST$_f$ vs. REST$_i$ in right mSTC. **(c)** Hit rate differences for all individuals as a function of variations of H in pre- vs. post-training in left V4/ITC. **(d)** Confidence ratings as a function of H in left pSTC/hMT+ in pre- vs. post-training. Automatically detected outliers are indicated by 'x'.

tions $\{M_{q,l,s} - M_{p,l,s}\}_{q>p}$ and has a better signal-to-noise ratio than the classical mean as simply averaging differences would be only sensitive to first and last values: $\frac{1}{3}\sum_{b=1}^{3}(M_{b+1,l,s} - M_{b,l,s}) = \frac{M_{4,l,s}-M_{1,l,s}}{3}$. The mean variation of self-similarity $\langle \Delta H_{.,l,s} \rangle$ was computed in the same manner.

As hypothesized, we found several regions in which changes in self-similarity and multifractality were anticorrelated (though more during task, Fig. 7.15b than rest, Fig. 7.15a). These results were consistent with Fig. 7.12b–d and with the opposite variations of H and M observed when switching from rest to task. In this dynamic coupling, the last question was thus which of the self-similarity or multifractality property dynamically drove the other.

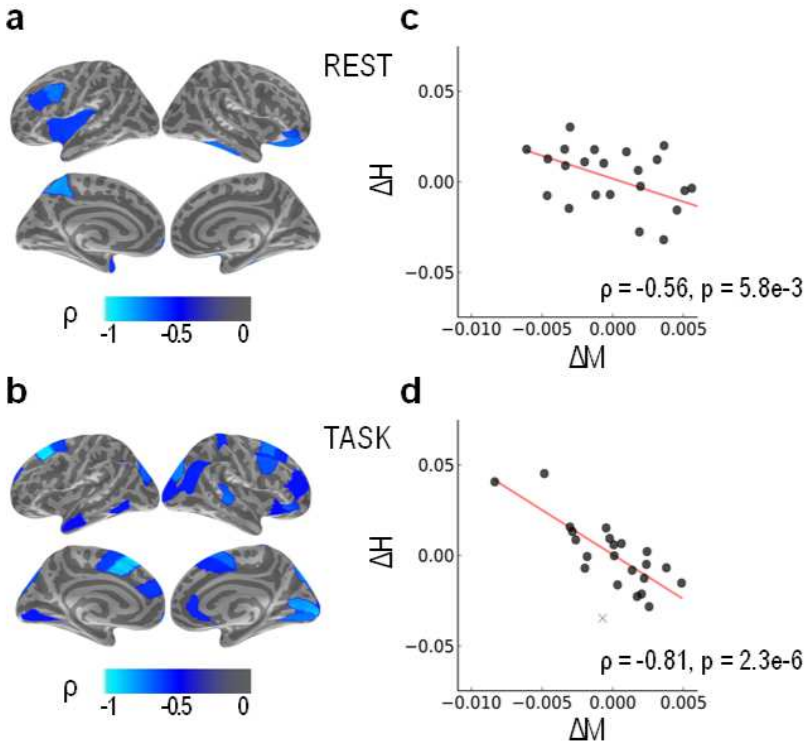

Figure 7.15: Self-similarity and multifractality variations are anticorrelated during rest and task. Only labels presenting a significant correlation ($\rho \neq 0$, $p < 0.05$ after FDR correction) between the variation of H and the corresponding variation of M measured in blocks of rest **(a)** and task **(b)** during training are displayed. The corresponding scatterplots averaged over all significant labels at rest **(c)** and during the task **(d)** are shown on the right side. Automatically detected outliers are indicated by 'x'.

7.2.1.4 Individuals' multifractalities converge towards an attractor during training

To disentangle the dynamics of self-similarity and multifractality, we asked whether a rule common to all individuals could predict independently the value of H or M based on previous values. To this end, we tested if the value of M in each block during training (task or rest) was correlated across individuals with the subsequent change in M (ΔM). To make this analysis more robust, the initial M and the corresponding ΔM were first averaged over the four training blocks as previously described in section 7.2.1.3, where the corresponding initial value estimated in the block b, label l for subject s is:

$$\langle M_{.,l,s} = \frac{3M_{1,l,s} + 2M_{2,l,s} + M_{3,l,s}}{6}.$$

The same analysis was carried out independently for H.

Whereas no significant correlation was found between H and ΔH, many cortical regions presented significant anti-correlations between M and ΔM during rest (Fig. 7.16a) and task (Fig. 7.16b). An example of such anti-correlation during rest (Fig. 7.16c) and task (Fig. 7.16d) is shown for the right pSTC/hMT+.

These observations can fruitfully be interpreted as *phase space* diagrams, from which four possible trajectories of M can be deduced depending on the value taken by the slope of the linear model relating ΔM to M (see Fig. 7.17).

These trajectories allow us to define a critical value M_∞ corresponding to $\Delta M = 0$, which plays the role of a repeller in two cases (M moves away from M_∞ either monotonically or by oscillating) and the role of an attractor in the other two (M converges towards M_∞ monotonically or by oscillating). Additionally, the value of the slope quantifies the average speed of convergence or divergence across participants. In this analysis, as the slope always ranged between -1 and 0, all cortical regions were associated with attractors M_∞ (case c in Fig. 7.17).

The behavior of M converging towards M_∞ can be observed when plotting the time course of the multifractal cortical topography averaged over all participants during the four training blocks (Fig. 7.18): indeed, the multifractal topography converges towards the asymptotic topography both at rest and during task. Consistent with our previous findings showing greater multifractality during task than rest (cf. Fig. 7.15), the attractors M_∞ turned out to be greater during task than rest. Finally, a speed of convergence can be derived from the slope a obtained via the linear regression by computing the quantity $1 - |a + 1|$.

7.2.1.5 The multifractal attractor reflects asymptotic behavioral performance

From these observations, we hypothesized that the asymptotic amount of multifractality M_∞ would correspond to the maximal level of performance that can be reached by participants. In other words, we predicted that the closer to the attractor

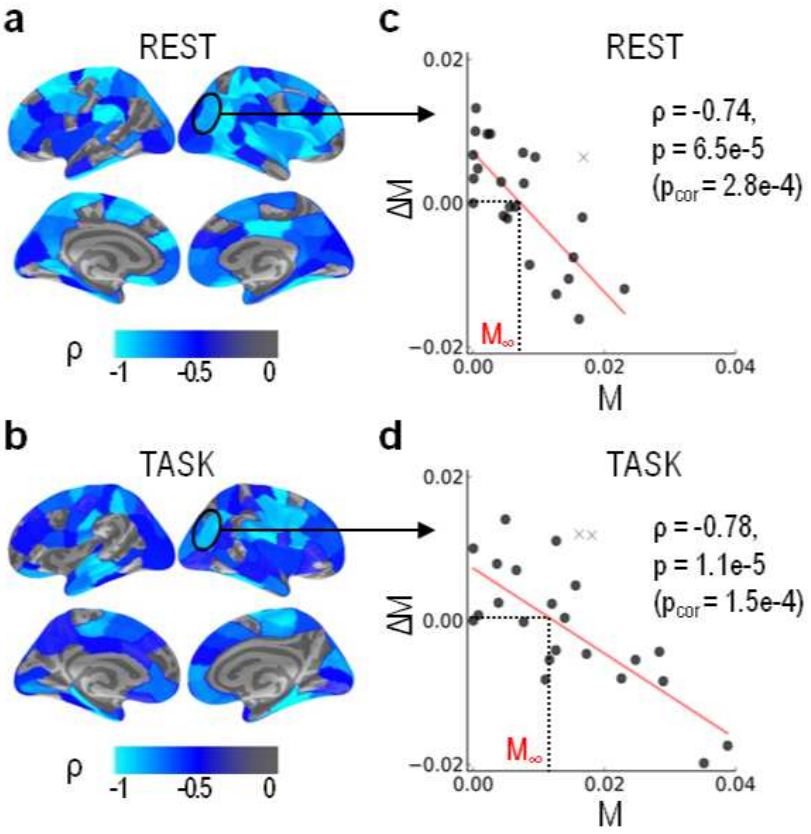

Figure 7.16: Multifractality converges towards an attractor M_∞ during rest and task. For each cortical label, Pearson correlation coefficients were computed between an individual's ΔM averaged over the four consecutive rest **(a)** or task **(b)** blocks and the initial average M. Correlations were corrected for multiple comparisons ($\rho \neq 0$, $p < 0.05$ after FDR correction). In both conditions, labels only showed anti-correlations. Each scatterplot observed in a cortical label — here, exemplified by the black circle corresponding to right pSTC/hMT+ at rest **(c)** and during task **(d)** — can be interpreted as the phase space diagram of M during training. Interestingly, the slope of the linear regression (here equal to -0.74 in **c**, and -0.59 in **d**) indicates that M converges towards an asymptotic attractor M_∞ corresponding to $\Delta M = 0$. The closer the slope is to -1, the faster the convergence.

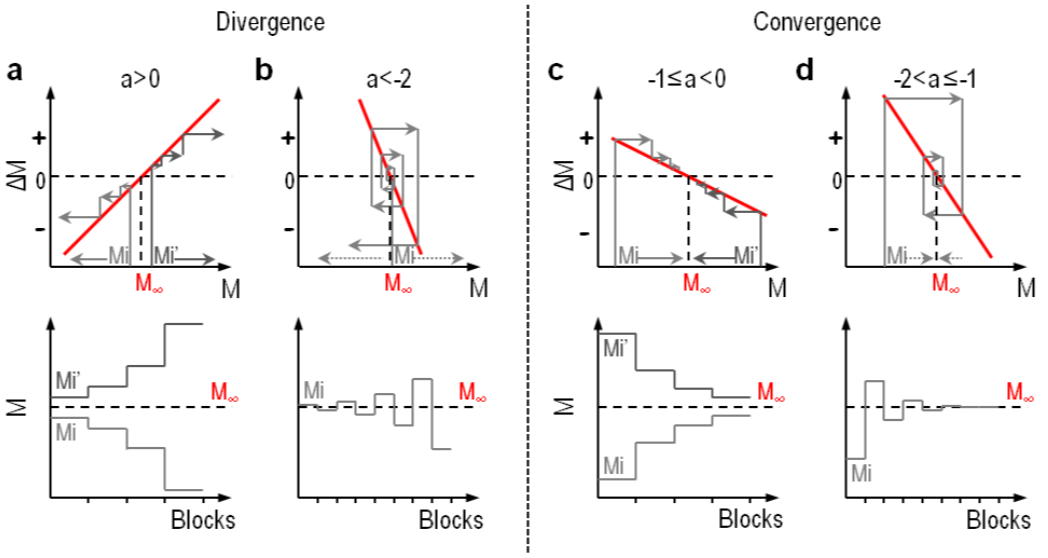

Figure 7.17: Four dynamic trajectories of M as a function of the slope a defined in the linear regression $\Delta M = aM + b$. Phase space diagrams are shown in the top row; corresponding time courses over blocks are provided in the bottom row. **(a, b)** M_∞ is a repeller. If $a > 0$, depending on the initial value $M_i < M_\infty$ or $M_{i'} > M_\infty$, M will move away from M_∞ monotonically **(a)**. If $a < -2$, M becomes more and more distant from M_∞ by oscillating around this value **(b)**. **(c, d)** M_∞ is an attractor. If $-1 \leq a < 0$, depending on the initial value $M_i < M_\infty$ or $M_{i'} > M_\infty$, M converges towards M_∞ in a ascending or descending manner **(c)**. If $-2 < a \leq -1$, M converges towards M_∞ by oscillating around this value **(d)**.

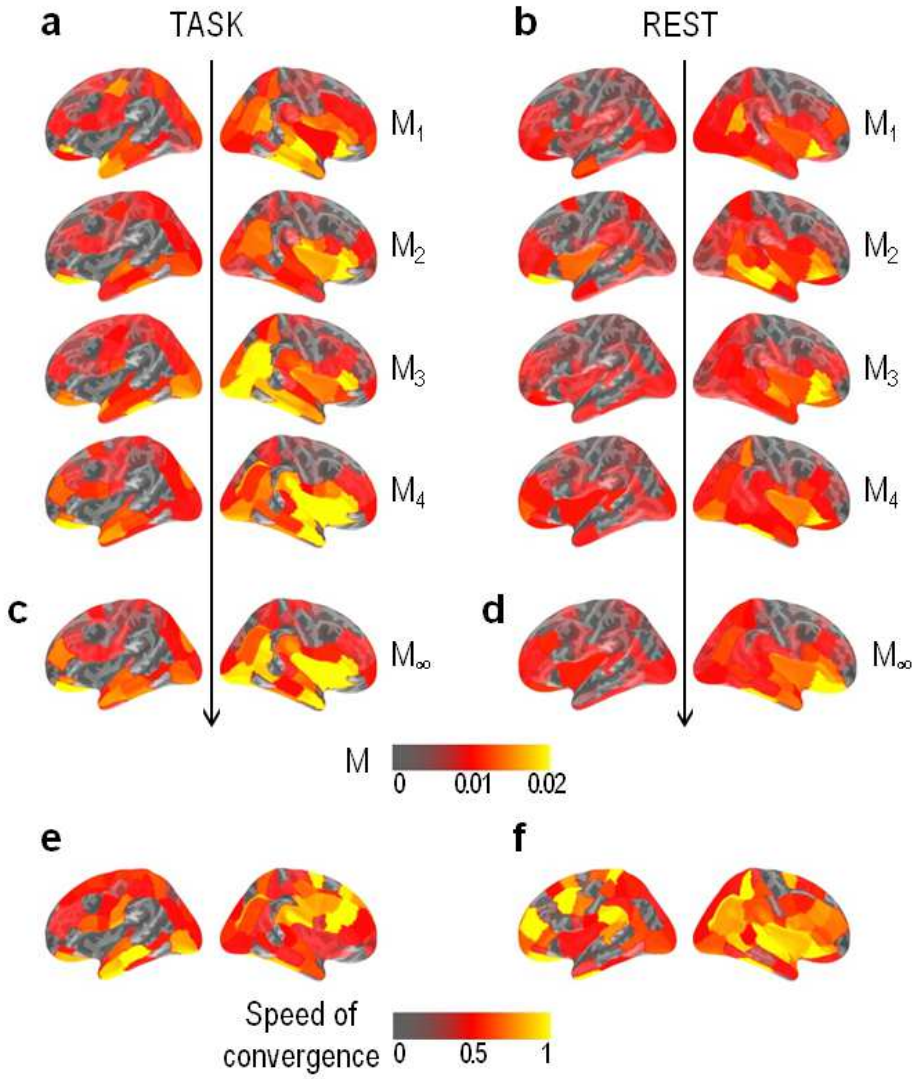

Figure 7.18: Cortical maps of multifractality converge towards an attractor map during training. **(a, b)** Time course of mean cortical maps averaged over all individuals in each task **(a)** and rest **(b)** block. In the course of training, maps become more and more similar to the asymptotic maps of M_∞ assessed in task- **(c)** and rest- **(d)** related activity. **(e, f)** In each label where M converges towards M_∞, the speed of convergence has been defined as the quantity $1 - |a + 1|$, where a is drawn from the linear regression $\Delta M = aM + b$. The speed of convergence is maximal at 1, and a negative value would indicate a divergent behavior (see Fig. 7.17). The maps of speed of convergence differ between task **(e)** and rest **(f)**.

M_∞ an individual's M was in post-training, the better the individual's performance would be (hit rate).

We tested this hypothesis by computing the correlation coefficients in post-training between each individual's hit rate and the absolute difference $M - M_\infty$ in all cortical labels. Significant negative correlations were found in three cortical regions (Fig 7.19A): the left human motion area (hMT+), the right intraparietal sulcus (IPS) and the right anterior superior temporal cortex (aSTC). Interestingly, an asymptotic hit rate could be extrapolated from the fitted straight line in the averaged scatterplot (Fig. 7.19b) for $M - M_\infty = 0$ which corresponded to a hit rate of $\sim 90\%$.

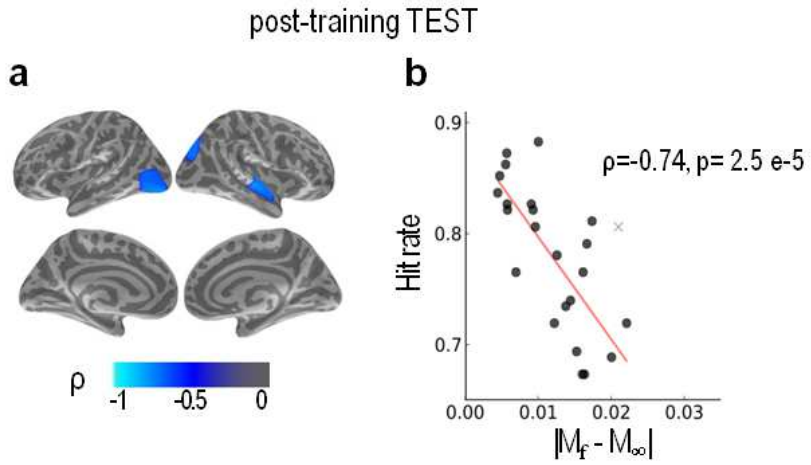

Figure 7.19: The closer the individual's multifractality to the group-level attractor M_∞, the better the individual's performance. (a) In each cortical label, the distance to the multifractal attractor was defined as the absolute difference between the individual amount of multifractality and the attractor M_∞. Labels presenting a significant correlation ($\rho \neq 0$, $p < 0.05$ after FDR correction) between the individual hit rate and this measure in post-training are displayed. Three cortical regions emerged and presented an anti-correlation: left human motion area (hMT+), right intraparietal sulcus (IPS) and right anterior superior temporal sulcus (aSTS). **(b)** Corresponding scatterplot averaged across all significant labels. Automatically detected outliers are indicated by 'x'.

Because multifractality also converged during rest blocks, we wondered whether this negative correlation could be observed when replacing the quantity $M - M_\infty$ measured in post-training TEST by that measured in REST$_f$. Although some cortical regions consistent with those observed during task (Fig. 7.20a, c) presented significant anti-correlations, none survived the FDR correction for multiple comparisons. A similar analysis carried on with confidence ratings did not survive FDR corrections (Fig. 7.20b, d).

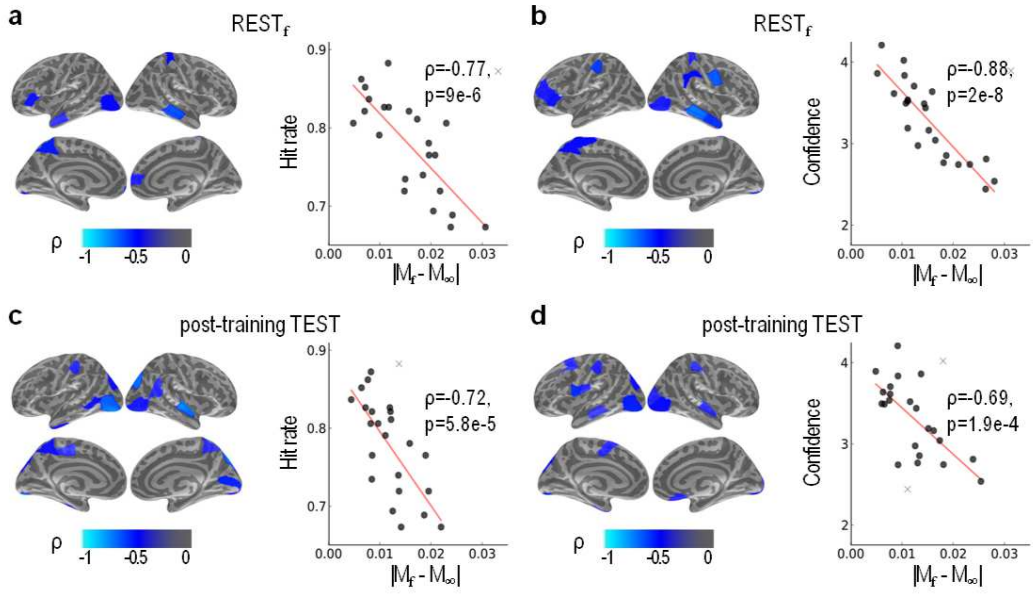

Figure 7.20: Other behavioral correlates of the individual distance to the multifractal attractor in the last block of rest and task. In each panel, the left figure shows labels in which the individual hit rate **(a, c)** or confidence rating **(b, d)** is correlated with the distance to the multifractal attractor measured in the last rest block **(a, b)** or in post-training test **(c, d)** ($\rho \neq 0$, $p < 0.05$ *without* correction for multiple comparisons). Remarkably, labels are relatively consistent between rest and task blocks, as well as between behavioral measures. Scatterplots averaged over all significant labels show strong anti-correlations in all cases. Automatically detected outliers are indicated by 'x'.

7.2.2 Discussion and conclusions

7.2.2.1 Discussion

In this study, we showed that scale-free properties of Human brain activity are modulated by learning. Specifically, cortical regions implicated in visual perceptual learning [Sasaki 2010] such as the dorsal path (hMT+, IPS, pSTC) for visual motion discrimination [Noguchi 2005] and the ventral path (V4, ITC, STC) for color categorization [Roe 2012] presented a decrease in self-similarity strongly associated with perceptual improvement (cf. ERF analyses in chapter 5). At first sight, this observation contradicts previous studies [Palva 2013] showing that neural scaling exponents measured with DFA (equivalent to H, cf. section 6.2.2) reflect behavioral scaling laws [Gilden 1995, Kello 2010, Proekt 2012]. However, these exponents were estimated from the amplitude envelope of narrow-band oscillations whereas, here, H was directly measured from MEG raw data (in the frequency range of 0.1–1.5 Hz). This suggests two different neural mechanisms that can be captured differently and that are not a priori incompatible.

Our results are consistent with the hypothesis that a decrease in self-similarity is commensurate with an increase in neural excitability [Maxim 2005, He 2011]. Such interpretation is primarily based on the contrast between neural activity at rest and during task [Ciuciu 2012, He 2011] with higher self-similarity observed at rest. Indeed, a decrease in H during task implies a decrease in the overall temporal correlation of the signal or, equivalently, richer temporal dynamics with more energy in higher frequencies. The occipito-frontal H-gradient ascent observed both in sensor (cf. preliminary analyses in section 7.1.1) and source space replicates previous studies [Weiss 2009, Dehghani 2010] and supports the fact that low-level sensory areas (associated with lower H values) process incoming information whereas frontal areas maintain memory, focused attention and executive control (higher H values). Alternatively, this could reflect a higher refresh rate in low sensory areas that decreases along the hierarchical pathway by integrating information towards frontal areas.

Conversely, some participants exhibited increased self-similarity in frontal regions (though not significantly so at the group-level) thereby accentuating the observed gradient. Because this increase did not correlate with task improvement, it might be attributed to changes in attention or cognitive strategies that are unrelated to perceptual learning per se. Surprisingly, and in contrast to other studies [Lewis 2009, Stevens 2010, Tambini 2010, Ma 2011, Baldassarre 2012, Sala-Llonch 2012], no significant changes in resting-state activity was captured by self-similarity or multifractality after training. However, the anti-correlation in right mSTC at rest between variations of self-similarity and hit rate shows that only great improvements are followed by a reduction of H at rest. Therefore, we would expect significant decreases of self-similarity for longer and more efficient training (here, only 20 minutes without feedback). Changes of self-similarity in resting-state activity might thus index efficient and long-term learning, as suggested by our previous analysis comparing V and AV trainings (cf. section 7.1.2).

The role of neural multifractality has hardly been addressed in the litera-

ture and with the notable exception of one study investigating EEG micro-states [Van de Ville 2010], studies converge in showing an endogenous origin of multifractality [Popivanov 2005, Popivanov 2006] that is specific to functional brain networks [Shimizu 2004, Ciuciu 2012]. The evidence for a dynamic coupling between self-similarity and multifractality with opposite effects (consistent with a previous study [Weiss 2009]) encourages future research to consider both characterizations when investigating scale-free dynamics in neural systems. Crucially, the value of H by itself was not indicative of within-group performance, namely the individual with the lowest H was not necessarily the best performer; however, the extent to which H decreases correlated with task improvement across all participants did. Taken together, these results suggest that self-similarity is more sensitive to an individual's history. This could explain inter-individual variability but also the significant differences found between young and old individuals [Suckling 2008] and between healthy individuals and Alzheimer patients [Maxim 2005]. Conversely, M appears to inform on an individual's performance in an absolute reference frame: the participant with the closest M to the attractor M_∞ was also the best performer. As such, multifractality appears to be more task-specific, less sensitive to inter-individual variability and more related to instantaneous processing. As a result, M can monitor the variations of H. This coupling does not hold actually in all cortical regions and may change over time depending on the nature of the task and the cognitive network implicated in the task.

A major finding is the convergence of multifractality towards an attractor observed during training in both rest and task. The large number of cortical regions involved in this convergence suggests a global mechanism directly or indirectly driven by the training whose "signature" would be the cortical topography of multifractal attractors (cf. Fig. 7.18c–d). However, only the attractors of specific particular regions (namely, left hMT+, right IPS and aSTC) can be directly related to training as they reflected the asymptotic performance. The implication of a high or low value of the attractor thus remains unclear: for instance, would a higher value of M_∞ in left hMT+ indicate a better asymptotic performance? Would it be at the expense of higher brain energy consumption [Laughlin 1998, He 2011]? Another interesting property that could be exploited is the speed of convergence towards the multifractal attractor: if we assume that the speed of convergence indicates how rapidly participants can reach the asymptotic performance, this index provides a new means to investigate neural correlates of learning.

7.2.2.2 Perspectives

In order to further understand the signification of this phenomenon of convergence, it would be interesting to compare the different maps of asymptotic multifractality and their speed of convergence for different types of training. Considering once again our three groups V, AV and AVn, we can see different patterns as illustrated in Fig. 7.21.

We can first notice that AV presents the highest speed of convergence across

cortical areas (mean speed averaged over all labels in AV: 0.86, in V: 0.25 and in AVn: 0.21) which might be thus a biomarker of the training efficiency (since AV>V⩾AVn in term of performance) as previously suggested. If we also look at the asymptotic maps of multifractality, we can readily see that they differ with the training type. This strongly suggests that M_∞ values are more specific to the training than the task per se. Consequently, we can first wonder if there exists an optimal value M_{task} of multifractality reflecting the best performance achievable for a given task. If so, M_∞ would be a powerful indicator of the asymptotic performance reachable by a given training: the closer M_∞ to M_{task}, the more efficient the training is. This also raises the question whether there can be "bad" attractors associated with "bad" tiresome trainings for instance. An interesting challenge would hence consist of assessing the value of M_{task}. In a first approach, it can be approximated by the M_∞ values obtained for the training yielding the best behavioral performance (thus here AV). Finally, it appears that areas converge systematically more quickly towards low than high M_∞. A relevant biomarker of learning might be therefore obtained by combining both information given by $|M_\infty - M_{\text{task}}|$ and the speed of convergence.

In this study, the asymptotic attractor M_∞ is *by construction* common to all individuals. In other words, our method is an "all or none" approach that tests for (necessarily common) attractors among individuals. Given the number of training blocks in our paradigm, we could not assess M_∞ for each individual and verify if they were indeed common (there would be only 3 points in our linear fit). To that aim, it would be hence very instructive to develop another paradigm with more training blocks (by replacing for instance the rest blocks by task). Note however that statistically testing for the equality between individual M_∞ values would not be an easy task.

One can be also interested in analyzing the scale-free properties of the amplitude of oscillatory bands [Linkenkaer-Hansen 2001] and seeing how they are related to the infraslow activity and the neural process implicated in learning. In addition, a first WLBMF analysis of the amplitude envelope in the α band (obtained after band-pass filtering between 8 and 12 Hz and applying the Hilbert transform) in one sensor and for one individual clearly reveals multifractality (Fig. 7.22).

Future work can also be dedicated to improving the WLBMF method by better adapting it to the inherent constraints of the analysis of electrophysiological data. Indeed, MEG can be easily corrupted by physiological and electronic artifacts. Crucially, the presence of sudden "jumps" in the data can dramatically bias the estimation (often resulting in aberrant extreme values of multifractality). This issue is usually easily overcome in standard MEG analysis by rejecting the data segment containing the artifact and concatenating the rest of the data. In scale-free analysis however, this solution is not possible as it would modify the temporal structure of the data. So far, we corrected as much as possible "bad channels" containing jumps by using the SSS method (cf. section 3.2.2). In the case where all channels were corrupted at the same time, the only solution was to ignore the left or right part of the signal (depending on how many samples would be left). For-

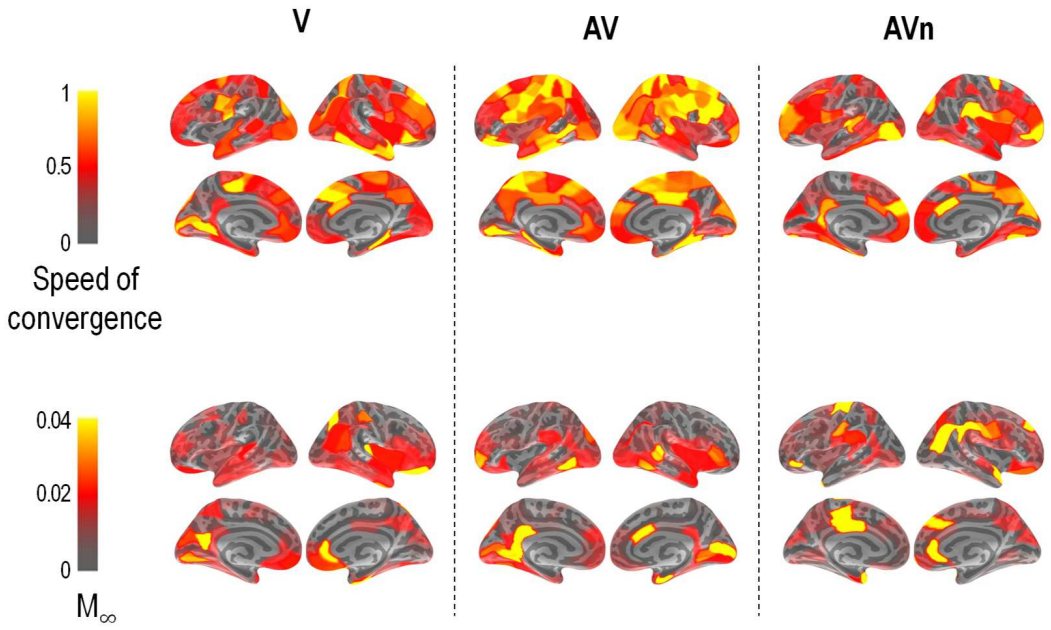

Figure 7.21: Maps of convergence speed and asymptotic multifractality as a function of training. The speed of convergence (top) was defined as the quantity $1 - |a + 1|$ where a comes from the linear regression $\Delta M = aM + b$ carried out in each label and each training group V (left), AV (middle) and AVn (right). The closer this value to 1, the faster multifractality converges towards its attractor M_∞ at the group level. It can be readily seen that AV training drives more quickly several areas towards their asymptotic amount of multifractality than V and AVn trainings. These maps can be jointly read with their correspondent M_∞ maps (bottom). Interestingly, it appears that most of areas converging rapidly are associated with a low M_∞ and conversely, areas attracted towards large M_∞ converge slowly.

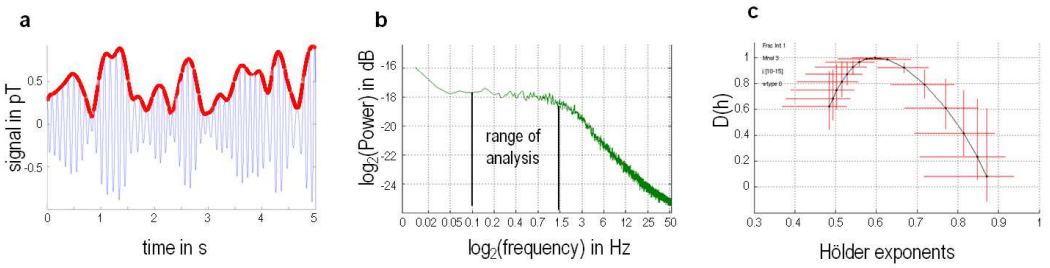

Figure 7.22: WLBMF analysis of the alpha amplitude envelope of a MEG signal. **(a)** The envelope (in red) is obtained by computing the Hilbert transform of a signal filtered between 8 and 12 Hz in a magnetometer. **(b)** The Welch's periodogram in logarithmic scales shows a $1/f$ behavior in the scale range $j = 10$–14 corresponding to $f = 0.1$–1.5 Hz). **(c)** Corresponding multifractal spectrum estimated with WLBMF. The width of the spectrum reflects the existence of multifractality in the alpha envelope.

tunately, this situation occurred very rarely. Therefore, a possible implementation would consist of selecting the wavelet coefficients corrupted by artifacts and to ignore them in the computation of the structure functions. Conversely, this would also allow the selection of events of interest in the same way that we select epochs in ERF analyses (under the condition that the epoch is long enough to have access to very large scales). By doing so, we might be able to disentangle the different neural mechanisms involved during task that are (unfortunately) encompassed in our scale-free analysis (e.g. perceptual processing, decision, motor response, introspection or awareness).

Last but not least, our study focused here only on univariate analysis of MEG signals. It would be thus very interesting to investigate the fractal connectivity [Achard 2008], i.e. the scale-free cross-temporal dynamics, between different cortical areas. In short, it consists of estimating the $1/f$ behavior of the cross-spectrum between two time series, i.e. the relative contribution of all frequencies (in the scaling range) to their cross-correlation. This can be simply done with the efficient wavelet fractal connectivity [Wendt 2009b]. A recent study (under review) in fMRI using this estimator reports indeed scale-free connectivity between networks and interesting behaviors [Ciuciu rev]: similarly to ours observations in univariate analysis, a reduction of the bivariate Hurst exponent H was also observed when switching from rest to task. Intriguingly, participants presenting a weak modulation between rest and task were the ones that showed the best performance in a visual detection task (measured in terms of reaction time).

Conclusion

In this thesis, we have investigated the neural processes of perceptual learning and plasticity by analyzing source-reconstructed MEG data with two different approaches: the standard ERF analysis, a method commonly used in neurosciences to temporally track the neural activity associated with the onset of events, and the scale-free analysis, a very unusual and original approach that characterizes the temporal organization of brain activity over several scales of time or frequency (restricted here in the infraslow domain exhibiting a $1/f$-type power spectrum).

Summary

Our first contribution consisted of elaborating a learning paradigm that would be sufficiently effective to rapidly observe performance improvement of all participants. Assuming that an appropriately designed multisensory training would allow us to achieve this goal, we developed novel audiovisual stimuli consisting of acoustic textures paired with the coherence of visual colored RDKs. More specifically, we hypothesized that supramodal processing (i.e. of both acoustic and visual coherence) during training would allow greater plasticity in areas such as hMT+ and hence entail greater behavioral improvements. This is why we tested three types of training: visual only (V), audiovisual using acoustic textures (AV), or random noise (AVn).

The psychophysical analyses have shown that all participants significantly improved after 20 minutes of training by reducing their visual coherence discrimination thresholds and their reaction times. Consistent with our hypothesis, perceptual thresholds were significantly better reduced after AV training. In addition, the absence of significant increases in confidence rating in AV seems to indicate that learning occurred implicitly, ruling out the possibility of a conscious cross-sensory mapping. Our first objective, i.e. to ensure an effective training, appears thus to be fulfilled. The question of plasticity was further addressed by carrying out the ERF analysis.

The ERF study has allowed us to overcome the limitations of psychophysics and to better understand the neural correlates of learning by comparing pre- and post-training brain activity reconstructed on the cortical surface. First, it appears that several mechanisms may underlie the improvements observed at the behavioral level: the increased neural response in the ventral visual stream (ITC) observed in the three groups suggests an enhancement of color-motion binding when coherence discrimination was easily achieved. Another common characteristic is the strong and selective implication of the prefrontal cortex (possibly reflecting the role of attention in learning), as suggested by the increased activity reported in vlPFC specifically to the learned coherence levels. Compared to V training, AV and AVn trainings altered in an opposite manner a larger network implicated in the analysis of visual motion and comprising multisensory areas such as pSTS and mSTS. Crucially,

selective plasticity in hMT+ (as captured by the shift of neurometric thresholds) was solely observed in the AV group. Consistent with the supramodal hypothesis and the reverse hierarchical theory (RHT), these findings suggest that pre-existing multisensory/supramodal computations elicited during AV training have enabled down-stream sensory plasticity, i.e. from vlPFC to hMT+.

To the best of our knowledge, this study provides the first MEG evidence that acoustic information can selectively alter the response profiles of visual cortices in healthy Humans thereby providing a stepping stone for the understanding of representational invariance and supramodal object processing in the cortex. Importantly, these results may have substantial practical implications in the elaboration of training protocols for sensory-impaired populations and users of sensory-substitution devices.

In parallel with the ERF analysis, we have assessed the scale-free properties of source-reconstructed MEG data acquired in every experimental block (rest and task) in V and AV participants by using the robust and accurate WLBMF method. Not only we reported the presence of self-similarity and multifractality in MEG data (both at the sensor and source levels), but we also found a modulation of these properties between rest and task and between pre- and post-training activity. More precisely, the training induced in task-related activity an increase of multifractality in some confined areas (such as hMT+/pSTS and IPS) and conversely a more extended decrease of self-similarity that correlated with learning in cortical regions implicated in the task (left V4/ITC and right hMT+/pSTS). This opposite coupling between self-similarity and multifractality is of particular interest since it also occurs between rest and task and it has never been reported in other dynamic systems (such as in hydrodynamic turbulence or in finance time series). In other words, infraslow brain activity can be strongly autocorrelated (such as during rest or *before* learning); should its dynamics become more complex (i.e. more multifractal), the temporal compression of information may increase in turn (such as during task and *after* learning), resulting in lower global autocorrelation. Most astonishing, the degree of multifractality observed for each individual converged during training towards an asymptotic value in numerous cortical areas; crucially, only the attractors of some specific areas such as hMT+ reflected asymptotic performance.

To the best of our knowledge, this study provides the first evidence that an individual's learning ability can be predicted by the multifractal indexing of his/her brain activity. This finding is novel and provocative as it offers a first neurophysiological interpretation of multifractality observed in Human brain activity. In addition, it brings into question the model of self-organized criticality usually proposed to interpret the presence of self-similarity in brain dynamics as it fails in explaining the origin of multifractality.

ERF vs. scale-free analyses

Both ERF and scale-free analyses reveal changes in the pattern of activity between pre- and post-training that can be interpreted as functional plasticity. Interestingly, common areas such as hMT+, pSTS, mSTS and ITC have been consistently exhibited with these two approaches; yet the neural interpretation is quite different. It is first worth reminding that the frequency range of analysis overlaps only slightly between ERF (1–40 Hz) and scale-free (0.1–1.5 Hz) analyses. In the case of ERF analysis, plasticity is mainly represented by an increase (or sometimes decrease) of brain activity at given latencies, reflecting thus either a finer tuning/sensitivity of neurons (as in hMT+) or the recruitment of a larger synchronized population of neurons (as possibly in pSTS) in response to a precise event. Conversely, a change of scale-free properties indicates a temporal reorganization of brain activity at a time scale greater than that of ERF analysis ($\sim$ 1 s) that encompasses thus several neural events.

This is indeed a crucial difference: thanks to the great time resolution of MEG, ERF analysis allows us to disentangle neural mechanisms by selecting a particular moment (e.g. in our study, the activity evoked by the onset of visual motion at a certain level of coherence). Scale-free analysis, as conducted here, does not make such distinction since it is carried out on the whole time series; this might explain why it exhibits a larger network associated with plasticity. For instance, IPS does not present any plasticity with the ERF analysis whereas it shows both decreased self-similarity and increased multifractality. However, the computation of the evoked responses was restricted to the neural processing of motion, excluding other mechanisms such as accumulation of sensory evidence, decision mechanisms, motor responses or self-confidence rating. We strongly expect IPS to show plasticity in one of these cases; this could be verified for instance by computing the evoked activity phase-locked to the participant's responses. In addition, accumulation of evidence is generally reflected by very slow drifts that might be filtered out with the current band-pass filter used for the ERF analysis (it might be hence worth reconsidering the lower cutoff frequency).

A major advantage of scale-free analysis is that it can be applied on any MEG data set, notably during rest or sleep. By considerably reducing the dimension of data to two values (i.e. self-similarity and multifractality) per sensor/vertex in each run, we were able to examine the dynamics of learning across the successive experimental blocks. The main difficulty of this analysis is to correctly chose the scale range of analysis and the parameter γ that determines the order to which data are integrated. This is done in practice by a meticulous inspection of the power spectra for each run, each sensor and each individual... As the amount of data increases, this becomes however a challenging issue. Although the ERF analysis is theoretically and conceptually more simple, it is not easier to carry out: it strongly depends indeed on the choice of the baseline and of the filtering and requires a very precise control of times of events (which becomes an issue if the trigger channels are defective, or if the stimuli are presented with an uncontrollable jitter/lag). Although

we were confronted to the same difficulty for both methods regarding the analysis at the sensor level (due to the complexity of the task and the absence of normalization across individuals), the choice of the source reconstruction method (MNE, dSPM or sLORETA?) had more impact on the reconstructed ERFs than on the scale-free properties extracted from cortical sources. Indeed, scale-free analysis is insensitive to any (non-null) linear transformation such as the normalization of MNE estimates by the dSPM and sLORETA methods.

Link with the oscillatory hierarchy

As a future work, we can examine the oscillatory properties of MEG signals, an approach that can be seen as the complement of the scale-free analysis (cf. section 6.1.2). This is of particular interest here since it would allow us not only to deepen our understanding of scale-free brain dynamics and to facilitate our interpretation by comparing the results with what we have obtained so far, but also to address the question of the large-scale integration in the context of multisensory and color/motion binding (i.e. how sensory inputs spatially segregated can interact at early levels before reaching higher-order associative areas).

An attractive theory based indeed on the oscillatory approach proposes that the large-scale neural networks interact by phase synchronization, enabling multisensory integration [Varela 2001]. Such mechanism was first evidenced in the gamma band [Rodriguez 1999, Tallon-Baudry 1999]. In a EEG study comparing the gamma synchronization in two conditions (faces vs. nonsense figures recognition), the presentation of faces induced a long-range gamma synchronization that considerably decreased before the motor response [Rodriguez 1999]. Other studies have shown that gamma synchronization was involved in the selective visual attention [Talsma 2009]. For instance, the gamma synchronization was higher for an attended stimulus than for a distractor in monkeys [Fries 2001]. The perception of the bouncing-streaming motion illusion could also be predicted by an increased gamma synchronization within a large-scale centro-temporal network measured with EEG [Hipp 2011]. Moreover, gamma activity is principally present during wakefulness and in brain areas processing the modality on which attention is focused, while disrupted gamma synchronization has been reported in dysfunctional states (such as Parkinson, schizophrenia and epilepsy) [Varela 2001].

Interestingly, the existence of a coupling between gamma amplitude and lower frequency phase led to the concept of nested frequencies [Buzsáki 2004, Fox 2007]. This oscillatory hierarchy is particularly of interest in audiovisual speech [van Wassenhove 2012] because a similar "nesting" exists in language that necessitates a complex processing to chunk each element of speech [Giraud 2007].

Added to this, it appears that the phase of a slow oscillation in a given modality can be reset by a salient input of another modality. Taken together, these two properties have a crucial impact on multisensory integration because one modality can interfere in advance with another to adjust the time of excitability with

the incoming input. For instance, the phase of ongoing neural oscillations in the auditory cortex of macaques was reset by somatosensory inputs to make the arrival of auditory inputs coincide with either the high-excitability phase (amplifying then the neuronal responses) or the low-excitability phase (reducing the neuronal response) [Lakatos 2008]. Likewise, oscillations in the visual cortex were shown to be reset by inhibitory inputs coming from direct connections with the auditory cortex [Iurilli 2012]. In the opposite direction, the visual inputs arriving (faster than sound) during an audiovisual conversation can modulate the spontaneous activity in the auditory cortex to make its high-excitability state coincide with the auditory input [Schroeder 2008].

The oscillatory hierarchy is therefore a very appealing concept that has the convenience to explain both positive and negative effects of multisensory interactions by accounting for temporal constraints. Crucially, the phenomenon of nested frequencies has been shown to occur also in the $1/f$-type arrhythmic brain activity [He 2010] but could not be captured by the sole self-similarity parameter. It would be thus interesting to test in turn if multifractality reflects such mechanism.

Other perspectives

The data acquired in this experiment have not been fully exploited yet and can be subject to other analyses. For instance, the question of multisensory integration can be more specifically addressed by carrying out standard ERF or time-frequency analyses on the four blocks of training. We can also wonder if the results regarding self-similarity and multifractality in the course of training are only specific to infraslow activity or if similar behaviors can also be reported when carrying out the WLBMF analysis on the amplitude envelopes of oscillatory bands. In the same idea, we can also ask if similar findings can be obtained in fMRI (although the sampling frequency does not allow the assessment of multifractality as accurately and robustly as with MEG data). A prediction regarding the data acquired during the resting-state fMRI session following the MEG experiment (not analyzed yet) would be that the two groups V and AV are distinguishable on the basis of their amount of multifractality (since the attractors are different between the two trainings).

Since the convergence towards asymptotic values of multifractality has been evidenced only at the group level, it would be interesting to test this intriguing property for each isolated individual by increasing the number of training blocks in the experiment. If the training is sufficiently long and effective, we also expect significant changes of scale-free properties even at rest. An interesting methodological contribution would be to allow the WLBMF analysis to select epochs of interest (long enough though) in order to separate the different neural mechanisms involved in the task. If we suppose for instance that multifractality somehow reflects the number of neural processes occurring at the same time and same location, this should result in reducing the amount of multifractality.

Finally, the natural next step in further investigating scale-free brain dynamics

would consist of proposing a multivariate extension of the WLBMF approach, in order to assess not only fractal but also *multifractal* connectivity. In parallel to that, it would be relevant to carry out standard analyses of connectivity with several metrics (e.g. coherence, phase-locking value, phase lag index) in order to compare the two approaches on MEG data.

Publications

Journal papers

N Zilber, P Ciuciu, A Gramfort, L Azizi and V van Wassenhove. *Supramodal processing optimizes visual perceptual learning and plasticity.* Neuroimage.

N Zilber, P Ciuciu, P Abry and V van Wassenhove. *Convergence to asymptotic multifractal brain dynamics predicts learning.* Resubmitted to J Neurosci.

Peer-reviewed conference proceedings

N Zilber, P Ciuciu, P Abry and V van Wassenhove. *Modulation of scale-free properties of brain activity in MEG.* In 9th Proc. IEEE ISBI, pages 1531–4, Barcelona, Spain, 2012.

N Zilber, P Ciuciu, P Abry and V van Wassenhove. *Learning-induced modulation of scale-free properties of brain activity measured with MEG.* In 10th Proc. IEEE ISBI, pages 986–9, San Francisco, USA, 2013.

Conference abstracts

N Zilber, P Ciuciu, A Gramfort and V van Wassenhove. *Acoustic textures improve motion discrimination: indexing metamodal plasticity with MEG.* In Biomag, Paris, France, 2012.

N Zilber, P Ciuciu, P Abry and V van Wassenhove. *Scale-free properties of MEG brain signals capture plasticity.* In Biomag, Paris, France, 2012.

N Zilber, P Ciuciu, A Gramfort and V van Wassenhove. *Acoustic textures and visual motion act in concert: metamodal plasticity observed with MEG.* In Society For Neuroscience, New Orleans, USA, 2012.

P Abry, N Zilber, P Ciuciu, A Gramfort and V van Wassenhove. *Beyond oscillations: are scale-free dynamics of MEG signals markers of neural plasticity?* In Society For Neuroscience, New Orleans, USA, 2012.

Appendices

Appendix A

ERF analysis: Supplementary figures

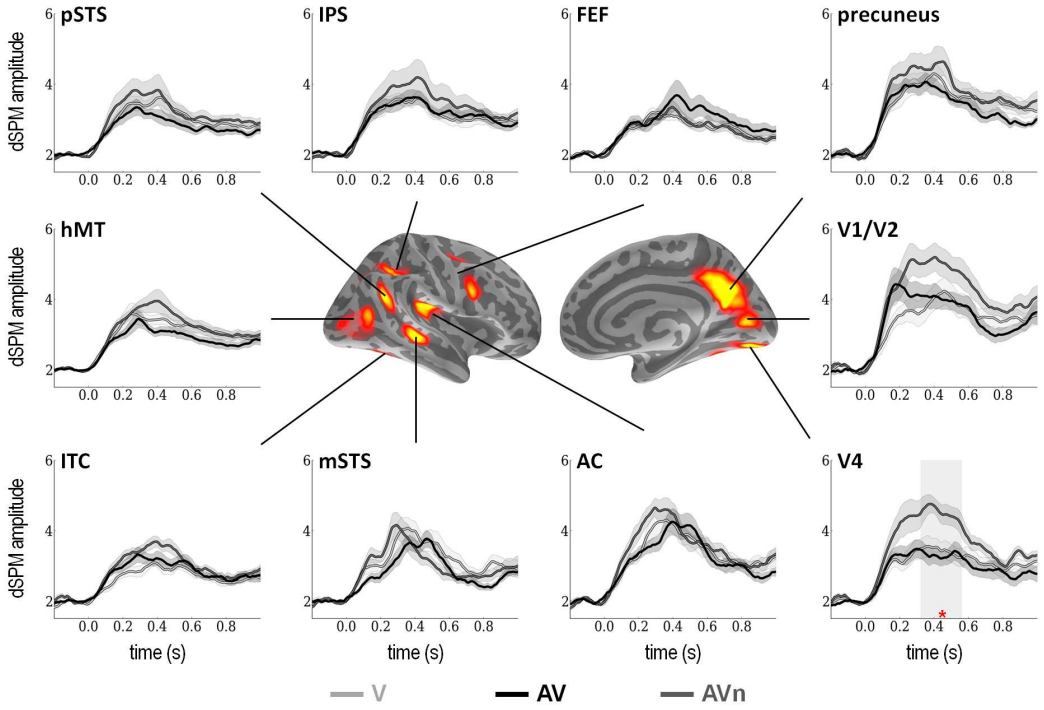

Figure A.1: Grand average source estimates in pre-training. Mean dSPM estimates (±1 s.e.m.) in pre-training across all RDK coherence levels were computed and extracted from each region of interests (see Fig. 5.1). Time series are separately reported for V (light grey), AV (black) and AVn (dark grey) training groups. To test the existence of group differences before training, a F-test contrasting the amplitude of the source estimates in V, AV and AVn groups was combined with a cluster permutation algorithm for all ROIs. Shaded areas highlight the latencies of significant differences between groups and red stars indicate the corresponding degree of significance. Significant differences were only found in V4. * corrected p values inferior to 0.05.

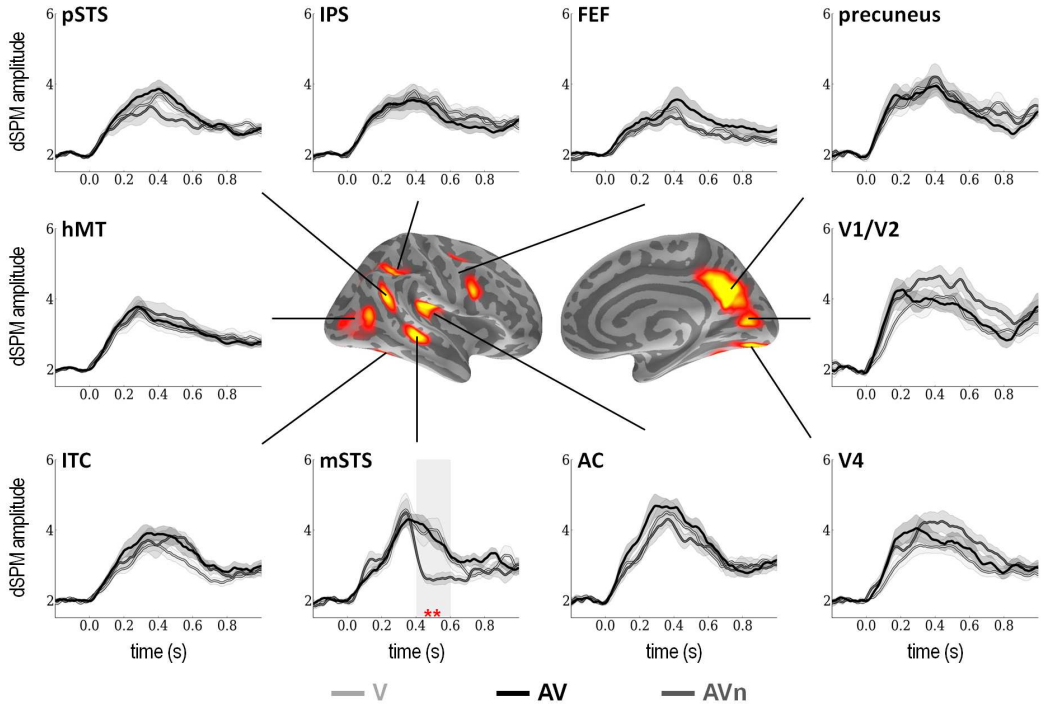

Figure A.2: Grand average source estimates in post-training. Mean dSPM estimates (±1 s.e.m.) in post-training across all RDK coherence levels were computed and extracted from each region of interests (see Fig. 5.1). Time series are reported for V (light grey), AV (black) and AVn (dark gray) training groups. To test the existence of differences between groups after training, a F-test between the amplitude of the source estimates in V, AV and AVn groups was combined with a cluster permutation algorithm for all ROIs. Shaded areas highlight the latencies of significant differences between groups and red stars indicate the corresponding degree of significance. Significant differences were found only in right mSTS. ** corrected p values inferior to 0.01.

Appendix B

The wavelet transform

It has been shown that the wavelet-based analysis of self-similarity displays better performance both in terms of estimation performance and of robustness against drifts and non-stationarities [Veitch 1999, Bullmore 2004]. Also, the wavelet framework is convenient as it naturally extends to the analysis of models other than self-similarity, such as multifractal processes.

The basic idea of the wavelet transform is to decompose a signal $X(t)$ in the time-scale plane by projecting the signal on time-shifted and dilated versions of an elementary function $\Psi_0(t)$ named *mother wavelet* that verifies:

$$\int_{\mathbb{R}} \Psi_0(t)dt = 0 \quad \text{and} \quad \int_{\mathbb{R}} |\Psi_0(t)|^2 dt = 1.$$

Ψ_0 is characterized by its number of vanishing moments $N_\Psi \geq 1$ defined as the largest integer such that:

$$\begin{cases} \int_{\mathbb{R}} \Psi_0(t)t^n dt &= 0, \quad \forall n = 0..N_\Psi - 1 \\ \int_{\mathbb{R}} \Psi_0(t)t^{N_\Psi} dt &\neq 0. \end{cases}$$

This means that the mother wavelet and its derivatives up to order N_Ψ decay exponentially in the time domain. Basically, the greater the number of vanishing moments N_Ψ, the more sensitive the wavelet is to high frequencies. According to the Heisenberg's uncertainty principle, resolution in scale and time domain cannot be simultaneously optimal: wavelets with larger N_Ψ are defined indeed on larger supports. Hence, the choice of the mother wavelet (see Fig. B.1 for some examples) depends on the type of analysis that is to be performed — e.g. wavelets with small (resp. large) N_Ψ are more adapted to analyze low (resp. high) frequencies.

Let $\Psi_{a,u}(t)$ a version of $\Psi_0(t)$ dilated to scale a and translated to position t:

$$\Psi_{a,t}(u) = \frac{1}{\sqrt{a}} \Psi_0(\frac{u-t}{a}).$$

The continuous wavelet coefficients $C_X(a,t)$ are given by:

$$C_X(a,t) = \langle X|\Psi_{a,t}\rangle = \int_{\mathbb{R}} X(u)\Psi_{a,t}(u)du.$$

Discrete wavelet coefficients are defined on a dyadic grid (scale $a = 2^j$ and time $t = k2^j$, cf. Fig. B.2) such that the family of wavelets $\{\Psi_{j,k}\}$ forms an orthonormal basis in $L^2(\mathbb{R})$. The normalized discrete wavelet coefficients $d_X(a,t)$ are then given by:

$$d_X(a,t) = 2^{-\frac{j}{2}} \langle X|\Psi_{j,k}\rangle = \int_{\mathbb{R}} X(u)2^{-j}\Psi_0(2^{-j}t - k)dt.$$

The advantage of using wavelet coefficients is that they reproduce exactly the scaling properties of $X(t)$ while being more easy to analyze: not only they are stationary, but they are also less correlated (i.e. less long-range dependent) than $X(t)$ if the number of vanishing moments N_Ψ is sufficiently high. This statement is particularly true for *self-similar* processes with stationary increments (if $N_\Psi \geq H + \frac{1}{2}$). Wavelet coefficients do not procure however satisfactory results for a complete *multifractal* analysis: their values are indeed very close to zero, making the computation of negative moments ($q < 0$) extremely unstable. This can be corrected using WTMM or WLBMF (cf. chapter 6).

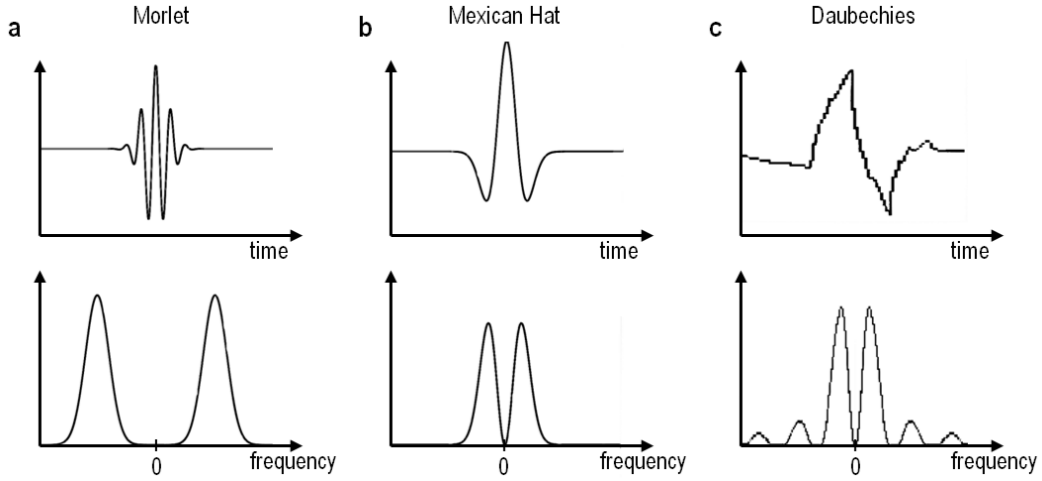

Figure B.1: Examples of common wavelets. Two continuous **(a–b)** and one discrete **(c)** mother wavelets are illustrated in time (top) and frequency (bottom) domain. **(a)** real-valued Morlet wavelet. **(b)** Mexican Hat, i.e. the negative normalized second derivative of a Gaussian function. **(c)** Daubechies mother wavelet with $N_\Psi = 4$. Note in this example that the number of vanishing moments is larger for the Morlet wavelet (as indicated by the number of oscillations); this is also reflected by the faster decay of its Fourier transform in low frequencies.

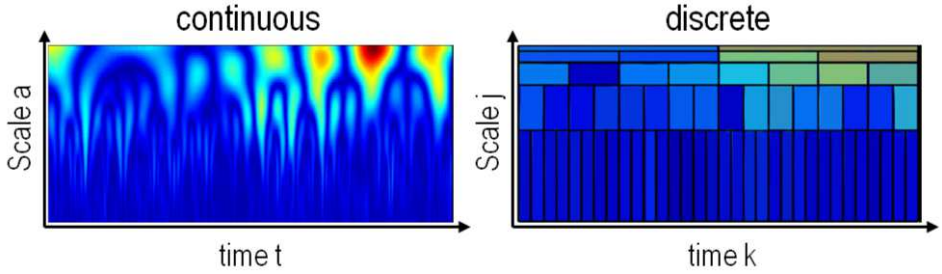

Figure B.2: Continuous vs. discrete wavelets. The scalogram, i.e. the time-scale representation of a time series can be computed by using either continuous (*left*) or discrete (*right*) wavelets. Discrete coefficients are computed on a dyadic grid: $a = 2^j$ and $t = k2^j$.

Bibliography

[Accardo 1997] A Accardo, M Affinito, M Carrozzi and F Bouquet. *Use of the fractal dimension for the analysis of electroencephalographic time series.* Biol Cybern, vol. 77, no. 5, pages 339–50, 1997. (Cited on page 107.)

[Achard 2008] S Achard, DS Bassett, A Meyer-Lindenberg and E Bullmore. *Fractal connectivity of long-memory networks.* Phys Rev E, vol. 77, no. 3, pages 1–12, 2008. (Cited on page 143.)

[Ahissar 1997] M Ahissar and S Hochstein. *Task difficulty and the specificity of perceptual learning.* Nature, vol. 387, no. 6631, pages 401–6, 1997. (Cited on pages 12 and 90.)

[Ahissar 2004] M Ahissar and S Hochstein. *The reverse hierarchy theory of visual perceptual learning.* Trends Cogn Sci, vol. 8, no. 10, pages 457–64, 2004. (Cited on pages 14, 87 and 90.)

[Ahissar 2009] M Ahissar, M Nahum, I Nelken and S Hochstein. *Reverse hierarchies and sensory learning.* Philos Trans R Soc Lond B Biol Sci, vol. 364, no. 1515, pages 285–99, 2009. (Cited on page 13.)

[Ahlfors 1999] SP Ahlfors, GV Simpson, AM Dale, JW Belliveau, AK Liu, A Korvenoja, J Virtanen, M Huotilainen, RBH Tootell, HJ Aronen and RJ Ilmoniemi. *Spatiotemporal activity of a cortical network for processing visual motion revealed by MEG and fMRI.* J Neurophysiol, vol. 82, no. 5, pages 2545–55, 1999. (Cited on pages 63 and 73.)

[Ahmadi 2013] K Ahmadi, M Ahmadlou, M Rezazade, E Azad-Marzabadi and F Sajedi. *Brain activity of women is more fractal than men.* Neurosci Lett, vol. 535, pages 7–11, 2013. (Cited on page 97.)

[Alais 2004] D Alais and D Burr. *No direction-specific bimodal facilitation for audiovisual motion detection.* Brain Res Cogn Brain Res, vol. 19, no. 2, pages 185–94, 2004. (Cited on pages 16 and 34.)

[Alink 2008] A Alink, W Singer and L Muckli. *Capture of auditory motion by vision is represented by an activation shift from auditory to visual motion cortex.* J Neurosci, vol. 28, no. 11, pages 2690–7, 2008. (Cited on pages 15, 88 and 90.)

[Amano 2006] K Amano, N Goda, S Nishida, Y Ejima, T Takeda and Y Ohtani. *Estimation of the timing of human visual perception from magnetoencephalography.* J Neurosci, vol. 26, no. 15, pages 3981–91, 2006. (Cited on pages 64 and 73.)

[Amedi 2007] A Amedi, WM Stern, JA Camprodon, F Bermpohl, L Merabet, S Rotman, C Hemond, P Meijer and A Pascual-Leone. *Shape conveyed by visual-to-auditory sensory substitution activates the lateral occipital complex.* Nat Neurosci, vol. 10, no. 6, pages 687–9, 2007. (Cited on page 90.)

[Aschwanden 2013] MJ Aschwanden. Self-organized criticality systems. Open Academic Press, Berlin, 2013. (Cited on pages 98 and 104.)

[Aspell 2005] JE Aspell, T Tanskanen and AC Hurlbert. *Neuromagnetic correlates of visual motion coherence.* Eur J Neurosci, vol. 22, no. 11, pages 2937–45, 2005. (Cited on pages 61, 62 and 73.)

[Babiloni 2011] C Babiloni, N Marzano, R Lizio, A Valenzano, AI Triggiani, A Petito, A Bellomo, B Lecce, C Mundi, A Soricelli, C Limatola, G Cibelli and C Del Percio. *Resting state cortical electroencephalographic rhythms in subjects with normal and abnormal body weight.* Neuroimage, vol. 58, no. 2, pages 698–707, 2011. (Cited on page 95.)

[Bach-y Rita 2003] P Bach-y Rita and SW Kercel. *Sensory substitution and the human−machine interface.* Trends Cogn Sci, vol. 7, no. 12, pages 541–6, 2003. (Cited on pages xvi, 4, 14, 17 and 90.)

[Bacry 2001] E Bacry, J Delour and J Muzy. *Multifractal random walk.* Phys Rev E, vol. 64, no. 2, pages 2–5, 2001. (Cited on pages 105, 106 and 117.)

[Baillet 2001] S Baillet, JC Mosher and RM Leahy. *Electromagnetic brain mapping.* IEEE Signal Process Mag, vol. 18, no. 6, pages 14–30, 2001. (Cited on pages 46, 47 and 50.)

[Bak 1987] P Bak, C Tang and K Wiesenfeld. *Self-organized criticality: An explanation of the $1/f$ noise.* Phys Rev Lett, vol. 59, no. 4, pages 381–4, 1987. (Cited on page 97.)

[Bak 1988] P Bak, C Tang and K Wiesenfeld. *Self-organized criticality.* Phys Rev A, vol. 38, no. 1, pages 364–74, 1988. (Cited on pages xiv, 2 and 97.)

[Baldassarre 2012] A Baldassarre, CM Lewis, G Committeri and AZ Snyder. *Individual variability in functional connectivity predicts performance of a perceptual task.* Proc Natl Acad Sci USA, vol. 109, no. 9, pages 3516–21, 2012. (Cited on pages 94 and 139.)

[Baranauskas 2012] G Baranauskas, E Maggiolini, A Vato, G Angotzi, A Bonfanti, G Zambra, A Spinelli and L Fadiga. *Origins of $1/f^2$ scaling in the power spectrum of intracortical local field potential.* J Neurophysiol, vol. 107, no. 3, pages 984–94, 2012. (Cited on page 98.)

[Barlow 1997] H Barlow and SP Tripathy. *Correspondence noise and signal pooling in the detection of coherent visual motion.* J Neurosci, vol. 17, no. 20, pages 7954–66, 1997. (Cited on page 23.)

[Bassett 2006] DS Bassett, A Meyer-Lindenber, S Achard, T Duke and E Bullmore. *Adaptive reconfiguration of fractal small-world human brain functional networks.* Proc Natl Acad Sci USA, vol. 103, no. 51, pages 19518–23, 2006. (Cited on page 98.)

[Bavelier 2002] D Bavelier and HJ Neville. *Cross-modal plasticity: where and how?* Nat Rev Neurosci, vol. 3, no. 6, pages 443–52, 2002. (Cited on pages 14 and 16.)

[Bavelier 2010] D Bavelier and EA Hirshorn. *I see where you're hearing: how cross-modal plasticity may exploit homologous brain structures.* Nat Neurosci, vol. 13, no. 11, pages 1309–11, 2010. (Cited on pages xvi, 4 and 18.)

[Beauchamp 2004a] MS Beauchamp, BD Argall, J Bodurka, JH Duyn and A Martin. *Unraveling multisensory integration: patchy organization within human STS multisensory cortex.* Nat Neurosci, vol. 7, no. 11, pages 1190–2, 2004. (Cited on pages 65, 66 and 89.)

[Beauchamp 2004b] MS Beauchamp, KE Lee, BD Argall and A Martin. *Integration of auditory and visual information about objects in superior temporal sulcus.* Neuron, vol. 41, no. 5, pages 809–23, 2004. (Cited on page 65.)

[Becker 2008] HGT Becker, M Erb and T Haarmeier. *Differential dependency on motion coherence in subregions of the human MT+ complex.* Eur J Neurosci, vol. 28, no. 8, pages 1674–85, 2008. (Cited on pages 61 and 62.)

[Bédard 2009] C Bédard and A Destexhe. *Macroscopic models of local field potentials and the apparent* $1/f$ *noise in brain activity.* Biophys J, vol. 96, no. 7, pages 2589–603, 2009. (Cited on page 98.)

[Bedny 2010] M Bedny, T Konkle, K Pelphrey, R Saxe and A Pascual-Leone. *Sensitive Period for a Multimodal Response in Human Visual Motion Area MT/MST.* Curr Biol, vol. 20, no. 21, pages 1900–6, 2010. (Cited on pages xvii, 4, 18 and 88.)

[Beggs 2003] JM Beggs and D Plenz. *Neuronal avalanches in neocortical circuits.* J Neurosci, vol. 23, no. 35, pages 11167–77, 2003. (Cited on page 97.)

[Bell 1995] AJ Bell and TJ Sejnowski. *An Information-Maximization Approach to Blind Separation and Blind Deconvolution.* Neural Comput, vol. 7, no. 6, pages 1129–59, 1995. (Cited on page 46.)

[Benevento 1977] LA Benevento, J Fallon, BJ Davis and M Rezak. *Auditory-visual interaction in single cells in the cortex of the superior temporal sulcus and the orbital frontal cortex of the macaque monkey.* Exp Neurol, vol. 57, no. 3, pages 849–72, 1977. (Cited on page 65.)

[Britten 1992] KH Britten, MN Shadlen, WT Newsome and JA Movshon. *The analysis of visual motion : a comparison of neuronal and psychophysical performance.* J Neurosci, vol. 12, no. 12, pages 4745–65, 1992. (Cited on page 73.)

[Bruce 1981] C Bruce, R Desimone and CG Gross. *Visual properties of neurons in a polysensory area in superior temporal sulcus of the macaque.* J Neurophysiol, vol. 46, no. 2, pages 369–84, 1981. (Cited on page 65.)

[Buiatti 2007] M Buiatti, D Papo, PM Baudonnière and C van Vreeswijk. *Feedback modulates the temporal scale-free dynamics of brain electrical activity in a hypothesis testing task.* Neuroscience, vol. 146, no. 3, pages 1400–12, 2007. (Cited on pages xv, 3, 97 and 102.)

[Bullmore 2004] E Bullmore, J Fadili, V Maxim, L Sendur, B Whitcher, J Suckling, M Brammer and M Breakspear. *Wavelets and functional magnetic resonance imaging of the human brain.* Neuroimage, vol. 23 Suppl 1, pages S234–49, 2004. (Cited on pages 96 and 157.)

[Bullmore 2009] E Bullmore and O Sporns. *Complex brain networks: graph theoretical analysis of structural and functional systems.* Nat Rev Neurosci, vol. 10, no. 3, pages 186–98, 2009. (Cited on page 98.)

[Bullmore 2012] E Bullmore and O Sporns. *The economy of brain network organization.* Nat Rev Neurosci, vol. 13, no. 5, pages 336–49, 2012. (Cited on page 98.)

[Bullock 2003] TH Bullock, MC Mcclune and JT Enright. *Are the electroencephalograms mainly rhythmic? Assessment of periodicity in wide-band time series.* Neuroscience, vol. 121, no. 1, pages 233–52, 2003. (Cited on pages xiv, 1 and 95.)

[Buzsáki 2004] G Buzsáki and A Draguhn. *Neuronal oscillations in cortical networks.* Science, vol. 304, no. 5679, pages 1926–9, 2004. (Cited on pages xxxi, 95 and 148.)

[Buzsaki 2012] G Buzsaki, CA Anastassiou and C Koch. *The origin of extracellular fields and currents–EEG, ECoG, LFP and spikes.* Nat Rev Neurosci, vol. 13, no. 6, pages 407–20, 2012. (Cited on page 97.)

[Chan 2013] AW Chan. *Functional organization and visual representations of human ventral lateral prefrontal cortex.* Frontiers in psychology, vol. 4, no. July, page 371, 2013. (Cited on page 87.)

[Chhabra 1989] A Chhabra and RV Jensen. *Direct determination of the $f(\alpha)$ singularity spectrum.* Phys Rev Lett, vol. 62, no. 12, pages 1327–30, 1989. (Cited on page 107.)

[Chialvo 2010] DR Chialvo. *Emergent complex neural dynamics.* Nat Phys, vol. 6, no. 10, pages 744–50, 2010. (Cited on page 97.)

[Ciuciu 2008] P Ciuciu, P Abry, C Rabrait and H Wendt. *Log Wavelet Leaders Cumulant Based Multifractal Analysis of EVI fMRI Time Series: Evidence of Scaling in Ongoing and Evoked Brain Activity.* IEEE J Sel Top Signal Process, vol. 2, no. 6, pages 929–43, 2008. (Cited on pages 108 and 109.)

[Ciuciu 2012] P Ciuciu, G Varoquaux, P Abry, S Sadaghiani and A Kleinschmidt. *Scale-Free and Multifractal Time Dynamics of fMRI Signals during Rest and Task.* Front Physiol, vol. 3, no. 6, page 186, 2012. (Cited on pages xv, 3, 97, 108, 116, 139 and 140.)

[Ciuciu rev] P Ciuciu, P Abry and BJ He. *Interplay between functional connectivity and scale-free dynamics in intrinsic fMRI networks.* Submitted to Proc Natl Acad Sci USA, under rev. (Cited on page 143.)

[Clayton 1997] K Clayton and BB Frey. *Studies of mental "noise".* Nonlinear Dynamics Psychol Life Sci, vol. 1, no. 3, pages 173–80, 1997. (Cited on page 101.)

[Cole 2010] DM Cole, SM Smith and CF Beckmann. *Advances and pitfalls in the analysis and interpretation of resting-state FMRI data.* Front Syst Neurosci, vol. 4, no. 4, page 8, 2010. (Cited on page 94.)

[Comon 1994] P Comon. *Independent component analysis, A new concept?* Signal processing, vol. 36, no. 3, pages 287–314, 1994. (Cited on page 46.)

[Dale 1999] AM. Dale, B Fischl and MI Sereno. *Cortical surface-based analysis. I. Segmentation and surface reconstruction.* Neuroimage, vol. 9, no. 2, pages 179–94, 1999. (Cited on page 53.)

[Dale 2000] AM Dale, AK Liu, BR Fischl and RL Buckner. *Dynamic statistical parametric mapping: combining fMRI and MEG for high-resolution imaging of cortical activity.* Neuron, vol. 26, no. 1, pages 55–67, 2000. (Cited on pages 52 and 54.)

[Darvas 2004] F Darvas, D Pantazis, E Kucukaltun-Yildirim and RM Leahy. *Mapping human brain function with MEG and EEG: methods and validation.* Neuroimage, vol. 23 Suppl 1, pages S289–99, 2004. (Cited on page 46.)

[de Arcangelis 2006] L de Arcangelis, C Perrone-Capano and HJ Herrmann. *Self-organized criticality model for brain plasticity.* Phys Rev Lett, vol. 96, no. 2, page 028107, 2006. (Cited on page 97.)

[de Arcangelis 2010] L de Arcangelis and HJ Herrmann. *Learning as a phenomenon occurring in a critical state.* Proc Natl Acad Sci USA, vol. 107, no. 9, pages 3977–81, 2010. (Cited on page 97.)

[de Pasquale 2010] F de Pasquale, S Della Penna, AZ Snyder, CM Lewis, D Mantini, L Marzetti, P Belardinelli, L Ciancetta, V Pizzella, GL Romani and M Corbetta. *Temporal dynamics of spontaneous MEG activity in brain networks.* Proc Natl Acad Sci USA, vol. 107, no. 13, pages 6040–5, 2010. (Cited on pages xiii, 1 and 95.)

[Dehghani 2010] N Dehghani, C Bédard, SS Cash, E Halgren and A Destexhe. *Comparative power spectral analysis of simultaneous elecroencephalographic and magnetoencephalographic recordings in humans suggests non-resistive extracellular media.* J Comput Neurosci, vol. 29, no. 3, pages 405–21, 2010. (Cited on pages 114 and 139.)

[Dehghani 2012] N Dehghani, NG Hatsopoulos, ZD Haga, RA Parker, B Greger, E Halgren, SS Cash and A Destexhe. *Avalanche Analysis from Multielectrode Ensemble Recordings in Cat, Monkey, and Human Cerebral Cortex during Wakefulness and Sleep.* Front Physiol, vol. 3, no. 8, page 302, 2012. (Cited on page 98.)

[Dienes 2008] Z Dienes. *Subjective measures of unconscious knowledge.* Prog Brain Res, vol. 168, no. 7, pages 49–64, 2008. (Cited on page 31.)

[Dietrich 1997] CR Dietrich and GN Newsam. *Fast and exact simulation of stationary Gaussian processes through circulant embedding of the covariance matrix.* SIAM J Sci Comput, vol. 18, no. 4, pages 1088–107, 1997. (Cited on page 100.)

[Dormal 2011] G Dormal and O Collignon. *Functional selectivity in sensory-deprived cortices.* J Neurophysiol, vol. 105, no. 6, pages 2627–30, 2011. (Cited on pages xvii, 4 and 18.)

[Drew 2006] PJ Drew and LF Abbott. *Models and properties of power-law adaptation in neural systems.* J Neurophysiol, vol. 96, no. 2, pages 826–33, 2006. (Cited on page 97.)

[Driver 2000] J Driver and C Spence. *Multisensory perception: beyond modularity and convergence.* Curr Biol, vol. 10, no. 20, pages R731–5, 2000. (Cited on page 15.)

[Eke 2002] A Eke, P Herman, L Kocsis and LR Kozak. *Fractal characterization of complexity in temporal physiological signals.* Physiol Meas, vol. 23, no. 1, pages R1–38, 2002. (Cited on pages 99 and 101.)

[Evans 2010] KK Evans and A Treisman. *Natural cross-modal mappings between visual and auditory features.* J Vis, vol. 10, no. 1, pages 1–12, 2010. (Cited on pages 23 and 34.)

[Fahle 2005] M Fahle. *Perceptual learning: specificity versus generalization.* Curr Opin Neurobiol, vol. 15, no. 2, pages 154–60, 2005. (Cited on pages 12 and 89.)

[Figliola 2010] A Figliola, E Serrano, G Paccosi and M Rosenblatt. *About the effectiveness of different methods for the estimation of the multifractal spectrum of natural series.* Int J Bifurcat Chaos, vol. 20, no. 2, pages 331–9, 2010. (Cited on page 107.)

[Fischl 1999a] B Fischl, MI Sereno and AM Dale. *Cortical Surface-Based Analysis. II: Inflation, Flattening, and a Surface-Based Coordinate System.* Neuroimage, vol. 9, no. 2, pages 195–207, 1999. (Cited on page 53.)

[Fischl 1999b] B Fischl, MI Sereno, RBH Tootell and AM Dale. *High-resolution intersubject averaging and a coordinate system for the cortical surface.* Hum Brain Mapp, vol. 8, no. 4, pages 272–84, 1999. (Cited on pages 53, 54 and 126.)

[Fischl 2000] B Fischl and AM Dale. *Measuring the thickness of the human cerebral cortex from magnetic resonance images.* Proc Natl Acad Sci USA, vol. 97, no. 20, pages 11050–5, 2000. (Cited on page 53.)

[Fox 2006] MD Fox, M Corbetta, AZ Snyder, JL Vincent and ME Raichle. *Spontaneous neuronal activity distinguishes human dorsal and ventral attention systems.* Proc Natl Acad Sci USA, vol. 103, no. 26, pages 10046–51, 2006. (Cited on page 94.)

[Fox 2007] MD Fox and ME Raichle. *Spontaneous fluctuations in brain activity observed with functional magnetic resonance imaging.* Nat Rev Neurosci, vol. 8, no. 9, pages 700–11, 2007. (Cited on pages xxxi, 94 and 148.)

[Freedman 2008] DJ Freedman and EK Miller. *Neural mechanisms of visual categorization: insights from neurophysiology.* Neurosci Biobehav Rev, vol. 32, no. 2, pages 311–29, 2008. (Cited on pages 12 and 64.)

[Freeman 2008] E Freeman and J Driver. *Direction of visual apparent motion driven solely by timing of a static sound.* Curr Biol, vol. 18, no. 16, pages 1262–6, 2008. (Cited on page 34.)

[Freeman 2009] WJ Freeman, SP Ahlfors and V Menon. *Combining fMRI with EEG and MEG in order to relate patterns of brain activity to cognition.* Int J Psychophysiol, vol. 73, no. 1, pages 43–52, 2009. (Cited on page 95.)

[Fries 2001] P. Fries. *Modulation of Oscillatory Neuronal Synchronization by Selective Visual Attention.* Science, vol. 291, no. 5508, pages 1560–3, 2001. (Cited on pages xxxi and 148.)

[Ghazanfar 2006] AA Ghazanfar and CE Schroeder. *Is neocortex essentially multisensory?* Trends Cogn Sci, vol. 10, no. 6, pages 278–85, 2006. (Cited on page 15.)

[Gibson 1963] EJ Gibson. *Perceptual learning.* Annu Rev Psychol, vol. 14, pages 29–56, 1963. (Cited on page 12.)

[Gilbert 2001] CD Gilbert, M Sigman and RE Crist. *The Neural Basis of Perceptual Learning.* Neuron, vol. 31, no. 5, pages 681–97, 2001. (Cited on pages 12, 13, 66 and 89.)

[Gilden 1995] DL Gilden, T Thornton and MW Mallon. $1/f$ *noise in human cognition.* Science, vol. 267, no. 5205, pages 1837–9, 1995. (Cited on pages 101 and 139.)

[Giraud 2007] AL Giraud, A Kleinschmidt, D Poeppel, TE Lund, RSJ Frackowiak and H Laufs. *Endogenous cortical rhythms determine cerebral specialization for speech perception and production.* Neuron, vol. 56, no. 6, pages 1127–34, 2007. (Cited on pages xxxi and 148.)

[Gireesh 2008] ED Gireesh and D Plenz. *Neuronal avalanches organize as nested theta- and beta/gamma-oscillations during development of cortical layer* 2/3. Proc Natl Acad Sci USA, vol. 105, no. 21, pages 7576–81, 2008. (Cited on page 95.)

[Gold 2010] JI Gold, CT Law, P Connolly and S Bennur. *Relationships between the threshold and slope of psychometric and neurometric functions during perceptual learning: implications for neuronal pooling.* J Neurophysiol, vol. 103, no. 1, pages 140–54, 2010. (Cited on pages 73 and 89.)

[Gold 2013] JI Gold and L Ding. *How mechanisms of perceptual decision-making affect the psychometric function.* Progress in neurobiology, vol. 103, pages 98–114, 2013. (Cited on page 89.)

[Goldberger 2002] AL Goldberger, LA Amaral, JM Hausdorff, PC Ivanov, CK Peng and HE Stanley. *Fractal dynamics in physiology: alterations with disease and aging.* Proc Natl Acad Sci USA, vol. 99 Suppl 1, pages 2466–72, 2002. (Cited on pages 102 and 107.)

[Goldstone 1998] RL Goldstone. *Perceptual learning.* Annu Rev Psychol, vol. 49, pages 585–612, 1998. (Cited on pages 12 and 89.)

[Gomez 2009] C Gomez, R Hornero, D Abasolo, A Fernandez and J Poza. *Study of the MEG background activity in Alzheimer's disease patients with scaling analysis methods.* In Conf Proc IEEE Eng Med Biol Soc, pages 3485–8, 2009. (Cited on page 97.)

[Grahn 2011] JA Grahn, MJ Henry and JD McAuley. *FMRI investigation of cross-modal interactions in beat perception: audition primes vision, but not vice versa.* Neuroimage, vol. 54, no. 2, pages 1231–43, 2011. (Cited on page 15.)

[Gramfort 2009a] A Gramfort. *Mapping, timing and tracking cortical activations with MEG and EEG: Methods and application to human vision.* Phd thesis, Telecom Paris, 2009. (Cited on pages 37, 41 and 48.)

[Gramfort 2009b] A Gramfort and M Kowalski. *Improving M/EEG source localization with an inter-condition sparse prior.* In Proc IEEE ISBI, pages 141–4, 2009. (Cited on page 52.)

[Gramfort 2011] A Gramfort, D Strohmeier, J Haueisen, M Hamalainen and M Kowalski. *Functional brain imaging with M/EEG using structured sparsity in time-frequency dictionaries.* Inf Process Med Imaging, vol. 22, pages 600–11, 2011. (Cited on page 52.)

[Gramfort 2012] A Gramfort, M Kowalski and M Hämäläinen. *Mixed-norm estimates for the M/EEG inverse problem using accelerated gradient methods.* Phys Med Biol, vol. 57, no. 7, pages 1937–61, 2012. (Cited on page 52.)

[Gramfort 2013] A Gramfort, M Luessi, E Larson, D Engemann, D Strohmeier, C Brodbeck, L Parkkonen and M Hämäläinen. *MNE software for processing MEG and EEG data.* Neuroimage, 2013. (Cited on pages 44, 47, 48, 53 and 54.)

[Grant 2000] KW Grant and PF Seitz. *The use of visible speech cues for improving auditory detection of spoken sentences.* J Acoust Soc Am, vol. 108, no. 3 Pt 1, pages 1197–208, 2000. (Cited on page 34.)

[Gu 2011] Y Gu, S Liu, CR Fetsch, Y Yang, S Fok, A Sunkara, GC DeAngelis and DE Angelaki. *Perceptual learning reduces interneuronal correlations in macaque visual cortex.* Neuron, vol. 71, no. 4, pages 750–61, 2011. (Cited on page 68.)

[Gusnard 2001] DA Gusnard and ME Raichle. *Searching for a baseline: functional imaging and the resting human brain.* Nat Rev Neurosci, vol. 2, no. 10, pages 685–94, 2001. (Cited on pages xiii, 1 and 94.)

[Guzman-Martinez 2012] E Guzman-Martinez, L Ortega, M Grabowecky, J Mossbridge and S Suzuki. *Interactive coding of visual spatial frequency and auditory amplitude-modulation rate.* Curr Biol, vol. 22, no. 5, pages 383–8, 2012. (Cited on page 23.)

[Hämäläinen 1989] MS Hämäläinen and J Sarvas. *Realistic conductivity geometry model of the human head for interpretation of neuromagnetic data.* IEEE Trans Biomed Eng, vol. 36, no. 2, pages 165–71, 1989. (Cited on page 54.)

[Hämäläinen 1993] M Hämäläinen, Riitta Hari and RJ Ilmoniemi. *Magnetoencephalography - theory, instrumentation, and applications to noninvasive studies of the working human brain.* Rev Mod Phys, vol. 65, no. 2, pages 413–97, 1993. (Cited on pages xxi, 38, 39, 41, 42, 46 and 50.)

[Hämäläinen 1994] MS Hämäläinen and RJ Ilmoniemi. *Interpreting magnetic fields of the brain: minimum norm estimates.* Med Biol Eng Comput, vol. 32, no. 1, pages 35–42, 1994. (Cited on page 51.)

[Hamamé 2011] CM Hamamé, D Cosmelli, R Henriquez and F Aboitiz. *Neural mechanisms of human perceptual learning: electrophysiological evidence for a two-stage process.* PLoS One, vol. 6, no. 4, page e19221, 2011. (Cited on page 68.)

[Hamker 2005] FH Hamker. *The reentry hypothesis: the putative interaction of the frontal eye field, ventrolateral prefrontal cortex, and areas V4, IT for attention and eye movement.* Cereb Cortex, vol. 15, no. 4, pages 431–47, 2005. (Cited on page 64.)

[Händel 2007] B Händel, W Lutzenberger, P Thier and T Haarmeier. *Opposite dependencies on visual motion coherence in human area MT+ and early visual cortex.* Cereb Cortex, vol. 17, no. 7, pages 1542–9, 2007. (Cited on pages 61, 62 and 73.)

[Hansen 2010] PC Hansen, ML Kringelbach and R Salmelin. MEG: An introduction to methods. Oxford university press, 2010. (Cited on pages 37, 41, 42, 43, 45, 49 and 60.)

[Hardstone 2012] R Hardstone, SS Poil, G Schiavone, R Jansen, VV Nikulin, HD Mansvelder and K Linkenkaer-Hansen. *Detrended fluctuation analysis: a scale-free view on neuronal oscillations.* Front Physiol, vol. 3, no. 11, page 450, 2012. (Cited on pages 97 and 102.)

[Haueisen 2002] J Haueisen, DS Tuch, C Ramon, PH Schimpf, VJ Wedeen, JS George and JW Belliveau. *The influence of brain tissue anisotropy on human EEG and MEG.* Neuroimage, vol. 15, no. 1, pages 159–66, 2002. (Cited on page 48.)

[Hauk 2011] O Hauk, DG Wakeman and R Henson. *Comparison of noise-normalized minimum norm estimates for MEG analysis using multiple resolution metrics.* Neuroimage, vol. 54, no. 3, pages 1966–74, 2011. (Cited on page 52.)

[He 2008] BJ He, AZ Snyder, JM Zempel, MD Smyth and ME Raichle. *Electrophysiological correlates of the brain's intrinsic large-scale functional architecture.* Proc Natl Acad Sci USA, vol. 105, no. 41, pages 16039–44, 2008. (Cited on page 96.)

[He 2009] BJ He and ME Raichle. *The fMRI signal, slow cortical potential and consciousness.* Trends Cogn Sci, vol. 13, no. 7, pages 302–9, 2009. (Cited on pages 96 and 97.)

[He 2010] BJ He, JM Zempel, AZ Snyder and ME Raichle. *The temporal structures and functional significance of scale-free brain activity.* Neuron, vol. 66, no. 3, pages 353–69, 2010. (Cited on pages xiv, xv, 2, 3, 95, 96, 97 and 149.)

[He 2011] BJ He. *Scale-free properties of the functional magnetic resonance imaging signal during rest and task.* J Neurosci, vol. 31, no. 39, pages 13786–95, 2011. (Cited on pages xv, 3, 97, 102, 116, 125, 139 and 140.)

[Heekeren 2008] HR Heekeren, S Marrett and LG Ungerleider. *The neural systems that mediate human perceptual decision making.* Nat Rev Neurosci, vol. 9, no. 6, pages 467–79, 2008. (Cited on page 63.)

[Helgason 2011] H Helgason, V Pipiras and P Abry. *Synthesis of multivariate stationary series with prescribed marginal distributions and covariance using circulant matrix embedding.* Signal processing, vol. 91, no. 8, pages 1741–58, 2011. (Cited on page 117.)

[Herault 1986] J Herault and C Jutten. *Space or time adaptive signal processing by neural network models.* In AIP Conference Proceedings, pages 206–11, Snowbird, UT, USA, 1986. (Cited on page 46.)

[Hesselmann 2008] G Hesselmann, CA Kell and A Kleinschmidt. *Ongoing activity fluctuations in hMT+ bias the perception of coherent visual motion.* J Neurosci, vol. 28, no. 53, pages 14481–5, 2008. (Cited on page 94.)

[Hidaka 2011] S Hidaka, W Teramoto, Y Sugita, Y Manaka, S Sakamoto and Y Suzuki. *Auditory motion information drives visual motion perception.* PLoS One, vol. 6, no. 3, page e17499, 2011. (Cited on page 34.)

[Hillebrand 2005] A Hillebrand, KD Singh, IE Holliday, PL Furlong and GR Barnes. *A new approach to neuroimaging with magnetoencephalography.* Hum Brain Mapp, vol. 25, no. 2, pages 199–211, 2005. (Cited on page 50.)

[Hipp 2011] JF Hipp, AK Engel and M Siegel. *Oscillatory Synchronization in Large-Scale Cortical Networks Predicts Perception.* Neuron, vol. 69, no. 2, pages 387–96, 2011. (Cited on page 148.)

[Howard 1996] RJ Howard, M Brammer, I Wright, PW Woodruff, ET Bullmore and S Zeki. *A direct demonstration of functional specialization within motion-related visual and auditory cortex of the human brain.* Curr Biol, vol. 6, no. 8, pages 1015–9, 1996. (Cited on page 66.)

[Hughes 1994] JR Hughes. EEG in Clinical Practice. Butterworth-Heinemann Medical, 2nd édition, 1994. (Cited on page 38.)

[Hyvärinen 2000] A Hyvärinen and E Oja. *Independent component analysis: algorithms and applications.* Neural Netw, vol. 13, no. 4-5, pages 411–30, 2000. (Cited on page 46.)

[Ilg 2004] UJ Ilg and J Churan. *Motion perception without explicit activity in areas MT and MST.* J Neurophysiol, vol. 92, no. 3, pages 1512–23, 2004. (Cited on pages 62 and 88.)

[Iurilli 2012] G Iurilli, D Ghezzi, U Olcese, G Lassi, C Nazzaro, R Tonini, V Tucci, F Benfenati and P Medini. *Sound-driven synaptic inhibition in primary visual cortex.* Neuron, vol. 73, no. 4, pages 814–28, 2012. (Cited on pages xxxi and 149.)

[Ivanov 1999] PC Ivanov, LA Amaral, AL Goldberger, S Havlin, MG Rosenblum, ZR Struzik and HE Stanley. *Multifractality in human heartbeat dynamics.* Nature, vol. 399, no. 6735, pages 461–5, 1999. (Cited on page 107.)

[Jaffard 2006] S Jaffard, B Lashermes and P Abry. *Wavelet leaders in multifractal analysis.* In T Qian, MI Vai and X Yuesheng, editeurs, Wavelet Analysis and Applications, pages 219–64. Birkhäuser, Cambridge, 2006. (Cited on page 108.)

[Jausovec 2010] N Jausovec and K Jausovec. *Resting brain activity: differences between genders.* Neuropsychologia, vol. 48, no. 13, pages 3918–25, 2010. (Cited on pages xv, 3, 95 and 97.)

[Kannathal 2005] N Kannathal, UR Acharya, CM Lim and PK Sadasivan. *Characterization of EEG–a comparative study.* Comput Methods Programs Biomed, vol. 80, no. 1, pages 17–23, 2005. (Cited on page 97.)

[Kantelhardt 2002] JW Kantelhardt, SA Zschiegnera, E Koscielny-Bunde, S Havlin, A Bunde and HE Stanley. *Multifractal detrended fluctuation analysis of nonstationary time series.* Physica A, vol. 316, pages 87–114, 2002. (Cited on page 107.)

[Kello 2010] CT Kello, GDA Brown, R Ferrer-I-Cancho, JG Holden, K Linkenkaer-Hansen, T Rhodes and GC Van Orden. *Scaling laws in cognitive sciences.* Trends Cogn Sci, vol. 14, no. 5, pages 223–32, 2010. (Cited on page 139.)

[Kendall 1977] MG Kendall and A Stuart. The Advanced Theory of Statistics: Distribution theory. Macmillan, 1 édition, 1977. (Cited on page 109.)

[Keshner 1982] MS Keshner. $1/f$ *noise.* Proc IEEE, vol. 70, no. 3, pages 212–8, 1982. (Cited on page 96.)

[Kim 2008] R Kim, AR Seitz and L Shams. *Benefits of stimulus congruency for multisensory facilitation of visual learning.* PLoS One, vol. 3, no. 1, page e1532, 2008. (Cited on pages 15 and 22.)

[Kim 2012] R Kim, MAK Peters and L Shams. $0 + 1 > 1$*: How adding noninformative sound improves performance on a visual task.* Psychol Sci, vol. 23, no. 1, pages 6–12, 2012. (Cited on page 22.)

[King 2009] AJ King. *Visual influences on auditory spatial learning.* Philos Trans R Soc Lond B Biol Sci, vol. 364, no. 1515, pages 331–9, 2009. (Cited on page 14.)

[Klaus 2011] A Klaus, S Yu and D Plenz. *Statistical analyses support power law distributions found in neuronal avalanches.* PLoS One, vol. 6, no. 5, page e19779, 2011. (Cited on page 97.)

[Klemen 2012] J Klemen and CD Chambers. *Current perspectives and methods in studying neural mechanisms of multisensory interactions.* Neurosci Biobehav Rev, vol. 36, no. 1, pages 111–33, 2012. (Cited on pages 14, 15, 16, 65, 66 and 67.)

[Kösem 2012] A Kösem and V van Wassenhove. *Temporal structure in audiovisual sensory selection.* PLoS One, vol. 7, no. 7, page e40936, 2012. (Cited on page 16.)

[Lakatos 2005] P Lakatos, AS Shah, KH Knuth, I Ulbert, G Karmos and CE Schroeder. *An oscillatory hierarchy controlling neuronal excitability and stimulus processing in the auditory cortex.* J Neurophysiol, vol. 94, no. 3, pages 1904–11, 2005. (Cited on page 95.)

[Lakatos 2008] P Lakatos, G Karmos, AD Mehta, I Ulbert and CE Schroeder. *Entrainment of neuronal oscillations as a mechanism of attentional selection.* Science, vol. 320, no. 5872, pages 110–13, 2008. (Cited on page 149.)

[Lam 2000] K Lam, Y Kaneoke, A Gunji, H Yamasaki, E Matsumoto, T Naito and R Kakigi. *Magnetic response of human extrastriate cortex in the detection of coherent and incoherent motion.* Neuroscience, vol. 97, no. 1, pages 1–10, 2000. (Cited on pages 61, 62 and 73.)

[Laufs 2003] H Laufs, K Krakow, P Sterzer, E Eger, A Beyerle, A Salek-Haddadi and A Kleinschmidt. *Electroencephalographic signatures of attentional and cognitive default modes in spontaneous brain activity fluctuations at rest.* Proc Natl Acad Sci USA, vol. 100, no. 19, pages 11053–8, 2003. (Cited on page 95.)

[Laughlin 1998] SB Laughlin, RR de Ruyter van Steveninck and JC Anderson. *The metabolic cost of neural information.* Nat Neurosci, vol. 1, no. 1, pages 36–41, 1998. (Cited on page 140.)

[Lee 1988] BB Lee, PR Martin and A Valberg. *The physiological basis of heterochromatic flicker photometry demonstrated in the ganglion cells of the macaque retina.* J Physiol, vol. 404, pages 323–47, 1988. (Cited on page 19.)

[Leistedt 2007] S Leistedt, M Dumont, N Coumans, JP Lanquart, F Jurysta and P Linkowski. *The modifications of the long-range temporal correlations of the sleep EEG due to major depressive episode disappear with the status of remission.* Neuroscience, vol. 148, no. 3, pages 782–93, 2007. (Cited on page 97.)

[Levina 2007] A Levina, JM Herrmann and T Geisel. *Dynamical synapses causing self-organized criticality in neural networks.* Nat Phys, vol. 3, no. 12, pages 857–60, 2007. (Cited on page 97.)

[Lewis 2009] CM Lewis, A Baldassarre, G Committeri, GL Romani and M Corbetta. *Learning sculpts the spontaneous activity of the resting human brain.* Proc Natl Acad Sci USA, vol. 106, no. 41, pages 17558–63, 2009. (Cited on pages xv, 3, 94, 120, 125 and 139.)

[Lewis 2010] R Lewis and U Noppeney. *Audiovisual synchrony improves motion discrimination via enhanced connectivity between early visual and auditory areas.* J Neurosci, vol. 30, no. 37, pages 12329–39, 2010. (Cited on pages 65, 66 and 89.)

[Li 2004] W Li, V Piëch and CD Gilbert. *Perceptual learning and top-down influences in primary visual cortex.* Nat Neurosci, vol. 7, no. 6, pages 651–7, 2004. (Cited on pages 12 and 14.)

[Lin 2006] FH Lin, JW Belliveau, AM Dale and MS Hämäläinen. *Distributed current estimates using cortical orientation constraints.* Hum Brain Mapp, vol. 27, no. 1, pages 1–13, 2006. (Cited on page 54.)

[Linkenkaer-Hansen 2001] K Linkenkaer-Hansen, VV Nikouline, JM Palva and RJ Ilmoniemi. *Long-range temporal correlations and scaling behavior in human brain oscillations.* J Neurosci, vol. 21, no. 4, pages 1370–7, 2001. (Cited on pages xv, 3, 97, 102 and 141.)

[Liu 2010] Z Liu, M Fukunaga, JA de Zwart and JH Duyn. *Large-scale spontaneous fluctuations and correlations in brain electrical activity observed with magnetoencephalography.* Neuroimage, vol. 51, no. 1, pages 102–11, 2010. (Cited on page 95.)

[Liu 2012] CC Liu and T Watanabe. *Accounting for speed-accuracy tradeoff in perceptual learning.* Vision Res, vol. 61, pages 107–14, 2012. (Cited on page 35.)

[Lopes 2009] R Lopes and N Betrouni. *Fractal and multifractal analysis: a review.* Med Image Anal, vol. 13, no. 4, pages 634–49, 2009. (Cited on page 105.)

[Lu 2004] H Lu, N Qian and Z Liu. *Learning motion discrimination with suppressed MT.* Vision Res, vol. 44, no. 15, pages 1817–25, 2004. (Cited on page 13.)

[Ma 2011] L Ma, S Narayana, DA Robin, PT Fox and J Xiong. *Changes occur in resting state network of motor system during 4 weeks of motor skill learning.* Neuroimage, vol. 58, no. 1, pages 226–33, 2011. (Cited on pages 94 and 139.)

[Maeda 2004] F Maeda, R Kanai and S Shimojo. *Changing pitch induced visual motion illusion.* Curr Biol, vol. 14, no. 23, pages R990–1, 2004. (Cited on pages 23 and 34.)

[Mantini 2007] D Mantini, MG Perrucci, C Del Gratta, GL Romani and M Corbetta. *Electrophysiological signatures of resting state networks in the human brain.* Proc Natl Acad Sci USA, vol. 104, no. 32, pages 13170–5, 2007. (Cited on page 95.)

[Maris 2007] E Maris and R Oostenveld. *Nonparametric statistical testing of EEG- and MEG-data.* J Neurosci Methods, vol. 164, no. 1, pages 177–90, 2007. (Cited on page 71.)

[Martin 2012] A Martin, KA Barnes and WD Stevens. *Spontaneous neural activity predicts individual differences in performance.* Proc Natl Acad Sci USA, vol. 109, no. 9, pages 3201–2, 2012. (Cited on page 94.)

[Maruyama 2002] K Maruyama, Y Kaneoke, K Watanabe and R Kakigi. *Human cortical responses to coherent and incoherent motion as measured by magnetoencephalography.* Neurosci Res, vol. 44, no. 2, pages 195–205, 2002. (Cited on pages 61 and 73.)

[Maxim 2005] V Maxim, L Sendur, J Fadili, J Suckling, R Gould, R Howard and E Bullmore. *Fractional Gaussian noise, functional MRI and Alzheimer's disease.* Neuroimage, vol. 25, no. 1, pages 141–58, 2005. (Cited on pages xv, 3, 97, 125, 139 and 140.)

[McGurk 1976] H McGurk and J MacDonald. *Hearing lips and seeing voices.* Nature, vol. 264, no. 5588, pages 746–8, 1976. (Cited on page 15.)

[Mercier 2009] M Mercier, S Schwartz, CM Michel and O Blanke. *Motion direction tuning in human visual cortex.* Eur J Neurosci, vol. 29, no. 2, pages 424–34, 2009. (Cited on page 73.)

[Meredith 1996] MA Meredith and BE Stein. *Spatial determinants of multisensory integration in cat superior colliculus neurons.* J Neurophysiol, vol. 75, no. 5, pages 1843–57, 1996. (Cited on page 16.)

[Miller 2010] KJ Miller, D Hermes, CJ Honey, M Sharma, RPN Rao, MD Nijs, EE Fetz, TJ Sejnowski, AO Hebb, JG Ojemann, S Makeig and EC Leuthardt. *Dynamic Modulation of Local Population Activity by Rhythm Phase in Human Occipital Cortex During a Visual Search Task.* Front Hum Neurosci, vol. 4, no. 10, page 197, 2010. (Cited on page 95.)

[Mitchel 2011] AD Mitchel and DJ Weiss. *Learning across senses: cross-modal effects in multisensory statistical learning.* J Exp Psychol Learn Mem Cogn, vol. 37, no. 5, pages 1081–91, 2011. (Cited on page 35.)

[Montez 2009] T Montez, SS Poil, BF Jones, I Manshanden, JPA Verbunt, BW van Dijk, AB Brussaard, A van Ooyen, CJ Stam, P Scheltens and K Linkenkaer-Hansen. *Altered temporal correlations in parietal alpha and prefrontal theta oscillations in early-stage Alzheimer disease.* Proc Natl Acad Sci USA, vol. 106, no. 5, pages 1614–9, 2009. (Cited on pages 97 and 102.)

[Monto 2008] S Monto, S Palva, J Voipio and JM Palva. *Very slow EEG fluctuations predict the dynamics of stimulus detection and oscillation amplitudes in humans.* J Neurosci, vol. 28, no. 33, pages 8268–72, 2008. (Cited on pages 95, 97 and 102.)

[Morrone 2010] MC Morrone. *Brain development: critical periods for cross-sensory plasticity.* Curr Biol, vol. 20, no. 21, pages R934–6, 2010. (Cited on pages xvii, 4, 18, 88 and 90.)

[Mosher 1999] JC Mosher, RM Leahy and PS Lewis. *EEG and MEG: forward solutions for inverse methods.* IEEE Trans Biomed Eng, vol. 46, no. 3, pages 245–59, 1999. (Cited on pages 46 and 54.)

[Moutoussis 1997] K Moutoussis and S Zeki. *A direct demonstration of perceptual asynchrony in vision.* Proc Biol Sci, vol. 264, no. 1380, pages 393–9, 1997. (Cited on page 64.)

[Movshon 1996] JA Movshon and WT Newsome. *Visual response properties of striate cortical neurons projecting to area MT in macaque monkeys.* J Neurosci, vol. 16, no. 23, pages 7733–41, 1996. (Cited on page 63.)

[Murray 2009] MM Murray and L Spierer. *Auditory spatio-temporal brain dynamics and their consequences for multisensory interactions in humans.* Hear Res, vol. 258, no. 1-2, pages 121–33, 2009. (Cited on pages 14, 16 and 17.)

[Nakamura 2003] H Nakamura. *Human V5 demonstrated by magnetoencephalography using random dot kinematograms of different coherence levels.* Neurosci Res, vol. 46, no. 4, pages 423–33, 2003. (Cited on pages 61, 62 and 73.)

[Noesselt 2007] T Noesselt, JW Rieger, MA Schoenfeld, M Kanowski, H Hinrichs, HJ Heinze and J Driver. *Audiovisual temporal correspondence modulates human multisensory superior temporal sulcus plus primary sensory cortices.* J Neurosci, vol. 27, no. 42, pages 11431–41, 2007. (Cited on page 89.)

[Noguchi 2005] Y Noguchi, Y Kaneoke, R Kakigi, HC Tanabe and N Sadato. *Role of the superior temporal region in human visual motion perception.* Cereb Cortex, vol. 15, no. 10, pages 1592–601, 2005. (Cited on pages 62, 90 and 139.)

[Novikov 1997] E Novikov, A Novikov, D Shannahoff-Khalsa, B Schwartz and J Wright. *Scale-similar activity in the brain.* Phys Rev E, vol. 56, no. 3, pages R2387–9, 1997. (Cited on pages xiv, 2, 96 and 101.)

[Overath 2010] T Overath, S Kumar, L Stewart, K von Kriegstein, R Cusack, A Rees and TD Griffiths. *Cortical mechanisms for the segregation and representation of acoustic textures.* J Neurosci, vol. 30, no. 6, pages 2070–6, 2010. (Cited on pages 23 and 64.)

[Palva 2013] JM Palva, A Zhigalov, J Hirvonen, O Korhonen, K Linkenkaer-Hansen and S Palva. *Neuronal long-range temporal correlations and avalanche dynamics are correlated with behavioral scaling laws.* Proc Natl Acad Sci USA, vol. 110, no. 9, pages 3585–90, 2013. (Cited on pages 97, 102 and 139.)

[Papo 2013] D Papo. *Why should cognitive neuroscientists study the brain's resting state?* Front Hum Neurosci, vol. 7, no. 2, page 45, 2013. (Cited on page 94.)

[Pascual-Leone 2001] A Pascual-Leone and R Hamilton. *The metamodal organization of the brain.* Prog Brain Res, vol. 134, pages 427–45, 2001. (Cited on pages xvi, 4 and 17.)

[Pascual-Marqui 2002] RD Pascual-Marqui. *Standardized low resolution brain electromagnetic tomography (sLORETA): technical details.* Methods Find Exp Clin Pharmacol, vol. 24 Suppl D, pages 5–12, 2002. (Cited on page 52.)

[Pelli 1997] DG Pelli. *The VideoToolbox software for visual psychophysics: transforming numbers into movies.* Spat Vis, vol. 10, no. 4, pages 437–42, 1997. (Cited on page 20.)

[Peng 1994] CK Peng, SV Buldyrev, S Havlin, M Simons, HE Stanley and AL Goldberger. *Mosaic organization of DNA nucleotides.* Phys Rev E Stat Phys Plasmas Fluids Relat Interdiscip Topics, vol. 49, no. 2, pages 1685–9, 1994. (Cited on pages xv, 3 and 101.)

[Petermann 2009] T Petermann, TC Thiagarajan, MA Lebedev, MA Nicolelis, DR Chialvo and D Plenz. *Spontaneous cortical activity in awake monkeys composed of neuronal avalanches.* Proc Natl Acad Sci USA, vol. 106, no. 37, pages 15921–26, 2009. (Cited on page 97.)

[Pitzalis 2013] S Pitzalis, C Bozzacchi, A Bultrini, P Fattori, C Galletti and F Di Russo. *Parallel motion signals to the medial and lateral motion areas V6 and MT+.* Neuroimage, vol. 67, pages 89–100, 2013. (Cited on page 63.)

[Plenz 2007] D Plenz and TC Thiagarajan. *The organizing principles of neuronal avalanches: cell assemblies in the cortex?* Trends Neurosci, vol. 30, no. 3, pages 101–10, 2007. (Cited on page 97.)

[Poil 2012] SS Poil, R Hardstone, HD Mansvelder and K Linkenkaer-Hansen. *Critical-state dynamics of avalanches and oscillations jointly emerge from balanced excitation/inhibition in neuronal networks.* J Neurosci, vol. 32, no. 29, pages 9817–23, 2012. (Cited on page 98.)

[Poirier 2005] C Poirier, O Collignon, AG Devolder, L Renier, A Vanlierde, D Tranduy and C Scheiber. *Specific activation of the V5 brain area by auditory motion processing: an fMRI study.* Brain Res Cogn Brain Res, vol. 25, no. 3, pages 650–8, 2005. (Cited on pages xvi, 4, 17, 66, 88 and 90.)

[Poirier 2006] C Poirier, O Collignon, C Scheiber, L Renier, A Vanlierde, D Tranduy, C Veraart and AG De Volder. *Auditory motion perception activates visual motion areas in early blind subjects.* Neuroimage, vol. 31, no. 1, pages 279–85, 2006. (Cited on pages 17, 66 and 88.)

[Popivanov 2005] D Popivanov, S Jivkova, V Stomonyakov and G Nicolova. *Effect of independent component analysis on multifractality of EEG during visual-motor task.* Signal processing, vol. 85, pages 2112–23, 2005. (Cited on pages xv, 3 and 140.)

[Popivanov 2006] D Popivanov, V Stomonyakov, Z Minchev, S Jivkova, P Dojnov, S Jivkov, E Christova and S Kosev. *Multifractality of decomposed EEG during imaginary and real visual-motor tracking.* Biol Cybern, vol. 94, no. 2, pages 149–56, 2006. (Cited on pages 107 and 140.)

[Powers 2012] AR Powers, MA Hevey and MT Wallace. *Neural correlates of multisensory perceptual learning.* J Neurosci, vol. 32, no. 18, pages 6263–74, 2012. (Cited on pages 65 and 90.)

[Proekt 2012] A Proekt, JR Banavar, A Maritan and DW Pfaff. *Scale invariance in the dynamics of spontaneous behavior.* Proc Natl Acad Sci USA, vol. 109, no. 26, pages 10564–9, 2012. (Cited on page 139.)

[Proulx 2012] MJ Proulx, DJ Brown, A Pasqualotto and P Meijer. *Multisensory perceptual learning and sensory substitution.* Neurosci Biobehav Rev, 2012. (Cited on pages 14, 15, 17, 18, 87, 88 and 90.)

[Raichle 2001] ME Raichle, AM MacLeod, AZ Snyder, WJ Powers, DA Gusnard and GL Shulman. *A default mode of brain function.* Proc Natl Acad Sci USA, vol. 98, no. 2, pages 676–82, 2001. (Cited on page 94.)

[Rauschecker 2000] JP Rauschecker and B Tian. *Mechanisms and streams for processing of "what" and "where" in auditory cortex.* Proc Natl Acad Sci USA, vol. 97, no. 22, pages 11800–6, 2000. (Cited on pages 63 and 81.)

[Ricciardi 2007] E Ricciardi, N Vanello, L Sani, C Gentili, EP Scilingo, L Landini, M Guazzelli, A Bicchi, JV Haxby and P Pietrini. *The effect of visual experience on the development of functional architecture in hMT+.* Cereb Cortex, vol. 17, no. 12, pages 2933–9, 2007. (Cited on pages xvi, 4 and 18.)

[Ricciardi 2011] E Ricciardi and P Pietrini. *New light from the dark: what blindness can teach us about brain function.* Curr Opin Neurol, vol. 24, no. 4, pages 357–63, 2011. (Cited on pages 14 and 18.)

[Ricciardi 2013] E Ricciardi, D Bonino, S Pellegrini and P Pietrini. *Mind the blind brain to understand the sighted one! Is there a supramodal cortical functional architecture?* Neurosci Biobehav Rev, 2013. (Cited on page 88.)

[Rodriguez 1999] E Rodriguez, N George, JP Lachaux, J Martinerie, B Renault and F Varela. *Perception ' s shadow : long- distance synchronization of human brain activity.* Nature, vol. 397, no. 6718, pages 430–3, 1999. (Cited on pages xxxi and 148.)

[Roe 2012] AW Roe, L Chelazzi, CE Connor, BR Conway, I Fujita, JL Gallant, H Lu and W Vanduffel. *Toward a unified theory of visual area V4.* Neuron, vol. 74, no. 1, pages 12–29, 2012. (Cited on page 139.)

[Romanski 2004] LM Romanski. *Domain specificity in the primate prefrontal cortex.* Cogn Affect Behav Neurosci, vol. 4, no. 4, pages 421–9, 2004. (Cited on pages 66 and 81.)

[Romanski 2007] LM Romanski. *Representation and integration of auditory and visual stimuli in the primate ventral lateral prefrontal cortex.* Cereb Cortex, vol. 17, no. 1, pages 61–9, 2007. (Cited on pages 66, 81 and 88.)

[Romanski 2012] LM Romanski and J Hwang. *Timing of audiovisual inputs to the prefrontal cortex and multisensory integration.* Neuroscience, vol. 214, pages 36–48, 2012. (Cited on pages 66, 81 and 88.)

[Ross 2007] LA Ross, D Saint-Amour, VM Leavitt, DC Javitt and JJ Foxe. *Do you see what I am saying? Exploring visual enhancement of speech comprehension in noisy environments.* Cereb Cortex, vol. 17, no. 5, pages 1147–53, 2007. (Cited on page 15.)

[Rousseeuw 1987] PJ Rousseeuw and AM Leroy. Robust regression and outlier detection. Wiley, New York, 1987. (Cited on page 73.)

[Sadaghiani 2009] S Sadaghiani, G Hesselmann and A Kleinschmidt. *Distributed and antagonistic contributions of ongoing activity fluctuations to auditory stimulus detection.* J Neurosci, vol. 29, no. 42, pages 13410–7, 2009. (Cited on page 94.)

[Sadaghiani 2010] S Sadaghiani, G Hesselmann, KJ Friston and A Kleinschmidt. *The relation of ongoing brain activity, evoked neural responses, and cognition.* Front Syst Neurosci, vol. 4, no. 6, page 20, 2010. (Cited on pages xiii, 1, 94 and 95.)

[Sadato 1996] N Sadato, A Pascual-Leone, J Grafman, V Ibañez, MP Deiber, G Dold and M Hallett. *Activation of the primary visual cortex by Braille reading in blind subjects.* Nature, vol. 380, no. 6574, pages 526–8, 1996. (Cited on page 17.)

[Sadato 2005] N Sadato, T Okada, M Honda, KI Matsuki, M Yoshida, KI Kashikura, W Takei, T Sato, T Kochiyama and Y Yonekura. *Cross-modal integration and plastic changes revealed by lip movement, random-dot motion and sign languages in the hearing and deaf.* Cereb Cortex, vol. 15, no. 8, pages 1113–22, 2005. (Cited on page 68.)

[Saenz 2008] M Saenz, LB Lewis and AG Huth. *Visual motion area MT+/V5 responds to auditory motion in human sight-recovery subjects.* J Neurosci, vol. 28, no. 20, pages 5141–8, 2008. (Cited on page 18.)

[Sakagami 2001] M Sakagami, Tsutsui KI, J Lauwereyns, M Koizumi, S Kobayashi and O Hikosaka. *A code for behavioral inhibition on the basis of color, but not motion, in ventrolateral prefrontal cortex of macaque monkey.* J Neurosci, vol. 21, no. 13, pages 4801–8, 2001. (Cited on page 64.)

[Sala-Llonch 2012] R Sala-Llonch, C Peña Gómez, EM Arenaza-Urquijo, D Vidal-Piñeiro, N Bargalló, C Junqué and D Bartrés-Faz. *Brain connectivity during resting state and subsequent working memory task predicts behavioural performance.* Cortex, vol. 48, no. 9, pages 1187–96, 2012. (Cited on pages 94 and 139.)

[Samorodnitsky 1994] G Samorodnitsky and MS Taqqu. Stable non-Gaussian random processes. Chapman and Hall, New York, 1994. (Cited on page 99.)

[Sapir 2005] A Sapir, G D'Avossa, M McAvoy, GL Shulman and M Corbetta. *Brain signals for spatial attention predict performance in a motion discrimination task.* Proc Natl Acad Sci USA, vol. 102, no. 49, pages 17810–5, 2005. (Cited on page 94.)

[Sasaki 2010] Y Sasaki, JE Nanez and T Watanabe. *Advances in visual perceptual learning and plasticity.* Nat Rev Neurosci, vol. 11, no. 1, pages 53–60, 2010. (Cited on pages xvi, 4, 12, 14, 68, 89 and 139.)

[Savitzky 1964] A Savitzky and MJE Golay. *Smoothing and differentiation of data by simplified least squares procedures.* Anal Chem, vol. 36, no. 8, pages 1627–39, 1964. (Cited on page 70.)

[Saygin 2007] AP Saygin. *Superior temporal and premotor brain areas necessary for biological motion perception.* Brain, vol. 130, no. Pt 9, pages 2452–61, 2007. (Cited on pages 62 and 90.)

[Schafer 2011] RW Schafer. *What is a Savitzky-Golay filter?* IEEE Signal Process Mag, vol. 28, no. 7, pages 111–7, 2011. (Cited on page 70.)

[Scheef 2009] L Scheef, H Boecker, M Daamen, U Fehse, MW Landsberg, DO Granath, H Mechling and AO Effenberg. *Multimodal motion processing in area V5/MT: evidence from an artificial class of audio-visual events.* Brain Res, vol. 1252, pages 94–104, 2009. (Cited on pages 18, 66, 88 and 90.)

[Schroeder 2008] CE Schroeder, P Lakatos, Y Kajikawa, S Partan and A Puce. *Neuronal oscillations and visual amplification of speech.* Trends Cogn Sci, vol. 12, no. 3, pages 106–13, 2008. (Cited on pages xxxi and 149.)

[Schwartz 2004] JL Schwartz, F Berthommier and C Savariaux. *Seeing to hear better: evidence for early audio-visual interactions in speech identification.* Cognition, vol. 93, no. 2, pages B69–78, 2004. (Cited on page 34.)

[Seitz 2005a] A Seitz and T Watanabe. *A unified model for perceptual learning.* Trends Cogn Sci, vol. 9, no. 7, pages 329–34, 2005. (Cited on pages 12 and 89.)

[Seitz 2005b] AR Seitz, JE Nanez, SR Holloway, S Koyama and T Watanabe. *Seeing what is not there shows the costs of perceptual learning.* Proc Natl Acad Sci USA, vol. 102, no. 25, pages 9080–5, 2005. (Cited on page 14.)

[Seitz 2006] AR Seitz, R Kim and L Shams. *Sound facilitates visual learning.* Curr Biol, vol. 16, no. 14, pages 1422–7, 2006. (Cited on pages 15, 22 and 34.)

[Seitz 2007] AR Seitz, R Kim, V van Wassenhove and L Shams. *Simultaneous and independent acquisition of multisensory and unisensory associations.* Perception, vol. 36, no. 10, pages 1445–53, 2007. (Cited on page 35.)

[Seitz 2009] AR Seitz and T Watanabe. *The phenomenon of task-irrelevant perceptual learning.* Vision Res, vol. 49, no. 21, pages 2604–10, 2009. (Cited on page 14.)

[Serletis 2012] D Serletis, BL Bardakjian, TA Valiante and PL Carlen. *Complexity and multifractality of neuronal noise in mouse and human hippocampal epileptiform dynamics.* J Neural Eng, vol. 9, no. 5, page 056008, 2012. (Cited on pages 97 and 107.)

[Shams 2008] Ladan Shams and Aaron R Seitz. *Benefits of multisensory learning.* Trends Cogn Sci, vol. 12, no. 11, pages 411–417, 2008. (Cited on pages xvi, 4, 14, 15, 16 and 34.)

[Shams 2010] L Shams and R Kim. *Crossmodal influences on visual perception.* Phys Life Rev, vol. 7, no. 3, pages 269–84, 2010. (Cited on pages 14 and 15.)

[Shibata 2011] K Shibata, T Watanabe, Y Sasaki and M Kawato. *Perceptual learning incepted by decoded fMRI neurofeedback without stimulus presentation.* Science, vol. 334, no. 6061, pages 1413–5, 2011. (Cited on page 14.)

[Shimizu 2004] Y Shimizu, M Barth, C Windischberger, E Moser and S Thurner. *Wavelet-based multifractal analysis of fMRI time series.* Neuroimage, vol. 22, no. 3, pages 1195–202, 2004. (Cited on pages xv, 3, 107 and 140.)

[Siegel 2012] M Siegel, TH Donner and AK Engel. *Spectral fingerprints of large-scale neuronal interactions.* Nat Rev Neurosci, vol. 13, no. 2, pages 20–5, 2012. (Cited on page 95.)

[Smit 2011] DJA Smit, EJC de Geus, ME van de Nieuwenhuijzen, CEM van Beijsterveldt, GCM van Baal, HD Mansvelder, DI Boomsma and K Linkenkaer-Hansen. *Scale-free modulation of resting-state neuronal oscillations reflects prolonged brain maturation in humans.* J Neurosci, vol. 31, no. 37, pages 13128–36, 2011. (Cited on page 97.)

[Song 2011] C Song, R Kanai, SM Fleming, RS Weil, DS Schwarzkopf and G Rees. *Relating inter-individual differences in metacognitive performance on different perceptual tasks.* Conscious Cogn, vol. 20, no. 4, pages 1787–92, 2011. (Cited on page 36.)

[Sowden 2000] PT Sowden, IR Davies and P Roling. *Perceptual learning of the detection of features in X-ray images: a functional role for improvements in adults' visual sensitivity?* J Exp Psychol Hum Percept Perform, vol. 26, no. 1, pages 379–90, 2000. (Cited on page 12.)

[Stam 2004] CJ Stam and EA de Bruin. *Scale-free dynamics of global functional connectivity in the human brain.* Hum Brain Mapp, vol. 22, no. 2, pages 97–109, 2004. (Cited on page 97.)

[Stam 2006] CJ Stam, BF Jones, I Manshanden, AM van Cappellen Van Walsum, T Montez, JPA Verbunt, JC de Munck, BW van Dijk, HW Berendse and P Scheltens. *Magnetoencephalographic evaluation of resting-state functional connectivity in Alzheimer's disease.* Neuroimage, vol. 32, no. 3, pages 1335–44, 2006. (Cited on page 95.)

[Stein 1993] BE Stein and MA Meredith. The merging of the senses. MIT Press, Cambridge, MA, US, 1993. (Cited on pages 15 and 90.)

[Stevens 2010] WD Stevens, RL Buckner and DL Schacter. *Correlated low-frequency BOLD fluctuations in the resting human brain are modulated by recent experience in category-preferential visual regions.* Cereb Cortex, vol. 20, no. 8, pages 1997–2006, 2010. (Cited on pages 94 and 139.)

[Stickgold 2000] R Stickgold, L James and JA Hobson. *Visual discrimination learning requires sleep after training.* Nat Neurosci, vol. 3, no. 12, pages 1237–8, 2000. (Cited on page 12.)

[Striem-Amit 2012] E Striem-Amit, O Dakwar, L Reich and A Amedi. *The large-Scale Organization of "Visual" Streams Emerges Without Visual Experience.* Cereb Cortex, vol. 22, no. 7, pages 1698–709, 2012. (Cited on page 17.)

[Suckling 2008] J Suckling, AM Wink, FA Bernard, A Barnes and E Bullmore. *Endogenous multifractal brain dynamics are modulated by age, cholinergic blockade and cognitive performance.* J Neurosci Methods, vol. 174, no. 2, pages 292–300, 2008. (Cited on pages xv, 3, 97, 107 and 140.)

[Sugihara 2006] T Sugihara, MD Diltz, BB Averbeck and LM Romanski. *Integration of auditory and visual communication information in the primate ventrolateral prefrontal cortex.* J Neurosci, vol. 26, no. 43, pages 11138–47, 2006. (Cited on page 88.)

[Swaminathan 2012] SK Swaminathan and DJ Freedman. *Preferential encoding of visual categories in parietal cortex compared with prefrontal cortex.* Nat Neurosci, vol. 15, no. 2, pages 315–20, 2012. (Cited on page 63.)

[Tagliazucchi 2013] E Tagliazucchi, F von Wegner, A Morzelewski, V Brodbeck, K Jahnke and H Laufs. *Breakdown of long-range temporal dependence in default mode and attention networks during deep sleep.* Proc Natl Acad Sci USA, vol. 110, no. 38, pages 15419–24, 2013. (Cited on pages 97 and 102.)

[Tallon-Baudry 1999] C Tallon-Baudry and O Bertrand. *Oscillatory gamma activity in humans and its role in object representation.* Trends Cogn Sci, vol. 3, no. 4, pages 151–62, 1999. (Cited on pages xxxi and 148.)

[Talsma 2009] D Talsma, D Senkowski and MG Woldorff. *Intermodal attention affects the processing of the temporal alignment of audiovisual stimuli.* Exp Brain Res, vol. 198, no. 2-3, pages 313–28, 2009. (Cited on pages xxxi and 148.)

[Talsma 2010] D Talsma, D Senkowski, S Soto-Faraco and MG Woldorff. *The multifaceted interplay between attention and multisensory integration.* Trends Cogn Sci, vol. 14, no. 9, pages 400–10, 2010. (Cited on pages 14, 16 and 35.)

[Tambini 2010] A Tambini, N Ketz and L Davachi. *Enhanced brain correlations during rest are related to memory for recent experiences.* Neuron, vol. 65, no. 2, pages 280–90, 2010. (Cited on pages 94 and 139.)

[Tanabe 2005] HC Tanabe, M Honda and N Sadato. *Functionally segregated neural substrates for arbitrary audiovisual paired-association learning.* J Neurosci, vol. 25, no. 27, pages 6409–18, 2005. (Cited on page 65.)

[Taulu 2004] S Taulu, M Kajola and J Simola. *Suppression of interference and artifacts by the Signal Space Separation Method.* Brain Topogr, vol. 16, no. 4, pages 269–75, 2004. (Cited on page 43.)

[Taulu 2006] S Taulu and J Simola. *Spatiotemporal signal space separation method for rejecting nearby interference in MEG measurements.* Phys Med Biol, vol. 51, no. 7, pages 1759–68, 2006. (Cited on page 53.)

[Taulu 2009] S Taulu and R Hari. *Removal of magnetoencephalographic artifacts with temporal signal-space separation: demonstration with single-trial auditory-evoked responses.* Hum Brain Mapp, vol. 30, no. 5, pages 1524–34, 2009. (Cited on page 44.)

[Teki 2011] S Teki, M Chait, S Kumar, K von Kriegstein and TD Griffiths. *Brain bases for auditory stimulus-driven figure-ground segregation.* J Neurosci, vol. 31, no. 1, pages 164–71, 2011. (Cited on page 64.)

[Thiele 2001] A Thiele, KR Dobkins and TD Albright. *Neural correlates of chromatic motion perception.* Neuron, vol. 32, pages 351–8, 2001. (Cited on page 63.)

[Tolkunov 2010] D Tolkunov, D Rubin and LR Mujica-Parodi. *Power spectrum scale invariance quantifies limbic dysregulation in trait anxious adults using fMRI: adapting methods optimized for characterizing autonomic dysregulation to neural dynamic time series.* Neuroimage, vol. 50, no. 1, pages 72–80, 2010. (Cited on pages 97 and 101.)

[Tootell 1995] RBH Tootell, JB Reppas, KK Kwong, R Malach, RT Born, TJ Brady, BR Rosen and JW Belliveau. *Functional analysis of human MT and related visual cortical areas using magnetic resonance imaging.* J Neurosci, vol. 15, no. 4, pages 3215–30, 1995. (Cited on page 61.)

[Tsushima 2006] Y Tsushima, Y Sasaki and T Watanabe. *Greater disruption due to failure of inhibitory control on an ambiguous distractor.* Science, vol. 314, no. 5806, pages 1786–8, 2006. (Cited on page 14.)

[Ungerleider 1982] LG Ungerleider and M Mishkin. Two cortical visual systems. MIT Press, Cambridge, MA, US, 1982. (Cited on pages 63, 66 and 81.)

[Ungerleider 1994] LG Ungerleider and JV Haxby. *'What' and 'where' in the human brain.* Curr Opin Neurobiol, vol. 4, no. 2, pages 157–65, 1994. (Cited on page 63.)

[Uusitalo 1997] MA Uusitalo and RJ Ilmoniemi. *Signal-space projection method for separating MEG or EEG into components.* Med Biol Eng Comput, vol. 35, no. 2, pages 135–40, 1997. (Cited on page 44.)

[Van de Ville 2010] D Van de Ville, J Britz and CM Michel. *EEG microstate sequences in healthy humans at rest reveal scale-free dynamics.* Proc Natl Acad Sci USA, vol. 107, no. 42, pages 18179–84, 2010. (Cited on pages xv, 3, 97, 108 and 140.)

[Van Veen 1997] BDD Van Veen, W van Drongelen, M Yuchtman and A Suzuki. *Localization of brain electrical activity via linearly constrained minimum variance spatial filtering.* IEEE Trans Biomed Eng, vol. 44, no. 9, pages 867–80, 1997. (Cited on page 50.)

[van Wassenhove 2007] V van Wassenhove and SS Nagarajan. *Auditory cortical plasticity in learning to discriminate modulation rate.* J Neurosci, vol. 27, no. 10, pages 2663–72, 2007. (Cited on pages 12 and 68.)

[van Wassenhove 2012] V van Wassenhove, AA Ghazanfar, KG Munhall, CE Schroeder and G Hall. *Bridging the gap between human and nonhuman studies of audiovisual integration.* In Barry E. Stein, editeur, The New Handbook of Multisensory Processing, chapitre II.9, page 153. MIT Press, Cambridge, 2012. (Cited on pages 14 and 148.)

[Varela 2001] F Varela, JP Lachaux, E Rodriguez and J Martinerie. *The brainweb : Phase synchronization and large-scale integration.* Nat Rev Neurosci, vol. 2, no. 4, pages 229–39, 2001. (Cited on pages xxxi and 148.)

[Veitch 1999] D Veitch and P Abry. *A wavelet-based joint estimator of the parameters of long-range dependence.* IEEE Trans Inf Theory, vol. 45, no. 3, pages 878–97, 1999. (Cited on pages xv, 3, 103 and 157.)

[Viviani 2001] P Viviani and C Aymoz. *Colour, form, and movement are not perceived simultaneously.* Vision Res, vol. 41, no. 22, pages 2909–18, 2001. (Cited on page 64.)

[von Kriegstein 2006] K von Kriegstein and AL Giraud. *Implicit multisensory associations influence voice recognition.* PLoS Biol, vol. 4, no. 10, page e326, 2006. (Cited on page 16.)

[von Saldern 2013] S von Saldern and U Noppeney. *Sensory and striatal areas integrate auditory and visual signals into behavioral benefits during motion discrimination.* J Neurosci, vol. 33, no. 20, pages 8841–9, 2013. (Cited on pages 65 and 88.)

[Voss 2012] P Voss and RJ Zatorre. *Organization and Reorganization of Sensory-Deprived Cortex.* Curr Biol, vol. 22, no. 5, pages R168–73, 2012. (Cited on pages 14, 17, 18, 65 and 88.)

[Watanabe 2001] T Watanabe, JE Nanez and Y Sasaki. *Perceptual learning without perception.* Nature, vol. 413, no. 6858, pages 844–8, 2001. (Cited on page 13.)

[Watanabe 2002] T Watanabe, JE Nanez, S Koyama, I Mukai, J Liederman and Y Sasaki. *Greater plasticity in lower-level than higher-level visual motion processing in a passive perceptual learning task.* Nat Neurosci, vol. 5, no. 10, pages 1003–9, 2002. (Cited on page 14.)

[Watson 1993] JDG Watson, R Myers, RSJ Frackowiak, JV Hajnal, RP Woods, JC Mazziotta, S Shipp and S Zeki. *Area V5 of the human brain: evidence from a combined study using Positron Emission Tomography and Magnetic Resonance Imaging.* Cereb Cortex, vol. 3, no. 2, pages 79–94, 1993. (Cited on page 61.)

[Weisberg 2005] S Weisberg. *Outliers and influence.* In Applied Linear Regression, chapitre 9, pages 194–210. Wiley, Hoboken, 3rd édition, 2005. (Cited on page 73.)

[Weiss 2009] B Weiss, Z Clemens, R Bódizs, Z Vágó and P Halász. *Spatio-temporal analysis of monofractal and multifractal properties of the human sleep EEG.* J Neurosci Methods, vol. 185, no. 1, pages 116–24, 2009. (Cited on pages xv, 3, 97, 114, 139 and 140.)

[Wendt 2007] H Wendt, P Abry and S Jaffard. *Bootstrap for Empirical Multifractal Analysis.* IEEE Signal Process Mag, vol. 24, no. 4, pages 38–48, 2007. (Cited on pages xv, 3, 108 and 109.)

[Wendt 2009a] H Wendt, SG Roux, S Jaffard and P Abry. *Wavelet leaders and bootstrap for multifractal analysis of images.* Signal Processing, vol. 89, no. 6, pages 1100–14, 2009. (Cited on page 110.)

[Wendt 2009b] H Wendt, A Scherrer, P Abry and S Achard. *Testing fractal connectivity in multivariate long memory processes.* In Proc IEEE Int Conf Acoust Speech Signal Process, pages 2913–16, 2009. (Cited on page 143.)

[Werner 2008] G Werner. *Brain dynamics across levels of organization.* J Physiol Paris, vol. 101, no. 4-6, pages 273–79, 2008. (Cited on page 97.)

[Werner 2010] S Werner and U Noppeney. *Distinct functional contributions of primary sensory and association areas to audiovisual integration in object categorization.* J Neurosci, vol. 30, no. 7, pages 2662–75, 2010. (Cited on pages 65 and 88.)

[Wichmann 2001] FA Wichmann and NJ Hill. *The psychometric function: I. Fitting, sampling, and goodness of fit.* Percept Psychophys, vol. 63, no. 8, pages 1293–313, 2001. (Cited on page 28.)

[Wierzchoń 2012] M Wierzchoń, D Asanowicz, B Paulewicz and A Cleeremans. *Subjective measures of consciousness in artificial grammar learning task.* Conscious Cogn, vol. 21, no. 3, pages 1141–53, 2012. (Cited on page 31.)

[Wink 2008] AM Wink, E Bullmore, A Barnes, F Bernard and J Suckling. *Monofractal and multifractal dynamics of low frequency endogenous brain oscillations in functional MRI.* Hum Brain Mapp, vol. 29, no. 7, pages 791–801, 2008. (Cited on pages xv, 3, 97 and 107.)

[Zeki 1993] S Zeki, JDG Watson and RSJ Frackowiak. *Going beyond the information given: the relation of illusory visual motion to brain activity.* Proc Biol Sci, vol. 252, no. 1335, pages 215–22, 1993. (Cited on page 61.)

[Zeki 1997] S Zeki and K Moutoussis. *Temporal hierarchy of the visual perceptive systems in the Mondrian world.* Proc Biol Sci, vol. 264, no. 1387, pages 1415–9, 1997. (Cited on page 64.)

[Zeki 2013] S Zeki and J Stutters. *Functional specialization and generalization for grouping of stimuli based on colour and motion.* Neuroimage, vol. 73, pages 156–66, 2013. (Cited on page 64.)

ERF and scale-free analyses of source-reconstructed MEG brain signals during a multisensory learning paradigm

Abstract: The analysis of Human brain activity in magnetoencephalography (MEG) can be generally conducted in two ways: either by focusing on the average response evoked by a stimulus repeated over time, more commonly known as an "event-related field" (ERF), or by decomposing the signal into functionally relevant oscillatory or frequency bands (such as alpha, beta or gamma). However, the major part of brain activity is arrhythmic and these approaches fail in describing its complexity, particularly in resting-state. As an alternative, the analysis of the $1/f$-type power spectrum observed in the very low frequencies, a hallmark of scale-free dynamics, can overcome these issues. Yet it remains unclear whether this scale-free property is functionally relevant and whether its fluctuations matter for behavior. To address this question, our first concern was to establish a visual learning paradigm that would entail functional plasticity during an MEG session. In order to optimize the training effects, we developed new audiovisual (AV) stimuli (an acoustic texture paired with a colored visual motion) that induced multisensory integration and indeed improved learning compared to visual training solely (V) or accompanied with acoustic noise (AVn). This led us to investigate the neural correlates of these three types of training using first a classical method such as the ERF analysis. After source reconstruction on each individual cortical surface using MNE-dSPM, the network involved in the task was identified at the group-level. The selective plasticity observed in the human motion area (hMT+) correlated across all individuals with the behavioral improvement and was supported by a larger network in AV comprising multisensory areas. On the basis of these findings, we further explored the links between the behavior and scale-free properties of these same source-reconstructed MEG signals. Although most studies restricted their analysis to the global measure of self-similarity (i.e. long-range fluctuations), we also considered local fluctuations (i.e. multifractality) by using the Wavelet Leader Based Multifractal Formalism (WLBMF). We found intertwined modulations of self-similarity and multifractality in the same cortical regions as those revealed by the ERF analysis. Most astonishing, the degree of multifractality observed in each individual converged during the training towards a single attractor that reflected the asymptotic behavioral performance in hMT+. Finally, these findings and their associated methodological issues are compared with the ones that came out from the ERF analysis.

Keywords: MEG, multisensory, audiovisual, colored motion, learning, plasticity, resting-state, infraslow activity, power law, scale invariance, multifractality, WLBMF

Analyses des champs évoqués et de l'invariance d'échelle des signaux cérébraux acquis en magnétoencéphalographie durant un paradigme d'apprentissage multisensoriel et reconstruits sur la surface corticale

Résumé : Il existe deux façons d'analyser l'activité cérébrale acquise en magnétoencéphalographie (MEG) : soit en moyennant les réponses suscitées par la répétition d'un stimulus afin d'observer le « champ évoqué » ; soit en décomposant le signal en bandes oscillatoires (tel que l'alpha, le beta ou le gamma), chacune étant associée à différents rôles fonctionnels. Ces méthodes ne prennent cependant pas compte de la complexité de l'activité cérébrale dont l'essentiel est arythmique, notamment au repos. Pour pallier à cela, une autre approche consiste à analyser le spectre de puissance en $1/f$ observable dans les très basses fréquences, une caractéristique des systèmes dont la dynamique est invariante d'échelle. Pour savoir si cette propriété joue un quelconque rôle dans le fonctionnement cérébral et si elle a des conséquences sur le comportement, nous avons établit un paradigme d'apprentissage visuel permettant d'observer de la plasticité fonctionnelle au cours d'une session MEG. Pour avoir un entraînement optimal, nous avons développé de nouveaux stimuli audiovisuels (AV) (une texture acoustique associée à un nuage de points colorés en mouvement) permettant une intégration multisensorielle et de ce fait un meilleur apprentissage que celui apporté par un entraînement visuel seul (V) ou accompagné d'un bruit acoustique (AVn). Nous avons ensuite étudié les corrélats neuronaux de ces trois types d'apprentissage par l'analyse classique des champs évoqués. Une fois l'activité reconstruite sur la surface corticale de chaque individu à l'aide de MNE-dSPM, nous avons identifié le réseau impliqué dans la tâche au sein de chaque groupe. En particulier, la plasticité sélective observée dans l'aire hMT+ associée au traitement du mouvement visuel corrélait avec les progressions comportementales des individus et était soutenue en AV par un plus vaste réseau comprenant notamment des aires multisensorielles. Parallèlement, nous avons exploré les liens reliant le comportement et les propriétés d'invariance d'échelle de ces mêmes signaux MEG reconstruits sur le cortex. Tandis que la plupart des études se limitent à analyser l'auto-similarité (une caractéristique globale synonyme de longue mémoire), nous avons aussi considéré les fluctuations locales (c-à-d la multifractalité) au moyen de l'analyse WLBMF. Nous avons trouvé des modulations couplées de l'auto-similarité et de la multifractalité dans des régions similaires à celles révélées par l'analyse des champs évoqués. Plus surprenant, Le degré de multifractalité relevé dans chaque individu convergeait durant l'entraînement vers un même attracteur reflétant la performance comportementale asymptotique.

Mots-clés : MEG, multisensoriel, audiovisuel, mouvement coloré, apprentissage, plasticité, repos, activité basse-fréquence, loi de puissance, invariance d'échelles, multifractalité, WLBMF